



# Functionalized Silica Nanostructures : Degradation Pathways and Biomedical Application from 2D to 3D

Yupeng Shi

## ► To cite this version:

Yupeng Shi. Functionalized Silica Nanostructures : Degradation Pathways and Biomedical Application from 2D to 3D. Material chemistry. Sorbonne Université, 2018. English. NNT : 2018SORUS122 . tel-02325780

**HAL Id: tel-02325780**

**<https://theses.hal.science/tel-02325780>**

Submitted on 22 Oct 2019

**HAL** is a multi-disciplinary open access archive for the deposit and dissemination of scientific research documents, whether they are published or not. The documents may come from teaching and research institutions in France or abroad, or from public or private research centers.

L'archive ouverte pluridisciplinaire **HAL**, est destinée au dépôt et à la diffusion de documents scientifiques de niveau recherche, publiés ou non, émanant des établissements d'enseignement et de recherche français ou étrangers, des laboratoires publics ou privés.

# Sorbonne Université

ED 397 Physique et chimie des matériaux

*Laboratoire de Chimie de la Matière Condensée de Paris, UMR 7574*

## **Functionalized Silica Nanostructures: Degradation Pathways and Biomedical Application from 2D to 3D**

Par Mr. Yupeng Shi

Thèse de doctorat de chimie des matériaux

Présentée et soutenue publiquement le 16 octobre 2018

Devant un jury composé de :

CHUBURU Françoise	PR Université de Reims Champagne-Ardenne	Rapporteur
GAZEAU Florence	DR CNRS Université Paris Diderot	Rapporteur
CUNIN Frédérique	CR CNRS Université de Montpellier	Examineur
NEVEU Sophie	MC HDR CNRS Sorbonne Université	Examineur
CORADIN Thibaud	DR CNRS Sorbonne Université	Directeur de thèse



# Acknowledgments

First of all, I would like to express my highest regards to my thesis supervisor Prof. Thibaud Coradin who brought me to this extraordinary field. I really appreciate his seriousness, kindness and full support during all the steps of this project from beginning to the end. He is one of the outstanding scientists and also my good friend, it was indeed a great honor to have him as my mentor. I will be always grateful for all that I have learned from him.

It is my great honor to work with all the faculty, staff, Ph.D. students and postdocs in LCMCP these three years. Thanks to Gervaise Mosser, Patrick LE Griel, Isabelle Genois, Haye Bernard for all the direct and help on the TEM, and SEM to observe the nanoparticle samples. Moreover, special thanks send to Christophe H  lary, from whom I learned a lot about the biological techniques. I also appreciate the MRI test and discussion with Flavien Guenneau. And furthermore, thanks to all the colleges who contribute to my thesis and life: Carole Aim  , Lea Trichet, Xiaolin Wang, Cl  ment Rieu, Dounia Dems, Lise Picaut, Kankan Qin, Nicolas Debons, Antoine Frayssinet, Kun Wang, *etc.*

Thank all my friends in Paris, like Teng Zhang, Wanli Gao, Ang Li, Bin Qiao *etc.* These guys always share the joy and happiness with me and give me support and encouragement when I need. They are truly good friends and deserve a lifetime of cherishing. I will I also appreciate the three years living in Cit   Universitaire which is a wonderful experience to meet a lot of people from all around the world. I would like to thank all people appeared in my life.

More importantly, I am very grateful to my family for their continued support. Thank you to my parents, who gave me the strongest support and love, although they haven't any sense about nanomaterials, and live in a small village for their whole life. Love them! Moreover, I also thank my two sisters for their support of the family during my absence. In addition, I would like to give my special thanks to my girlfriend, Ms. Meixia Li, thank you for her silent dedication to me for three years, I hope that her future days will be like a child every day.

At last, I dedicated this thesis to my grandfather who taught lots of knowledge and skills from the beginning of my life. Hope for his happiness in heaven.





« Je suis de ceux qui pensent que la science est d'une grande beauté. Un scientifique dans son laboratoire est non seulement un technicien : il est aussi un enfant placé devant des phénomènes naturels qui l'impressionnent comme des contes de fées..... Telle est bien la beauté et la noblesse de la science : désir sans fin de repousser les frontières du savoir, de traquer les secrets de la matière et de la vie sans idée préconçue des conséquences éventuelles »

— Marie Curie



## Table of Contents

<b>Acknowledgments.....</b>	<b>1</b>
<b>Table of Contents .....</b>	<b>5</b>
<b>General Introduction .....</b>	<b>9</b>
<b>Chapter 1 Literature review.....</b>	<b>13</b>
<b>1.1 The development of nanotechnology and nanomedicine .....</b>	<b>15</b>
1.1.1 Nanotechnology and its applications.....	15
1.1.2 Nanomedicine.....	16
<b>1.2 Drug delivery .....</b>	<b>18</b>
1.2.1 Overview .....	18
1.2.2 Nanocarriers used in drug delivery system .....	19
<b>1.3 Preparation of silica-based nanomaterials.....</b>	<b>27</b>
1.3.1 The solution chemistry of silica .....	28
1.3.2. Preparation of silica nanoparticles .....	30
1.3.3 Surface functionalization of silica nanoparticles .....	35
<b>1.4 Silica-based nanomaterials in biology and medicine .....</b>	<b>39</b>
1.4.1 Toxicity of silica nanoparticles in vitro and in vivo.....	39
1.4.2 Degradation of silica nanoparticles .....	40
1.4.3 Drug delivery applications .....	42
<b>1.5 Silica-biopolymer composite hydrogels .....</b>	<b>49</b>
1.5.1 Nanocomposite hydrogels .....	49
1.5.2 Silica-collagen hydrogels .....	51
1.5.3 Open questions and motivations of this work .....	54
<b>Chapter 2 Comparison of extracellular and intracellular degradation of nanostructured silica particles.....</b>	<b>73</b>
<b>2.1 Introduction .....</b>	<b>75</b>
<b>2.2 Experimental Section .....</b>	<b>76</b>
2.2.1 Materials.....	76
2.2.2 Synthesis of PEGylated silica nanostructures .....	76
2.2.3 Nanoparticle characterization and instruments. ....	79
2.2.4 Dissolution and degradation assays in buffer and culture medium.....	82
2.2.5 Cells and treatments with nanoparticles.....	82
2.2.6 Nanoparticle internalization, degradation and release. ....	82

2.2.7 Toxicological assays. ....	83
2.2.8 Statistical analysis. ....	83
<b>2.3 Results .....</b>	<b>83</b>
2.3.1 Synthesis and functionalization of nanostructured silica particles.....	83
2.3.2 Behaviour of nanoparticles in buffer and cell culture medium. ....	88
2.3.3 Nanoparticles behaviour in the presence of fibroblasts. ....	91
2.3.4 Degradation and release kinetics. ....	93
<b>2.4 Discussion .....</b>	<b>94</b>
<b>2.5 Conclusion.....</b>	<b>97</b>
<b>Chapter 3 Synthesis and properties of theranostic nanoplateform from 2D to 3D .....</b>	<b>101</b>
<b>3.1 Introduction .....</b>	<b>103</b>
<b>3.2 Materials and methods.....</b>	<b>105</b>
3.2.1 Materials and reagents.....	105
3.2.2 Preparation of HMSNs@MnO <sub>2</sub> /apt.....	105
3.2.3 Drug loading and release <i>in vitro</i> .....	106
3.2.5 <i>In vitro</i> cytotoxicity assays and cell uptake studies .....	107
3.2.6 Measurement of MRI relaxation properties .....	108
3.2.7. Cytotoxicity and functionality within 3D models .....	108
3.2.8. Statistical Analysis .....	109
<b>3.3. Results and discussion.....</b>	<b>109</b>
3.3.1 Preparation and characterization of the nanoplateforms .....	109
3.3.2 Drug release and MRI imaging properties of the nanoplateforms.....	114
3.3.3 Functionality of nanoplateforms in 3D biomimetic collagen matrices.....	119
<b>3.4 Conclusion.....</b>	<b>122</b>
<b>Chapter 4 Silica nanorods-collagen composite hydrogels: preparation, properties and magnetic engineering .....</b>	<b>131</b>
<b>4.1 Introduction .....</b>	<b>133</b>
<b>4.2 Experimental section.....</b>	<b>134</b>
4.2.1 Chemicals .....	134
4.2.2 Synthesis of SiNRs/collagen hydrogel composite .....	135
4.2.3 Characterizations .....	136
4.2.4 Cell experiments.....	138
4.2.5 Statistical Analysis .....	139
<b>4.3 Results and discussion.....</b>	<b>139</b>

4.3.1 Synthesis and characterization of Fe <sub>3</sub> O <sub>4</sub> -coated silica nanorods .....	139
4.3.2 SiNRs-collagen hydrogel composites .....	144
4.3.3 Magnetic SiNR-collagen hydrogels .....	154
<b>4.4 Conclusion.....</b>	<b>158</b>
<b>Conclusions and perspectives .....</b>	<b>161</b>
<b>List of Abbreviations.....</b>	<b>165</b>
<b>List of Figures.....</b>	<b>167</b>
<b>List of Tables.....</b>	<b>173</b>
<b>Appendix .....</b>	<b>175</b>



# General Introduction

In recent years, nanoscience and nanotechnology have attracted a lot of sight in many areas such as food safety, medicine, energy, environment science, and information technology<sup>1-4</sup>. At present, governments, organizations and research institutes invest more and more human and financial resources for their development and already achieved unprecedented progress. Data indicated that the USA have invested \$3.7 billion using its NNI in 2012, whereas the European Union has invested \$1.2 billion, and \$750 million for Japan<sup>5</sup>. More importantly, such investment is still developing rapidly that not only contributes to social benefits, but also greatly promotes economic growth. This area of science concerned with nanomaterials focuses on the following aspects: synthesis (new materials, or methods), manipulation, assembly, and application.

Among the most studied inorganic or organic materials, nanomaterials such as gold nanoparticles, silica, magnetic oxides ( $\text{Fe}_3\text{O}_4$ ), carbon materials and semiconductors attract a lot of attention<sup>6</sup>. These nanoparticles already play an important role in the real life, such as colloidal gold for immunological analysis<sup>7</sup>, carbon nanotubes suitable for electron transistor<sup>8</sup>, and QDs utilized as colourful screen materials<sup>9</sup>. One of the interests of these nanoparticles is the possibility to control the shape, size, composition and even the structures during the synthesis process that make them much flexible for the further surface functionalization and applications.

Silica is widely considered as a type of promising materials that can be used in the biomedical field. The reason is that there are many advantages of silicon dioxide. For examples, silica is a relatively common substance and its source of raw materials is very rich. Moreover, the synthesis and functionalization of silica nanoparticles by molecules, polymers, proteins, genes, are relatively easy to implement<sup>10</sup>. In addition, silica also has many excellent biological properties: low toxicity, degradation, good biocompatibility *etc.* Silica is already used in the food industry, environmental science, and medical field<sup>11</sup>. There are many current or planned applications of silica nanoparticles in bioimaging, drug delivery, gene therapy<sup>12</sup>. However, it inevitably raises several important questions, especially for the biological and medical areas. To develop the use of silica nanoparticles in the biomedical field, it is particularly important to understand their behavior in physiological conditions and intracellularly, including colloidal stability, biotoxicity, endocytosis, biodegradation, *etc.* Moreover, to understand to what extent



the control of particle characteristics allows to modify their behavior will optimize the nanoparticles adjusted to the intended applications.

Nanomaterial-based drug delivery system is an emerging drug delivery method. Nanocarriers for drug delivery can overcome many shortcomings of the traditional drug administration, such as improving drug solubility, controlling drug release, and targeting characteristics, all of which confer to this drug delivery method promising application prospects. At present, many organic nanocarriers, such as liposomes or polymeric microspheres<sup>13</sup>, inorganic nanocarriers, such as carbon nanomaterials, titanium dioxide, silicon dioxide<sup>14</sup>, alone or associated to hydrogels, were used for the delivery of drugs, genes, polypeptide proteins<sup>15</sup>, *etc.* Again, silica has been a widely studied nanocarrier.

The objective of this doctoral work is to study the physicochemical properties and biological interactions of different silica nanostructures, and evaluate their potential biomedical applications in imaging and drug delivery either in a 2D culture or within 3D collagen hydrogel matrices. With this purpose, the study was conducted at different levels. In the following pages, we first provide a literature review of the development of nanotechnology and nanomedicine, introduce the current drug delivery strategies and the problems they encountered. Then we focus on the physicochemical properties and surface functionalization of silica nanomaterials, as well as their reported applications in drug delivery. Their biological properties including toxicity, uptake, degradation of silica *in vitro* and *in vivo* are also summarized (Chapter 1).

In the second part, we present the first part of our project dedicated to the understanding of the intracellular fate of silica nanoparticles. We synthesized three types of fluorescent silica nanoparticles with various internal structures (core-shell bio-composite, multi-layered and hollow mesoporous). Then, the structures and surface properties of the nanoparticles were characterized, after which their biological toxicity and colloidal stability and dissolution were studied in a buffer and in a biological medium. Finally, fibroblasts were exposed to these particles in order to determine the interactions between the cells and the silica particles and their consequences on both the cellular activity and the fate of the colloids (Chapter 2).

The encouraging outcomes of this study led us to explore further biomedical applications of silica nanostructures. Here, we constructed multifunctional silica-based nanocarriers intended to be used as nanotheranostics platform. These nanostructures consist of hollow silica nanoparticles as the core containing the drugs and a thin layer of MnO<sub>2</sub> as a shell, acting both

as a gatekeeper and a source of paramagnetic species. In addition, a targeting agent aptamer (AS1411) was added on the outer layer. These nanocarriers exhibit excellent targeted and stimulated response properties for magnetic resonance imaging and doxorubicin release both in 2D conditions and in 3D biomimetic environments (Chapter 3).

One step further we explored 3D composite biomaterials consisting of two types of well-known bio-materials: silica and collagen. Collagen is the main structural protein mostly existed in fibrous tissues such as tendons, ligaments, and skin which owns excellent biocompatibility. Combining these two materials to form a composite gel material offer almost unlimited space for imagination. In the work, we prepared a composite collagen hydrogel incorporating silica nanorods. Here, silica nanorods can have two functions: regulating mechanical properties and acting as a drug carrier. The mechanical and chemical properties of the composite hydrogel could be tuned by adjusting the ratio of silica to collagen. The influence of the composite hydrogel on fibroblast cells growth and proliferation was studied. Lastly, magnetic hydrogels were prepared using magnetite nanoparticles attached to silica rods. It was found that this new type of magnetic composite can be structured under the action of an external magnetic field. (Chapter 4).

A conclusion section gathers our main results, enlightening our contribution to the area of silica nanoparticles in biomedicine, and provides some perspectives in the different fields relevant to this work.

## References

1. Kagan, C. R., At the Nexus of Food Security and Safety: Opportunities for Nanoscience and Nanotechnology. *Acs Nano* **2016**, 10, (3), 2985-2986.
2. Ranjan, S.; Dasgupta, N.; Chakraborty, A. R.; Samuel, S. M.; Ramalingam, C.; Shanker, R.; Kumar, A., Nanoscience and nanotechnologies in food industries: opportunities and research trends. *Journal Of Nanoparticle Research* **2014**, 16, (6).
3. Zach, M.; Hagglund, C.; Chakarov, D.; Kasemo, B., Nanoscience and nanotechnology for advanced energy systems. *Current Opinion In Solid State & Materials Science* **2006**, 10, (3-4), 132-143.
4. Chan, W. W. C.; Chhowalla, M.; Glotzer, S.; Gogotsi, Y.; Hafner, J. H.; Hammond, P. T., et al. Weiss, P. S., Nanoscience and Nanotechnology Impacting Diverse Fields of Science, Engineering, and Medicine. *Acs Nano* **2016**, 10, (12), 10615-10617.

5. Apply nanotech to up industrial, agri output Archived. *The Daily Star (Bangladesh)* **2012**, 17, (April).
6. Keller, A. A.; McFerran, S.; Lazareva, A.; Suh, S., Global life cycle releases of engineered nanomaterials. *Journal Of Nanoparticle Research* **2013**, 15, (6).
7. Song, C. Y.; Wang, Z. Y.; Zhang, R. H.; Yang, J.; Tan, X. B.; Cui, Y. P., Highly sensitive immunoassay based on Raman reporter-labeled immuno-Au aggregates and SERS-active immune substrate. *Biosensors & Bioelectronics* **2009**, 25, (4), 826-831.
8. Wong, H. S. P., Beyond the conventional transistor. *Ibm Journal Of Research And Development* **2002**, 46, (2-3), 133-168.
9. Gao, X. H.; Chan, W. C. W.; Nie, S. M., Quantum-dot nanocrystals for ultrasensitive biological labeling and multicolor optical encoding. *Journal Of Biomedical Optics* **2002**, 7, (4), 532-537.
10. Karakoti, A. S.; Das, S.; Thevuthasan, S.; Seal, S., PEGylated Inorganic Nanoparticles. *Angewandte Chemie-International Edition* **2011**, 50, (9), 1980-1994.
11. De, M.; Ghosh, P. S.; Rotello, V. M., Applications of Nanoparticles in Biology. *Advanced Materials* **2008**, 20, (22), 4225-4241.
12. Trewyn, B. G.; Slowing, II; Giri, S.; Chen, H. T.; Lin, V. S. Y., Synthesis and functionalization of a mesoporous silica nanoparticle based on the sol-gel process and applications in controlled release. *Accounts Of Chemical Research* **2007**, 40, (9), 846-853.
13. Lebhardt, T.; Roesler, S.; Beck-Broichsitter, M.; Kissel, T., Polymeric nanocarriers for drug delivery to the lung. *Journal Of Drug Delivery Science And Technology* **2010**, 20, (3), 171-180.
14. Paul, W.; Sharma, C. P., *Inorganic nanoparticles for targeted drug delivery*. **2010**; p 204-235.
15. Dalby, M. J.; Lee, L. L. C.; Yang, J. L.; MacIntyre, A.; McCully, M., Hydrogel nanoparticles for drug delivery. *Nanomedicine* **2013**, 8, (11), 1744-1745.

# Chapter 1 Literature review

“千里之行，始于足下”

《道德经》

## ***Abstract***

Since the beginning of the century, nanoparticles have developed with possible applications in many fields such as energy, materials and the medical and pharmaceutical field. Silica, thanks to the great ease and adaptability of particle synthesis and its biological inertia in the macroscopic state, is very widely studied for medical applications. Moreover, silica nanoparticles are already present in many products of daily life (cosmetics, food ...). In this chapter will first gather some key information about the synthesis and physicochemical properties of silica-based nanomaterials. Then, we will present the known elements concerning the internalization mechanisms, the toxicity as well as the fate of the silica nanomaterials. Finally, some of the biomedical applications of silica nanomaterials in 2D and the 3D matrix will be reviewed.

<b>1.1 The development of nanotechnology and nanomedicine .....</b>	<b>15</b>
1.1.1 Nanotechnology and its applications.....	15
1.1.2 Nanomedicine.....	16
<b>1.2 Drug delivery .....</b>	<b>18</b>
1.2.1 Overview .....	18
1.2.2 Nanocarriers used in drug delivery system .....	19
<b>1.3 Preparation of silica-based nanomaterials.....</b>	<b>27</b>
1.3.1 The solution chemistry of silica .....	28
1.3.2. Preparation of silica nanoparticles .....	30
1.3.3 Surface functionalization of silica nanoparticles .....	35
<b>1.4 Silica-based nanomaterials in biology and medicine .....</b>	<b>39</b>
1.4.1 Toxicity of silica nanoparticles in vitro and in vivo.....	39
1.4.2 Degradation of silica nanoparticles .....	40
1.4.3 Drug delivery applications .....	42
<b>1.5 Silica-biopolymer composite hydrogels.....</b>	<b>49</b>
1.5.1 Nanocomposite hydrogels .....	49
1.5.2 Silica-collagen hydrogels .....	51
1.5.3 Open questions and motivations of this work .....	54

## **Revue de la littérature**

### **Résumé**

Depuis le début du siècle, les nanoparticules se sont développées avec des applications possibles dans de nombreux domaines tels que l'énergie, les matériaux et le domaine médical et pharmaceutique. La silice, grâce à la grande facilité et adaptabilité de la synthèse des nanoparticules et à son inertie biologique à l'état macroscopique, est très largement étudiée pour des applications médicales. De nombreuses voies de synthèse, de structuration et de nanomatériaux à base de silice sont décrites dans la littérature. Leurs interactions avec les cellules (toxicité, internalisation, devenir) ont déjà fait l'objet de nombreuses études. Certaines applications biomédicales des nanomatériaux de silice en 2D et en matrice 3D paraissent particulièrement prometteuses.

## **1.1 The development of nanotechnology and nanomedicine**

### **1.1.1 Nanotechnology and its applications**

Nanotechnology is the manipulation of matter on an atomic, molecular, and supramolecular scale, widely considered as one of the most important breakthroughs in the last century<sup>1</sup>. Actually, the concept of nanotechnology was first introduced by Richard Feynman in 1959. The advent of scanning tunneling microscopy and atomic force microscopy enabled humans to observe the structure and surface properties of atoms and molecules that greatly speed up the development of nanotechnology. According to the predictions by experts, nanotechnology will become the three major supports for economic and social development in this century together with biotechnology and information technology.

#### **Figure 1-1** Nanotechnology is a highly interdisciplinary field of science

Nanomaterials generally defined as materials in which at least one dimension sized from 1 to 100 nanometers from the three-dimensional space or the substances are made up of basic structural units in nanoscale range<sup>2</sup>. Nanomaterials can be made of metals, ceramics, polymers, biomacromolecules, and as hybrids of these. They show a variety of morphology including nanospheres, nanoclusters, nanorods, nanotubes, nanofibers, nanowires, nanofilms and core-shell nanostructures, *etc.* To date, numerous bottom-up and top-down nanofabrication technologies<sup>3</sup> (such as sol-gel, electrospinning, self-assembly, phase separation, thin film

deposition, chemical vapor deposition, chemical etching, nano-imprinting, photolithography) are available to synthesize nanomaterials with ordered or random nanotopographies.

Materials with structure at the nanoscale often have unique properties because when the scale of macroscopic materials gradually decreases, the density of electron states changes from a continuous distribution to an independent distribution similar to the energy level of the atom, giving rise to a series of peculiar effects<sup>4</sup>, such as small size effects, surface effects, volume effects, quantum size effects, and macroscopic tunneling effects, *etc.* Today, nanotechnology is integrated with many disciplines including chemistry, materials, biology, medicine, physics and has been successfully used in fields of catalysis, bioanalysis, energy storage, environment, human health and microelectronics processing<sup>5-8</sup> *etc.* (**Figure 1-1**)

### **Figure 1-2** Various of nanomaterials in biomedical applications<sup>9</sup>

Among them, nanotechnology for biological and medical applications is considered as one of the most important branches, which has shown great promising as biomarkers for the investigation of biological processes that are hard to access with conventional approaches as well as for advanced therapeutic/imaging solutions. Nanomaterials have unique advantages for biological research because their size is similar to that of most biological molecules and structures. Thus various kinds of functional nanomaterials have been well developed which offers exciting opportunities in biomedical applications<sup>10, 11</sup>. A wide variety of nanostructured materials have been described in the literature such as gold and silver nanoparticles, quantum dots, magnetic nanoparticles, carbon nanotubes, silica-based nanomaterials, titania nanoparticles, liposomes, and soft polymer nanoparticles used for imaging, sensing, drug

delivery, tissue engineering and medical device *etc.* A very general scheme summarizing the materials, and their applications are reported in **Figure 1-2**.

### 1.1.2 Nanomedicine

Nanomedicine refers to the medical application of nanotechnology which involved in a wide range of biomedical areas. It is currently available to overcome some of the difficulties experienced by traditional medical approaches in the field of targeted drug delivery, diagnostic imaging as well as the production of hybrid treatments. At present, nanomedicine already has been used globally to improve the treatments and lives of patients suffering from a range of disorders including malignant tumor<sup>12</sup>, fungal infections<sup>13</sup>, elevated cholesterol, multiple sclerosis<sup>14</sup>, chronic pain<sup>15</sup>, asthma<sup>16</sup>. These benefits of nanomedicine can be classified as the advantages produced by nanotherapeutics, nanodiagnostics, and nanotheranostics (**Figure 1-3**).

#### **Figure 1-3** Applications of nanomedicine in clinical theranostics

Most drug molecules have low solubility in water and are very difficult to absorb and utilize at the desired lesion<sup>17</sup>. Nanotechnology has been used to increase absorption capacity via produced nano-drugs<sup>18, 19</sup>. In some cases, the drug is metabolized too quickly and may be effective only just after treatment. Therefore, nanomedicine can also increase the cycle time that the drug remains active in the body. It is also important to specifically treat damaged cells to avoid damage to surrounding healthy cells. With the ability to increase the specificity of drug targets, nanotherapeutics can also reduce the amount of drugs used, avoiding serious side effects.



Nanotechnology has also been applied to diagnostics because of the distinct optical, magnetic and structural properties of nanomaterials which make them suitable for diagnostic imaging and tumor detection. Nanoparticles have the excellent optical features benefit of quantum effects at the nanoscale<sup>20</sup>. This is especially useful for color coding and labeling of materials used during diagnostic tests<sup>21</sup>. Nanotechnology has been used to enhance current medical imaging methods such as US, CT, MR, SPECT and PET<sup>22</sup>.

Theranostics is a new field of medicine which combines targeted therapy with specific diagnostic tests. Nanotechnology is particularly suitable for the provision of materials with both imaging and drug agents that can produce practical theranostic tools. An advantage of this technique is that it provides the capacity for personalized and precision medicine.

## **1.2 Drug delivery**

### **1.2.1 Overview**

Drug delivery is a strategy for transferring drug compounds to the body as needed to safely achieve their desired therapeutic effect. This process is related to specific targeting, distribution, and systemic pharmacokinetics of the drug in the body<sup>23</sup>.

#### **Figure 1-4** Five types of common routes of drug administration

Accurate drug delivery and good metabolism in the body can improve the efficacy and reduce the side effects of the drug. Drug delivery is usually approached by chemical formulations of

drugs, but it may also involve medical devices or drug-device combination products. Drug delivery technologies modify drug release profile, absorption, distribution and elimination for the benefit of improving product efficacy and safety, as well as patient convenience and compliance. Currently, most common routes of administration include the preferred non-invasive oral route as well as topical, transmucosal, inhalation, and intravenous routes<sup>24</sup>(**Figure 1-4**). However, many drugs such as peptides and proteins, and gene-based drugs, are very susceptible to enzymatic degradation or cannot be effectively absorbed into the systemic circulation due to molecular size and charge problems. Therefore, many proteins and peptide drugs must be delivered by injection or nanoneedle arrays. When the drugs reached the desired site, the drug release from the system consists of the following processes: dynamic diffusion, progressive degradation, infiltration, and affinity-based mechanisms<sup>25</sup>.

An ideal dosage regimen in the drug therapy of any disease is one which immediately attains the desired therapeutic concentration of drug in plasma and maintains it constant for the entire duration of treatment. This is possible through the administration of conventional dosage forms in a particular dose and at a particular frequency. The frequency of administration or dose interval of any drugs depends upon its half-life or mean residence time and its therapeutic index (*i.e.* ratio between therapeutic efficiency and toxicity). In most cases, dosing interval is much shorter than the half-life of the drug, resulting in a number of limitations associated with such a conventional dosage form. For example, some patients have poor compliance and may often miss the time of administration. In other situations, the typical peak-valley plasma concentration-time profile is obtained which makes attainment of steady state condition difficult. Moreover, the unavoidable fluctuation in the concentration may lead to adverse effects especially for a drug with a small therapeutic index.

To overcome above-discussed limitations of conventional dosage forms, two methods are possible. On the one hand, it should be developed new, better and safer drugs with a long half-life and large therapeutic indices. On the other hand, effective and safer use of existing drugs may be obtained through concepts and techniques of sustained/controlled and targeted drug delivery systems. This approach can be achieved by designing a drug-device, which of course requires first ensuring the biosafety of the device material.

### **1.2.2 Nanocarriers used in drug delivery system**

A drug carrier is any substance or device used in the process of drug delivery which serves to improve the selectivity, safety and efficacy of drug administration. In terms of a successful drug

carrier, it must not only protect the drug from degradation but also control the release of the drug into the systemic circulation for therapeutic purposes. As noted above, nanomaterials typically exhibit different physicochemical properties, including small size, high surface area, and flexible structure, that make them of potential interest as drug carriers. Moreover, their intrinsic properties of light, heat, magnetism and electricity are of great significance for the preparation of functional and stimuli-responsive carriers<sup>26</sup>. In addition, some studies have shown that larger objects with optimized size and shape are more easily uptaken by cells.

Nanocarriers are nanomaterials that are used as transport modules for drugs (small molecules, peptides, proteins, *etc.*) into the body. The way the drugs are conjugated to the nanocarrier is either by adsorption, covalent linking, or encapsulation. Drug loading strategy affects the amount of drug, stability, the release of drugs, and even the surface properties of nanocarriers.

**Figure 1-5** Different types of nanocarriers. (a) lipid; (b) polymer; (c) inorganic nanoparticles

Nanocarriers used for medical applications must be biocompatible, nontoxic and functional. Undesirable effects of nanoparticles strongly depend on their hydrodynamic size, shape, amount, surface chemistry, the route of administration, reaction of the immune system and residence time in the bloodstream. Although it is rather difficult to predict the fate of nanocarriers in the body, it is generally accepted that too small nanoparticles are subject to tissue extravasations and renal clearance whereas large one are quickly opsonized and removed from the bloodstream via the macrophages of the reticuloendothelial system<sup>27</sup>. Therefore,

nanoparticles with a hydrodynamic diameter of 10-100 nm are considered to have optimal pharmacokinetic properties for *in vivo* applications. Nowadays, liposomes, solid lipid nanoparticles, dendrimers, polymers, silica or carbon materials, and magnetic nanoparticles<sup>28</sup> are the examples of nanocarriers that have been tested as drug delivery systems (**Figure 1-5**).

#### **1.2.2.1 Lipid based nanocarriers**

Lipid-based drug delivery systems consist of liposomes, solid lipid nanoparticles (SLN), microemulsions, nanosuspensions and lipid nanotubes. Liposomes are vesicles surrounded by a lipid bilayer, much like a cell membrane, separating the internal aqueous core from the outside, ranging in diameter from about 25-1000 nm. Since first being described by the hematologist Alec Bangham in 1964, liposomes have long been defined as good candidates for effective drug delivery<sup>29</sup>. In terms of structure, liposomes can be classified into multilamellar vesicles (MLV), small unilamellar vesicles (SUV), large unilamellar vesicles (LUV), and cochlear vesicles. There are several methods for liposomes preparation which include injection method, film dispersion method, ultrasonic dispersion, and reverse evaporation<sup>30</sup>. Liposomes were used for the first nanoscale anticancer drug (Doxil®) to approved by F.D.A. for clinical use in 1995. Today, there are already more than 15 liposomal drug formulations on the market for indications such as cancer, fungal infections, macular degeneration, pain management and vaccines.

#### **Figure 1-6** The structure of liposome nanocarriers

As a drug delivery system, liposomes offer several advantages including biocompatibility, the ability to protect drugs from degradation, reach targeted sites, and reduce toxic and side effects. In addition, the unique feature of liposomes is their ability to entrap both hydrophilic and hydrophobic molecules, in the aqueous core and bilayer membrane, respectively. Furthermore,

in order to prolong liposome circulation times, surface modification can be achieved through the introduction of polymers, such as PEG, PEI, PVP (**Figure 1-6**). Yuda et al. studied various lipid derivatives of polyethyleneglycols and found that terminal PEG groups can effectively prolong the circulation time of liposomes<sup>31</sup>. Moreover, ability of the cholesterol derivative of PEG in prolonging the circulation time of liposomes was proportional to the average molecular weight.

It is also very interesting to modify such lipid structures form multifunctional liposomes with specific proteins, antigens, or other biological substances, that can be used to design drugs for targeted delivery of therapeutics<sup>32</sup>. Much of the current research involving liposomes is focused on improving the delivery of anticancer drugs<sup>33</sup>, neurotransmitters<sup>34</sup>, antibiotics<sup>35</sup> *etc.* Disadvantages associated with using liposomes as drug carriers include low encapsulation efficiency, easy rupture of liposomal membranes, leakage of drugs, poor reproducibility, instability in the body, and rapid drug release. Drugs which have high membrane-permeability can readily leak from the carrier, while optimization of in vivo stability can cause drug release by diffusion to be a slow and inefficient process. Moreover, an increasing number of studies have shown that liposomes are not as immunologically inert as initially suggested.

Solid lipid nanoparticles (SLN) are a new generation of nanodrug delivery systems, which show typically spherical structure, and possess a solid lipid core matrix stabilized by surfactants. SLN combines the advantages of lipid emulsions and polymer nanoparticle systems while overcoming the stability issues that plague conventional and polymeric nanoparticle drug delivery methods.<sup>36</sup> In addition, they can be mass-produced by high-pressure emulsion homogenization. A recent study used solid lipid nanoparticles as nanocarriers for oral delivery of the iron nutrient by incorporating ferrous sulfate ( $\text{FeSO}_4$ ) into a lipid matrix composed of stearic acid<sup>37</sup>. Altogether, solid lipid nanoparticles have important development potential in future drug delivery systems.

#### **1.2.2.2 Polymer-based nanocarriers**

Polymer-based nanocarriers have emerged as a promising approach for drug delivery by dendrimers, polymer self-assembly micelles, nanoparticles, polymersomes *etc.* Dendrimers are large, complex molecules with a radius ranging from 2.5 to 8 nm. They are spherical, with a three-dimensional branched structure, which contains three parts: a core, branching repeat units, and outer terminal functional groups (**Figure 1-7**). The size of the dendrimer is easily controlled via polymerization of branches using monomers to form repeat layers, with each layer making

up a generation. Dendrimers can be made cationic, anionic, or neutral depending on their terminal groups<sup>38</sup>. Some natural molecules possess dendritic structures such as glycogen, amylopectin, and proteoglycans.

Dendrimers have a high drug-loading capacity and may encapsulate both hydrophilic and hydrophobic drugs. The drug may be encapsulated in the internal structure of dendrimers or it can be chemically attached or physically adsorbed on dendrimers surface. Clementi et al. utilized PEG-dendrimers loaded with both hydrophobic paclitaxel (PTX) and hydrophilic alendronate (ALN) and show enhanced activity compared with free drugs<sup>39</sup>. However, a possible disadvantage of dendrimers is that steric crowding of the branching arms occurs at higher generation numbers, which limits growth to a larger size and results in decreased drug encapsulation.

**Figure 1-7** Architecture of dendrimer involves different construction units

Polymeric nanoparticles are solid colloidal systems. A very wide range of biocompatible and, when required, biodegradable polymers, either natural or synthetic, can be used to design such nanoparticles. According to different preparation methods, nanospheres or nanocapsules (i.e. hollow nanoparticles) can be obtained. Drugs can be physically dispersed, dissolved or chemically conjugated to the polymer chain. Main advantage of nanoparticle stems from the ability to incorporate large molecules such as proteins as well hydrophobic drugs at concentrations above their inherent water solubility<sup>40</sup>.

Polymeric micelles are self-assembled core-shell nanostructures generated with amphiphilic block copolymers in an aqueous solution at or above critical micelle concentration <sup>41</sup> (**Figure 1-8**). Both the intrinsic and modifiable properties of polymeric micelles enable the system to incorporate poorly soluble drugs thus improving their bioavailability while protecting them

from inactivation in biological media. The typical methods used for encapsulation of poorly water-soluble drugs are dialysis, emulsion solvent evaporation, and solid dispersion<sup>42</sup>.

The last decade has seen significant progress in the development of various micellar systems and proved already to be a relevant approach for the delivery of hydrophobic drugs and hydrophilic contrast agents, drugs and biomacromolecules (DNA, SiRNA, protein), with the possibility to be functionalized by many different ligands<sup>43</sup>. However, much improvement is still needed for the existing systems with respect to drug-loading capacity and formulation stability.

## **Figure 1-8** Polymeric micelles as supramolecular nanomedicines

### **1.2.2.3 Inorganic-based nanocarriers**

In recent years, inorganic nanomaterials, such as QDs, gold/silver nanoparticles, iron oxide nanoparticles, carbon-based nanomaterials, and silica nanoparticles, have demonstrated distinctive advantages for drug delivery including high specific surface, controllable size and shape, tunable internal structures, and easy surface modification<sup>44</sup>. Compared with organic nanocarriers, inorganic nanomaterials have better stability and controllability; moreover, some inherent properties of these nanomaterials can contribute to enlarge the versatility of nanocarriers.

*Quantum dots* (QDs) are nanocrystals ranging from 2 to 10 nm in diameter composed of semiconductor materials<sup>45</sup>. These QDs have excellent fluorescence properties due to quantum size effects. QDs have high surface-to-volume ratios and are easily combined with therapeutic agents for multifunctional applications. Bagalkot et al. linked A10 RNA aptamer on the surfaces of CdSe/ZnS core-shell fluorescent QDs and then loaded doxorubicin(DOX) forming a QD-aptamer(DOX) conjugate (**Figure 1-9**) for targeted cancer imaging, therapy, and sensing in

vitro based on FRET mechanism<sup>46</sup>. Although there have been many related studies, the direct use of QDs for drug delivery remains questionable due to their potential long-term toxicity<sup>47</sup>.

**Figure 1-9** Schematic illustration of QD-aptamer (DOX) Bi-FRET system

*Carbon*-based nanomaterials<sup>48</sup> have attracted tremendous attention in drug delivery due to various advantages, including their high resistance, large specific surface area, cross cell membrane easily, and convenient surface modification. Among all those materials, carbon nanotubes (CNTs) are one of the most interesting nanocarriers currently under investigation. They possess a cylindrical nanostructure that can be used to encapsulate or bind diagnosis and therapy agents.

**Figure 1-10** A schematic diagram of preparing DOX-MWCNTs-PEG-TAT for drug delivery

Dhar et al have trapped a strongly hydrophobic Pt(IV) prodrug in carbon nanotubes and shown that chemical reduction causes a dramatic reversal in CNT hydrophobicity leading to the release of the active Pt(II) complex<sup>49</sup>. Surface modification of CNTs by anchoring of polymers, such as PEG, hyaluronic acid *etc.*, or covalent linking of targeting ligands, including folic acid (FA), peptides and antibodies, may remarkably reduce their cytotoxic effects and side effects<sup>50</sup>. Hu et



al. linked a cell-penetrating peptide (transactivating transcriptional factor TAT) to PEGylated multi-walled carbon nanotubes (MWCNTs) to create a highly effective antitumor multifunctional drug delivery system <sup>51</sup> (**Figure 1-10**). Graphene oxide <sup>52</sup> has also attracted recent interest in nanomedicine. Pan and co-workers synthesized ultra-small graphene oxide (carbon dots) around 10 nm that displayed photoluminescence ranging from the visible to the NIR<sup>53</sup>. Zheng et al integrated the optical properties of carbon dots and the anticancer function of oxaliplatin in theranostic nanomedicine (CD-Oxa) that could be used for simultaneous drug delivery and fluorescent tracking<sup>54</sup>. Recently, hollow carbon nanoparticles also showed promise as drug delivery systems. DOX-hollow carbon sphere drug delivery systems exhibited high drug-loading capacity, pH-controlled release and rapid uptake by cells <sup>55</sup>.

*Iron oxide* nanoparticles, mainly as magnetite ( $\text{Fe}_3\text{O}_4$ ) or maghemite ( $\gamma\text{-Fe}_2\text{O}_3$ ) phase, have attracted extensive interest in the biomedical field due to their superparamagnetic properties as well as due to the low toxicity of iron. For instance, Shen et al constructed a drug carrier DOX@ES-MION<sub>3</sub>@RGD<sub>2</sub>@mPEG<sub>3</sub> which is based on the exceedingly small 3.6 nm magnetic iron oxide nanoparticles (ES-MIONs) with modification by the RGD<sub>2</sub> peptide and mPEG<sub>3</sub> for T1-weighted tumor imaging and chemotherapy<sup>56</sup>. The results showed this drug delivery system is promising for high-resolution T1-weighted MR imaging and precise chemotherapy of tumors. Magnetic iron oxide nanoparticles can also be used for controlled drug release at a targeted site in order to reduce the cytotoxicity, enhance drug uptake or allow magnetic hyperthermia under high-gradient of external magnetic fields. Espinosa and co-workers introduced novel multifunctional iron oxide nanoparticles with the dual capacity to act as both magnetic and photothermal agents. Todd et al. co-loaded small molecule drugs with iron oxide nanoparticles onto diatoms. Using an external magnetic field, diatoms could be attracted to the tumor site for systemic administration<sup>57</sup>.

*Gold* nanoparticles are noble metal nanoparticles with special optical properties due to localized surface plasmon resonance phenomenon. Gold nanoparticles can be used to optimize the biodistribution of drugs to diseased organs, tissues or cells, in order to improve and target drug delivery. Hong et al. reported that intracellular glutathione (GSH) can displace the thiol monolayer on gold nanospheres, thus releasing the therapeutic cargo covalently bound to the monolayer <sup>58</sup>. Faroo et al. reported a facile one-step method to synthesize stable AuNPs loaded with the combination of two anticancer therapeutics, bleomycin, and doxorubicin. The results show that the therapeutic efficacy of hybrid nanomedicine based on gold nanoparticles is significantly enhanced by active targeting of HeLa cells<sup>59</sup>. Gold nanorods (GNRs) possess

stronger size-normalized absorption cross-sections than common gold nanospheres. Scattered photons can be used for imaging applications, while the absorbed photons can be utilized for photothermal effects<sup>60</sup>. Such NIR-active nanostructures have shown tremendous potential in controlled release drug delivery. The generated heat can also be used to increase drug efficacy. In particular, the combined effects of heat and chemotherapeutic agents can synergistically improve the efficacy of drug delivery. Zhang et al. synthesized a thiolated pH-responsive DNA conjugated gold nanorod (GNR) as a multifunctional nanocarrier for targeted, pH- and near infrared (NIR) radiation dual-stimuli triggered the drug delivery<sup>61</sup>. A further surface modification was developed by a thiolated poly(ethylene glycol)-biotin to improve its cancer-targeting ability, reduce side effects and increase blood circulation time (**Figure 1-11**).

**Figure 1-11** A dual-stimuli triggered anti-cancer drug delivery system based on GNRs

As pointed out above, each delivery platform has its advantages and disadvantages. Lipid and polymer carriers are highly versatile in terms of chemistry and their cyto/biocompatibility can be rationally engineered. However, this often requires extensive synthetic efforts and stability issues are still faced in many systems. Inorganic nanocarriers presented so far mainly benefit from their intrinsic physical properties and quite easy surface functionalization. However, besides cytotoxicity issues and standing questions about their biodegradability, drug loadings are often quite low. Interestingly, as described in the following section, silica nanoparticles stand quite in between these two categories.

### 1.3 Preparation of silica-based nanomaterials

Silica (silicon oxide, SiO<sub>2</sub>) is one of the most complex and abundant families of materials. It is already used in many different forms in structural materials, microelectronics, and as

components in the food and pharmaceutical industries<sup>62, 63</sup>, thanks to its many attractive physicochemical properties such as large specific surface area, high mechanical stability, easy functionalization, good biocompatibility and low toxicity *etc.* Therefore, there is not surprising that silica nanomaterials have been widely studied for biomedical applications: detection, biosensing, medical imaging, drug delivery, and theranostics<sup>64</sup>. In particular, the evaluation of silica-based nanomaterials as drug carriers has become very popular over the past decades. In 2011, an investigational new drug application for exploring an ultra-small nonporous silica NP for targeted molecular imaging of cancer was approved by the US Food and Drug Administration (FDA) for a first-in-human clinical trial, highlighting the great potential and the most recent progress of clinical translation of silica NP drug delivery platform.

### 1.3.1 The solution chemistry of silica

Silica has a tetrahedral structure with each silicon covalently bonded to four oxygen atoms. Most oxygen atoms will be bonded to two silicon atoms so that two tetrahedra are joined at a corner<sup>65</sup>. This orientation can be random, leading to an amorphous structure. To date, a large number of techniques have been available for preparing silica nanoparticles, such as flame spray pyrolysis, chemical vapor deposition, ball milling, sol-gel<sup>66-69</sup>. Among these, preparation by sol-gel techniques has been the focus of research as the synthesis is straightforward, scalable and controllable.

**Figure 1-12** The hydrolysis (1) and condensation (2a, 2b) reaction of silicon alkoxide precursors

The sol-gel synthesis typically involves the hydrolysis (1) and condensation (2) of a silicon alkoxide precursor ( $\text{Si}(\text{OR})_4$ ), where R is typically Et or Me, under basic or acidic catalysis (**Figure 1-12**). The hydrolysis of silanes leads to reactive silanol species ( $-\text{Si}-\text{O}-\text{H}$ ) which

condense with other silane (2b) or silanol (2a) groups to form covalent siloxane bonds (Si-O-Si) <sup>70</sup>.

If hydrolysis is complete, the alkoxide groups are replaced by hydroxyl groups and orthosilicic acid  $\text{Si}(\text{OH})_4$  is formed. Orthosilicic acid is stable in water at room temperature as long as its concentration remains below the solubility limit of the amorphous phase (typically 100 ppm,  $\sim 1 \text{ mM}$ ) <sup>71</sup>. Above this concentration, it will undergo autopolycondensation to lower the concentration of orthosilicic acid in solution and generate oligomers. These serve as nuclei for the formation of particles. As the levels of orthosilicic acid above the solubility limit decrease, smaller, more soluble particles dissolve, releasing silicic acid that redeposits onto the larger particles present, a process is known as Ostwald ripening. At circumneutral pH (6.0-8.0), particles can continue growing as isolated particles until the levels of soluble silica reach the solubility of amorphous silica, as the particles carry a negative charge and repel one another. In more acidic conditions and/or if salts or other charged species are present, then the surface charge that causes repulsion between individual particles is reduced or canceled, and the particles aggregate to form dense 3D networks <sup>72</sup>(**Figure 1-13**). More generally, many reaction conditions such as precursors nature, pH, temperature, molar ratios of reactants, solvent composition have an important influence on the sol-gel process, in terms of kinetics, particle size and condensation state and properties of the final gels<sup>73</sup>.

**Figure 1-13** The process of sol-gel in silica formation with different conditions

In addition to tetrafunctional silicon alkoxides  $\text{Si}(\text{OR})_4$ , organosilanes bearing one non-hydrolysable groups can also be used to form organically-modified silica materials. While the hydrolysis/condensation reactions remain identical, the nature of these additional organic

moieties impact on the solubility and reactivity of the silane and, therefore on the structure and properties of the obtained particles or gels. Because only three Si-O-Si bonds can be formed, the resulting networks are less stable than pure silica ones but are usually more flexible. They also incorporate an additional function that can be useful for further modification of the material.

### 1.3.2. Preparation of silica nanoparticles

#### 1.3.2.1 Main synthetic pathways

In practice, a wide variety of methods and procedures have been introduced and applied for the fabrication of different silica particles of various sizes, shapes, structures and physicochemical characteristics.

**Figure 1-14** Two mainly methods to synthesis of silica nanoparticles. (a) Stöber method; (b) Reverse phase microemulsion

The Stöber method<sup>74</sup> is the most popular route to obtain colloidal silica. The synthesis procedure involves the controlled hydrolysis and condensation of a silica precursor in ethanol and water mixture solution with ammonia as a catalyst (**Figure 1-14a**). The particle formation process is strongly influenced by the surface potential of the silica particles and the ionic strength of the reaction medium so that a careful control of process parameters (volume, stirring, mixing rate) is required to get access to monodisperse populations, especially in small size domain. To improve the size distribution, a seed-growth strategy was explored that starts from well-defined small colloids that are further grown in a TEOS/ammonia solution<sup>75</sup>.

An aqueous route using water glass solutions (i.e. highly concentrated aqueous solutions of sodium silicates) allows to form silica nanoparticles by simple mixing with an aqueous acidic

solution<sup>76</sup>. The size of the particles is controlled by the concentrations of the two reagents as well as other processing parameters, such as addition rate, stirring rate, temperature, *etc.* The microemulsion method<sup>77</sup> is a widely used technique to prepare materials with novel and unique properties at the nanoscale. A microemulsion consists of two types of homogenous systems of water-in-oil (W/O) or oil-in-water (O/W) that are thermodynamically stable thanks to surfactant molecules (**Figure 1-14b**). The system is composed of a dispersion of nanodroplets, also known as nanoreactors, that act as cages that limiting particle growth and therefore determining the final size of nanoparticles. Several other factors can affect the morphology of nanoparticles, such as the texture of these nano-droplets, reactant concentration, type of surfactant, concentration of capping agent *etc*<sup>78</sup>. Finally, silica particles can also be obtained using spray-drying techniques but this approach has been mainly applied to hybrid and porous nanomaterials<sup>79</sup>, as described below.

### 1.3.2.2 Size control

By the Stöber method, the size of the particles can be tuned by adjusting the reaction condition. Monodisperse silica spheres with uniform diameters ranging from 50 nm to 2  $\mu$ m were successfully prepared in this system in one step. The particle size can be very uniform, but the particle size distribution broadens as the reaction conditions are changed to form larger particles. Boissière et al. developed a two-step process whereby the hydrolysis at low pH (1-4) is completed before the condensation reaction is initiated by the addition of sodium fluoride (NaF), yielding to spherical particles in the micrometric size range<sup>80</sup>. Smaller NPs that can be prepared by a modified Stöber method without aggregation have diameters as small as 12 nm using an heterogeneous reaction with lysine or arginine instead of ammonia as a basic catalyst<sup>81</sup>. Rida et. al. reported that amorphous silica was synthesized using sodium silicate and hydrochloric acid by precipitation, the average size of silica nanoparticles can be finely tuned in the range 148-212 nm by changing the chain length of a cationic surfactant<sup>82</sup>.

The diameter of silica NPs that obtained from reverse microemulsion depends on the diameter of water nanodroplets in which the hydrolysis reaction is limited as well as the ratio of water to surfactant. The particle size decreases and the particle population become more monodisperse with increasing water-to-surfactant molar ratio. The particles obtained by this method have higher uniformity of particle size ranging from 20 to 100 nm. The other approach for the preparation of spherical, ultra-small silica NPs is the oil-in-water microemulsion. This process has been mostly used for synthesizing organically modified silica nanoparticles known as

ORMOSIL nanoparticles<sup>83</sup>. The results showed that the properties of the surfactants, such as solubility, play a significant role in the obtained size distribution of the resulting nanoparticles. Large-scale preparation of silica microspheres via a spray drying process could be achieved and the size could be easily controlled from ~50 to 100  $\mu\text{m}$  from the same diameter nozzle via changing the initial solute content or changing the drying temperature<sup>84</sup>.

#### **1.3.2.3. Shape control**

The shape of nanoparticles dramatically affects their blood circulation and cell penetration behavior. It has been reported that nanorods penetrate tumor tissues more rapidly than nanospheres likely because of improved transport through tumor vasculature pores<sup>85</sup>. These results suggest the importance of controlling the shape of nanomedicine for favored circulation or tissue penetration properties. Although there are many methods for the size-controlled preparation of silica nanospheres, only a handful of methods have been reported for the preparing of silica nanostructures with different shape: cone<sup>86</sup>, sphere, matchstick<sup>87</sup>, rod, wire<sup>88</sup>(**Figure 1-15**).

#### **Figure 1-15** Silica nanoparticles with various shape: cone, sphere, matchstick, hollow rod

The methods for shape control of silica nanomaterials are mainly using templates or through polymer adsorption. For example, silica nanotubes can be prepared with various templates, including metal salts, porous anodic alumina or polycarbonate membranes, cylindrical polymer brushes, and nickel-hydrazine complex nanorods<sup>89</sup>. Recently, Kuijk et al. reported the PVP-mediated synthesis of monodisperse silica nanorods with a tunable aspect ratio in an emulsion system<sup>90</sup>. Using the similar method, Zhang et al. prepared a series of silica nanowires by adjusting the temperature and time of the reaction<sup>91</sup>.

#### **1.3.2.4. Structure control**

Silica nanoparticles can be divided into non-porous silica and porous silica nanoparticles. The non-porous silica particles, as typically obtained by the Stöber process, have some porosity in the micropore range that means these pores are too small to serve as host. Drug incorporation

can therefore only be achieved by encapsulation or surface grafting. Thus a wide amount of work been devoted to the preparation of particles with pores of dimensions compatible with the incorporation of drugs.

**Mesoporous silica nanoparticles (MSNs)** The first reported mesoporous silica materials were molecular sieves called M41S but MCM-41 and SBA-15 materials with larger pore size and better organization rapidly became the most studied, with the pore size ranging from 2-10 nm and 2D-hexagonal and 3D-cubic structural characteristics<sup>92</sup>. Further on, mesoporous silica nanoparticles (MSN) could be synthesized using a simple Stöber-like sol-gel method in the presence of a template made of micellar rods. The result is a collection of nanosized spheres or rods that are filled with a regular arrangement of pores. The template can then be removed by washing with a solvent adjusted to the proper conditions (**Figure 1-16**).

**Figure 1-16** Soft template synthesis of mesoporous silica nanoparticles

Mesoporous nanoparticles are obtained after removal of the structure directing agent leading to the opening of the porosity. MSNs typically have a high specific surface area ( $600\text{-}1000\text{ m}^2.\text{g}^{-1}$ ) and a large pore volume ( $0.6\text{-}1.0\text{ cm}^3.\text{g}^{-1}$ ) that allow for high levels of drug loadings to be achieved. Typical pore dimensions of MSNs are 2-4 nm, but recent advances have made it possible to synthesize MSNs with pore dimensions as large as 50 nm, which are generally referred as large-pore MSNs<sup>93</sup>. Several synthetic methods have been proposed to enlarge the pore sizes of MSNs including post-enlargement by introducing a swelling agent (1,3,5-trimethylbenzene)<sup>94</sup> into the core part of micelles or using large molecular weight block copolymers (F127, P123, and PS-b-PEO) with long organic molecular chains as mesopore template<sup>95</sup>.

**Periodic mesoporous organosilicas (PMO)** have both organic and inorganic groups as an integral part of the porous framework<sup>96</sup>. The framework of PMOs consists of inorganic components (polysilsesquioxanes) uniformly bridged by organic linkers. Most of the bridged



polysilsesquioxane can be generically represented by the formula  $\text{O}_{1.5}\text{Si-R-SiO}_{1.5}$ , where R represents the organic bridging group. Each individual organic group is covalently bonded to two or more silicon atoms in the framework (**Figure 1-17**). Depending on the synthetic conditions used to make mesoporous organosilicas, the mesoscale structure can either be amorphous or crystalline. The methods used to make mesoporous organosilicas are evaporation-induced self-assembly, surfactant-mediated synthesis, post-synthetic grafting, and co-condensation<sup>97,98</sup>.

**Figure 1-17** Synthesis routes of periodic mesoporous organosilicas

**Hollow/rattle-type particles.** With the rapid development of a variety of applications, new demands for mesoporous silica nanoparticles with special structure and performance gradually increase. Recently, hollow and rattle-type nanomaterials have been actively explored for enzyme immobilization, catalysis, DNA delivery<sup>99-101</sup>. Hollow/rattle-type MSNs with interstitial hollow space and mesoporous shell have low density and high specific area, which are ideal as new-generation drug delivery systems with extraordinarily high loading capacity (**Figure 1-18**).

Conventionally, hollow-type mesoporous silica nanoparticles are fabricated using a dual template method with a hard template or soft template to generate a hollow interior and a soft template as a pore-forming agent to induce mesopores in the shell. After the sol-gel process around the pore template to generate silica matrix coating on the core template, the templates could be removed by thermal calcination or/and solvent extraction. For rattle-type particles, the multi-step coating on the core particles is needed to generate a removable middle layer. The fabrication is tedious, high-cost and difficult to fabricate nanoparticles with small size and complicated structure. Therefore, new methods should be investigated for developing simple, controllable, and scalable fabrication.

Dependent on the fabrication method, hollow/rattle-type MSN can be divided into ordered pore particles and disordered, non-oriented counterparts. Ordered straight channels are believed to be favorable for diffusion of adsorbed molecules, whereas disordered pore in the shell is considered to be advantageous for controlled and multi-stage drug release<sup>102</sup>. Compared with conventional ordered MSN, hollow/rattle-type particles present an additional challenge: all of the pores connected to the hollow interior must be controlled. In hollow particles with multiple pore connectivity to the hollow center, the absence of control would result in the loss of all of the contents of the particles. Up to now, development of hollow/rattle-type MSN is still in its very early stage in terms of both synthesis and applications.

**Figure 1-18** The structures of the hollow and rattle-type mesoporous silica nanoparticles

### **1.3.3 Surface functionalization of silica nanoparticles**

The surface functionalization of silica nanoparticles can not only increase the colloids stability but also produce unprecedented properties. Most importantly, the surface properties of nanoparticles influence their interaction with the biological system, which includes cellular internalization, cellular trafficking, biodistribution<sup>103</sup>. Therefore, surface modification of nanoparticles is essential in order to enhance the disease targeting and therapeutic effects. There are currently three main surface modification methods that can be summarized as co-condensation, post-synthetic grafting silanization, surface polymerization.

#### **1.3.3.1 Co-condensation**

In the co-condensation technique, it is possible to directly functionalize the surface of silica nanoparticles during the synthesis process<sup>104</sup>. This approach incorporates the organic groups into the silica framework during the one-pot synthesis process via sol-gel method by introducing the corresponding organosilane (APTES, CTES, *etc.*) in the reaction solution

containing the tetrafunctional silane. Co-condensation revealed to be superior for the functionalization of the internal surface of the mesoporous silica nanoparticles.

### **1.3.3.2 Post-synthetic grafting strategy**

Post-synthesis grafting is usually implemented for functionalizing the external surface of silica nanoparticles<sup>105</sup>. The coupling of surface silanols and organosilanes occurs by hydrolysis of the latter and its condensation so that care must be taken to avoid its self-condensation. Thus organic solvents with trace water are frequently employed to perform silanization. However, it frequently leads to a heterogeneous surface chemistry, where grafting occurs with higher density in pore openings but at a lower efficiency on the interior framework<sup>106</sup>.

### **1.3.3.3 Polymer coating**

Surface polymerization of silica nanoparticles can be achieved by physical absorption and chemical conjunction. The silica surface is negatively charged at pH above ca. 3, that means it can easily adsorb positively-charged polymers for simple surface modification, such as PEI, for DNA delivery<sup>107</sup>. Covalent grafting includes both “grafting to” and “grafting from” approaches<sup>108</sup>. “Grafting to” is performed via coupling of functionalized polymer with well-matched silica surface groups. This method can lead to low grafting yield due to steric crowding of reactive sites. The “grafting from” method provides a higher control of functionality and density of the polymer coating. In this process, a higher grafting density can be attained by implementing small monomers with no steric limitation thus providing ease of access to the reactive sites on the particles surface. For instance, the hyperbranched ring-opening polymerization of aziridine induced by silanol groups constitutes hyperbranched polyethyleneimine-modified particle surfaces, which makes high positively-charged particles that have elevated electrostatic stability under physiological conditions<sup>109</sup>. The surface of organically-modified silica nanoparticles can also be grafted by various biomacromolecule agents such as carbohydrates, polypeptides, antibodies or nucleic acid aptamers<sup>110</sup>. Overall, many functional moieties can be conjugated to the surface of the silica nanoparticles due to the versatile silane chemistry. Thus, silica nanoparticles make it easy to obtain many of the desired surface properties for biomedical applications.

## **1.3.4 Composite and hybrid silica nanoparticles**

Besides surface modification, incorporation of additional molecules, polymers or particles to silica at the nanoscale has been widely described. For instance, silica-based composite nanostructures have been extensively studied. Three main approaches are possible: surface modification, internal encapsulation, and uniform compounding (**Figure 1-19**).

The first approach where polymers are localized on the silica particles surface has been described above. But silica/polymer nanoparticles can also be achieved by “encapsulating” polymer nanoparticles or biomacromolecule with a silica shell. This core-shell nanohybrid usually start from polymer nanoparticles and then grow a silica layer on their surface.

**Figure 1-19** The three approaches for silica/polymer nanocomposites synthesis. (a) Surface modification. (b) Internal encapsulation. (c) Uniform compounding

This structure can effectively overcome the flexibility of polymer materials and improve their stability in biological applications. Quesada et al. reported a novel type of hybrid material based on a PLGA nanoparticle core and a redox-responsive amorphous organosilica shell<sup>111</sup>. This silica/polymer nanoparticle exhibit excellent stability and show great potential as stimuli-responsive vehicles for drug delivery. Moreover, the rigid inorganic silica layer can protect the biological macromolecules such as proteins or nucleic acids from being prematurely degraded when these molecules encapsulated inside. Fujiwara and co-workers succeeded in the direct encapsulation of bovine serum albumin (BSA) and duplex DNA in silica microcapsules by microemulsion<sup>112</sup>. They found these systems can achieve controlled release by carefully design the silica shell. These microcapsule materials encapsulating biomacromolecules also have been applied to biotechnologies such as immobilized enzyme *etc.* The other strategy for silica/polymer nanocomposite refers to construct homogenous silica/polymer nanocomposites. One possibility is to introduce the polymer in the initial silica precursor solution, and then spontaneous form a uniform silica/polymer materials by sol-gel or microemulsion methods, as

shown for PLLA or PEG<sup>113</sup>. Alternatively, the use of spray-drying techniques has been efficiently used for one-pot preparation of silica/poly-L-lysine/alginate nanocomposites that exhibit homogeneous structures<sup>114</sup>.

Alternatively, hybrid functional silica nanoparticles or nanohybrids can be designed that own specific optical, magnetic or thermal properties from small molecular or inorganic nanoparticles associated with silica. The encapsulation approach can be realized during the process of silica polymerization either with Stöber or reverse micelle method. Tan and co-workers develop a series of dye-doped silica nanoparticles using a reverse microemulsion method which exhibit an excellent optical stability in biomedical imaging<sup>115</sup>. In parallel, many MRI contrast agents, photosensitizers, and inorganic nanoparticles, such as gold, iron oxide, quantum dots, Gd<sub>2</sub>O<sub>3</sub> *etc* also used to build the core-shell structured hybrid silica nanoparticles with different structures<sup>22, 116, 117</sup> (**Figure 1-20**).

**Figure 1-20** Schematic (a-e) pictures of different structure of core-shell nanoparticles

Zhao et al. encapsulated gold nanorods with a mesoporous silica shell by the modified Stöber method. After modifying with a targeting peptide RGD, the hybrid nanoparticles showed significantly enhanced sensitization of triple-negative breast cancer to megavoltage energy<sup>118</sup>. Many examples of inorganic colloids grafted onto the surface of silica nanoparticles are also found in the literature. Stoeva et al. used an amino-modified silica as a core, and then the assembly of iron oxide nanoparticles as a first shell, followed by the electrostatic-mediated deposition of Au seeds to form a gold shell around the SiO<sub>2</sub>-Fe<sub>3</sub>O<sub>4</sub> particles. The multilayer

magnetic nanoparticles exhibited multifunctional properties including magnetic and optical, as well as cooperative DNA binding<sup>119</sup>.

## **1.4 Silica-based nanomaterials in biology and medicine**

### **1.4.1 Toxicity of silica nanoparticles in vitro and in vivo**

In recent years, large-scale production and application of silica nanoparticles lead to the risk of increased exposure to workplace staff. Silica food additive also in a nanometer size range so the general population may be more exposed than initially expected. In addition, medical applications of silica nanoparticles will also introduce them into the human body for disease diagnosis and treatment. Therefore, this growing exposure potential has caused global concern about the safety of silica nanoparticles. More and more research was devoted to the toxicology research of silica nanomaterials. Although it remains to be clarified, studies have shown that physicochemical properties such as size, surface area, and surface characteristics play a key role in the toxicity of silica nanoparticles.

Nanoparticle-induced oxidative stress (reactive oxygen species production, ROS) may damage cellular components and cause cell death through the interaction between surface silanol groups and cell membrane<sup>120</sup>. Yu et al. explored the impacts of geometry, porosity, and surface charge of SiO<sub>2</sub> on cellular toxicity and hemolytic activity. Results demonstrated that toxicity of SiO<sub>2</sub> was highly cell typed and nanoparticle concentration dependent<sup>121</sup>. For non-porous silica nanoparticles, toxicity increases with decreasing particle size. However, mesoporous materials have the opposite effect with increasing porosity. Interestingly, a recent study showed that the mesoporosity of some silica particles tends to collapse with time, increase the plain surface of the colloid and there or its toxicity<sup>122</sup>. Along the same lines, grafting the particle surface with cationic groups (such as amino) or neutral hydrophilic groups (such as PEG )or preparing hybrid particles incorporating cationic polymer (such as chitosan) decreases the observed toxicity<sup>123</sup>. Indeed, all these effects were shown to dose-and cell-dependent.

Several *in vivo* toxicity studies of silica-based nanoparticles have been carried out using rats and mice, and exposure through various routes of administration<sup>124, 125</sup>. In general, short-term exposure to SiNPs induced adverse effects in the lungs, kidneys, liver, and brain. SiNPs administered mainly via inhalation, ingestion, and intravenous routes were majorly distributed in the liver, lungs, spleen, and kidneys, and in the brain of the intranasally exposed rats. Most of the administered SiNPs were excreted via feces and to a lesser extent via urine, in a size and

shape dependent manner. However, in most cases, the administered doses were very high compared to relevant human inhalation and ingestion exposures to amorphous silica. Some studies showed an accumulation of SiNPs in organs such as the liver, but such accumulation was not associated with any major effects<sup>126</sup>. However, long-term effects of accumulated SiNPs were not studied. It is surprising that in contrast to acute studies, no toxicity (local or systemic) was observed in chronic oral and dermal exposure studies, regardless of the size of SiNPs and the high doses used. Moreover, surface-modified SiNPs showed a significant increase in absorption by the GI tract compared to bare SiNPs. Dosing SiNPs via intravenous injection showed in all studies some sign of damage/toxicity<sup>127</sup>. No clear type or size-dependent effect can be identified from the set of reviewed studies. Furthermore, where genotoxicity was studied, it was not clear whether SiNPs were taken up by the target cells or were able to reach the tissue examined, which is obviously needed to exert a direct genotoxic effect.

#### **1.4.2 Degradation of silica nanoparticles**

Typically, the produced silica nanoparticles aqueous suspension stored at or below room temperature with relatively high silica concentration and low ionic strength (less than 0.01 M to avoid aggregation). However, when placed in simulated (*in vitro*) or effective (*in vivo*) human conditions, a fast dissolution in physicochemical conditions occur, especially at higher temperatures and ionic strength<sup>128</sup>. The dissolution process of amorphous silica in aqueous media includes three steps: i) hydration, in which water is absorbed onto the siloxane framework, ii) hydrolysis, in which siloxane are hydrolyzed into silanols, and ii) ion exchange processes, which consists of nucleophilic attack of OH<sup>-</sup> leading to the leaching of silicic acid (**Figure 1-21**). As a result, the synthetic process, post treatments and surface functionalization of silica NPs ought to affect their hydrolytic stability. Investigations have thus been carried out to assess the direct influence of the following parameters on the degradation of silica NPs, including size and porosity, morphology and degradation medium, ipore size, condensation degree, functional groups, and concentration of the particles. Kuroda and co-workers studied the dissolution behavior of colloidal silica with various diameters under static aqueous conditions. The results showed that nonporous silica nanoparticles were degraded much more slowly than mesoporous silica nanoparticles and the 10 nm particles were degraded more slowly than the 5 nm ones<sup>129</sup>. This highlights that the diameter of the silica NPs does affect their degradability rate as the relative outer surface of NPs increases as the NPs diameter decreases.

**Figure 1-21** Mechanisms and regulating factors of the degradation of silica nanoparticles in aqueous media<sup>122</sup>.

The key role of the surface area was further demonstrated by the comparison between aggregated MSN (non-dialyzed) and colloidal MSNs (dialyzed), which revealed that aggregated MSNs were not fully degraded (65 wt%) even after 2 weeks. However, Lu and co-workers showed that the degradation of MSNs is independent of their diameter with 390, 310, 200, and 150 nm NPs in simulated body fluid (SBF) at 37 °C. This suggests that for large particles whose accessible surface is mainly internal (i.e. porosity) a variation of the NP diameter would play an insignificant role in the degradation<sup>130</sup>. Varying condensation degrees of the silica matrices also allow for tuning their dissolution rate. Hence, calcined mesoporous silica hardly degrades in months, well-condensed MSNs slowly degrade in weeks, and partly condensed MSNs degrade in a few days (down to 24 h for large-pore MSNs). Nanospheres have been shown to dissolve faster than nanorods, and so do smaller nanorods when compared with longer ones<sup>131</sup>.

The surface functionalization and aggregation of the NPs, as well as the degradation media (water, PBS, serum, pH, NPs concentration, closed or continuous flow systems), impacted significantly the degradation kinetics. The incorporation of organic moieties was reported to also control the degradation kinetics. Noncovalently doped silica NPs were prepared in order to create defects in the silica matrix and to accelerate its dissolution while releasing a molecule of biological interest<sup>132</sup>. Silica or PMOs were also covalently linked with specific redox-cleavable (disulfides, tetrasulfide, platinum complexes) or enzymatically cleavable (oxamide, lysine, ester) organic moieties in order to trigger the degradation of the NPs inside cells<sup>133</sup>. These concepts were demonstrated both in solution and in cells via various techniques. On the



contrary, stable silica nanoparticles and PMOs have been designed to inhibit hydrolytic degradation, thanks to hydrophobic and chemically stable ethylene, ethylene-coumarin, ethenylene, and phenylene bridges. The degradation in aqueous solution could thus be inhibited for at least 15 to 28 d, or, triggered in a few days via external stimuli and the careful selection of silsesquioxane bridges<sup>134</sup>.

Much less is known about the intracellular degradation of silica nanoparticles. Earlier reports on the evolution of silica-biopolymer nanoparticles within the intracellular space of mammalian cells have suggested that, after 24 h, only the bio-organic fraction was degraded while the inorganic part remained intact<sup>135, 136</sup>. Further experiments performed with mesoporous nanoparticles evidenced that after uptake and intracellular trafficking, they can be released by the cells.<sup>137</sup> However no modification in particle size or morphology was reported. Later on, it was demonstrated that plain silica particles could undergo a surface erosion process within endosomal compartments, with the release of soluble forms of silica outside the cells<sup>138</sup>. Since then, further evidences of the ability of silica to dissolve intracellularly were accumulated<sup>139-142</sup>. So far, the most plausible mechanism is related to the dissolution equilibrium of silica between intracellular compartments exhibiting a high silica content and the intracellular space where the concentration of silica species is low. Hence, no specific biodegradation pathway has been identified.

### **1.4.3 Drug delivery applications**

#### **1.4.3.1 Drug loading**

The use of silica materials for delivery and controlled release of drug payloads was reported as early as 1983. Initially, silica was used mainly in the form of xerogels loaded with bioactive agents. For example, silica xerogels have been used as an implantable carrier for controlled drug release<sup>143</sup>. Silica nanoparticles emerged as a popular drug delivery system about 10 years later. A wide range of different kinds of payloads, including small molecule drugs, photosensitizers for photodynamic therapy (PDT), proteins, peptides, DNAs, and RNAs, have been incorporated into silica nanoparticles to target diseases such as cancer, heart disease, and Parkinson's disease<sup>144-146</sup>. Using silica nanoparticles to deliver bioactive molecules can protect them from degradation under physiological conditions, allow for controlled release, prolong their blood circulation, improve disease targeting, and minimize side effects on healthy tissues.

Depending on the properties of the cargoes delivered, different formulation strategies were used for preparing silica nanomedicines.

There are several strategies for loading drugs into silica nanoparticles: encapsulation and surface grafting, mesoporous adsorption.

**Encapsulation.** The simplest method is to capture a hydrophilic drug or imaging agent in a silica matrix by non-covalent interaction. Initially, this method was typically used for the preparation of fluorescent silica nanoparticles for optical imaging. Luminescent metal complexes such as  $\text{Ru}(\text{bpy})_3^{2+}$  have also been incorporated into SiNPs for fluorescent imaging, for instance allowing to follow their biodistribution and urinary excretion<sup>147</sup>. Further this method was used to construct silica nanocarriers for drug delivery. Schmidt et al. prepared green fluorescent protein (GFP)-doped silica nanoparticles with a narrow size distribution. GFP was chosen as a model protein using for intracellular protein delivery<sup>148</sup>. However, neither the previously described Stöber method nor the inverse microemulsion method effectively binds hydrophobic molecules to the silica matrix. In order to solve this problem, organically modified silica nanoparticles can be used. The hydrophobic drug is first dissolved in the organic phase of the inverse microemulsion, which allows for more efficient distribution into the aqueous water droplets and is more efficiently captured within the silica nanoparticles by hydrolysis of the silane precursor<sup>149</sup>. Some recent experimental results indicate that some therapeutic photosensitizing agents can be encapsulated within the nanoparticles as nano-therapeutic agents. On the one hand, the photosensitizer retains the function of producing singlet oxygen after being embedded in the silica matrix, and on the other hand, the negative effects of the photosensitizer, such as toxicity or hydrophobicity, are reduced when embedded in the silica<sup>150</sup>.

**Figure 1-22** Structure of mesoporous silica nanoparticles applied for delivery of siRNA

**Surface grafting.** Drugs can also be grafted on the surface of silica nanoparticles by chemical binding or physical adsorption. A typical example is fluorescent dyes or contrast agents

decorating silica nanoparticle via covalent cross-linking, such as EDC/NHS condensation chemistry. Rieter et al. synthesized silica nanoparticles containing  $\text{Ru}(\text{bpy})_3^{2+}$  via the reverse microemulsion method and functionalized the surface of the silica with  $\text{Gd}^{3+}$ -chelating ligands for intracellular dual-functional imaging<sup>151</sup>. Other methods of grafting include a click reaction or a disulfide bond<sup>152, 153</sup>. However, the electrostatic forces that govern the physical adsorption of biocompatible macromolecules are often the most simple and efficient method for immobilization. Many macromolecules (protein, DNA, RNA) can be physically adsorbed onto the nanoparticles surface for drug delivery<sup>154, 155</sup>. As shown in **Figure 1-22**, phosphonate-modified mesoporous silica nanoparticles were further surface modified using electrostatic attachment of a polyethyleneimine (PEI) polymer, which was used for subsequent covalent attachment of poly(ethylene glycol) (PEG) or electrostatic based loading of siRNA<sup>107</sup>.

**Pore impregnation.** The MSN-based drug loading method mainly involves physical adsorption as a result of particle impregnation by a highly concentrated solution of the active molecule. Wang et al. reported a method in which MSN was immersed in a drug-containing solution until equilibrium was reached, and most of the drug penetrated deeply into the pores or hollow shell of the carrier<sup>156</sup>.

#### 1.4.3.2 Targeted delivery and control release

**Targeted delivery.** One of the main issues in biomedical sciences nowadays is to develop drug systems that can be specifically targeted to the desired site where there is solely diseased tissue, thereby avoiding interaction with healthy tissue. Cell-specific targeting with nanocarriers may be accomplished by using passive or active mechanisms<sup>157</sup> (**Figure 1-23**). Passive route is directly related to circulation time and can be realized by the enhanced permeability and retention (EPR) effect<sup>158</sup>. Polymers are the most commonly used passive targeting agents, which exhibits relatively long blood circulation and low uptake of the reticuloendothelial system (RES) organs. As a result, when these passive groups are used to modify SiNPs these show better passive targeting of tumor sites<sup>159</sup>. Xia and coworkers reported 50 nm mesoporous silica nanoparticles coated with PEI/PEG copolymer reached a high passive accumulation of about 12% at the tumor site, compared with 1% of 100 nm phosphonate-coated mesoporous silica nanoparticles. The increased tumor accumulation further brought an enhanced tumor inhibition rate<sup>160</sup>. Active targeting involves surface modification with antibodies, peptides, folic acid, or aptamers. For example, SiNPs modified with folic acids through EDC-NHS

conjugation showed an excellent to label cells <sup>161</sup>. Dye-doped SiNPs modified with two aptamers allowed to improve their efficiency for cancer imaging and therapy<sup>162</sup>.

**Figure 1-23** Passive or active mechanisms of silica nanoparticles applied for drug delivery

**Prolonged release.** The simplest method to control the drug release behavior is through encapsulation inside the silica matrix that can change the release by adjusting the composition and structure of silica nanoparticles. Mebert et al. encapsulated two types of antibiotics via multilayer silica shell forming core-shell silica particles. In particular the silica shell deposition was favored by the positively charged layer of gentamicin coating on the core particle surface. Shell modification by thiol groups finally allowed for rifamycin sorption. The antibacterial activity of the core-shell particles against *Staphylococcus aureus* and *Pseudomonas aeruginosa* demonstrated the dual release and action of the two antibiotics<sup>163</sup>. The porous features of MSNs also offer an interesting parameter to control the drug release. Recently, Zhang et al. discovered that mesoporous silica improves the dissolution rate and bioavailability of hydrophobic telmisartan (TEL) after oral administration<sup>164</sup>. Increasing the pore size also improves the drug dissolution rate because of decreased diffusion hindrance. Pore morphology is believed to greatly affect the properties of the material and the loading of the drug. Wang et al. found that cilostazol has a faster diffusion rate from MCM-48 with interconnected pore structure compared to MCM-41 with an unconnected pore network<sup>165, 166</sup>.

**Endogenous stimuli-responsive drug delivery.** Endogenous stimuli are intrinsic conditions of diseased tissues, such as strong redox conditions, acidic environments, and the presence of certain types of enzymes. The design of nanocarriers that are sensitive to endogenous stimuli

can provide good inspiration for controlled drug delivery. Silica nanoparticles with pH-sensitive gates have been developed. Many materials including polyelectrolytes, supramolecular, pH-sensitive linkers, and acid decomposable inorganic materials are commonly used as drug barriers for pH-responsive drug delivery systems. Feng et al. constructed MSN-based pH-responsive drug delivery systems using polyelectrolyte multilayers. Doxorubicin was loaded into the polyelectrolyte layers and nanopores of the prepared MSN. The results show that MSN can achieve controlled release of the drug under acidic conditions<sup>167</sup> (**Figure 1-24**).

**Figure 1-24** Schematic illustration for the fabrication of pH-responsive carrier systems based on polyelectrolyte multilayer-MSN

Disulfide bonds have caused great interest in controlled drug delivery systems due to its high redox sensitivity, particularly in tumor tissue. Giri and coworkers synthesize an MCM-41-based controlled release delivery system that is capped with disulfide bonds and superparamagnetic Fe<sub>3</sub>O<sub>4</sub> nanoparticles and was stimuli-responsive and chemically inert to guest molecules entrapped in the matrix<sup>168</sup>. The upregulated expression profile of specific enzymes (matrix metalloproteinases, Cathepsin B,  $\beta$ -d-galactosidase) in pathological conditions such as cancer or inflammation, makes it an interesting stimulus to achieve enzyme-mediated drug release<sup>169</sup>.

In addition, there are some biological substances including glucose, ATP, and  $H_2O_2$ , which are also used to design responsive drug delivery systems<sup>170</sup>. Sun et al. introduced a glucose response controlled the release of the new insulin system by applying a multi-layer of glucose oxidase and catalase to the surface of the MSN<sup>171</sup>. MSN is used as a drug reservoir, and a multi-layer of glutaraldehyde cross-linked enzyme is used as a valve to control the release of insulin in response to exogenous glucose levels.

***Exogenous stimuli-responsive drug delivery.*** Unlike endogenous stimuli, exogenous stimuli are performed by externally applied stimuli, including temperature changes, magnetic fields, ultrasound, and light and electric fields. Although this approach appears to be unattractive, exogenously stimulating reactive drug delivery systems may be more beneficial due to heterogeneous physiological conditions in the population.



**Figure 1-25** Schematic illustration of the behavior of dual-responsive release system in aqueous medium

As an example, Poly(N-isopropylacrylamide) (PNIPAM) is well-known as a thermally responsive polymer. Chen et al. reported the thermal response of silica nanoparticles covalently modified with PNIPAM. The nanocarriers prevent drug release above 30 ° C, whereas at temperatures between 25 ° C and 30 ° C, the embedded drug can be released quickly due to the polymer chain stretching and swelling in aqueous solution<sup>172</sup>. Drug release can also be controlled by the application of a magnetic field. Chen et al. used a simple technique to conjugate amine-modified MSNs and 2,3-dimercaptosuccinic acid-functionalized  $Fe_3O_4$  nanoparticles<sup>173</sup>. While a negligible amount of drug is released in the absence of a magnetic field, its application removes some of the iron oxide nanoparticles by breaking the chemical bonds, which in turn leads to a rapid release of the drug. Furthermore, the results show that the

release profile depends on the intensity and duration of the magnetic field. An ultrasound-responsive MSN drug delivery system was also developed by Paris and coworkers<sup>174</sup>. As illustrated in **Figure 1-25**, the temperature-ultrasound dual responsive random copolymer was grafted on the MSN surface to act as a gatekeeper. The temperature conversation is an on-off switch for model drug loading. At low temperature, 4°C, the model drug molecules could be diffused into the open nanopores, whereas at a temperature of 37°C, the hydrophobic polymer tightly collapsed onto the MSN to block the drug molecules in the nanopores. Upon ultrasound irradiation, the sensitive polymer changes its hydrophobicity and conformation toward coil-like gate-opening and cargo-releasing.

### 1.4.3.3 Summary

Here gathered selected examples illustrate the tremendous past developments and recent activity in the field of silica-based nanomaterials intended as carriers for controlled drug delivery. The versatility of silica chemistry combined with elaborated organic synthesis offers an unlimited playground to design more and more sophisticated devices. These developments are indeed not limited to silica and are fed by advances in biology and medicine to enhance targeting specificity and therapeutic efficiency. Although not thoroughly discussed here, similar trends exist in the area of biomedical imaging and the emerging field of theranostics clearly demonstrate how nanotechnology should, in a close future, allow to strongly improve healthcare.

However, the use of nanoscale materials still raises many safety concerns that explain, at least for some part, why nanomedicine products are still scarce on the market. A major issue currently faced is related to the evaluation of these safety concerns while avoiding animal tests. In particular, while the *in vivo* behavior of molecules can be quite well-predicted on the basis of simple physicochemical parameters (pKa, solubility, hydrophilicity), colloidal stability, tissue adhesion/penetration, extra- and intracellular degradation are, among many others, parameters that have to be fully taken into account for nanomaterials. Going from a 2D perspective to a 3D approach may allow progress in the study, understanding, and applications of nanomedicine.

## 1.5 Silica-biopolymer composite hydrogels

### 1.5.1 Nanocomposite hydrogels

Hydrogels are polymeric three-dimensional networks that can maintain up to 99% of water and are increasingly attractive as scaffolds for tissue engineering and drug delivery because of their similarity to microenvironments of native tissues<sup>175</sup> (**Figure 1-26**). They can exhibit several remarkable characteristics, such as versatility in fabrication, variety in composition, high tunability in the physical, and chemical properties, high moldability in shape and excellent biocompatibility. Moreover, some hydrogels could undergo reversible and significant changes in structure, shape, or property after being exposed to external stimuli, such as pH value, temperature, ionic strength, enzymatic activity *etc.* Therefore, hydrogels as promising materials are of greatest significance in the biomedical fields and have been extensively studied in drug delivery.

#### **Figure 1-26** Cross-linked nanocellulose hydrogel and their applications in wound dressing

Since Wichterle and Lim first reported a hydrogel for contact lens application in 1960 based on crosslinked poly-2-hydroxy-ethylmethacrylate (PHEMA) hydrogel by use of ethylene glycol dimethacrylate (EGDMA), significant progress has been achieved and a diverse range of polymers have been used for the synthesis and fabrication of hydrogels for various applications<sup>176</sup>. Besides PHEMA, a great number of synthetic polymers were explored for the preparation of hydrogels by polymerization or cross-linking, such as PEG, PVA, PAA, PVP, PHPMA as well as polypeptides and polyesters. Polymeric hydrogels from synthetic sources are advantageous because they usually possess controllable chemical structure and architecture, degradation rates, and mechanical strengths. However, most of them lack biological cues for biological applications<sup>177, 178</sup>. Natural hydrogels derived from natural sources, such as chitosan, hyaluronic acid, gelatin, collagen, alginate are appealing for biological applications because of



their cell-interactive properties, cell adhesion and cell signaling, as well as biodegradability and excellent biocompatibility<sup>179-182</sup>.

Hydrogels have a variety of properties, such as absorption capacity, swelling behavior, stability, permeability, mechanical properties. The highly porous structure of hydrogel allows for a depot maintaining a high local concentration of drug at the targeted tissues. Despite the many favorable characteristics of hydrogels, problems still exist in many aspects, for example, for the hydrogel-based drug delivery system, the homogeneity and quantity of drug loading into hydrogels is often very difficult, particularly in the case of hydrophobic drugs<sup>183</sup>. The large pore sizes and high water content of most hydrogels often lead to relatively rapid drug release. The premature drug release outside the targeted site not only decreases the therapeutic efficacy but also causes serious local or systemic toxicity. Besides, some hydrophobic drug crystal precipitation tends to occur in the hydrogels, generally causing poor formulation stability and a low drug-loading capacity<sup>184</sup>. Moreover, hydrogels are generally prepared from a single polymer network, which often does not hold all the required mechanical and biological properties for tissue engineering applications. As a result, it is imperative to develop new materials and novel strategies for the introduction of physicochemical, mechanical, and biological functionality into hydrogels to meet the rigorous and diverse demands.

**Figure 1-27** Schematic illustration of typical nanocomposite hydrogels from hydrogels and drug-loaded nanoparticles

One of the efficient and simple approaches to improve the hydrogels properties and to include multiple functionalities is the incorporation of different entities into hydrogels to fabricate composite hydrogel matrices. A variety of nanoparticles have distinct physicochemical properties and favorable functions that are not commonly found in polymers. Recently, considerable efforts have been made to incorporate various kinds of nanoparticles into gel matrices to create novel nanocomposite hydrogels with superior properties and tailored functionalities. In particular, the previously mentioned challenges in the application of

hydrogels and NPs could potentially be overcome by the fabrication of bionanocomposites that associate biomacromolecules and inorganic nanoparticles<sup>185, 186</sup>. For instance, incorporation of drug-loaded nanocarriers within a biocompatible matrix would allow (i) to avoid direct contact between nanoparticles and living tissues, (ii) increase the mechanical stability of the hydrogel and (iii) control the drug release as the bioactive molecule must escape both the NPs and the hydrogels while the polymer/particle interface may decrease the NPs degradation.

The nanocomposite hydrogels can be defined as composite material that physically or covalently incorporates nanosized particles or nanostructures into a matrix of cross-linked polymer networks (**Figure 1-27**). These nanocomposite hydrogels have found fascinating interest for various biomedical applications due to combining the characteristics of a nanoparticulate material with hydrogel system. As a result, the challenges in the application of hydrogels and NPs, as mentioned above, could potentially be overcome by the fabrication of nanocomposite hydrogels. In recent reports, nanocomposite hydrogels prepared by incorporation of silica nanoparticles with hydrogels showed remarkable improvements in mechanical stiffness, tissue stickiness and bioactivity compared with unmodified hydrogels.

Various kinds of silica-based nanoparticles have been incorporated in different synthetic and natural polymers via physical or chemical approaches to obtain bioactive nanocomposite hydrogels. These resulting hydrogels with enhanced mechanical properties, good biocompatibility and biodegradability, tunable cell and tissue adhesion, or improved drug loading and drug release profiles, have exhibited plenty of important applications in biomedical and pharmaceutical fields, such as injectable or implantable sustained drug delivery system, controlled cell and tissue adhesion surfaces, antimicrobial films or wound dressings, tissue engineering and cell-based therapies. The study demonstrated that incorporating silica nanoparticles at a high density within a polymer hydrogel can not only result in mechanically strong and tissue-adhesive nanocomposite hydrogels but also fabricate soft materials with a unique and counterintuitive response to environment-stimuli. The protease responsive hydrogel nanocomposites reported in this study could offer avenues in degradation-stiffening and collapsing materials for a variety of biomaterial applications.

### **1.5.2 Silica-collagen hydrogels**

Collagens are the most abundant proteins in the mammalian body, accounting for 20-30% of the total protein. Collagens form a large family of triple helical molecules with about 28 different types described, with types I, II, III, and IV being the most commons.

All collagens share the same triple-helical structure where three parallel polypeptides,  $\alpha$ -chains, coil around each other forming a right-handed triple helix chain <sup>187</sup>

In animals, these collagen triple helices are known as tropocollagen and its hierarchical organization into more complex structures generates the fibers and networks in tissues such as bone, skin, and tendons<sup>188</sup>(**Figure 1-28**).

**Figure 1-28** The hierarchical structure of collagen fibers

The primary functions of type I collagen are to provide mechanical support and to control cell adhesion and migration. Thanks to the above-mentioned characteristics, collagen is frequently used to prepare wound dressings <sup>189</sup>. (**Figure 1-29**). However, collagen-based materials suffer from uncontrolled degradation and low mechanical strength, which necessitate the chemical and physical modifications of the collagen.

**Figure 1-29** (A) Collagen hydrogel. (B) Collagen sponge. (C) Collagen hydrogel scaffold. (D) Hematoxylin and eosin staining of collagen hydrogel scaffold

Composite collagen-based hydrogels obtained by introducing other natural (e.g. elastin, hyaluronan) or synthetic (e.g. PEG) polymers and particulates (e.g. calcium phosphate particles, silica nanoparticles) have been widely used to add strength and functionality to the system<sup>190</sup>. As an example, Raftery et al. studied collagen-based scaffolds for localized gene delivery, where chitosan-DNA was loaded by surface adsorption<sup>191</sup>. The scaffolds used in the study include a collagen scaffold and collagen-hydroxyapatite (CHA) scaffold for bone repair, and a collagen-hyaluronic acid (CHyA) with properties optimized for cartilage regeneration. Sustained gene expression from mesenchymal stem cells (MSCs) seeded on the scaffolds was maintained for 28 days, and its efficiency depended on the composition of the scaffold.

**Figure 1-30** Various configurations for gene delivery in silica-collagen nanocomposites: (1) particles out/cells in; (2) particles and cells in; (3) particles in/cells out

The ease to prepare collagen hydrogel facilitates the incorporation of other ingredients (e.g. cell culture medium, bioactive proteins, drugs), which makes collagen-based materials appealing candidates for bioactive wound dressing fabrication. However, fast release of biomolecules and limited mechanical strength remains drawbacks of this system. In this context, it has been suggested that the combination of collagen hydrogels with silica could improve their performance. Various silica species have been reported for silicification of soluble collagen, fibrils, fibers, films, gels or scaffolds for different medical applications<sup>192</sup>. In our group, preliminary biocompatibility studies by subcutaneous implantation of collagen-silica bionanocomposites in rats showed the absence of significant inflammation, efficient infiltration of fibroblast cells and initiation of vascularization<sup>193</sup>. The controlled release of antibiotics, initially encapsulated within Stöber silica nanoparticles, from collagen-silica nanocomposites was demonstrated *in vitro* and *in vivo*<sup>194</sup>. However, no noticeable improvement of the hydrogel mechanical stability was measured. Finally, the co-encapsulation of silica nanoparticles coated with PEI as gene carriers and of fibroblast cells within collagen hydrogels allowed to evidence the possible gene delivery within the matrix<sup>195, 196</sup>. However, it was also shown that the

efficiency of this process depends on the chemical bonding between silica and PEI and also whether the particles and cells are co-encapsulated or if only one of the components is immobilized within the collagen hydrogel (**Figure 1-30**).

### **1.5.3 Open questions and motivations of this work**

These results open many intriguing questions. First, the success of gene delivery requires very specific events occurring intracellularly, especially the escape of the plasmid from endosomal compartments. How this happens with silica particles remains unclear and is strongly related to the intracellular fate of these particles. As a matter of fact, if one could predict the degradation pathway of such nanocarriers inside the cells, it should allow to optimize their composition and/or structure for intracellular drug delivery. The second question is related to the role of the 3D environment (i.e. the collagen hydrogel) on the cell-particle interactions. Indeed, it is expected that diffusion issues can affect the particle mobility while cell motility may also be at stake. This is an interesting point to consider knowing that, in many *in vivo* applications, targeted cells are not free floating or on a surface but within an extracellular 3D matrix. Answering these two questions was the first goal of this PhD project and my research along this direction is presented in the following chapters **2** and **3**.

Considering the bionanocomposite approach *per se*, we have already pointed out that while its benefit to tune the drug release rate from silica nanoparticles was clearly demonstrated, its advantage for the stability of the collagen network was not yet clearly evidenced. As it is well-known in the area of nanocomposite, improved mechanical properties of a polymer matrix can be achieved by enhancing particle/polymer chemical interactions and/or creating a percolating network of nanoparticles. As such a percolation is more easily achieved with high aspect ratio particles rather than with spherical ones, we explored the possibility to design and use silica-based nanorods to tune the mechanical behavior of collagen hydrogels and, at the same time, using them to study the cells growth and reproduction performance which is very important for the further drug delivery and biological applications. Moreover, a novel magnetic composite hydrogel has also been prepared for the magnetic manipulation in 3D hydrogels. This part of my PhD work is presented in chapter **4** of this manuscript.

### **Reference**

1. Drexler, K. E., Engines of Creation: The Coming Era of Nanotechnology. *Doubleday* **1986**.

2. Buzea, C.; Pacheco, II; Robbie, K., Nanomaterials and nanoparticles: Sources and toxicity. *Biointerphases* **2007**, 2, (4), MR17-MR71.
3. Singh, A. V.; Mehta, K. K., Top-Down Versus Bottom-Up Nanoengineering Routes to Design Advanced Oropharmacological Products. *Curr. Pharm. Des.* **2016**, 22, (11), 1534-1545.
4. Hubler, A. W.; Osuagwu, O., Digital Quantum Batteries: Energy and Information Storage in Nanovacuum Tube Arrays. *Complexity* **2010**, 15, (5), 48-55.
5. MacDonald, V., Nanotechnology finds some growing applications. *Chem. Week* **2005**, 167, (16), 35-+.
6. Reverchon, E., An introduction to nanotechnologies and their applications. *Chimica Oggi-Chemistry Today* **2004**, 22, (9), 12-13.
7. Seidel, K., Practical Applications of Nanotechnology. *Elektrotechnik Und Informationstechnik* **2009**, 126, (5), A26-A28.
8. West, J. L., Diagnostic and Therapeutic Applications of Nanotechnology. *Cancer Res.* **2009**, 69, (24), 484S-484S.
9. Zhao, F. L.; Liu, H. M.; Mathe, S. D. R.; Dong, A. J.; Zhang, J. H., Covalent Organic Frameworks: From Materials Design to Biomedical Application. *Nanomaterials* **2018**, 8, (1).
10. Cao, Y. C., Nanomaterials for biomedical applications. *Nanomedicine* **2008**, 3, (4), 467-469.
11. Bououdina, M.; Rashdan, S.; Bobet, J. L.; Ichiyanagi, Y., Nanomaterials for Biomedical Applications: Synthesis, Characterization, and Applications. *Journal Of Nanomaterials* **2013**.
12. Ganipineni, L. P.; Danhier, F.; Preat, V., Drug delivery challenges and future of chemotherapeutic nanomedicine for glioblastoma treatment. *J. Control. Release* **2018**, 281, 42-57.
13. Gratieri, T.; Gelfuso, G. M.; Lopez, R. F. V.; Souto, E. B., Current efforts and the potential of nanomedicine in treating fungal keratitis. *Expert Review Of Ophthalmology* **2010**, 5, (3), 365-384.
14. Metcalfe, S., NANOMEDICINE: DEVELOPMENT OF LIF-NANO FOR TREATMENT OF MULTIPLE SCLEROSIS. *Glia* **2013**, 61, S38-S38.
15. Chakravarthy, K. V.; Boehm, F. J.; Christo, P. J., Nanotechnology: A Promising New Paradigm for the Control of Pain. *Pain Med.* **2018**, 19, (2), 232-243.

16. Sahebkar, A.; Badiie, A.; Ghayour-Mobarhan, M.; Goldouzian, S. R.; Jaafari, M. R., A simple and effective approach for the treatment of dyslipidemia using anionic nanoliposomes. *Colloids And Surfaces B-Biointerfaces* **2014**, 122, 645-652.
17. Ritchie, T. J.; Macdonald, S. J. F., The impact of aromatic ring count on compound developability - are too many aromatic rings a liability in drug design? *Drug Discovery Today* **2009**, 14, (21-22), 1011-1020.
18. Ali, I.; Rahis, U.; Salim, K.; Rajora, A. K.; Rather, M. A.; Wani, W. A.; Haque, A., Advances in Nano Drugs for Cancer Chemotherapy. *Curr. Cancer Drug Targets* **2011**, 11, (2), 135-146.
19. Ali, I., Nano Drugs: Novel Agents for Cancer Chemo-Therapy. *Curr. Cancer Drug Targets* **2011**, 11, (2), 130-130.
20. Zhang, J. Z., Ultrafast studies of electron dynamics in semiconductor and metal colloidal nanoparticles: Effects of size and surface. *Acc. Chem. Res.* **1997**, 30, (10), 423-429.
21. Agrawal, A.; Zhang, C. Y.; Byassee, T.; Tripp, R. A.; Nie, S. M., Counting single native biomolecules and intact viruses with color-coded nanoparticles. *Anal. Chem.* **2006**, 78, (4), 1061-1070.
22. Kim, J.; Piao, Y.; Hyeon, T., Multifunctional nanostructured materials for multimodal imaging, and simultaneous imaging and therapy. *Chem. Soc. Rev.* **2009**, 38, (2), 372-390.
23. Serralheiro, A.; Alves, G.; Fortuna, A.; Falcao, A., Intranasal administration of carbamazepine to mice: A direct delivery pathway for brain targeting. *Eur. J. Pharm. Sci.* **2014**, 60, 32-39.
24. Shah, R. B.; Patel, M.; Maahs, D. M.; Shah, V. N., Insulin delivery methods: Past, present and future. *International Journal Of Pharmaceutical Investigation* **2016**, 6, (1), 1-9.
25. Bertrand, N.; Leroux, J. C., The journey of a drug-carrier in the body: An anatomophysiological perspective. *J. Control. Release* **2012**, 161, (2), 152-163.
26. Freire, R. M.; Longhinotti, E.; Sousa, E. H. S.; Fechine, P. B. A., *Inorganic Nanoparticle Materials for Controlled Drug Delivery Systems*. **2014**; p 327-348.
27. Desai, N., Challenges in Development of Nanoparticle-Based Therapeutics. *Aaps Journal* **2012**, 14, (2), 282-295.
28. Bertrand, N.; Leroux, J.-C., The journey of a drug-carrier in the body: An anatomophysiological perspective. *J. Control. Release* **2012**, 161, (2), 152-163.

29. Bangham, A. D.; Horne, R. W., Negative staining of phospholipids and their structural modification by surface-active agents as observed in the electron microscope. *J. Mol. Biol.* **1964**, 8, (5), 660-IN10.
30. Wagner, A.; Vorauer-Uhl, K., Liposome Technology for Industrial Purposes. *Journal Of Drug Delivery* **2011**.
31. Yoshioka, H., SURFACE MODIFICATION OF HEMOGLOBIN-CONTAINING LIPOSOMES WITH POLYETHYLENE-GLYCOL PREVENTS LIPOSOME AGGREGATION IN BLOOD-PLASMA. *Biomaterials* **1991**, 12, (9), 861-864.
32. Guo, X. Q.; Wu, Z. M.; Guo, Z. W., New Method for Site-Specific Modification of Liposomes with Proteins Using Sortase A-Mediated Transpeptidation. *Bioconjug. Chem.* **2012**, 23, (3), 650-655.
33. Schiffelers, R. M.; Ansari, A.; Xu, J.; Zhou, Q.; Tang, Q. Q.; Storm, G., et al. Woodle, M. C., Cancer siRNA therapy by tumor selective delivery with ligand-targeted sterically stabilized nanoparticle. *Nucleic Acids Res.* **2004**, 32, (19).
34. Pinato, G.; Raffaelli, T.; D'Este, E.; Tavano, F.; Cojoc, D., Optical delivery of liposome encapsulated chemical stimuli to neuronal cells. *Journal Of Biomedical Optics* **2011**, 16, (9).
35. Latif, N. A.; Mandal, C., LIPOSOME AS AN ADJUVANT FOR THE PRODUCTION OF ESTRADIOL ANTIBODIES. *Immunol. Lett.* **1987**, 15, (3), 237-242.
36. Mukherjee, S.; Ray, S.; Thakur, R. S., Solid Lipid Nanoparticles: A Modern Formulation Approach in Drug Delivery System. *Indian J. Pharm. Sci.* **2009**, 71, (4), 349-358.
37. Zariwala, M. G.; Elsaid, N.; Jackson, T. L.; Lopez, F. C.; Farnaud, S.; Somavarapu, S.; Renshaw, D., A novel approach to oral iron delivery using ferrous sulphate loaded solid lipid nanoparticles. *Int. J. Pharm.* **2013**, 456, (2), 400-407.
38. Marquez-Miranda, V.; Penaloza, J. P.; Araya-Duran, I.; Reyes, R.; Vidaurre, S.; Romero, V., et al. Otero, C., Effect of Terminal Groups of Dendrimers in the Complexation with Antisense Oligonucleotides and Cell Uptake. *Nanoscale Research Letters* **2016**, 11.
39. Clementi, C.; Miller, K.; Mero, A.; Satchi-Fainaro, R.; Pasut, G., Dendritic Poly(ethylene glycol) Bearing Paclitaxel and Alendronate for Targeting Bone Neoplasms. *Mol. Pharm.* **2011**, 8, (4), 1063-1072.



40. Kumar, S.; Dilbaghi, N.; Saharan, R.; Bhanjana, G., Nanotechnology as Emerging Tool for Enhancing Solubility of Poorly Water-Soluble Drugs. *Bionanoscience* **2012**, 2, (4), 227-250.
41. Xu, W.; Ling, P. X.; Zhang, T. M., Polymeric Micelles, a Promising Drug Delivery System to Enhance Bioavailability of Poorly Water-Soluble Drugs. *Journal Of Drug Delivery* **2013**.
42. Lu, Y.; Park, K., Polymeric micelles and alternative nanonized delivery vehicles for poorly soluble drugs. *Int. J. Pharm.* **2013**, 453, (1), 198-214.
43. Guo, X.; Wang, L.; Wei, X.; Zhou, S. B., Polymer-Based Drug Delivery Systems for Cancer Treatment. *Journal Of Polymer Science Part a-Polymer Chemistry* **2016**, 54, (22), 3525-3550.
44. Chen, S. Z.; Hao, X. H.; Liang, X. J.; Zhang, Q.; Zhang, C. M.; Zhou, G. Q., et al. Zhang, J. C., Inorganic Nanomaterials as Carriers for Drug Delivery. *Journal Of Biomedical Nanotechnology* **2016**, 12, (1), 1-27.
45. Gerhold, M.; Xu, J., Quantum Dots. *Journal Of Nanophotonics* **2009**, 3.
46. Bagalkot, V.; Zhang, L.; Levy-Nissenbaum, E.; Jon, S.; Kantoff, P. W.; Langer, R.; Farokhzad, O. C., Quantum dot - Aptamer conjugates for synchronous cancer imaging, therapy, and sensing of drug delivery based on Bi-fluorescence resonance energy transfer. *Nano Letters* **2007**, 7, (10), 3065-3070.
47. Tang, Y.; Han, S. L.; Liu, H. M.; Chen, X.; Huang, L.; Li, X. H.; Zhang, J. X., The role of surface chemistry in determining in vivo biodistribution and toxicity of CdSe/ZnS core-shell quantum dots. *Biomaterials* **2013**, 34, (34), 8741-8755.
48. Carbon Based Nanomaterials. In *Carbon Based Nanomaterials*, Ali, N.; Ochsner, A.; Ahmed, W., Eds. **2010**; Vol. 65-66, pp 1-322.
49. Dhar, S.; Liu, Z.; Thomale, J.; Dai, H. J.; Lippard, S. J., Targeted single-wall carbon nanotube-mediated Pt(IV) prodrug delivery using folate as a homing device. *J. Am. Chem. Soc.* **2008**, 130, (34), 11467-11476.
50. Rastogi, V.; Yadav, P.; Bhattacharya, S. S.; Mishra, A. K.; Verma, N.; Verma, A.; Pandit, J. K., Carbon Nanotubes: An Emerging Drug Carrier for Targeting Cancer Cells. *Journal Of Drug Delivery* **2014**.
51. Hu, S. S.; Wang, T.; Pei, X. B.; Cai, H.; Chen, J. Y.; Zhang, X., et al. Wang, J., Synergistic Enhancement of Antitumor Efficacy by PEGylated Multi-walled Carbon Nanotubes Modified with Cell-Penetrating Peptide TAT. *Nanoscale Research Letters* **2016**, 11.

52. Yu, H. T.; Zhang, B. W.; Bulin, C. K.; Li, R. H.; Xing, R. G., High-efficient Synthesis of Graphene Oxide Based on Improved Hummers Method. *Sci. Rep.* **2016**, 6.
53. Pan, L. L.; Sun, S.; Zhang, L.; Jiang, K.; Lin, H. W., Near-infrared emissive carbon dots for two-photon fluorescence bioimaging. *Nanoscale* **2016**, 8, (39), 17350-17356.
54. Zheng, M.; Liu, S.; Li, J.; Qu, D.; Zhao, H. F.; Guan, X. G., et al. Sun, Z. C., Integrating Oxaliplatin with Highly Luminescent Carbon Dots: An Unprecedented Theranostic Agent for Personalized Medicine. *Advanced Materials* **2014**, 26, (21), 3554-3560.
55. Zhang, L.; Yao, M. C.; Yan, W.; Liu, X. N.; Jiang, B. F.; Qian, Z. Y., et al. Wang, Q. L., Delivery of a chemotherapeutic drug using novel hollow carbon spheres for esophageal cancer treatment. *International Journal Of Nanomedicine* **2017**, 12, 6759-6769.
56. Shen, Z. Y.; Chen, T. X.; Ma, X. H.; Ren, W. Z.; Zhou, Z. J.; Zhu, G. Z., et al. Wu, A. G., Multifunctional Theranostic Nanoparticles Based on Exceedingly Small Magnetic Iron Oxide Nanoparticles for T-1-Weighted Magnetic Resonance Imaging and Chemotherapy. *Acs Nano* **2017**, 11, (11), 10992-11004.
57. Todd, T.; Zhen, Z. P.; Tang, W.; Chen, H. M.; Wang, G.; Chuang, Y. J., et al. Xie, J., Iron oxide nanoparticle encapsulated diatoms for magnetic delivery of small molecules to tumors. *Nanoscale* **2014**, 6, (4), 2073-2076.
58. Hong, R.; Han, G.; Fernandez, J. M.; Kim, B. J.; Forbes, N. S.; Rotello, V. M., Glutathione-mediated delivery and release using monolayer protected nanoparticle carriers. *J. Am. Chem. Soc.* **2006**, 128, (4), 1078-1079.
59. Farooq, M. U.; Novosad, V.; Rozhkova, E. A.; Wali, H.; Ali, A.; Fateh, A. A., et al. Wang, Z. M., Gold Nanoparticles-enabled Efficient Dual Delivery of Anticancer Therapeutics to HeLa Cells. *Sci. Rep.* **2018**, 8.
60. Huang, X. H.; El-Sayed, M. A., Gold nanoparticles: Optical properties and implementations in cancer diagnosis and photothermal therapy. *Journal Of Advanced Research* **2010**, 1, (1), 13-28.
61. Zhang, W. J.; Wang, F. H.; Wang, Y.; Wang, J. N.; Yu, Y. N.; Guo, S. R., et al. Zhou, D. J., pH and near-infrared light dual-stimuli responsive drug delivery using DNA-conjugated gold nanorods for effective treatment of multidrug resistant cancer cells. *J. Control. Release* **2016**, 232, 9-19.

62. Payne, C. C., APPLICATIONS OF COLLOIDAL SILICA - PAST, PRESENT AND FUTURE. *Abstracts Of Papers Of the American Chemical Society* **1990**, 200, 188-COLL.
63. Go, M. R.; Bae, S. H.; Kim, H. J.; Yu, J.; Choi, S. J., Interactions between Food Additive Silica Nanoparticles and Food Matrices. *Frontiers In Microbiology* **2017**, 8.
64. Bitar, A.; Ahmad, N. M.; Fessi, H.; Elaissari, A., Silica-based nanoparticles for biomedical applications. *Drug Discovery Today* **2012**, 17, (19-20), 1147-1154.
65. Dinsdale, A., SILICATE SCIENCE - SILICATE STRUCTURES. *Physics And Chemistry Of Glasses* **1965**, 6, (2), 68-&.
66. Cho, K.; Chang, H.; Kil, D. S.; Park, J.; Jang, H. D.; Sohn, H. Y., Mechanisms of the Formation of Silica Particles from Precursors with Different Volatilities by Flame Spray Pyrolysis. *Aerosol Science And Technology* **2009**, 43, (9), 911-920.
67. Rezaei, S.; Manoucheri, I.; Moradian, R.; Pourabbas, B., One-step chemical vapor deposition and modification of silica nanoparticles at the lowest possible temperature and superhydrophobic surface fabrication. *Chemical Engineering Journal* **2014**, 252, 11-16.
68. Salavati-Niasari, M.; Javidi, J.; Dadkhah, M., Ball Milling Synthesis of Silica Nanoparticle from Rice Husk Ash for Drug Delivery Application. *Comb. Chem. High Throughput Screen.* **2013**, 16, (6), 458-462.
69. Singh, L. P.; Bhattacharyya, S. K.; Kumar, R.; Mishra, G.; Sharma, U.; Singh, G.; Ahalawat, S., Sol-Gel processing of silica nanoparticles and their applications. *Adv. Colloid Interface Sci.* **2014**, 214, 17-37.
70. Cheng, X. L.; Chen, D. R.; Liu, Y. J., Mechanisms of Silicon Alkoxide Hydrolysis-Oligomerization Reactions: A DFT Investigation. *Chemphyschem* **2012**, 13, (9), 2392-2404.
71. Belton, D. J.; Deschaume, O.; Perry, C. C., An overview of the fundamentals of the chemistry of silica with relevance to biosilicification and technological advances. *Febs Journal* **2012**, 279, (10), 1710-1720.
72. Lazaro, A.; Vilanova, N.; Torres, L. D. B.; Resoort, G.; Voets, I. K.; Brouwers, H. J. H., Synthesis, Polymerization, and Assembly of Nanosilica Particles below the Isoelectric Point. *Langmuir* **2017**, 33, (51), 14618-14626.
73. Karasinski, P., Influence of technological parameters on the properties of sol-gel silica films. *Optica Applicata* **2005**, 35, (1), 117-128.

74. Stöber, W.; Fink, A.; Bohn, E., Controlled growth of monodisperse silica spheres in the micron size range. *J. Colloid Interface Sci.* **1968**, 26, (1), 62-69.
75. Yamamoto, E.; Kitahara, M.; Tsumura, T.; Kuroda, K., Preparation of Size-Controlled Monodisperse Colloidal Mesoporous Silica Nanoparticles and Fabrication of Colloidal Crystals. *Chem. Mater.* **2014**, 26, (9), 2927-2933.
76. Zulfiqar, U.; Subhani, T.; Husain, S. W., Synthesis and characterization of silica nanoparticles from clay. *Journal of Asian Ceramic Societies* **2016**, 4, (1), 91-96.
77. Finnie, K. S.; Bartlett, J. R.; Barbe, C. J. A.; Kong, L. G., Formation of silica nanoparticles in microemulsions. *Langmuir* **2007**, 23, (6), 3017-3024.
78. Arriagada, F. J.; Osseasare, K., SYNTHESIS OF NANOSIZE SILICA IN AEROSOL OT REVERSE MICROEMULSIONS. *J. Colloid Interface Sci.* **1995**, 170, (1), 8-17.
79. Waldron, K.; Wu, Z.; Zhao, D.; Chen, X. D.; Selomulya, C., On Spray Drying of Uniform Mesoporous Silica Microparticles. *Materials Today: Proceedings* **2016**, 3, (2), 646-651.
80. Boissiere, C.; van der Lee, A.; El Mansouri, A.; Larbot, A.; Prouzet, E., A double step synthesis of mesoporous micrometric spherical MSU-X silica particles. *Chemical Communications* **1999**, (20), 2047-2048.
81. Masalov, V. M.; Sukhinina, N. S.; Emel'chenko, G. A., Synthesis of Monodisperse Silica Nanoparticles via Heterogeneous Tetraethoxysilane Hydrolysis Using L-Arginine as a Catalyst. *Inorganic Materials* **2018**, 54, (2), 156-162.
82. Rida, M. A.; Harb, F., Synthesis and characterization of amorphous silica nanoparticles from aqueous silicates using cationic surfactants. *Journal of Metals, Materials and Minerals* **2014**, 24, (1).
83. Roy, I., Synthesis, surface modification, characterization, and biomedical in vitro applications of organically modified silica (ORMOSIL) nanoparticles. In *Nanoparticles in Biology and Medicine*, Springer: **2012**; pp 365-379.
84. Nandiyanto, A. B. D.; Okuyama, K., Progress in developing spray-drying methods for the production of controlled morphology particles: From the nanometer to submicrometer size ranges. *Advanced Powder Technology* **2011**, 22, (1), 1-19.
85. Chauhan, V. P.; Popović, Z.; Chen, O.; Cui, J.; Fukumura, D.; Bawendi, M. G.; Jain, R. K., Fluorescent nanorods and nanospheres for real - time in vivo probing of

nanoparticle shape - dependent tumor penetration. *Angewandte Chemie International Edition* **2011**, 50, (48), 11417-11420.

86. Hagemans, F.; van der Wee, E. B.; van Blaaderen, A.; Imhof, A., Synthesis of cone-shaped colloids from rod-like silica colloids with a gradient in the etching rate. *Langmuir* **2016**, 32, (16), 3970-3976.

87. Morgan, A. R.; Dawson, A. B.; Mckenzie, H. S.; Skelhon, T. S.; Beanland, R.; Franks, H. P.; Bon, S. A., Chemotaxis of catalytic silica–manganese oxide “matchstick” particles. *Materials Horizons* **2014**, 1, (1), 65-68.

88. Gille, W., *Particle and particle systems characterization: small-angle scattering (SAS) applications*. CRC Press: **2016**.

89. Farid, G.; Kruk, M., Silica Nanotubes with Widely Adjustable Inner Diameter and Ordered Silicas with Ultralarge Cylindrical Mesopores Templated by Swollen Micelles of Mixed Pluronic Triblock Copolymers. *Chem. Mater.* **2017**, 29, (11), 4675-4681.

90. Kuijk, A.; van Blaaderen, A.; Imhof, A., Synthesis of monodisperse, rodlike silica colloids with tunable aspect ratio. *Journal of the American Chemical Society* **2011**, 133, (8), 2346-2349.

91. Tang, X.; Sun, A.; Chu, C.; Yu, M.; Ma, S.; Cheng, Y., et al. Xu, G., A novel silica nanowire-silica composite aerogels dried at ambient pressure. *Materials & Design* **2017**, 115, 415-421.

92. Slowing, I. I.; Vivero-Escoto, J. L.; Trewyn, B. G.; Lin, V. S.-Y., Mesoporous silica nanoparticles: structural design and applications. *J. Mater. Chem.* **2010**, 20, (37), 7924-7937.

93. Krajišnik, D.; Čalijs, B.; Cekić, N., Polymeric Microparticles and Inorganic Micro/Nanoparticulate Drug Carriers: An Overview and Pharmaceutical Application. In *Microsized and Nanosized Carriers for Nonsteroidal Anti-Inflammatory Drugs*, Elsevier: **2017**; pp 31-67.

94. Mehmood, A.; Ghafar, H.; Yaqoob, S.; Gohar, U.; Ahmad, B., Mesoporous silica nanoparticles: a review. *J. Dev. Drugs* **2017**, 6, 1000174.

95. Yu, L.; Chen, Y.; Lin, H.; Du, W.; Chen, H.; Shi, J., Ultrasmall mesoporous organosilica nanoparticles: Morphology modulations and redox-responsive biodegradability for tumor-specific drug delivery. *Biomaterials* **2018**, 161, 292-305.

96. Kresge, C.; Leonowicz, M.; Roth, W. J.; Vartuli, J.; Beck, J., Ordered mesoporous molecular sieves synthesized by a liquid-crystal template mechanism. *Nature* **1992**, 359, (6397), 710.
97. Wahab, M. A.; Sudhakar, S.; Yeo, E.; Sellinger, A., Evaporation-induced self-assembly of mesoscopically ordered organic/organosilica nanocomposite thin films with photoluminescent properties and improved hardness. *Chem. Mater.* **2008**, 20, (5), 1855-1861.
98. AlOthman, Z. A., A review: fundamental aspects of silicate mesoporous materials. *Materials* **2012**, 5, (12), 2874-2902.
99. Chen, Y.; Chen, H.; Guo, L.; He, Q.; Chen, F.; Zhou, J., et al. Shi, J., Hollow/rattle-type mesoporous nanostructures by a structural difference-based selective etching strategy. *ACS nano* **2009**, 4, (1), 529-539.
100. Chang, F. P.; Chen, Y. P.; Mou, C. Y., Intracellular implantation of enzymes in hollow silica nanospheres for protein therapy: cascade system of superoxide dismutase and catalase. *Small* **2014**, 10, (22), 4785-4795.
101. Popat, A.; Hartono, S. B.; Stahr, F.; Liu, J.; Qiao, S. Z.; Lu, G. Q. M., Mesoporous silica nanoparticles for bioadsorption, enzyme immobilisation, and delivery carriers. *Nanoscale* **2011**, 3, (7), 2801-2818.
102. Tang, F.; Li, L.; Chen, D., Mesoporous silica nanoparticles: synthesis, biocompatibility and drug delivery. *Advanced materials* **2012**, 24, (12), 1504-1534.
103. Zhao, F.; Zhao, Y.; Liu, Y.; Chang, X.; Chen, C.; Zhao, Y., Cellular uptake, intracellular trafficking, and cytotoxicity of nanomaterials. *Small* **2011**, 7, (10), 1322-1337.
104. Huh, S.; Wiench, J. W.; Yoo, J.-C.; Pruski, M.; Lin, V. S.-Y., Organic functionalization and morphology control of mesoporous silicas via a co-condensation synthesis method. *Chem. Mater.* **2003**, 15, (22), 4247-4256.
105. Lubbad, S.; Buchmeiser, M. R., A New Approach to High-Capacity Functionalized Monoliths via Post-Synthesis Grafting. *Macromolecular rapid communications* **2003**, 24, (9), 580-584.
106. Hoffmann, F.; Fröba, M., Vitalising porous inorganic silica networks with organic functions—PMOs and related hybrid materials. *Chem. Soc. Rev.* **2011**, 40, (2), 608-620.
107. Buchman, Y. K.; Lellouche, E.; Zigdon, S.; Bechor, M.; Michaeli, S.; Lellouche, J.-P., Silica nanoparticles and polyethyleneimine (PEI)-mediated functionalization: a

new method of PEI covalent attachment for siRNA delivery applications. *Bioconjug. Chem.* **2013**, 24, (12), 2076-2087.

108. Minko, S., Grafting on solid surfaces: “Grafting to” and “grafting from” methods. In *Polymer surfaces and interfaces*, Springer: **2008**; pp 215-234.

109. Kim, C. O.; Cho, S. J.; Park, J. W., Hyperbranching polymerization of aziridine on silica solid substrates leading to a surface of highly dense reactive amine groups. *J. Colloid Interface Sci.* **2003**, 260, (2), 374-378.

110. Sperling, R. A.; Parak, W. J., Surface modification, functionalization and bioconjugation of colloidal inorganic nanoparticles. *Philosophical Transactions of the Royal Society of London A: Mathematical, Physical and Engineering Sciences* **2010**, 368, (1915), 1333-1383.

111. Quesada, M.; Muniesa, C.; Botella, P., Hybrid PLGA-organosilica nanoparticles with redox-sensitive molecular gates. *Chem. Mater.* **2013**, 25, (13), 2597-2602.

112. Fujiwara, M.; Shiokawa, K.; Hayashi, K.; Morigaki, K.; Nakahara, Y., Direct encapsulation of BSA and DNA into silica microcapsules (hollow spheres). *Journal of Biomedical Materials Research Part A* **2007**, 81, (1), 103-112.

113. Zou, H.; Wu, S.; Shen, J., Polymer/silica nanocomposites: preparation, characterization, properties, and applications. *Chem. Rev.* **2008**, 108, (9), 3893-3957.

114. Roosen, J.; Pype, J.; Binnemans, K.; Mullens, S., Shaping of alginate–silica hybrid materials into microspheres through vibrating-nozzle technology and their use for the recovery of neodymium from aqueous solutions. *Ind. Eng. Chem. Res.* **2015**, 54, (51), 12836-12846.

115. Bagwe, R. P.; Yang, C.; Hilliard, L. R.; Tan, W., Optimization of dye-doped silica nanoparticles prepared using a reverse microemulsion method. *Langmuir* **2004**, 20, (19), 8336-8342.

116. Qian, J.; Wang, D.; Cai, F.; Zhan, Q.; Wang, Y.; He, S., Photosensitizer encapsulated organically modified silica nanoparticles for direct two-photon photodynamic therapy and in vivo functional imaging. *Biomaterials* **2012**, 33, (19), 4851-4860.

117. Kopanja, L.; Kralj, S.; Zunic, D.; Loncar, B.; Tadic, M., Core-shell superparamagnetic iron oxide nanoparticle (SPION) clusters: TEM micrograph analysis, particle design and shape analysis. *Ceramics International* **2016**, 42, (9), 10976-10984.

118. Zhao, N.; Yang, Z. R.; Li, B. X.; Meng, J.; Shi, Z. L.; Li, P.; Fu, S., RGD-conjugated mesoporous silica-encapsulated gold nanorods enhance the sensitization of triple-

negative breast cancer to megavoltage radiation therapy. *International Journal Of Nanomedicine* **2016**, 11, 5595-5610.

119. Stoeva, S. I.; Huo, F. W.; Lee, J. S.; Mirkin, C. A., Three-layer composite magnetic nanoparticle probes for DNA. *J. Am. Chem. Soc.* **2005**, 127, (44), 15362-15363.

120. Wang, F.; Gao, F.; Lan, M. B.; Yuan, H. H.; Huang, Y. P.; Liu, J. W., Oxidative stress contributes to silica nanoparticle-induced cytotoxicity in human embryonic kidney cells. *Toxicol. In Vitro* **2009**, 23, (5), 808-815.

121. Yu, T.; Malugin, A.; Ghandehari, H., Impact of Silica Nanoparticle Design on Cellular Toxicity and Hemolytic Activity. *Acs Nano* **2011**, 5, (7), 5717-5728.

122. Croissant, J. G.; Fatieiev, Y.; Khashab, N. M., Degradability and Clearance of Silicon, Organosilica, Silsesquioxane, Silica Mixed Oxide, and Mesoporous Silica Nanoparticles. *Advanced Materials* **2017**, 29, (9).

123. Intracellular Delivery: Fundamentals and Applications. In *Intracellular Delivery: Fundamentals And Applications*, Prokop, A., Ed. **2011**; Vol. 5, pp 1-867.

124. Subramanian, K.; Sankaramourthy, D.; Gunasekaran, M., Chapter 18 - Toxicity Studies Related to Medicinal Plants. In *Natural Products and Drug Discovery*, Mandal, S. C.; Mandal, V.; Konishi, T., Eds. Elsevier: **2018**; pp 491-505.

125. Chan, W. T.; Liu, C. C.; Chiau, J. S. C.; Tsai, S. T.; Liang, C. K.; Cheng, M. L., et al. Hou, S. Y., In vivo toxicologic study of larger silica nanoparticles in mice. *International Journal Of Nanomedicine* **2017**, 12, 3421-3432.

126. Ivanov, S.; Zhuravsky, S.; Yukina, G.; Tomson, V.; Korolev, D.; Galagudza, M., In Vivo Toxicity of Intravenously Administered Silica and Silicon Nanoparticles. *Materials* **2012**, 5, (10), 1873-1889.

127. Murugadoss, S.; Lison, D.; Godderis, L.; Van den Brule, S.; Mast, J.; Brassinne, F., et al. Hoet, P. H., Toxicology of silica nanoparticles: an update. *Arch. Toxicol.* **2017**, 91, (9), 2967-3010.

128. Braun, K.; Pochert, A.; Beck, M.; Fiedler, R.; Gruber, J.; Linden, M., Dissolution kinetics of mesoporous silica nanoparticles in different simulated body fluids. *Journal Of Sol-Gel Science And Technology* **2016**, 79, (2), 319-327.

129. Yamada, H.; Urata, C.; Ujiie, H.; Yamauchi, Y.; Kuroda, K., Preparation of aqueous colloidal mesostructured and mesoporous silica nanoparticles with controlled particle size in a very wide range from 20 nm to 700 nm. *Nanoscale* **2013**, 5, (13), 6145-6153.



130. Chen, G. T.; Teng, Z. G.; Su, X. D.; Liu, Y.; Lu, G. M., Unique Biological Degradation Behavior of Stober Mesoporous Silica Nanoparticles from Their Interiors to Their Exteriors. *Journal Of Biomedical Nanotechnology* **2015**, 11, (4), 722-729.
131. Zhao, Y. T.; Wang, Y.; Ran, F.; Cui, Y.; Liu, C.; Zhao, Q. F., et al. Wang, S. L., A comparison between sphere and rod nanoparticles regarding their in vivo biological behavior and pharmacokinetics. *Sci. Rep.* **2017**, 7.
132. Sapsford, K. E.; Algar, W. R.; Berti, L.; Gemmill, K. B.; Casey, B. J.; Oh, E., et al. Medintz, I. L., Functionalizing nanoparticles with biological molecules: developing chemistries that facilitate nanotechnology. *Chem. Rev.* **2013**, 113, (3), 1904-2074.
133. Vallet-Regí, M.; Colilla, M.; Izquierdo-Barba, I.; Manzano, M., Mesoporous Silica Nanoparticles for Drug Delivery: Current Insights. *Molecules* **2017**, 23, (1), 47.
134. Mizoshita, N.; Tani, T.; Inagaki, S., Syntheses, properties and applications of periodic mesoporous organosilicas prepared from bridged organosilane precursors. *Chem. Soc. Rev.* **2011**, 40, (2), 789-800.
135. Boissière, M.; Meadows, P. J.; Brayner, R.; Hélarý, C.; Livage, J.; Coradin, T., Turning biopolymer particles into hybrid capsules: the example of silica/alginate nanocomposites. *Journal of materials chemistry* **2006**, 16, (12), 1178-1182.
136. Allouche, J.; Boissiere, M.; Hélarý, C.; Livage, J.; Coradin, T., Biomimetic core-shell gelatine/silica nanoparticles: a new example of biopolymer-based nanocomposites. *Journal of Materials Chemistry* **2006**, 16, (30), 3120-3125.
137. Slowing, I. I.; Vivero-Escoto, J. L.; Zhao, Y.; Kandel, K.; Peeraphatdit, C.; Trewyn, B. G.; Lin, V. S. Y., Exocytosis of mesoporous silica nanoparticles from mammalian cells: from asymmetric cell-to-cell transfer to protein harvesting. *Small* **2011**, 7, (11), 1526-1532.
138. Quignard, S.; Mosser, G.; Boissière, M.; Coradin, T., Long-term fate of silica nanoparticles interacting with human dermal fibroblasts. *Biomaterials* **2012**, 33, (17), 4431-4442.
139. Zhai, W.; He, C.; Wu, L.; Zhou, Y.; Chen, H.; Chang, J.; Zhang, H., Degradation of hollow mesoporous silica nanoparticles in human umbilical vein endothelial cells. *Journal of Biomedical Materials Research Part B: Applied Biomaterials* **2012**, 100, (5), 1397-1403.

140. Chen, G.; Teng, Z.; Su, X.; Liu, Y.; Lu, G., Unique biological degradation behavior of Stöber mesoporous silica nanoparticles from their interiors to their exteriors. *Journal of biomedical nanotechnology* **2015**, 11, (4), 722-729.
141. Kempen, P. J.; Greasley, S.; Parker, K. A.; Campbell, J. L.; Chang, H.-Y.; Jones, J. R., et al. Jokerst, J. V., Theranostic mesoporous silica nanoparticles biodegrade after pro-survival drug delivery and ultrasound/magnetic resonance imaging of stem cells. *Theranostics* **2015**, 5, (6), 631.
142. Bergman, L.; Kankaanpää, P.; Tiitta, S.; Duchanoy, A.; Li, L.; Heino, J.; Lindén, M., Intracellular degradation of multilabeled poly (ethylene imine)–mesoporous silica–silica nanoparticles: implications for drug release. *Molecular pharmaceutics* **2013**, 10, (5), 1795-1803.
143. Kortesoja, P.; Ahola, M.; Karlsson, S.; Kangasniemi, I.; Yli-Urpo, A.; Kiesvaara, J., Silica xerogel as an implantable carrier for controlled drug delivery—evaluation of drug distribution and tissue effects after implantation. *Biomaterials* **2000**, 21, (2), 193-198.
144. Tang, L.; Cheng, J., Nonporous silica nanoparticles for nanomedicine application. *Nano today* **2013**, 8, (3), 290-312.
145. Debele, T. A.; Peng, S.; Tsai, H.-C., Drug carrier for photodynamic cancer therapy. *International journal of molecular sciences* **2015**, 16, (9), 22094-22136.
146. Torney, F.; Trewyn, B. G.; Lin, V. S.-Y.; Wang, K., Mesoporous silica nanoparticles deliver DNA and chemicals into plants. *Nature nanotechnology* **2007**, 2, (5), 295.
147. Bae, S. W.; Tan, W.; Hong, J.-I., Fluorescent dye-doped silica nanoparticles: new tools for bioapplications. *Chemical communications* **2012**, 48, (17), 2270-2282.
148. Schmidt, S.; Tavernaro, I.; Cavelius, C.; Weber, E.; Kümper, A.; Schmitz, C., et al. Kraegeloh, A., Silica Nanoparticles for Intracellular Protein Delivery: a Novel Synthesis Approach Using Green Fluorescent Protein. *Nanoscale research letters* **2017**, 12, (1), 545.
149. Bharali, D. J.; Klejbor, I.; Stachowiak, E. K.; Dutta, P.; Roy, I.; Kaur, N., et al. Stachowiak, M. K., Organically modified silica nanoparticles: a nonviral vector for in vivo gene delivery and expression in the brain. *Proceedings of the National Academy of Sciences* **2005**, 102, (32), 11539-11544.
150. Hautala, R.; King, R.; Sweet, E.; Little, J.; Shields, A. W., Preparation of silica-supported diaryl ketones for use as photosensitizers: A novel synthetic application of silica-supported phenyllithium. *J. Organomet. Chem.* **1981**, 216, (3), 281-286.

151. Rieter, W. J.; Kim, J. S.; Taylor, K. M.; An, H.; Lin, W.; Tarrant, T.; Lin, W., Hybrid silica nanoparticles for multimodal imaging. *Angewandte Chemie International Edition* **2007**, 46, (20), 3680-3682.
152. Akeroyd, N.; Klumperman, B., The combination of living radical polymerization and click chemistry for the synthesis of advanced macromolecular architectures. *European Polymer Journal* **2011**, 47, (6), 1207-1231.
153. Luo, Z.; Cai, K.; Hu, Y.; Zhao, L.; Liu, P.; Duan, L.; Yang, W., Mesoporous silica nanoparticles end-capped with collagen: redox-responsive nanoreservoirs for targeted drug delivery. *Angewandte Chemie* **2011**, 123, (3), 666-669.
154. Puddu, V.; Perry, C. C., Peptide adsorption on silica nanoparticles: evidence of hydrophobic interactions. *ACS nano* **2012**, 6, (7), 6356-6363.
155. Gao, F.; Botella, P.; Corma, A.; Blesa, J.; Dong, L., Monodispersed mesoporous silica nanoparticles with very large pores for enhanced adsorption and release of DNA. *The Journal of Physical Chemistry B* **2009**, 113, (6), 1796-1804.
156. Wang, T.; Chai, F.; Fu, Q.; Zhang, L.; Liu, H.; Li, L., et al. Duan, B., Uniform hollow mesoporous silica nanocages for drug delivery in vitro and in vivo for liver cancer therapy. *J. Mater. Chem.* **2011**, 21, (14), 5299-5306.
157. Mignot, T.; Shaevitz, J. W., Active and passive mechanisms of intracellular transport and localization in bacteria. *Curr. Opin. Microbiol.* **2008**, 11, (6), 580-585.
158. Maeda, H.; Wu, J.; Sawa, T.; Matsumura, Y.; Hori, K., Tumor vascular permeability and the EPR effect in macromolecular therapeutics: a review. *J. Control. Release* **2000**, 65, (1-2), 271-284.
159. Maeda, H.; Bharate, G.; Daruwalla, J., Polymeric drugs for efficient tumor-targeted drug delivery based on EPR-effect. *Eur. J. Pharm. Biopharm.* **2009**, 71, (3), 409-419.
160. Xia, T.; Kovichich, M.; Liong, M.; Meng, H.; Kabehie, S.; George, S., et al. Nel, A. E., Polyethyleneimine coating enhances the cellular uptake of mesoporous silica nanoparticles and allows safe delivery of siRNA and DNA constructs. *ACS nano* **2009**, 3, (10), 3273-3286.
161. Santra, S.; Liesenfeld, B.; Dutta, D.; Chatel, D.; Batich, C. D.; Tan, W., et al. Mericle, R. A., Folate conjugated fluorescent silica nanoparticles for labeling neoplastic cells. *Journal of nanoscience and nanotechnology* **2005**, 5, (6), 899-904.
162. Jo, H.; Her, J.; Ban, C., Dual aptamer-functionalized silica nanoparticles for the highly sensitive detection of breast cancer. *Biosens. Bioelectron.* **2015**, 71, 129-136.

163. Mebert, A. M.; Aimé, C.; Alvarez, G. S.; Shi, Y.; Flor, S. A.; Lucangioli, S. E., et al. Coradin, T., Silica core-shell particles for the dual delivery of gentamicin and rifamycin antibiotics. *Journal of Materials Chemistry B* **2016**, 4, (18), 3135-3144.
164. Zhang, Y.; Wang, J.; Bai, X.; Jiang, T.; Zhang, Q.; Wang, S., Mesoporous silica nanoparticles for increasing the oral bioavailability and permeation of poorly water soluble drugs. *Mol. Pharm.* **2012**, 9, (3), 505-513.
165. Wang, Y.; Sun, L.; Jiang, T.; Zhang, J.; Zhang, C.; Sun, C., et al. Wang, S., The investigation of MCM-48-type and MCM-41-type mesoporous silica as oral solid dispersion carriers for water insoluble cilostazol. *Drug Dev. Ind. Pharm.* **2014**, 40, (6), 819-828.
166. Hu, Y.; Zhi, Z.; Zhao, Q.; Wu, C.; Zhao, P.; Jiang, H., et al. Wang, S., 3D cubic mesoporous silica microsphere as a carrier for poorly soluble drug carvedilol. *Microporous and Mesoporous Materials* **2012**, 147, (1), 94-101.
167. Feng, W.; Zhou, X.; He, C.; Qiu, K.; Nie, W.; Chen, L., et al. Zhang, Y., Polyelectrolyte multilayer functionalized mesoporous silica nanoparticles for pH-responsive drug delivery: layer thickness-dependent release profiles and biocompatibility. *Journal of Materials Chemistry B* **2013**, 1, (43), 5886-5898.
168. Giri, S., Mesoporous silica nanomaterials and magnetic nanoparticles based stimuli-responsive controlled-release delivery systems. **2008**.
169. Giusti, I.; D'Ascenzo, S.; Millimaggi, D.; Taraboletti, G.; Carta, G.; Franceschini, N., et al. Dolo, V., Cathepsin B mediates the pH-dependent proinvasive activity of tumor-shed microvesicles. *Neoplasia* **2008**, 10, (5), 481-488.
170. Song, Y.; Li, Y.; Xu, Q.; Liu, Z., Mesoporous silica nanoparticles for stimuli-responsive controlled drug delivery: advances, challenges, and outlook. *International journal of nanomedicine* **2017**, 12, 87.
171. Sun, Y.; Yan, F.; Yang, W.; Sun, C., Multilayered construction of glucose oxidase and silica nanoparticles on Au electrodes based on layer-by-layer covalent attachment. *Biomaterials* **2006**, 27, (21), 4042-4049.
172. Chen, J.; Liu, M.; Chen, C.; Gong, H.; Gao, C., Synthesis and characterization of silica nanoparticles with well-defined thermoresponsive PNIPAM via a combination of RAFT and click chemistry. *ACS applied materials & interfaces* **2011**, 3, (8), 3215-3223.
173. Chen, P.-J.; Hu, S.-H.; Hsiao, C.-S.; Chen, Y.-Y.; Liu, D.-M.; Chen, S.-Y., Multifunctional magnetically removable nanogated lids of Fe<sub>3</sub>O<sub>4</sub>-capped mesoporous

- silica nanoparticles for intracellular controlled release and MR imaging. *J. Mater. Chem.* **2011**, 21, (8), 2535-2543.
174. Paris, J. L.; Cabañas, M. V.; Manzano, M.; Vallet-Regí, M., Polymer-grafted mesoporous silica nanoparticles as ultrasound-responsive drug carriers. *ACS nano* **2015**, 9, (11), 11023-11033.
175. Asghar, W.; El Assal, R.; Shafiee, H.; Pitteri, S.; Paulmurugan, R.; Demirci, U., Engineering cancer microenvironments for in vitro 3-D tumor models. *Materials Today* **2015**, 18, (10), 539-553.
176. Wichterle, O.; Lim, D., Hydrophilic gels for biological use. *Nature* **1960**, 185, (4706), 117.
177. Li, X.; Kondo, S.; Chung, U.-i.; Sakai, T., Degradation behavior of polymer gels caused by nonspecific cleavages of network strands. *Chem. Mater.* **2014**, 26, (18), 5352-5357.
178. Anseth, K. S.; Bowman, C. N.; Brannon-Peppas, L., Mechanical properties of hydrogels and their experimental determination. *Biomaterials* **1996**, 17, (17), 1647-1657.
179. Bhattarai, N.; Gunn, J.; Zhang, M. Q., Chitosan-based hydrogels for controlled, localized drug delivery. *Advanced Drug Delivery Reviews* **2010**, 62, (1), 83-99.
180. Augst, A. D.; Kong, H. J.; Mooney, D. J., Alginate hydrogels as biomaterials. *Macromol. Biosci.* **2006**, 6, (8), 623-633.
181. Burdick, J. A.; Prestwich, G. D., Hyaluronic Acid Hydrogels for Biomedical Applications. *Advanced Materials* **2011**, 23, (12), H41-H56.
182. Amudeswari, S.; Reddy, C. R.; Joseph, K. T., HYDROGELS BASED ON GRAFT-COPOLYMERS OF COLLAGEN-SYNTHESIS. *Journal Of Applied Polymer Science* **1986**, 32, (5), 4939-4944.
183. Feksa, L. R.; Troian, E. A.; Muller, C. D.; Viegas, F.; Machado, A. B.; Rech, V. C., Chapter 11 - Hydrogels for biomedical applications. In *Nanostructures for the Engineering of Cells, Tissues and Organs*, Grumezescu, A. M., Ed. William Andrew Publishing: **2018**; pp 403-438.
184. Hoare, T. R.; Kohane, D. S., Hydrogels in drug delivery: Progress and challenges. *Polymer* **2008**, 49, (8), 1993-2007.
185. Darder, M.; Aranda, P.; Ruiz-Hitzky, E., Bionanocomposites: a new concept of ecological, bioinspired, and functional hybrid materials. *Advanced Materials* **2007**, 19, (10), 1309-1319.

186. Aimé, C.; Coradin, T., Nanocomposites from biopolymer hydrogels: Blueprints for white biotechnology and green materials chemistry. *Journal of polymer science part B: Polymer physics* **2012**, 50, (10), 669-680.
187. Ricard-Blum, S., The Collagen Family. *Cold Spring Harb. Perspect. Biol.* **2011**, 3, (1).
188. Privalov, P. L.; Tiktopulo, E. I.; Tischenko, V. M., STABILITY AND MOBILITY OF THE COLLAGEN STRUCTURE. *J. Mol. Biol.* **1979**, 127, (2), 203-216.
189. Parenteau-Bareil, R.; Gauvin, R.; Berthod, F., Collagen-based biomaterials for tissue engineering applications. *Materials* **2010**, 3, (3), 1863-1887.
190. Zhang, D.; Wu, X.; Chen, J.; Lin, K., The development of collagen based composite scaffolds for bone regeneration. *Bioactive materials* **2017**.
191. Raftery, R. M.; Tierney, E. G.; Curtin, C. M.; Cryan, S. A.; O'Brien, F. J., Development of a gene-activated scaffold platform for tissue engineering applications using chitosan-pDNA nanoparticles on collagen-based scaffolds. *J. Control. Release* **2015**, 210, 84-94.
192. Heinemann, S.; Coradin, T.; Desimone, M. F., Bio-inspired silica–collagen materials: Applications and perspectives in the medical field. *Biomaterials Science* **2013**, 1, (7), 688-702.
193. Desimone, M. F.; Hélyary, C.; Quignard, S.; Rietveld, I. B.; Bataille, I.; Copello, G. J., et al. Meddahi-Pellé, A., In vitro studies and preliminary in vivo evaluation of silicified concentrated collagen hydrogels. *ACS applied materials & interfaces* **2011**, 3, (10), 3831-3838.
194. Alvarez, G. S.; Hélyary, C.; Mebert, A. M.; Wang, X.; Coradin, T.; Desimone, M. F., Antibiotic-loaded silica nanoparticle–collagen composite hydrogels with prolonged antimicrobial activity for wound infection prevention. *Journal of Materials Chemistry B* **2014**, 2, (29), 4660-4670.
195. Wang, X. L.; Hélyary, C.; Coradin, T., Local and Sustained Gene Delivery in Silica-Collagen Nanocomposites. *Acs Applied Materials & Interfaces* **2015**, 7, (4), 2503-2511.
196. Wang, X.; Coradin, T.; Hélyary, C., Modulating inflammation in a cutaneous chronic wound model by IL-10 released from collagen–silica nanocomposites via gene delivery. *Biomaterials science* **2018**, 6, (2), 398-406.



# Chapter 2 Comparison of extracellular and intracellular degradation of nanostructured silica particles

“路曼曼其修远兮， 吾将上下而求索”

《离骚》

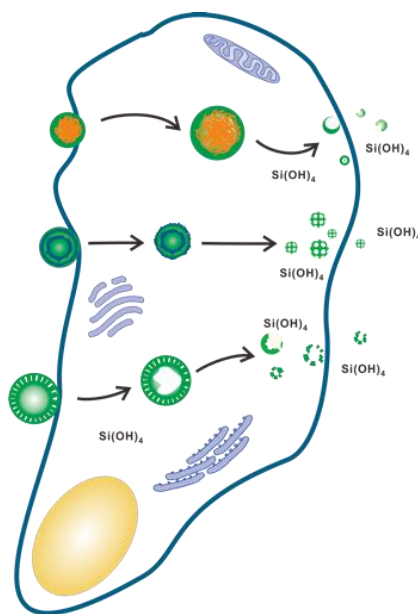
## Abstract

This study aimed to better understand the intracellular fate of silica nanoparticles. We have prepared three types of particles with different nanostructures and studied their degradation in a buffer, a culture medium and in contact with human dermal fibroblasts. All the particles dissolve in solution, leading to an increase in the porosity and / or the precipitation of new colloids and finally to their fragmentation, and more rapidly in culture medium than in buffer. All particles are also internalized without significant cytotoxic effect. Their intracellular degradation occurs faster than in suspension but following quite similar dissolution mechanisms. These results strongly suggest that, under these conditions, the silica nanoparticles must be mainly considered as degraded by hydrolysis and not biodegraded.

<b>2.1 Introduction .....</b>	<b>75</b>
<b>2.2 Experimental Section .....</b>	<b>76</b>
2.2.1 Materials .....	76
2.2.2 Synthesis of PEGylated silica nanostructures .....	76
2.2.3 Nanoparticle characterization and instruments. ....	79
2.2.4 Dissolution and degradation assays in buffer and culture medium.....	82
2.2.5 Cells and treatments with nanoparticles.....	82
2.2.6 Nanoparticle internalization, degradation and release. ....	82
2.2.7 Toxicological assays. ....	83
2.2.8 Statistical analysis. ....	83
<b>2.3 Results .....</b>	<b>83</b>
2.3.1 Synthesis and functionalization of nanostructured silica particles.....	83
2.3.2 Behaviour of nanoparticles in buffer and cell culture medium. ....	88
2.3.3 Nanoparticles behaviour in the presence of fibroblasts. ....	91
2.3.4 Degradation and release kinetics.....	93
<b>2.4 Discussion .....</b>	<b>94</b>
<b>2.5 Conclusion.....</b>	<b>97</b>



# Comparaison de la dégradation extracellulaire et intracellulaire de particules de silice nanostructurées



## Résumé

Cette étude vise à mieux comprendre le devenir intracellulaire des nanoparticules de silice. Nous avons préparé trois types de particules avec différentes nanostructures et étudié leur dégradation dans un tampon, un milieu de culture et au contact de fibroblastes dermiques humains. Toutes les particules se dissolvent en solution, conduisant à une augmentation de la porosité et/ou à la précipitation de nouveaux colloïdes et finalement à leur fragmentation, et ce plus rapidement en milieu de la culture qu'en tampon. Toutes les particules sont également internalisées sans effet cytotoxique significatif. Leur dégradation intracellulaire survient plus rapidement qu'en suspension mais suivant des mécanismes de dissolution assez similaires. Ces résultats suggèrent fortement que, dans ces conditions, les nanoparticules de silice doivent être principalement considérées comme dégradées par hydrolyse et non biodégradées.

## Publié dans

Y. Shi, C. Hélary, B. Haye, T. Coradin, Extracellular versus Intracellular Degradation of Nanostructured Silica Particles, *Langmuir*, **2018**, 34, 406-415.

## 2.1 Introduction

As pointed in the previous chapter, very little is known about the intracellular fate of silica nanoparticles. Earlier reports using mesoporous nanoparticles evidenced that their cellular uptake was followed by their exocytosis<sup>1</sup>. In addition, the released particles were associated with proteins located in the cellular membrane or involved in the vesicular trafficking. However, no modification in particle size or morphology was reported. A first insight in the intracellular dissolution pathway of plain silica nanoparticles was obtained by Quignard *et al.* through a combination of TEM imaging and identification of the products of their degradation<sup>2</sup>. A decrease of particle size was observed and attributed to surface erosion as a result of the dissolution equilibrium of silica. Since then, further evidences of the ability of silica to dissolve intracellularly were accumulated<sup>3-6</sup>. Yet, considering the complexity of the accompanying trafficking events, that can include pH modifications and protein deposition, defining the exact conditions in which silica particles are degraded remains highly challenging.

At present, there are mainly three strategies to load small molecular drugs and biological macromolecules within silica nanomaterials. The first is to mix the drugs with the silica precursor to form nanocomposites<sup>7, 8</sup>. The second is through the layer-by-layer method<sup>9, 10</sup>. The third involves the impregnation of mesoporous or hollow silica nanoparticles<sup>11, 12</sup>. As far as we know, there is no report comparing the degradation behavior of these three types of silica nanoparticles in biologically-relevant conditions. With this purpose, we have prepared PEGylated fluorescent silica particles with different internal structures (bio-composite, multilayered and hollow mesoporous) and studied their time evolution in abiotic (phosphate buffer, culture medium) conditions and then in the presence of normal human dermal fibroblasts. Structural degradation and dissolution kinetics of the nanoparticles were studied in parallel with their cytotoxicity. The here-gathered data suggest that, for these systems, the intracellular fate of silica nanoparticles can be explained on the sole basis of physico-chemical processes. This provides new and strong evidences that, in the intracellular space, silica nanoparticles should be considered as hydrolytically-degradable rather than biodegradable materials, a result of great consequences for the design of silica-based biomaterials.

## 2.2 Experimental Section

### 2.2.1 Materials

Tetraethyl orthosilicate (TEOS), (3-Aminopropyl)triethoxysilane (APTES), Branched PEI trimethylammonium bromide (CTAB) were obtained from Sigma-Aldrich. Fluorescein Isothiocyanate (Isomer I) (FITC), N-hydroxysuccinimide (NHS) and 1-ethyl-3-(3-dimethylaminopropyl)-carbodiimide (EDC) were obtained from Alfa Aesar. Methoxypolyethylene glycol acetic acid N-succinimidyl ester (NHS-PEG<sub>5000</sub>-MAL), dimethylsulfoxide (DMSO), triethanolamine (TEA) and ethylenediamine tetraacetic acid (EDTA) were obtained from Sigma-Aldrich. Dubelcco's Modified Eagle Medium (DMEM) and Fetal Calf Serum (FCS) was purchased from Gibco BRL. Unless specified, all the commercial products were used without further purification.

### 2.2.2 Synthesis of PEGylated silica nanostructures

The sol-gel synthesis used makes it possible to obtain spherical particles. A series of fluorescent silica nanoparticles of different sizes (10 to 200 nm) were prepared by the method described by modified Stöber method. Here we add the APTES-FITC solution during the hydrolysis of tetraethoxysilane in a solution of ammonia in ethanol, which is obtained by condensation of 3-aminopropyl)triethoxysilane with fluorescein isothiocyanate<sup>13</sup>. The structure of the three PEGylated silica nanoparticles mentioned above is as shown in **Figure 2-1**

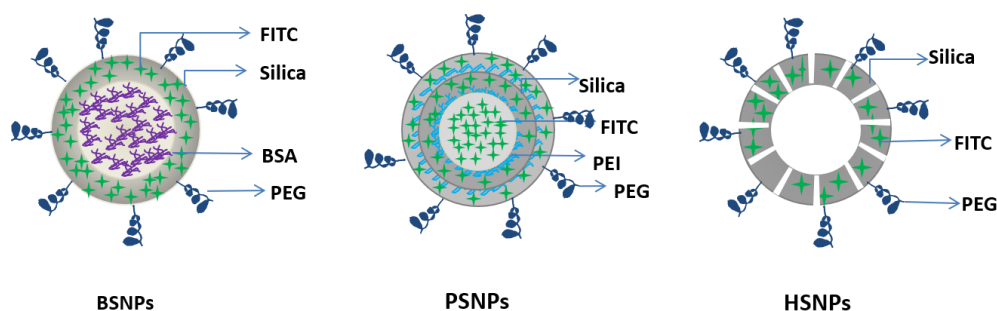


**Figure 2-1** The structure of PEGylated silica nanoparticles (BSNPs, PSNPs, HSNPs)

#### PEGylated BSA@silica nanoparticles (BSNPs)

BSA@silica nanoparticles were synthesized via a modified Stöber method<sup>14</sup>. First, 30 mg BSA were diluted in 3 mL deionized (DI) water and then added to 20 mL of ethanol containing 2 mL ammonia. After 5 minutes, 1 mL TEOS was added under stirring for 1 hour. Lastly, 50  $\mu$ L APTES-FITC was added three times every two hours, followed by vigorous stirring for 24

hours. Another 50  $\mu\text{L}$  APTES was added and after for 24 hours under stirring, amine-functionalized BSA@silica- $\text{NH}_2$  particles were obtained, recovered by centrifugation and washed with ethanol twice. Next, BSA@silica- $\text{NH}_2$  were re-dispersed in 5 mL of PBS (phosphate buffer saline, 1X), and 8 mg of NHS-PEG<sub>5000</sub>-MAL was added<sup>15</sup>. The mixture was then stirred at room temperature for 2 hours before harvesting PEGylated particles by centrifugation (**Figure 2-2**).

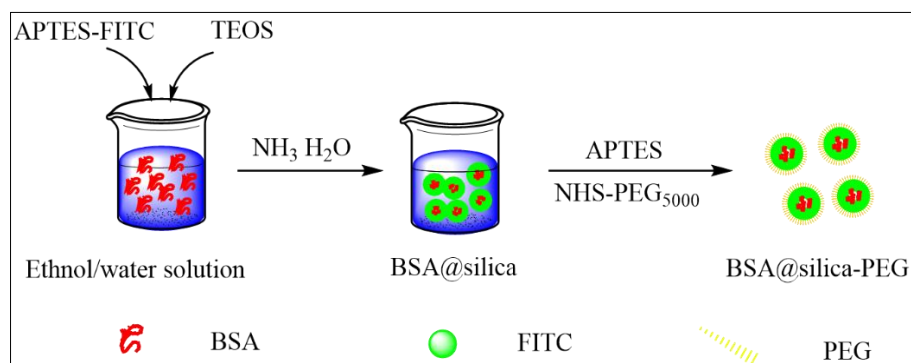


**Figure 2-2** Process for preparing PEGylated BSA@silica nanoparticles

### Synthesis of PEGylated double-layered PEI-Silica nanoparticles (PSNPs).

For the synthesis of  $\text{SiO}_2$ @PEI, 20 mL of a suspension of 100 nm FITC-doped silica nanoparticles (*vide supra*) was added dropwise to the same volume of an aqueous solution of PEI (10 mg/mL)<sup>16</sup>.

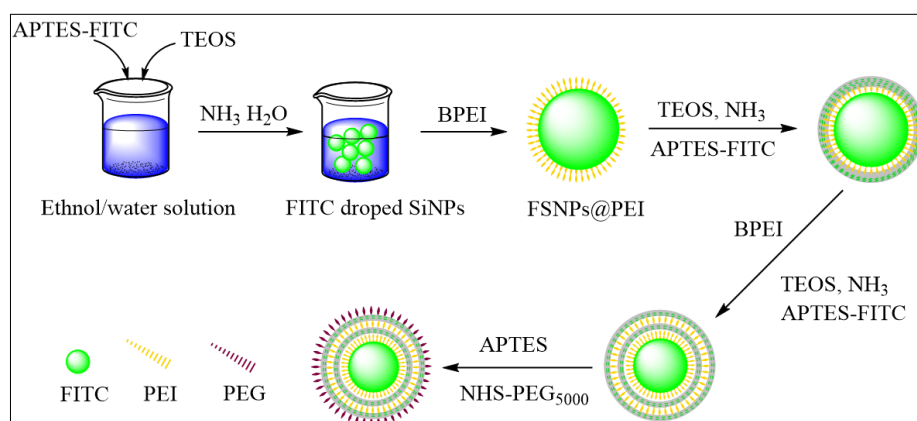


**Figure 2-3** Process for preparing PEGylated double-layered PEI-silica nanoparticles

After 3 additional hours of mixing, particles were recovered by centrifugation, washed 2 times in DI water and finally re-suspended in DI water. For the synthesis of  $\text{SiO}_2$ @PEI@ $\text{SiO}_2$ <sup>10</sup>, 8.0 mL of the  $\text{SiO}_2$ @PEI solution was mixed with 5.0 mL absolute ethanol and 0.8 mL of ammonia and stirred for 10 minutes at room temperature. Then 0.2 mL of TEOS and 20  $\mu\text{L}$  APTES-FITC

was added and the mixture was allowed to react at room temperature for 16 h. Afterward,  $\text{SiO}_2\text{@PEI@SiO}_2$  nanoparticles were washed with water and ethanol and suspended in 20 mL of water. For the deposition of the second PEI and silica layers, the synthetic procedure was similar to the previous one, except for the final addition of 200  $\mu\text{L}$  APTES to obtain  $\text{SiO}_2\text{@PEI@SiO}_2\text{@PEI@SiO}_2\text{-NH}_2$  nanoparticles. Next, these particles were re-dispersed in 5 mL of DMSO, and 8 mg of NHS-PEG<sub>5000</sub>-MAL was added. The mixture was then stirred at room temperature for 2 hours under anhydrous conditions before harvesting by centrifugation (**Figure 2-3**).

### Synthesis of PEGylated hollow mesoporous silica nanoparticles (HSNPs).

Fluorescent uniform ~100 nm sized  $\text{SiO}_2$  nanoparticles were obtained using a modified Stöber method<sup>17</sup> (**Figure 2-4**).

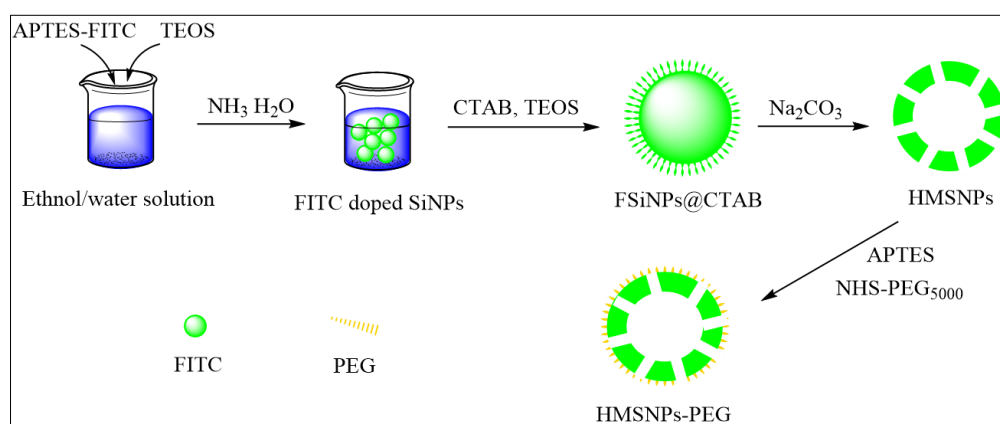


**Figure 2-4** Process for preparing PEGylated hollow mesoporous silica nanoparticles

In a typical synthesis, 35.7 mL of absolute ethanol was mixed with 5 mL water and 0.8 mL of ammonia and stirred for 5~10 minutes at room temperature. Then 1.0 mL of TEOS and 1.0 mL of APTES-FITC were added and the mixture was allowed to react at room temperature for 1 h. Afterward,  $\text{SiO}_2$  nanoparticles were washed with water and ethanol and suspended in 20 mL of water. To prepare hollow mesoporous silica nanoparticles<sup>18</sup>, CTAB (2.0 g) and TEA (20 mg) were dissolved in 20 mL of DI water and stirred at room temperature for 1 h. Then, 10 mL of the previous  $\text{SiO}_2$  suspension was added and stirred at room temperature for 1 h before addition of 0.15 mL of TEOS. The mixture was stirred for 1 h at 80 °C in a water bath and the mixture was then cooled down to 50°C followed by addition of 636 mg of sodium carbonate ( $\text{Na}_2\text{CO}_3$ ), under constant stirring for 30 min. To remove the CTAB, the product was extracted for 24 h with a 1 wt% solution of NaCl in methanol at room temperature. This process was carried out for at least 3 times to ensure complete removal of CTAB. For PEG grafting, 8 mg of the

recovered particles were dispersed in 50 mL of DMSO and then 500  $\mu$ L of APTES were added. After the mixture was stirred for 20 hours, amine-functionalized HSNPs (HSNP-NH<sub>2</sub>) were recovered by centrifugation and washed with ethanol twice. Next, HSNP-NH<sub>2</sub> particles were re-dispersed in 5 mL of DMSO, and 8 mg of NHS-PEG<sub>5000</sub>-MAL was added. The mixture was then stirred at room temperature for 2 hours under anhydrous conditions before being harvested by centrifugation.

### **2.2.3 Nanoparticle characterization and instruments.**

#### **Size distribution and Zeta potential**

The particle size measured in a dynamic light scattering (DLS) instrument is the diameter of a sphere that diffuses at the same rate as the particle being measured. The zetasizer system determines the size of the measured nanoparticles by first measuring the Brownian motion of the particles in the sample using DLS and then using established theories.

#### **Figure 2-5 Process for measurement of nanoparticles by DLS**

Brownian motion is due to the random motion of the particles in the liquid due to the bombardment of the molecules around them. The speed at which the particles in the liquid move randomly can be used to determine the size of the particles. Experienced surface small particles move or spread faster in larger liquids, and this movement is ongoing. Therefore, if we separate the two "pictures" of the sample for a short period of time, we can see the moving distance of the particles and calculate their size according to the existing theory (**Figure 2-5**). If there is minimal particle movement between the two images, the particles in the sample can be inferred to be large, and similarly, if there is a large amount of movement between the two images, the particle diameter in the sample is smaller. Using these theories and the relationship between diffusion speed and size, the size of these particles can be determined.

Most liquids contain charged cations and anions. When charged particles are suspended in the liquid, oppositely charged ions will be attracted to the surface of the suspended particles. If the negatively charged particles attract positive ions in the liquid, conversely, the positively charged particles attract negative ions. Ions near the surface of the particle will be strongly bound, while ions that are further apart will loosely combine to form a so-called diffusion layer. There is a nominal boundary in the diffusing layer. When the particles move in the liquid, any ions in the boundary will move with the particles, but any ions outside the boundary will stay where they are - this boundary is called the sliding plane. There is a potential between the surface of the particle and the dispersion which varies according to the distance from the surface of the particle - this potential on the sliding plane is called the zeta potential (**Figure 2-6**). At present, the Zeta potential is mainly measured by laser Doppler electrophoresis. This method measures the speed at which particles move in a liquid when an electric field is applied to its velocity. Once we know the particle's velocity and the applied electric field, we can calculate the zeta potential from the known sample viscosity and dielectric constant.

**Figure 2-6** The principle of zeta point measurement

### **TEM**

Transmission electron microscopy projects an accelerated and concentrated electron beam onto a very thin sample. The electrons collide with atoms in the sample to change direction, resulting in solid angle scattering. The size of the scattering angle is related to the density and thickness of the sample so that images with different brightness and darkness can be formed, and the image will be displayed on the imaging device, and photosensitive coupling component) after being enlarged and focused. Since the electron De Broglie wavelength is very short, the resolution of the transmission electron microscope is much higher than that of the optical

microscope and can reach 0.1 to 0.2 nm, and the magnification is tens of thousands to millions of times. **Figure 2-7** shows the two basic operation modes of TEM-imaging and diffraction modes. In both cases, the specimen is illuminated with the parallel beam, formed by electron beam shaping with the system of Condenser lenses and Condenser aperture. After interaction with the sample, on the exit surface of the specimen two types of electrons exist- unscattered (which will correspond to the bright central beam on the diffraction pattern) and scattered electrons (which change their trajectories due to interaction with the material).

**Figure 2-7** Schematic view of imaging and diffraction modes in TEM

### **Characterization**

Particle size distribution, polydispersity index and zeta potential ( $\zeta$ ) were measured in DI water or cell culture medium (DMEM) using a ZetaSizer Nano (Malvern Instruments Ltd., Worcestershire, UK). Particles were also imaged using Transmission Electron Microscopy (TEM) on a Tecnai G2 Spirit electron microscope (TEM) (FEI Company, Philips, Netherlands). Dynamic Light Scattering (DLS) was used to determine the hydrodynamic diameter of the nanoparticles in Milli-Q water or in culture medium. The reading was carried out at an angle of 90° to the incident beam (632 nm). The Contin algorithm was used to analyze the autocorrelation functions. Fluorescence spectra of the particles suspended in water were recorded on a Horiba Jobin Yvon fluorescence spectrometer with an excitation wavelength of 485 nm. Nitrogen (N<sub>2</sub>) sorption measurements were performed at 77K using an accelerated surface area and porosimetry analyzer with Brunauer-Emmett-Teller (BET) calculations for the surface area.



#### **2.2.4 Dissolution and degradation assays in buffer and culture medium.**

To carry out the *in vitro* degradation experiments in abiotic conditions, a suspension of each type of PEGylated particles at a 0.4 mg/mL concentration was left under mild stirring at 37°C in phosphate buffer saline (PBS) 1X or DMEM. The fluorescence intensity of the medium was analyzed at selected time intervals after centrifugation in a Nanosep® 3kD centrifugal device to separate particles, that were further used for TEM observation, and solutions to monitor the proportion of released silane-FITC over time<sup>2</sup>. All experiments were performed in triplicate.

#### **2.2.5 Cells and treatments with nanoparticles.**

Normal human dermal fibroblasts (from Promocell) were grown in DMEM supplemented with FCS (10%), penicillin (100 units/mL), streptomycin (100 mg/mL, from Gibco BRL) and fungizone (0.25 mg/mL, from Gibco BRL). The culture flasks (75 cm<sup>2</sup>) were kept at 37 °C in 95% humidity and 5% CO<sub>2</sub> atmosphere. At confluence, fibroblasts were removed from cultured flasks by treatment with 0.1% trypsin and 0.02% EDTA. Cells were rinsed, centrifuged and dispersed in the supplemented DMEM medium. Fibroblasts were used at passage 8 for the experiments.

#### **2.2.6 Nanoparticle internalization, degradation and release.**

The cells were seeded at a density of 30,000 cells per well in 24-well plate with round glass coverslips at the bottom of the wells and kept 24 h with culture medium at 37 °C in 95% humidity and 5% CO<sub>2</sub> atmosphere previous to incubation with 0.4 mg/mL of the three types of silica nanoparticles. For fluorescence microscopy, cells were collected at day 1, 2 and 7, washed three times with PBS 1X, and fixed with 4% paraformaldehyde in PBS (1 h, 4 °C). Staining of the nuclei with DAPI (Invitrogen) was performed via incubation for 15 min at room temperature and rinsing with HBSS 1X before observation with a fluorescent microscope (Axio 100, Carl Zeiss). For TEM, cells were fixed at day 1, 2 and 7 using 3.63% glutaraldehyde in a 0.05 M sodium cacodylate buffer with 0.3 M saccharose for 1 h at 4 °C. Samples were washed three times before post-fixing with 2% osmium tetroxide for 1 h at 4 °C. Cells were then detached from the culture flasks by scratching and centrifuged. The pellets were embedded in a 4 mg/mL collagen hydrogel to ease sectioning and cellular observations. With this purpose, 50 µL of the type I collagen solution (in 17 mM acetic acid) was neutralized by 5 µL of PBS and mixed with the pellet. Mixtures were left for 30 minutes at 20°C to allow collagen gelation. Recovered

hydrogels were fixed with 4% paraformaldehyde in PBS (1 h, 4 °C). Last, cell-containing collagen hydrogels were dehydrated with an ascending ethanol series ending with propylene oxide and embedded in araldite. Ultrathin sections were prepared with an Ultracut ultramicrotome (Leica, France). Slides were analyzed with a Tecnai G2 Spirit electron microscope operating at 120 kV.

To follow the kinetics of particles degradation and release, continuous cultures were first performed over 1 week in the presence of 0.4 mg/mL silica nanoparticles. After this delay, the culture medium was removed and cells were rinsed before adding fresh medium and performing an additional incubation period of 7 days. Fluorescence and TEM imaging, as well as fluorescence measurements of the whole medium and of its soluble content were performed as described above. All experiments were performed in triplicate.

### **2.2.7 Toxicological assays.**

Cellular metabolic activity of cells in 24-well plate after 2 days of contact with silica particles at concentrations 0.025-0.400 mg/mL and after 1, 2, 7 and 14 days of incubation with 0.4 mg/mL silica nanoparticles was evaluated using Alamar Blue assay (n=6). After incubation, cells were rinsed with medium and incubated at 37 °C in a humidified 5% CO<sub>2</sub> air atmosphere for 4 h with a 10% solution of Alamar blue in phenol red-free culture medium. Absorbance of the medium at 570 nm and 600 nm was recorded with a UV-visible spectrophotometer and the percentage of dye reduction was calculated. The results were expressed as a percentage of viability assessed in control samples (incubated with no nanoparticles). It is worth mentioning that incubation of the particles alone with Alamar Blue gave negligible absorbance values.

### **2.2.8 Statistical analysis.**

Graphical results are presented as mean  $\pm$  SD (standard deviation). Statistical significance was assessed using the student's-test compared with control groups. The level of significance in all statistical analyses was set at a probability of  $P < 0.05$ .

## **2.3 Results**

### **2.3.1 Synthesis and functionalization of nanostructured silica particles**

Silica nanoparticles with different internal structures were synthesized and characterized using transmission electron microscopy (TEM), dynamic light scattering (DLS) and zeta potential

measurements. PEGylated BSA-coated silica nanoparticles, PEI-coated silica nanoparticles and hollow mesoporous silica nanoparticles were named as BSNPs, PSNPs and HSNPs respectively.

Fairly uniform BSNPs were prepared by using a modified Stöber method in the presence of BSA. As shown in the TEM images (**Figure 2-8a, d**), the BSNPs are spherical in shape with a mean diameter of ~45 nm. They exhibit a well-contrasted core-shell structure suggesting that they consist of a silica-rich layer coating a BSA-rich internal domain<sup>14</sup>.

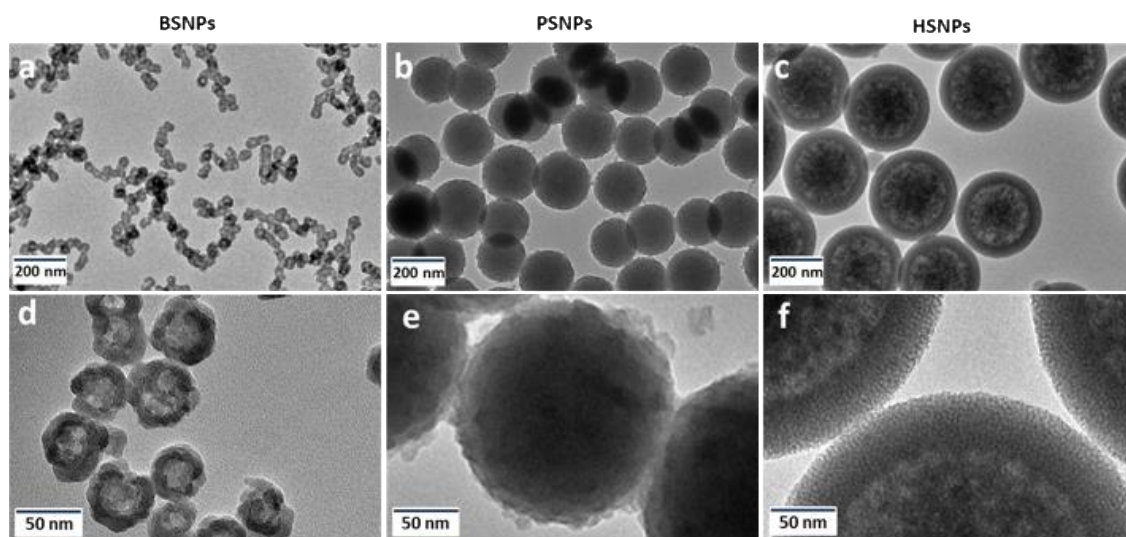


**Figure 2-8** TEM images of the as-prepared PEGylated fluorescent silica nanoparticles: (a, d) BSNPs; (b, e) PSNPs and (c, f) HSNPs

DLS measurements in deionized water indicated a two-fold increase in the mean diameter  $D_m$ , compared to TEM, suggesting that some aggregation occurred, although to a limited extent (**Table 2-8**). This aggregation was confirmed by performing a DLS analysis of a BSNPs suspension just after sonication, yielding to a  $D_m$  value of  $44 \pm 10$  nm. Successful functionalization with amine and PEG groups was confirmed by the changes of size and  $\zeta$  value (**Table 2-1**): whereas the as-prepared BSA@SiO<sub>2</sub> exhibited a strongly negative  $\zeta$  value, APTES grafting led to a slightly positive  $\zeta$  value due to ammonium groups. This was correlated with an increase in the  $D_m$  value as obtained by DLS, in agreement with the decrease of  $\zeta$  absolute value leading to a lower colloidal stability. After PEG grafting, the  $D_m$  value obtained by DLS decreased, due to the ability of the polymer coating to limit BSNPs aggregation, and the  $\zeta$  value became negative, due to the reaction of some of the surface amine groups with NHS-PEG<sub>5000</sub>-MAL.

**Table 2-1** Mean diameter  $D_m$  from DLS and TEM, Zeta potential  $\zeta$  in deionized water and culture medium

	$D_m$ DLS (nm)	$D_m$ TEM (nm)	Z water (mV)	Z medium (mV)
BSNPs	$109 \pm 6$	$44 \pm 2$	$-15 \pm 1$	$-8 \pm 1$
PSNPs	$190 \pm 6$	$176 \pm 4$	$-8 \pm 1$	$-5 \pm 1$
HSNPs	$310 \pm 10$	$261 \pm 7$	$-11 \pm 1$	$-7 \pm 1$

PSNPs were obtained from plain silica nanoparticles by a layer-by-layer method using branched PEI (25 kDa). Starting from  $\sim 100$  nm Stöber nanoparticles, two successive sequences of PEI deposition/silica coating were performed. Variations in  $\zeta$  value occurred as expected, *i.e.*  $\zeta > 0$  for outer PEI layer and  $\zeta < 0$  after silica deposition (**Table 2-2**). Again, APTES grafting turned the particle surface positive while PEG conjugation ultimately led to negatively-charged PSNPs in deionized water (**Table 2-1**).

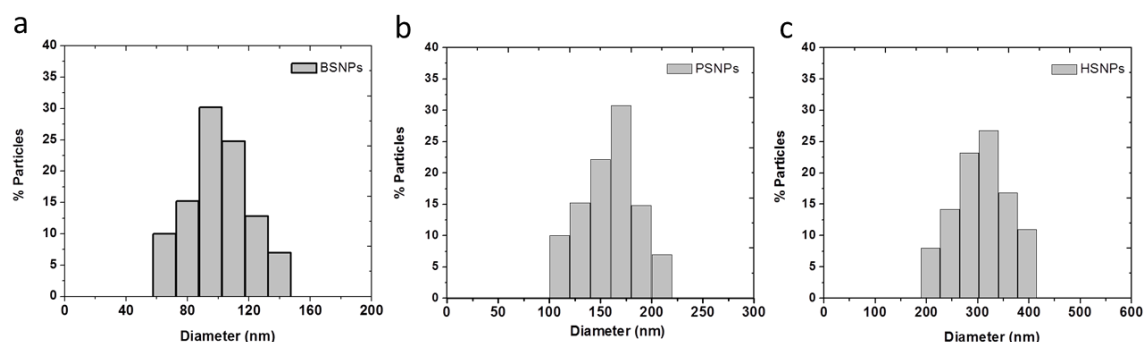


**Figure 2-9** Particle size distribution of a) BSNPs; b) PSNPs; c) HSNPs d) BSNPs just after sonication measured by DLS in deionized water

The accompanying modifications of hydrodynamic diameter, as obtained by DLS, are difficult to analyze in detail in terms of size variations as they are the result of PEI conformation on the particle surface, silica layer thickness as well of the aggregation tendency of the different systems. Nevertheless, TEM imaging (**Figure 2-8b**) provides a  $D_m$  value of  $\sim 175$  nm and therefore an overall coating thickness of  $\sim 35$  nm, clearly evidenced at higher magnification (**Figure 2-8e**). Hollow HSNPs were prepared by etching 100 nm-Stöber nanoparticles following the method proposed by Chen et al.<sup>18</sup>. TEM imaging clearly showed that HSNPs have a spherical morphology and uniform particle size  $\sim 260$  nm, with a porous shell thickness of  $\sim 50$  nm and a highly porous core, although a central denser region, corresponding to unreacted part of the starting Stöber particles, could sometimes be distinguished (**Figure 2-8c, f**).

**Table 2-2** Average diameter (by DLS) and zeta-potentials of nanoparticles at various stages of their synthesis

		$D_m$ (nm) (n=3)	$\zeta$ (mV) (n=3)
BSNPs	BSA@SiO <sub>2</sub>	77±3	-54±9
	BSA@SiO <sub>2</sub> -NH <sub>2</sub>	130±4	10.5±2
	BSA@SiO <sub>2</sub> -PEG(BSNPs)	109 ±6	-15 ±1
PSNPs	SiO <sub>2</sub>	104±5	-40 ±1
	SiO <sub>2</sub> @PEI	134±4	21 ±2
	SiO <sub>2</sub> @PEI@SiO <sub>2</sub>	171±6	-44 ±3
	SiO <sub>2</sub> @PEI@SiO <sub>2</sub> @PEI	166±7	20 ±1
	SiO <sub>2</sub> @PEI@SiO <sub>2</sub> @PEI@SiO <sub>2</sub>	195±5	-36 ±7
	SiO <sub>2</sub> @PEI@SiO <sub>2</sub> @PEI@SiO <sub>2</sub> -NH <sub>2</sub>	242±8	12 ± 2
	SiO <sub>2</sub> @PEI@SiO <sub>2</sub> @PEI@SiO <sub>2</sub> -PEG(PSNPs)	190±6	-8 ± 1
HSNPs	SiO <sub>2</sub>	104±5	-40 ±1
	HSNP-CTAB	376±9	-22 ±1
	HSNP-NH <sub>2</sub>	780±40	16 ± 1
	HSNP-PEG (HSNPs)	310±10	-11 ± 1

The overall synthetic process was also followed by DLS and  $\zeta$ -metry (**Table 2-2**), showing that despite the fact that APTES-modified intermediates are particularly prone to aggregation ( $D_m = 780 \pm 40$  nm), the PEG coating efficiently enhances the colloidal stability of final HSNPs particles ( $D_m = 310 \pm 10$  nm in deionized water compared to  $260 \pm 7$  nm from TEM) (**Table 2-1**). Nitrogen adsorption-desorption isotherm measurements indicated that the HSNPs had a relatively high specific surface area of *ca.* 550 m<sup>2</sup>/g and a well-defined mean pore size of 3.9 nm (**Figure 2-3**).

Altogether, when the three types of particles are compared, their size, as obtained from both DLS in deionized water and TEM, vary in the order HSNPs > PSNPs > BSNPs. In terms of surface properties, their zeta potential in deionized water (pH 6.5) is always negative and follows the PSNPs > HSNPs > BSNPs evolution.

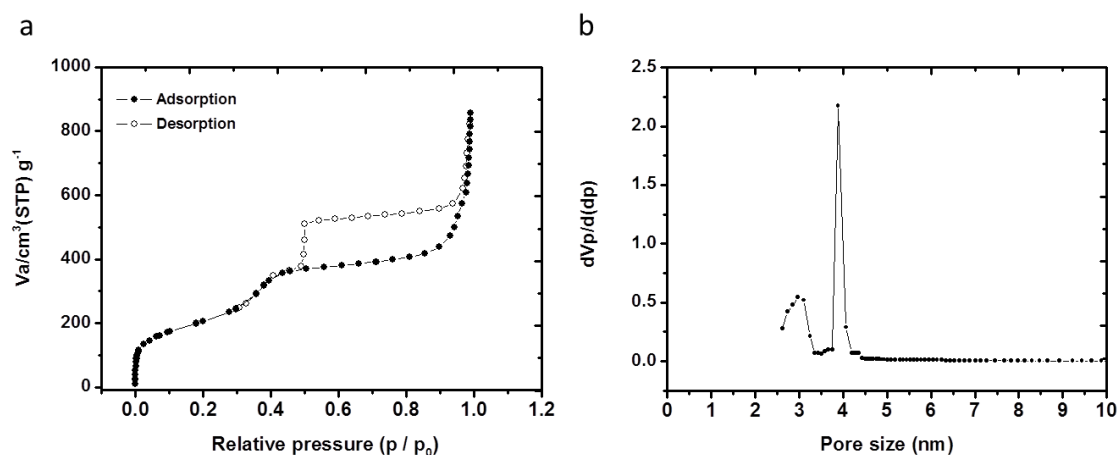


**Figure 2-10** N<sub>2</sub>-sorption isotherms at 77 K and pore size distribution of HSNPs particles

Interestingly, the same order of  $\zeta$  values is found for NH<sub>2</sub>-grafted particles, suggesting that the PEG coupling occurred in a similar extent for the three systems. This order is preserved over the whole pH 2-11 range with apparent isoelectric points (IEP) of ca. 4.5, 5.5 and 6.2 for BSNPs, HSNPs and PSNPs, respectively (**Figure 2-10**).

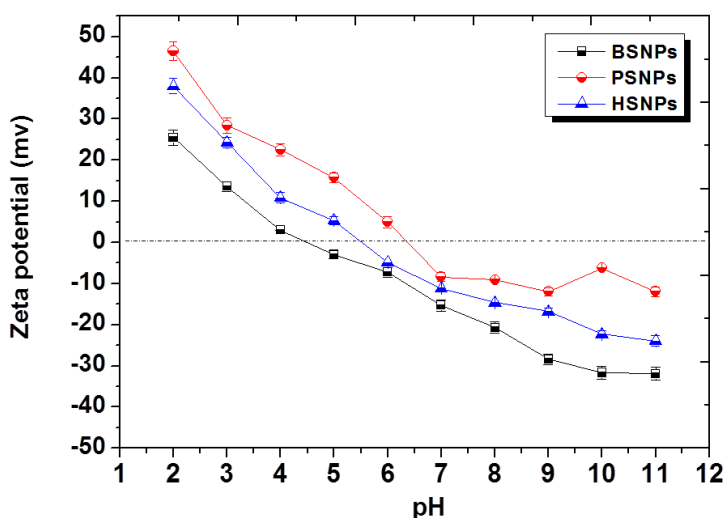


**Figure 2-11** Evolution of the zeta potential of BSNP, PSNP and HSNP nanoparticles with pH

It is also maintained in cell culture medium although with some minor variations between the different particles. A systematic increase in  $\zeta$  values compared to deionized water is observed that very likely indicates the surface adsorption of positively-charged proteins present in FCS-enriched DMEM (**Table 2-1**)<sup>19</sup>.

The incorporation of FITC within the different nanoparticles was checked by fluorescence measurements. As shown in **Figure 2-12**, the FITC-doped silica nanoparticles gave rise to a

strong emission, with no significant shift in the maximum wavelength compared to the dye alone. However, at a constant particle concentration, the signal intensity varied from one particle type to the other. Such a difference may reflect various silica contents in the nanoparticle structures. For instance, the lowest intensity was obtained for BSNPs, *i.e.* hybrid nanoparticles containing large amounts of BSA. However, other processes such as FITC fluorescence variations due to different dye environment and mobility may also contribute to these differences<sup>20</sup>.

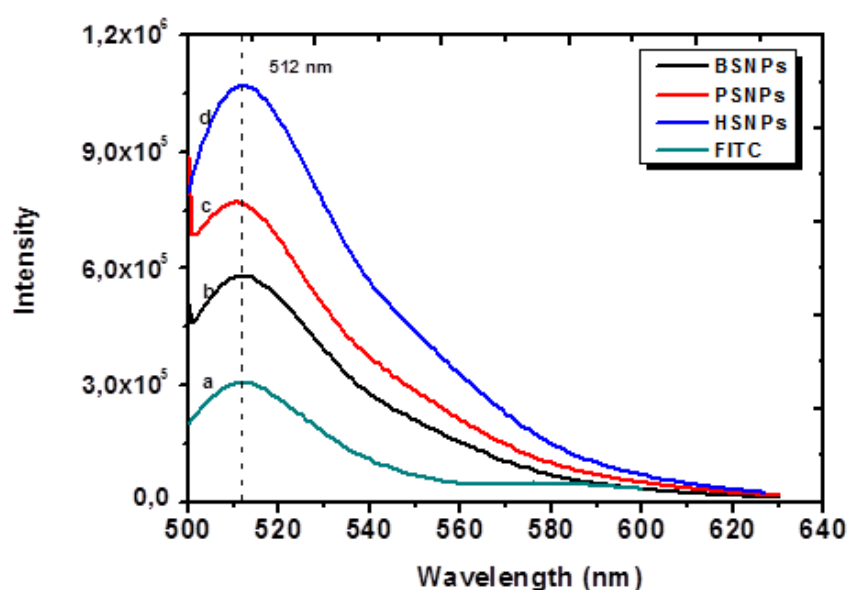


**Figure 2-12** FITC fluorescence spectra in solution and within silica nanoparticles: a) FITC, 1.0  $\mu\text{g/mL}$  and b) BSNPs; c) PSNPs; d) HSNPs 50  $\mu\text{g/mL}$ , respectively

### 2.3.2 Behaviour of nanoparticles in buffer and cell culture medium.

To investigate the influence of the internal structure of silica nanoparticles on their degradation in abiotic (*i.e.* cell-free) media, TEM imaging and monitoring of the kinetics of silica dissolution was first performed in a PBS buffer (pH 7.4) at 37 °C over 2 weeks. After one week, all nanoparticles showed a clear tendency to form aggregates under TEM imaging conditions.

As shown in **Figure 2-13**, the core-shell structure of BSNPs is overall preserved but some particles appear to have grown in size and the contrast between the inside and outside parts has increased compared to the initial particles. For PSNPs, the outer silica shell is less well-defined. No further evolution could be evidenced for these two sets of particles after one additional week, except for a higher tendency to aggregate. In parallel, the internal structure of HSNPs does not appear much modified after one week but some deformed particles are observed. After

two weeks, they have turned into highly porous particles with a weaker contrast between the shell and the core parts, some of them being obviously fractured.

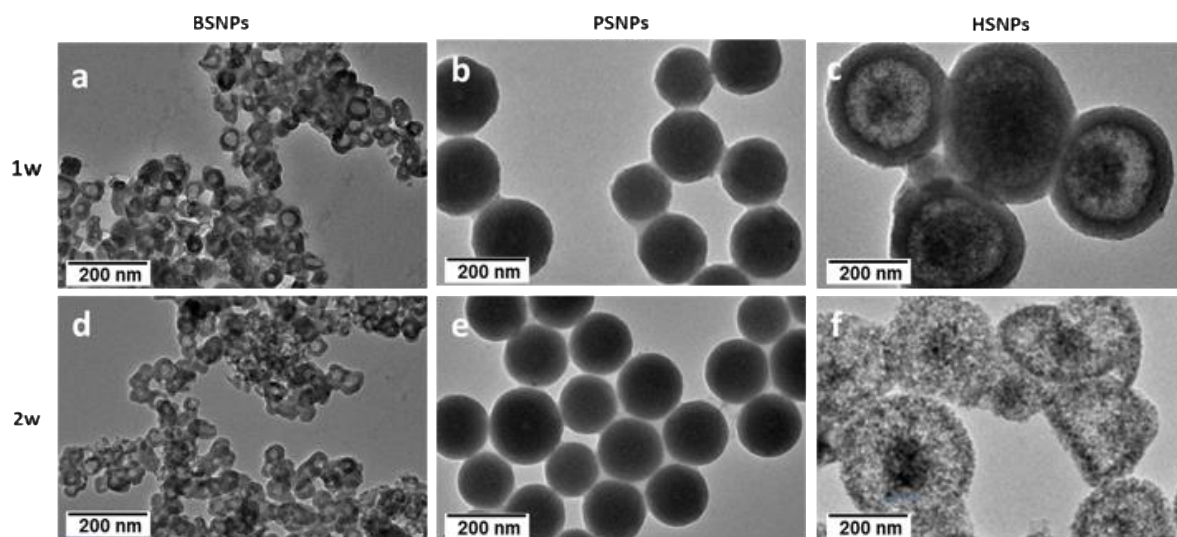


**Figure 2-13** TEM imaging of the structural evolution of silica nanoparticles in PBS after (a-c) one and (d-f) two weeks

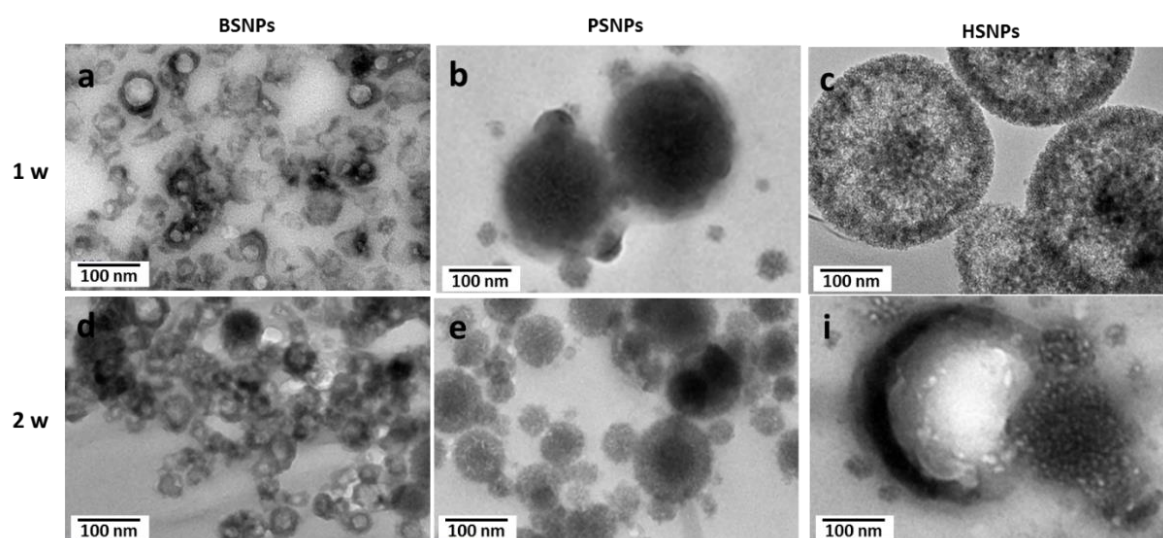


**Figure 2-14** TEM imaging of the structural evolution of silica nanoparticles in DMEM culture medium after (a-c) one week and (d-f) two weeks. (scale bar = 100 nm)

The dissolution of these different particles was also studied in the DMEM cell culture medium at 37 °C (**Appendix 1** and **Figure 2-14** for higher magnification images). For BSNPs, after one week, some particles have grown in size while others are broken. Only small fragments could be recovered after 2 weeks. For PSNP samples after 1 week, the outer coating has a shallow appearance and is decorated with porous particles 10-30 nm in diameter. Strikingly, after two weeks, two populations of particles are observed: larger ones, *ca.* 100-150 nm in diameter,



exhibiting a dense core and a porous shell, and smaller ones, 20-50 nm in size, with a porous internal structure resembling that of previously-observed decorating particles.

For HSNPs, TEM images after 1 week are highly reminiscent of those previously obtained in PBS after 2 weeks (**Figure 2-13** and **2-14**). Within two weeks, after centrifugation and washing, only a few of these nanoparticles could be recovered with an intact morphology and imaged. These particles seem to have grown in size and the shell and core particle appear denser and separated by a highly porous, if not empty, region. Hence, overall, the culture medium appears to speed up the degradation process of all particles compared to PBS at a similar pH.

In parallel, the dissolution rate of the particles in culture medium was investigated through the monitoring of the fluorescence of the solution after centrifugation and filtration. Because these steps eliminate silica particles and since FITC forms a stable covalent bond with the silica network, the fluorescence signal can only correspond to FITC-silane or soluble FITC-polysiloxane molecules released upon silica dissolution<sup>2</sup>.

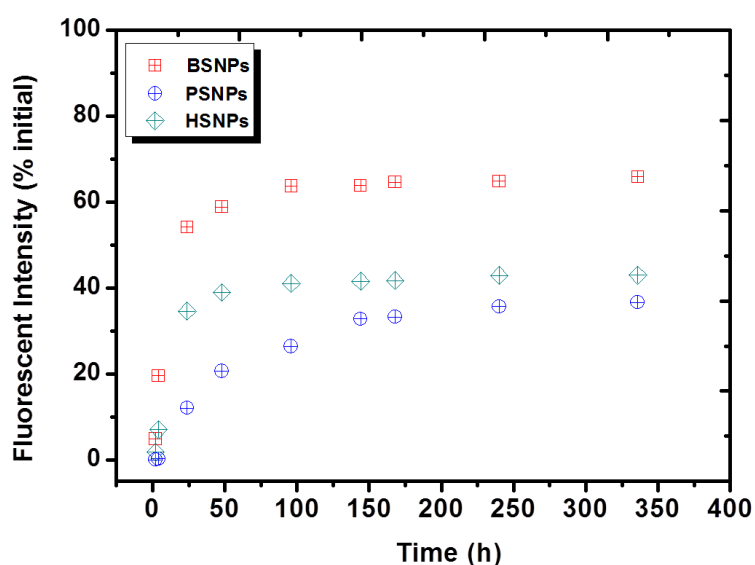


**Figure 2-15** Evolution of the content of the culture medium over 2 weeks in the presence of silica nanoparticles as monitored by the fluorescence intensity of FITC-labelled soluble forms of silica

After 1 day, more than 50 % of the BSNPs particles are dissolved and the maximum dissolution of 65 % is reached after 1 week (**Figure 2-15**). For HSNPs, a similar rapid dissolution is observed but the maximum dissolution of 40 % is reached after 1 week. PSNPs dissolve much more slowly (*ca.* 10 % after 1 day) and, after 2 weeks, only 30 % of the initial fluorescent silanes are present in a soluble form. These data confirm the low stability of BSNPs in DMEM.

For PNSPs, the low degradation rate and extent are in favor of the proposed mechanism of progressive reprecipitation of the soluble forms originating from the shell and then core particle dissolution. HSNPs represent an intermediate case, with fast initial dissolution rate followed by a plateau and low dissolution extent, suggesting that some reprecipitation reactions also occur, but in a less efficient manner than in PNSPs

### 2.3.3 Nanoparticles behaviour in the presence of fibroblasts.

To study the possible impact of nanoparticle structure and degradation on cell viability, NHDF cells were used as model organisms and the Alamar Blue method, which measures the mitochondrial activity of the cells, was selected to monitor the cellular response to nanoparticles (Figure 2-16).

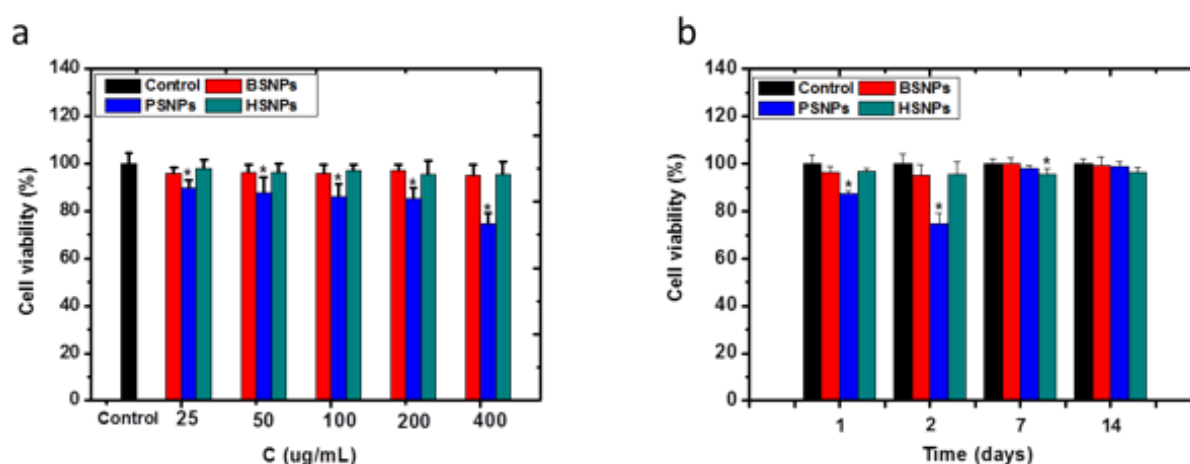


**Figure 2-16** (a) NHDF cells after incubation with silica nanoparticles at various concentrations (25-400 µg/mL) for 2 days. (b) NHDF cells after incubation with 400 µg/mL of silica nanoparticles at various time intervals

After a 48 h incubation period, in all the range of concentrations tested, BSNPs and HSNPs did not show a significant toxicity while PNSPs induced an initial slight reduction of cell viability in all conditions, down to 75% of cell viability at a 400 µg/mL dose. However, at this concentration, NHDFs recovered from PNSPs cytotoxicity after 1 week. Referring to the dissolution kinetics shown in **Figure 2-15**, neither BSNPs nor their degradation products have significant cytotoxic effects. PNSPs are cytotoxic on the short term, a period where the outer layers are slowly dissolving. This result can be correlated to previous reports showing that the presence of an external silica layer decreases the toxicity of poly-lysine-coated gold nanoparticles<sup>21</sup>. On this basis, it can be suggested that the initial dissolution of the silica layers

leads to the release of cytotoxic PEI. However, the redeposition of smaller silica particles on PNSPs surface, as observed in Figure 2-14, may circumvent this effect on the longer term.

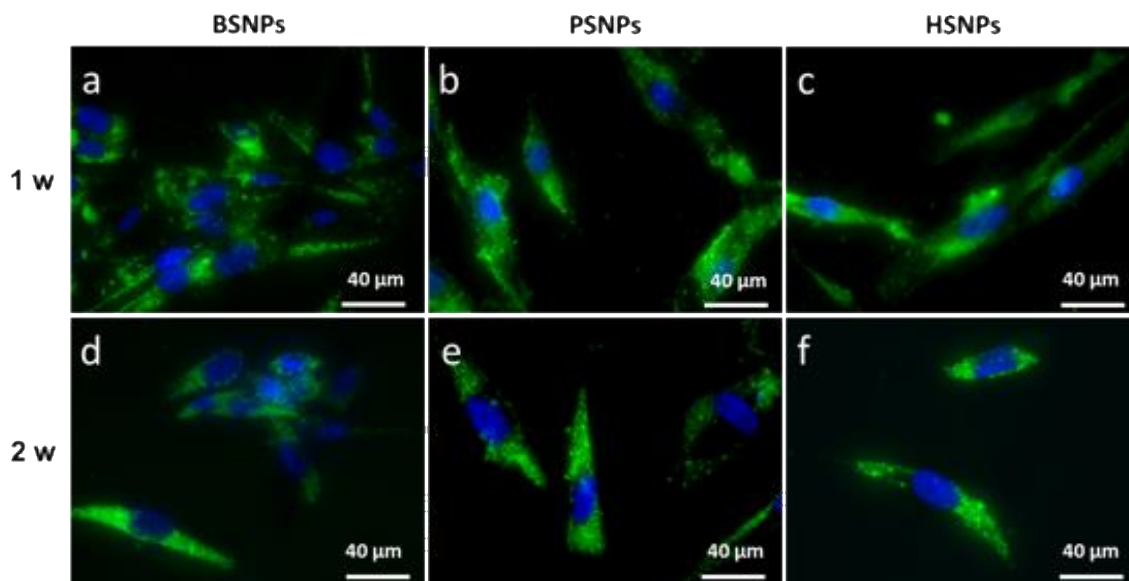


**Figure 2-17** Fluorescence optical imaging of human dermal fibroblast cells after (a-c) 7 days and (d-f) 14 days of contact with 400  $\mu\text{g/mL}$  silica nanoparticles

The particle uptake by NHDFs in culture medium was followed by fluorescent microscopy using the same silica concentration (400  $\mu\text{g/mL}$ ) (**Figure 2-17**). Silica nanoparticles associated with cells were evidenced but many of them appeared to be attached to the cell membrane as aggregates. With time, these aggregates became less visible and the fluorescent signal appeared confined within the cell interior, with a higher intensity for PSNPs and HSNPs compared to BSNPs after 2 weeks.

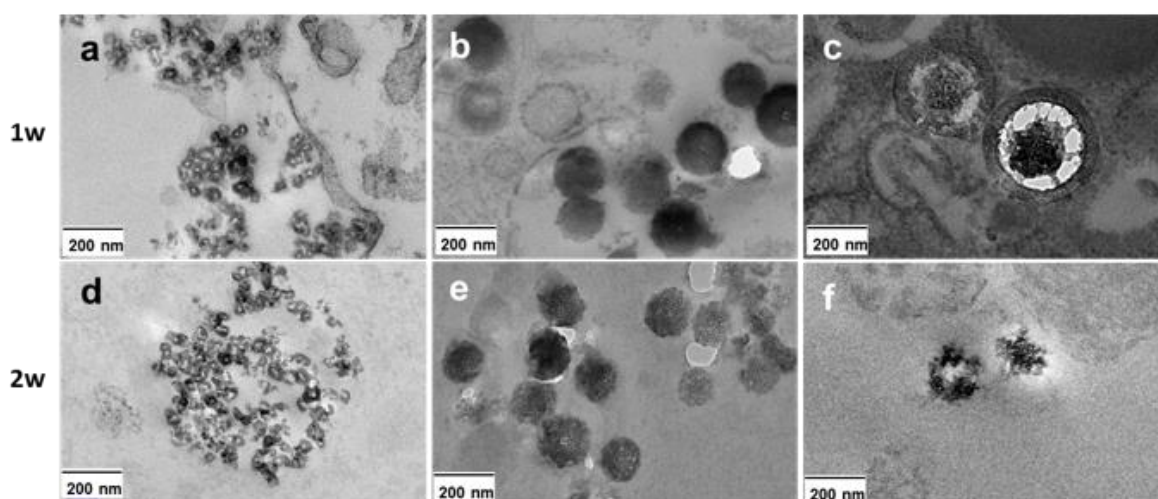


**Figure 2-18** TEM images of NHDF cells after (a-c) 1 week and (d-f) 2 weeks of contact with 400  $\mu\text{g/mL}$  silica nanoparticles

However, to fully ascertain particle internalization, TEM imaging was performed (**Figure 2-18**). After 1 week, BSNPs are sparingly found as intracellular aggregates of particles that have decreased in size as an apparent consequence of shrinking after core material removal. PSNPs and HSNPs are more easily distinguished both outside and inside the cells. The former appear as plain particles decorated with smaller particles. For HSNPs the shell has grown in thickness while the internal structure has started to degrade, as previously observed in DMEM after 2 weeks.

### 2.3.4 Degradation and release kinetics.

The kinetics of degradation and release of the nanoparticles was further studied by keeping NHDFs in contact with silica nanoparticles for 1 week after which the cells were rinsed off the remaining external particles and incubated in fresh culture medium for an additional week. Over the first 24 h, for all particles, the total fluorescence of the solution is initially very low and then increase progressively up to *ca.* 80 % of the intensity of the initial particle suspension (**Figure 2-19a**). This can be correlated with fluorescence optical imaging indicating that particles first adhere on the cell surface (decreasing the amount of free particles in solution) and are then progressively detached. Yet a decrease in total fluorescence intensity is observed after 48 h, that may reflect enhanced particle internalization<sup>2</sup>. Considering the release of soluble forms in the culture medium, the kinetics profiles are very similar to those obtained in the absence of NHDF. However, the maximum apparent dissolution ratio is significantly smaller for BSNPs (50 % compared to 60 % without NHDF) and PSNPs (20 % compared to 30 %). This would suggest that a fraction of the soluble forms is retained by the cells.

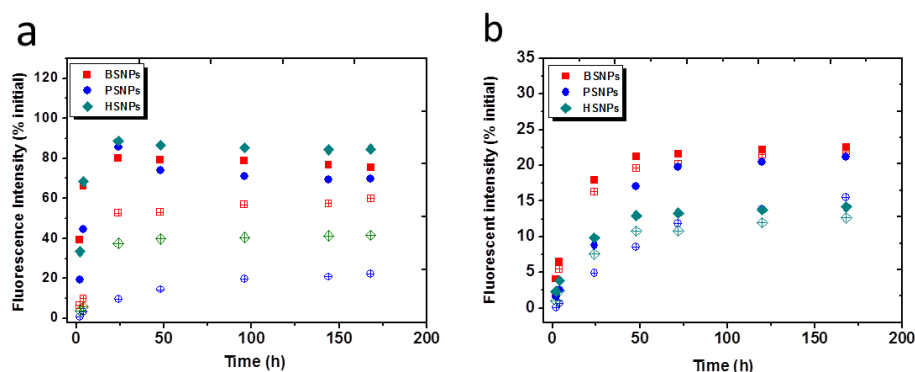


**Figure 2-19** Evolution of the content of the NHDF cells culture medium as monitored by the fluorescence intensity of FITC-labelled condensed and soluble forms of silica (filled symbols)

and soluble forms only (open symbols) (a) over 1 week in the presence of silica nanoparticles and (b) over 1 additional week in a fresh medium

After cell rinsing and incubation in a fresh, particle-free medium for an additional week, intracellular nanoparticles were more difficult to observe in TEM imaging fields (**Figure 2-18** and **Figure 2-19**). When this was possible, we did not evidence any clear change for BSNPs compared to day 7. PSNPs have significantly decreased in size and exhibit a porous structure. No well-defined HSNPs could be observed after this period and only fragments could be imaged that may originate from their full dissociation. In parallel, the total FITC fluorescence intensity in the culture medium, initially equal to zero because of the incubation in a fresh medium, increased with time (**Figure 2-19b**). At the end of this additional period, almost all the initial fluorescence intensity (as calculated by adding 1 week values obtained from **Figure 2-19a** and 2 weeks values from **Figure 2-19b**) was recovered for the three kinds of particles, indicating that a negligible fraction of silica remains inside the cells, in agreement with TEM experiments. However, whereas BSNPs and HSNPs were almost fully released in a soluble form, more than 30 % of PSNPs were externalized in a colloidal form.

## 2.4 Discussion

Here gathered data clearly evidence that the pathways by which the three types of nanoparticles are degraded are rather similar in the three considered environments, i.e. buffer, culture medium and intracellular space of fibroblasts. However the resulting structural evolution is highly dependent on their initial composition and nanostructure. In this discussion, we have tried to analyze and compare the degradation of each type of particle.

BSNPs initially show TEM-contrasting internal features that suggest that they consist of a protein-rich interior surrounded by a silica-rich coating. In PBS, these particles grow in size, with an apparent leakage of the core material, the process being accelerated in culture medium. Finally, particle degradation occurs, leaving much smaller empty particles. A similar process seems to occur within the NHDF cells, although at a higher rate. Additional experiments performed using BSNPs incorporating FITC-labelled BSA showed that, after one week of contact with NHDF, the protein was hardly detectable within or at the vicinity of the cells whereas silica was still present in large amounts (compare **Figure 2-20** with **Figure 2-17a**). The most likely explanation of these evolutions is that water penetration within the particle leads to the swelling of the BSA core, disruption of the silica shell and leakage of the protein

(**Figure 2-21**). As suggested earlier, the enzymatic degradation of BSA in the intracellular compartment may contribute to accelerate these processes.

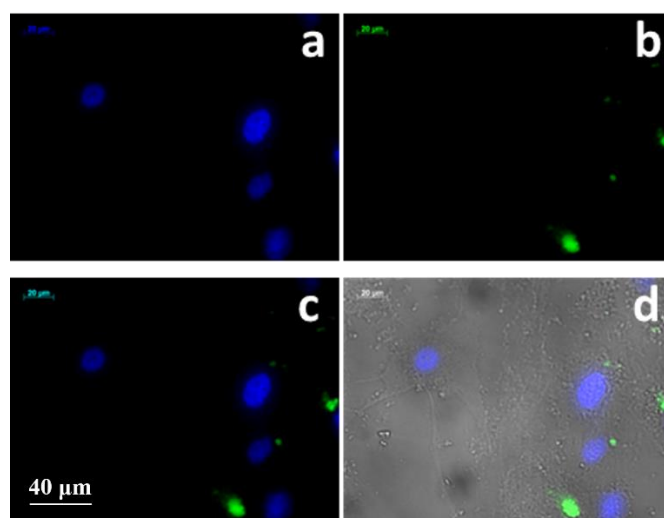


**Figure 2-20** Fluorescence optical imaging of human dermal fibroblast cells after 7 days of contact with 400 µg/mL BSNPs nanoparticles using FITC-labelled BSA. (Scale bar = 40 µm)

For HSNPs, silica dissolution in PBS apparently occurs first from the shell, resulting in particles that are almost uniformly porous except for the central part and are prone to deformation and breaking (**Figure 2-21**). The same process occurs in culture medium but after two weeks, the only remaining particles exhibit a highly contrasted shell and a denser central part, separated by a nearly empty corona. Such structures were also observed after one week within cells and evolved towards a complete disintegration after 2 weeks. While the initial shell dissolution should be favored by its mesoporous structure, the following process can be explained considering the dissolution of the more porous (*i.e.* more soluble) silica corona located between the shell and the core particle and its reprecipitation on these two denser (*i.e.* less soluble) regions, based on the Ostwald ripening principle.

Overall BSNPs and HSNPs evolve more rapidly but along similar pathways in PBS, in DMEM and in the intracellular space. When experiments in buffer and culture medium are compared, pH and total silica concentration are similar. Ionic strength of DMEM is 0.13 M, being therefore comparable with the 0.16 M value for PBS 1X. However, DMEM supplemented with FCS contains several bio-organic components (amino acids, proteins) that can interact with silica. For instance, it was shown that histidine and phenylalanine could promote silica dissolution<sup>22</sup>. Extending this discussion to intracellular compartments is indeed difficult as their composition is complex and variable. Nevertheless it is worth pointing out that lysosomes were reported to

contain a high fraction of free amino acids<sup>23</sup>. It is also interesting to note that intracellular compartments that are involved in nanoparticle trafficking are reported to be slightly (endosomes) to significantly (lysosomes) acidic so that a decrease of silica dissolution rate could be expected compared to neutral conditions of PBS/DMEM medium. While this point would require a detailed investigation of the particle structural modification in the first hours of the internalization process, our experiments suggest that the difference in pH conditions is not of primary importance for their long-term fate.

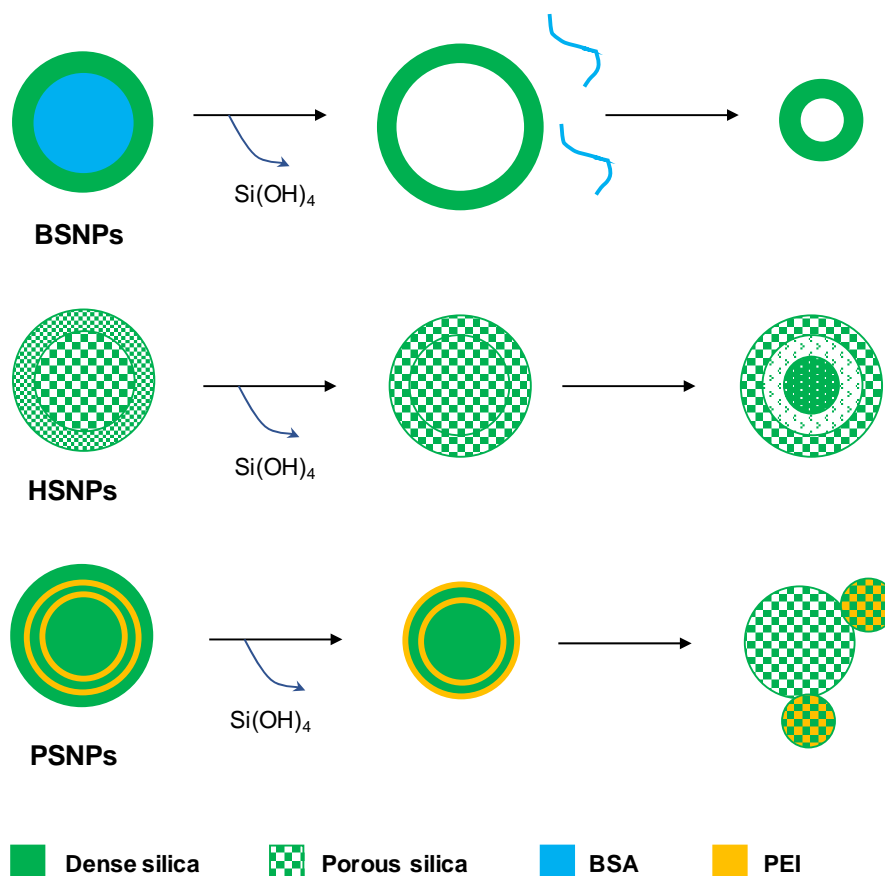


**Figure 2-21** Schematic representation of the degradation pathways of BSNPs, HSNPs and PSNPs in DMEM culture medium

However, another important point must be taken into consideration. The full release of silicon species from the cells to the medium clearly demonstrates that the products of the intracellular dissolution reaction can be externalized in a continuous manner. Hence, whereas the extent of particle dissolution in solution is limited by the silica limit of solubility, the conditions of degradation within intracellular compartments can be compared to that of an open reactor, although previous reports evidenced that the exocytosis extent was dependent on the amount of silica in the medium<sup>24</sup>. This can explain the difference evidenced for PSNPs in DMEM and within NHDFs. In the culture medium, a decrease in initial particle size is observed after 1 week

and smaller particles are clearly visible at their vicinity (Figure 2-21). This suggests that the outer PEI/silica layers first dissolve but, because PEI is known to promote silica precipitation<sup>25</sup>, the released soluble silica species and the polyelectrolyte chains can react together to form these new particles, as previously suggested<sup>26</sup>. In a second stage, the largest particles turn porous, indicating that further dissolution occurs and feeds the growth of the external smaller particles. Noticeably, within the cells, these additional particles are hardly distinguished although the transformation from plain to porous large particles is also observed. This result nicely correlates with our observation that, whereas BSNPs and HSNPS are almost exclusively released in soluble forms during the second week, almost 30 % of PNSPs are externalized in a colloidal form that may correspond to the newly-formed silica nanoparticles that are small enough to be expelled.

## 2.5 Conclusion

By following the evolution of silica nanoparticles with different internal nanostructures in solution and within normal human dermal fibroblasts, we show that their degradation pathways are very similar in all conditions although their structure, composition and their precise environment can impact on the kinetics of the degradation. This supports previous assumptions that within such cells silica nanoparticles undergo a hydrolytic degradation process, related to silica chemistry, and not a biodegradation route, that would involve a specific biological activity<sup>27</sup>. It must be pointed out that these results cannot fully exclude that some biodegradation is at stake, but it does not seem to prevail in the here-investigated system. Indeed these studies would deserve to be performed in other types of cells, including macrophages that have specific modes of degradation or cancer cells, that are responsible for acidic conditions that should strongly impact on silica stability. Bone cells that are known to respond to the presence of silica would also be interesting to study<sup>28</sup>. Another point of importance is the pathway by which particles are internalized, that impact on their following intracellular trafficking. In this matter, a detailed study of the influence of inhibitors of specific endocytosis pathways (such as clathrin- and caveolae-mediated routes) or of the grafting cell-penetrating peptides would be of particular interest.

From a more practical point of view, our study implies that the intracellular fate of silica-based nanomaterials can be controlled and predicted on the basis of physico-chemical considerations. However a different situation is met when these nanomaterials integrate some bio-responsive moieties. In this case the intrinsic complexity of biological systems makes a prediction of



nanoparticle behavior more difficult. Nevertheless, as shown in the next chapter, the set-up of biomimetic environmental conditions may be useful to perform more reliable in vitro evaluation of functional nanomaterials.

## References

1. Slowing, II; Vivero-Escoto, J. L.; Zhao, Y.; Kandel, K.; Peeraphatdit, C.; Trewyn, B. G.; Lin, V. S. Y., Exocytosis of Mesoporous Silica Nanoparticles from Mammalian Cells: From Asymmetric Cell-to-Cell Transfer to Protein Harvesting. *Small* **2011**, 7, (11), 1526-1532.
2. Quignard, S.; Mosser, G.; Boissiere, M.; Coradin, T., Long-term fate of silica nanoparticles interacting with human dermal fibroblasts. *Biomaterials* **2012**, 33, (17), 4431-4442.
3. Zhai, W. Y.; He, C. L.; Wu, L.; Zhou, Y.; Chen, H. R.; Chang, J.; Zhang, H. F., Degradation of hollow mesoporous silica nanoparticles in human umbilical vein endothelial cells. *Journal Of Biomedical Materials Research Part B-Applied Biomaterials* **2012**, 100B, (5), 1397-1403.
4. Chen, G. T.; Teng, Z. G.; Su, X. D.; Liu, Y.; Lu, G. M., Unique Biological Degradation Behavior of Stober Mesoporous Silica Nanoparticles from Their Interiors to Their Exteriors. *Journal Of Biomedical Nanotechnology* **2015**, 11, (4), 722-729.
5. Kempen, P. J.; Greasley, S.; Parker, K. A.; Campbell, J. L.; Chang, H. Y.; Jones, J. R., et al. Jokerst, J. V., Theranostic Mesoporous Silica Nanoparticles Biodegrade after Pro-Survival Drug Delivery and Ultrasound/Magnetic Resonance Imaging of Stem Cells. *Theranostics* **2015**, 5, (6), 631-642.
6. Bergman, L.; Kankaanpää, P.; Tiitta, S.; Duchanoy, A.; Li, L.; Heino, J.; Linden, M., Intracellular Degradation of Multilabeled Poly(Ethylene imine)-Mesoporous Silica-Silica Nanoparticles: Implications for Drug Release. *Molecular Pharmaceutics* **2013**, 10, (5), 1795-1803.
7. Couleaud, P.; Morosini, V.; Frochot, C.; Richeter, S.; Raehm, L.; Durand, J. O., Silica-based nanoparticles for photodynamic therapy applications. *Nanoscale* **2010**, 2, (7), 1083-1095.
8. Montalti, M.; Prodi, L.; Rampazzo, E.; Zaccheroni, N., Dye-doped silica nanoparticles as luminescent organized systems for nanomedicine. *Chemical Society Reviews* **2014**, 43, (12), 4243-4268.
9. Li, Z. B.; Yuan, D.; Jin, G. R.; Tan, B. H.; He, C. B., Facile Layer-by-Layer Self-Assembly toward Enantiomeric Poly(lactide) Stereocomplex Coated Magnetite

Nanocarrier for Highly Tunable Drug Deliveries. *Acs Applied Materials & Interfaces* **2016**, 8, (3), 1842-1853.

10. Mebert, A. M.; Aime, C.; Alvarez, G. S.; Shi, Y. P.; Flor, S. A.; Lucangioli, S. E., et al. Coradin, T., Silica core-shell particles for the dual delivery of gentamicin and rifamycin antibiotics. *Journal Of Materials Chemistry B* **2016**, 4, (18), 3135-3144.

11. Andersson, J.; Rosenholm, J.; Areva, S.; Linden, M., Influences of material characteristics on ibuprofen drug loading and release profiles from ordered micro- and mesoporous silica matrices. *Chemistry Of Materials* **2004**, 16, (21), 4160-4167.

12. Bouledjoudja, A.; Masmoudi, Y.; Van Speybroeck, M.; Schueller, L.; Badens, E., Impregnation of Fenofibrate on mesoporous silica using supercritical carbon dioxide. *International Journal Of Pharmaceutics* **2016**, 499, (1-2), 1-9.

13. Nyffenegger, R.; Quellet, C.; Ricka, J., Synthesis of Fluorescent, Monodisperse, Colloidal Silica Particles. *J. Colloid Interface Sci.* **1993**, 159, (1), 150-157.

14. Zhou, Z. J.; Zhang, C. L.; Qian, Q. R.; Ma, J. B.; Huang, P.; Zhang, X., et al. Cui, D. X., Folic acid-conjugated silica capped gold nanoclusters for targeted fluorescence/X-ray computed tomography imaging. *Journal Of Nanobiotechnology* **2013**, 11.

15. Nakamura, T.; Sugihara, F.; Matsushita, H.; Yoshioka, Y.; Mizukami, S.; Kikuchi, K., Mesoporous silica nanoparticles for F-19 magnetic resonance imaging, fluorescence imaging, and drug delivery. *Chemical Science* **2015**, 6, (3), 1986-1990.

16. Wang, X. L.; Masse, S.; Laurent, G.; Helary, C.; Coradin, T., Impact of Polyethylenimine Conjugation Mode on the Cell Transfection Efficiency of Silica Nanovectors. *Langmuir* **2015**, 31, (40), 11078-11085.

17. Vanblaaderen, A.; Vrij, A., SYNTHESIS AND CHARACTERIZATION OF COLLOIDAL DISPERSIONS OF FLUORESCENT, MONODISPERSE SILICA SPHERES. *Langmuir* **1992**, 8, (12), 2921-2931.

18. Chen, F.; Hong, H.; Shi, S. X.; Goel, S.; Valdovinos, H. F.; Hernandez, R., et al. Cai, W. B., Engineering of Hollow Mesoporous Silica Nanoparticles for Remarkably Enhanced Tumor Active Targeting Efficacy. *Scientific Reports* **2014**, 4.

19. Drescher, D.; Orts-Gil, G.; Laube, G.; Natte, K.; Veh, R. W.; Osterle, W.; Kneipp, J., Toxicity of amorphous silica nanoparticles on eukaryotic cell model is determined by particle agglomeration and serum protein adsorption effects. *Analytical And Bioanalytical Chemistry* **2011**, 400, (5), 1367-1373.

20. Noble, J. E.; Wang, L.; Cole, K. D.; Gaigalas, A. K., The effect of overhanging nucleotides on fluorescence properties of hybridising oligonucleotides labelled with Alexa-488 and FAM fluorophores. *Biophysical Chemistry* **2005**, 113, (3), 255-263.
21. Soule, S.; Bulteau, A. L.; Faucher, S.; Haye, B.; Aime, C.; Allouche, J., et al. Martinez, H., Design and Cellular Fate of Bioinspired Au-Ag Nanoshells@Hybrid Silica Nanoparticles. *Langmuir* **2016**, 32, (39), 10073-10082.
22. Ehrlich, H.; Demadis, K. D.; Pokrovsky, O. S.; Koutsoukos, P. G., Modern Views on Desilicification: Biosilica and Abiotic Silica Dissolution in Natural and Artificial Environments. *Chemical Reviews* **2010**, 110, (8), 4656-4689.
23. Tappel, A. L.; Shibko, S.; Stein, M.; Susz, J. P., Studies on the Composition of Lysosomes. *Journal of food science* **1965**, 30, 498-503.
24. Chu, Z. Q.; Huang, Y. J.; Tao, Q.; Li, Q., Cellular uptake, evolution, and excretion of silica nanoparticles in human cells. *Nanoscale* **2011**, 3, (8), 3291-3299.
25. Demadis, K. D.; Pachis, K.; Ketsetzi, A.; Stathouloupoulou, A., Bioinspired control of colloidal silica in vitro by dual polymeric assemblies of zwitterionic phosphomethylated chitosan and polycations or polyanions. *Advances In Colloid And Interface Science* **2009**, 151, (1-2), 33-48.
26. Chen, K. H.; Zhang, J. X.; Gu, H. C., Dissolution from inside: a unique degradation behaviour of core-shell magnetic mesoporous silica nanoparticles and the effect of polyethyleneimine coating. *Journal Of Materials Chemistry* **2012**, 22, (41), 22005-22012.
27. Croissant, J. G.; Fatieiev, Y.; Khashab, N. M., Degradability and Clearance of Silicon, Organosilica, Silsesquioxane, Silica Mixed Oxide, and Mesoporous Silica Nanoparticles. *Advanced Materials* **2017**, 29, (9).
28. Shie, M. Y.; Ding, S. J.; Chang, H. C., The role of silicon in osteoblast-like cell proliferation and apoptosis. *Acta Biomaterialia* **2011**, 7, (6), 2604-2614.

# Chapter 3 Synthesis and properties of theranostic nanoplateform from 2D to 3D

“天行健，君子以自强不息”

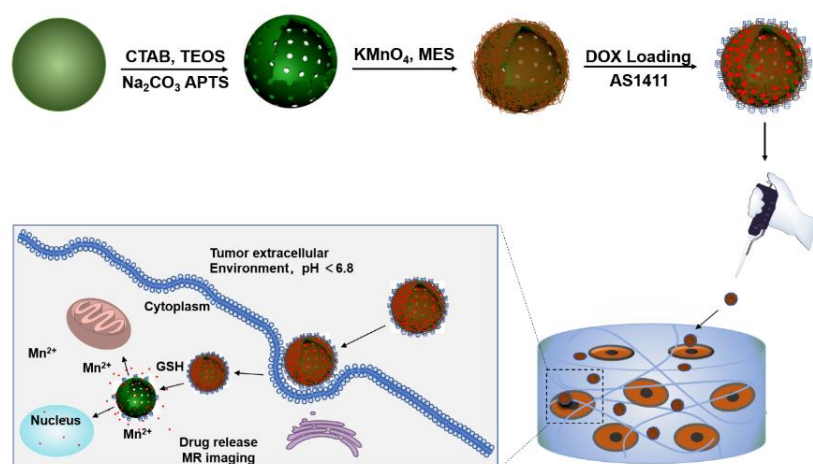
《易经》

## Abstract

This study aimed to synthesize nanoparticles for theranostic applications and to evaluate the influence of a three-dimensional environment on their functionality. These particles combining controlled drug delivery properties, MRI contrast agent and cancer cell targeting were prepared by combining hollow mesoporous silica particles containing doxorubicin, MnO<sub>2</sub> nanosheets and an aptamer. Monolayer cultures showed that these particles penetrated model cancer cells, leading to increased MRI signals and releasing doxorubicin, both effects being significantly more significant than in healthy cells. In addition, the functionality and specificity of the particles were preserved when the cells were immobilized in collagen hydrogels. This approach could therefore be used for a rapid assessment of the biofunctionality of nanoparticles before setting up in vivo experiments.

<b>3.1 Introduction .....</b>	<b>103</b>
<b>3.2 Materials and methods.....</b>	<b>105</b>
3.2.1 Materials and reagents.....	105
3.2.2 Preparation of HMSNs@MnO <sub>2</sub> /apt.....	105
3.2.3 Drug loading and release <i>in vitro</i> .....	106
3.2.5 <i>In vitro</i> cytotoxicity assays and cell uptake studies .....	107
3.2.6 Measurement of MRI relaxation properties .....	108
3.2.7. Cytotoxicity and functionality within 3D models .....	108
3.2.8. Statistical Analysis .....	109
<b>3.3. Results and discussion.....</b>	<b>109</b>
3.3.1 Preparation and characterization of the nanoplateforms.....	109
3.3.2 Drug release and MRI imaging properties of the nanoplateforms.....	114
3.3.3 Functionality of nanoplateforms in 3D biomimetic collagen matrices.....	119
<b>3.4 Conclusion.....</b>	<b>122</b>

# Synthèse et propriétés de nanoplateformes pour la théranostique: du 2D au 3D



## Résumé

Cette étude vise à synthétiser des nanoparticules pour des applications théranostiques et évaluer l'influence d'un environnement tri-dimensionnel sur leur fonctionnalité. Ces particules alliant des propriétés de délivrance contrôlée de médicaments, d'agent de contraste pour l'IRM et de ciblage de cellules cancéreuses ont été préparées en combinant des particules de silice mésoporeuses creuses contenant de la doxorubicine, des nanofeuillets de MnO<sub>2</sub> et un aptamère. Les cultures monocouches ont montré que ces particules pénétraient les cellules cancéreuses modèles, conduisant à l'augmentation des signaux IRM et libérant la doxorubicine, les deux effets étant nettement plus significatifs que dans des cellules saines. De plus, la fonctionnalité et la spécificité des particules ont été préservées lorsque les cellules ont été immobilisées dans des hydrogels de collagène. Cette approche pourrait donc servir pour une évaluation rapide de la biofonctionnalité des nanoparticules avant de mettre en place des expériences *in vivo*.

Y. Shi, F. Guenneau, W. Wang, C. Hélary, T. Coradin, MnO<sub>2</sub>-gated Nanoplatforms with Targeted Controlled Drug Release and Contrast-Enhanced MRI Properties: from 2D Cell Culture to 3D Biomimetic Hydrogels, *Nanotheranostics*, 2018; 2(4): 403-416.

### 3.1 Introduction

Despite the rapid improvement of modern medicine, the early diagnosis and therapy of cancer is still a challenge. The continuous development of nanotechnology and the emergence of targeted treatments provide an inequivalent opportunity in this area. The past decade has witnessed the engineering of many theranostic nanosystems, where the integration of different imaging agents and therapeutic drugs into a single nanoparticle (NP) has made it possible to exhibit multiple functionalities<sup>1-4</sup>. Extensive efforts have also allowed for the identification of active targeting reagents, such as folic acid, hyaluronic acid, aptamers, or transferrin, that bind with high specificity to the cancerous cell membrane<sup>5-8</sup>. At the same time, strategies were developed to achieve a controlled drug release triggered by intrinsic physiological microenvironment changes (pH, redox, enzyme, heat, *etc.*) and/or external stimuli (including light, magnetic/electronic field, ultrasound, *etc.*)<sup>9-11</sup>. All those developments taken together, it becomes possible to simultaneously reduce the side-effects of anticancer agents to normal tissues and enhance their therapeutic efficiency<sup>12</sup>. Indeed, there still is some room for large improvement, in terms of drug loading and targeting efficiency.

From an imaging perspective, signals of most previously-reported nanosystems are “always on” regardless of the absence or presence of the target cells, resulting in a low contrast detection<sup>13</sup>. Among available nanoparticles, Mesoporous Silica Nanoparticles (MSNs) have been widely considered for the delivery of anticancer drugs<sup>11, 14, 15</sup>. To tackle MSNs intrinsic limited loading capacity, Hollow MSNs (HMSNs) with rattle or hollow structure have been prepared as they can efficiently accommodate drugs not only into mesoporous channels of their shell but also within their internal cavity<sup>16-18</sup>. Moreover, recent progress in the design of gated HMSNs has shown some promise in the development of controlled-release theranostic nanosystems. Different “gatekeepers”, such as organic molecules, biomacromolecules and nanoparticles, have been used, allowing pore-opening under the stimulation of pH change, temperature, nucleotides, antibodies, enzymes, glucose, or photoirradiation<sup>19-21</sup>. However, these gated nanosystems usually require a highly-sophisticated design that has a strong impact on synthesis time and development cost, ultimately hindering their transfer to the market, despite their demonstrated functionality.

Recently, MnO<sub>2</sub> nanosheets, a 2D ultrathin semiconductor material with wide applications in the energy field<sup>22</sup>, has attracted large attention as a gatekeeper for drug nanocarriers<sup>23-25</sup>. They exhibit a broad and intense absorption band at around 374 nm, making MnO<sub>2</sub> nanosheets an efficient broad-spectrum quencher<sup>26</sup>. Moreover, MnO<sub>2</sub> can be converted to Mn<sup>2+</sup> via reduction

by endogenous glutathione (GSH), leading to decomposition of the MnO<sub>2</sub> nanosheets<sup>27</sup>. While manganese (IV) ions in the nanosheets are shielded from water due to their 6-fold coordination with oxygen atoms, free solvated Mn<sup>2+</sup> ions are efficient T<sub>1</sub> contrast agents for Magnetic Resonance Imaging (MRI)<sup>28</sup>. GSH is an essential endogenous antioxidant that has many cellular functions and high GSH levels are implicated in many diseases typically associated with cancer, liver damage, or heart problems<sup>29</sup>. Therefore, much attention has been paid to the use of GSH to design intracellular controlled release systems<sup>30</sup>. In addition, whereas the extracellular pH of normal tissues and blood is constant at 7.4, the measured extracellular values of most solid tumors range from pH 6.5 to 7.2, such lower pH values being more favorable for the reaction between MnO<sub>2</sub> and GSH<sup>31</sup>. Based on this principle, several MnO<sub>2</sub>@SiO<sub>2</sub>-based controlled-release nanosystems with GSH-induced contrast-enhanced magnetic resonance signal have already been described<sup>23, 32, 33</sup>.

Another key challenge in this area lies in the precise control of the drug release using stimuli-responsive systems. Thus, tumor microenvironment, that has a crucial role in cancer progression, exhibit several specific biological and physico-chemical features that can be exploited to trigger the drug release at the tumor site<sup>34</sup>. However, the efficiency and stimulation of nanosystems are often tested in two-dimensional (2D) systems, in which seeded cancer cells do not experience the real microenvironment they find in *vivo*, where physiological fluids, tissues as well as interactions between cancer and stromal cells may impair the drug delivery or its functionality. The transfer from 2D data to *in vivo* during preclinical studies may therefore be extremely time-consuming and costly. Therefore, the design of three-dimensional (3D) environments exhibiting some features of *in vivo* tumors, such as three-dimensional architecture, cell-cell interaction and hypoxia should provide highly useful tumor tissue *in vitro* models for testing anticancer therapeutics<sup>35, 36</sup>. In this context, the use of type I collagen, the major protein in most animal tissues, to prepare biomimetic constructs is of particularly relevant<sup>37-39</sup>. Most importantly, it has been shown in our group that they could act as models to study the interactions between nanoparticles and cells in a 3D environment<sup>40, 41</sup>.

In this work, we aimed at designing multifunctional nanoprobe for contrast-enhanced bimodal cellular imaging and targeted therapy and to study how their interactions with normal human cells and model cancer cells could be impacted by in traditional 2D cell culture and in cellularized 3D hydrogels. Our strategy for the design of the nanoplateforms was to use the above-described MnO<sub>2</sub> nanosheets as a coating of doxorubicin-loaded HMSNs that could act as both gatekeeper for DOX release from and contrast agent for MRI. Another key element of our nanoplateforms was the use of a cancer cell-targeting aptamer (AS1411), that bind to nucleolin, a nucleolar

phosphoprotein which is overexpressed on the surface of certain cancer cells<sup>28,42,43</sup>. Noticeably, at the time where we started this project, there was only one paper available in the literature that used a quite similar strategy<sup>23</sup> but other related works were published while we were developing our own project, especially for Yang et al. and Li group<sup>32,33</sup>. However none used HMSNs as starting silica nanostructures and our attempt to evaluate their behavior in 3D models was not reported so far.

## 3.2 Materials and methods

### 3.2.1 Materials and reagents

All chemical reagents were analytical grade and used without further purification. Cetyltrimethylammonium bromide (CTAB), tetraethyl orthosilicate (TEOS), sodium carbonate ( $\text{Na}_2\text{CO}_3$ ), absolute ethanol, concentrated hydrochloric acid, ammonium aqueous solution (25-28%), triethanolamine (TEA), 3-triethoxysilylpropylamine (APTES), potassium permanganate ( $\text{KMnO}_4$ ), 2-(N-Morpholino)ethanesulfonic acid hydrate (MES), doxorubicin hydrochloride (DOX) and fluorescein isothiocyanate (FITC) were purchased from Sigma-Aldrich. MilliQ water (18M $\Omega$ , Millipore, France) was used for the preparation of the solutions and for all rinses. 4,6-diamidino-2-phenylindole (DAPI). Fetal bovine serum, Dulbecco's Modified Eagle's Medium (DMEM), trypsin, glutamine, penicillin-streptomycin solution and AS1411 aptamer (5'-NH<sub>2</sub>-GGTGGTGGTGGTTGTGGTGGTGGTGG-3') were purchased from ThermoFisher.

### 3.2.2 Preparation of HMSNs@MnO<sub>2</sub>/apt

#### *Synthesis*

Bare HMSNs were prepared using previously reported methods<sup>44,45</sup>. To functionalize the particle surface with amine groups, as-synthesized HMSNs were first dispersed in 20 mL of toluene, followed by addition of 1mL of APTES. The system was sealed and refluxed at 120 °C in oil bath for 12 h. Afterward, the mixture was centrifuged and washed with ethanol for several times to remove the residual APTES. Then, 20 mg of HMSNs-NH<sub>2</sub> was dispersed in 4.2 mL MES buffer (0.1M, pH 6.0) and then 0.8 mL of 5 mM  $\text{KMnO}_4$  in water was added to the mixture under ultrasonic condition. The resulting mixture was sonicated for another one hour during which brown-black colloids were observed. Subsequently, the raw product was collected by centrifugation, washed several times with deionized water and alcohol to remove any possible residual reactants, and redispersed in 2 mL PBS solution (pH 7.4). The physical



adsorption of aptamer on HMSNs@MnO<sub>2</sub> was carried out by mixing 0.8 mL of HMSNs@MnO<sub>2</sub> (20 mg/mL) in PBS and 200  $\mu$ L of AS1411 (1  $\mu$ M). After 3 h of incubation, the solution was centrifuged at 6000 rpm, washed several times, and then dispersed in PBS (pH 7.4) for further application. The preparation of fluorescently-labeled hollow mesoporous silica nanoparticles was performed by adding FITC to the starting solution used for bare HSMNs preparation.

### ***Characterization***

Transmission Electron Microscopy (TEM) studies were performed on a FEI Tecnai G2 Spirit microscope operating at 120 kV. Scanning electron microscopy (SEM) images were obtained on a Hitachi S-3400N scanning electron microscope with a field emission electron gun. Nitrogen sorption-desorption isotherms were measured at 77 K with a Micromeritics ASAP2010 analyzer. Fluorescence images were recorded on a LEICA microscope. Dynamic Light Scattering (DLS) was used to determine the hydrodynamic diameter of the nanoparticles in Milli-Q water or in culture medium with Mastersizer 3000 Particle Size Analyzer. The reading was carried out at an angle of 90° to the incident beam (632 nm). The Contin algorithm was used to analyze the autocorrelation functions. X-ray Photoelectron Spectroscopy (XPS) analyses were performed with a PHOIBOS 100 spectrometer from SPECS GmbH. Inductively Coupled Plasma Mass Spectrometry (ICP-MS) was used to determine the Mn content of the nanoparticles.

### **3.2.3 Drug loading and release *in vitro***

10 mg of HMSNs@MnO<sub>2</sub> nanoparticles were mixed with 1.5 mg of DOX in 1.5 mL of PBS/DMSO (1:1) mixture solution and then stirred under dark conditions for 24 h. Subsequently, the product was collected by centrifugation and washed several times with PBS to remove the free DOX. Then 100  $\mu$ L of AS1411 (1  $\mu$ M) in PBS was added, and after 3 h of stirring, the resulting HMSNs@MnO<sub>2</sub>(DOX)/apt nanoparticles were collected by centrifugation and re-dispersed in PBS solution for subsequent use. To evaluate the DOX loading, the remaining DOX molecules in the supernatant solutions were determined by fluorescence spectroscopy ( $\lambda_{\text{ex}}$  = 500 nm,  $\lambda_{\text{em}}$  = 590 nm). The loading of the nanoparticles was expressed as the mass percentage of DOX with respect to the total mass of HMSNs@MnO<sub>2</sub>(DOX)/apt nanoparticles.

*In vitro* DOX release from the HMSNs@MnO<sub>2</sub>(DOX)/apt nanoparticles was studied in PBS buffer in absence or presence of GSH at pH values of 7.4 and 5.5. For each release study, 1.0 mL of DOX-loaded nanoparticles (1.0 mg/mL) were dispersed inside a dialysis bag that was soaked in 9.0 mL PBS and shaken at room temperature. At selected time intervals, the sample was collected and 2 mL of solution outside the dialysis bag was removed. Then, 2 mL of fresh PBS buffer was added. The removed solution was properly diluted and the amount of DOX molecules present was measured by fluorescence spectroscopy. The same amount of the DOX solution was introduced in the dialysis bag and was used as control.

### **3.2.5 *In vitro* cytotoxicity assays and cell uptake studies**

#### ***Cell culture***

Normal Human Dermal Fibroblasts (NHDF) and HeLa cells were cultured in complete cell culture medium (DMEM with GlutaMAX™, without phenol red supplement, with 10% fetal serum, 100 U.mL<sup>-1</sup> penicillin, 100 µg/mL streptomycin). Tissue culture flasks (75 cm<sup>2</sup>) were kept at 37 °C in a 95% air: 5% CO<sub>2</sub> atmosphere. Before confluence, the cells were removed from culture flasks by treatment with 0.1% trypsin and 0.02% EDTA. Cells were rinsed and resuspended in the above culture medium before use.

#### ***In vitro* cytotoxicity assays**

First, HeLa were seeded in a 24-well plate at a density of  $\sim 5 \times 10^4$  cells/well overnight to allow cell attachment onto the surface of the wells. Then, 0.5 mL of fresh medium containing various concentrations of HMSNs@MnO<sub>2</sub>(DOX)/apt was added into the wells. After incubation for 24 h, cell activity was evaluated by the Alamar Blue assay. Control experiments were performed by incubating HeLa cells with free DOX and HMSNs@MnO<sub>2</sub>(DOX) at various drug contents or HMSNs@MnO<sub>2</sub>(DOX)/apt at equivalent particle concentration for 24 h. To confirm the cytotoxicity of DOX released from the nanoplatfrom under GSH, control similar experiments were performed with NHDF cells incubated in presence of 5 mM GSH.

#### ***Cell uptake studies by fluorescence imaging***

NHDFs and HeLa cells were seeded in a round glass disk that was inserted in 24-well plate ( $\sim 5 \times 10^4$  cells per well) and cultured for 24 h. The cell medium was removed, and then cells were incubated with 0.5 mL of fresh cell medium containing FITC labeled HMSNs@MnO<sub>2</sub>(DOX)/apt nanoparticles for another 12 h. After medium removal, the cells

were washed with PBS for several times, and then 0.5 mL of fresh cell medium with or without 5 mM GSH was added and incubated for another 3 hours. Fixation of the cells was carried out using 4% (v/v) paraformaldehyde (PFA) for 2 h and rinsed three times using PBS. After washing, cellular nuclei were stained with 1% (v/v) solution of DAPI in PBS buffer for 20 min and washed with PBS three times. Last, cell imaging was carried out by fluorescence microscopy. For the HeLa cells imaging, the procedure was similar, except that HMSNs@MnO<sub>2</sub>(DOX) or HMSNs@MnO<sub>2</sub>(DOX)/apt particles were added and no GSH treatment was performed.

### **3.2.6 Measurement of MRI relaxation properties**

Imaging of MRI phantoms measurement was performed with a Bruker Avance 3 HD 300 spectrometer, equipped with a 10 mm micro imaging probe, having a maximum gradient capacity of 3 T m<sup>-1</sup> in the x, y and z directions. The Multi Slice Multi Echo (MSME) pulse sequence was used, acquiring 1 echo but 8 slices with a slice thickness of 1 mm. The size of the images was: 128×128 with a Field of View of 9.5×9.5 mm, resulting in a voxel size of 74×74 μm. Images were acquired with 1 scan and T<sub>1</sub> weighting was obtained by using a short repetition time (TR) of 200 ms and using the shortest possible echo time (TE), namely 4.92 ms, in order to minimize the effect of T<sub>2</sub> relaxation.

### **3.2.7. Cytotoxicity and functionality within 3D models**

#### ***Preparation of hydrogel 3 D models***

Type I collagen was purified from rat tails and the final concentration was estimated by hydroxyproline titration, as previously described<sup>37</sup>. Tubes separately filled with collagen solution (2 mg/mL in 17 mM acetic acid), whole cell culture medium, and 0.1 M NaOH were kept in ice bathes for 1 h before preparation to slow down the gelling kinetics of collagen. Firstly, 500 μL of collagen solution and 400 μL of culture medium were added to a 1.5 mL tube and vortexed vigorously. After addition of 30 μL of 0.1 M NaOH and strong vortexing, 125 μL of the NHDF or HeLa cell suspension at a density of 10<sup>6</sup> cells/mL was added and mixed homogeneously. Then 0.9 mL was sampled from the mixture and deposited into a 24-well plate. The plate was then incubated at room temperature for 10 min for complete gelling of collagen.

#### ***Cytotoxicity and functionality***

Two sets of experiments were designed<sup>41</sup>. In a first approach, selected particles were introduced in the cell suspension prior to their addition to the collagen solution, at a final concentration of  $100\ \mu\text{g mL}^{-1}$ . Then collagen gels were formed by pH increase to 7. After 48 h of incubation, the cell viability was assessed in the same way as for 2D tests except that 800  $\mu\text{L}$  water were first added to the collagen gel, left for 0.5 h at room temperature in order to extract the Alamar Blue solution trapped in the gel, and then collected for the absorbance measurements. Particle internalization was also studied in the same configuration. For this, after the 48 h incubation period, the gels were rinsed 3 times with PBS, and fixed with 4% paraformaldehyde overnight. Next, the fixed samples were dehydrated in ethanol and butanol, and incorporated in paraffin to be able to obtain 10  $\mu\text{m}$  histological sections with a manual microtome. Before observation, the as-obtained samples were immersed in toluene, ethanol, and then water for rehydration. The cell nuclei were stained with DAPI for 10 min and rinsed with PBS before observation. The second approach consisted in adding 1.0 mL of a 0.2 mg/mL suspension of the HMSNs@MnO<sub>2</sub>(DOX)/apt particles onto the surface of particle-free cellularized collagen gels. After 3 hours of contact, the MR imaging experiments were performed as described above.

### 3.2.8. Statistical Analysis

Graphical results are presented as mean  $\pm$  SD (standard deviation). Statistical significance was assessed using the student's-test compared with control groups. The level of significance in all statistical analyses was set at a probability of  $P < 0.05$ .

## 3.3. Results and discussion

### 3.3.1 Preparation and characterization of the nanoplateforms

The HMSN@MnO<sub>2</sub>/apt nanoparticles were prepared according to the process depicted in **Figure 3-1**. In brief, monodisperse solid SiO<sub>2</sub> nanoparticles (sSiO<sub>2</sub>) were prepared using a modified Stöber method. They were then coated with a CTAB/SiO<sub>2</sub> shell via base-catalyzed hydrolysis of TEOS and condensation of silica onto the surface of CTAB pre-coated sSiO<sub>2</sub>. The resulting particles were simultaneously treated with Na<sub>2</sub>CO<sub>3</sub> to remove sSiO<sub>2</sub>, and NH<sub>4</sub>NO<sub>3</sub> to remove CTAB, resulting in HMSNs with hollow cores and penetrating pore channels.<sup>44</sup> APTES was grafted on the surface of nanoparticles to get HMSN-NH<sub>2</sub>. Finally, ultrathin MnO<sub>2</sub> nanosheets were formed onto the surface of HMSN-NH<sub>2</sub> thanks to the reaction with MES and KMnO<sub>4</sub> to obtain HMSN@MnO<sub>2</sub>. DOX was then loaded inside or on the surface of the

nanoparticles by the impregnation. To end, AS1411 aptamers were attached on the surface of  $\text{MnO}_2$  nanosheets thanks to  $\pi$ - $\pi$  interaction.

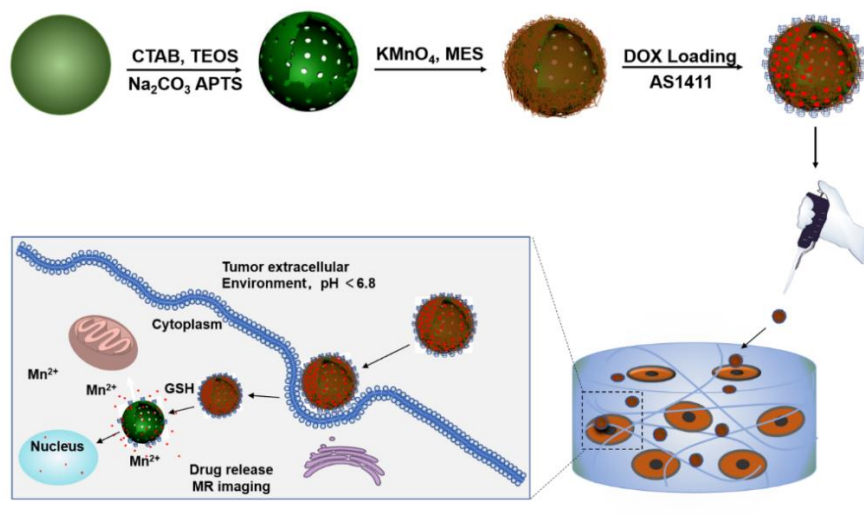


**Figure 3-1** Schematic illustration of the preparation of HMSN@ $\text{MnO}_2(\text{DOX})/\text{apt}$  and the drug release mechanism

As shown in the TEM image of **Figure 3-2**, the prepared hollow mesoporous HMSN nanoparticles exhibit a uniform diameter of  $\sim 140$  nm and form a colorless well-dispersed suspension in deionized water (DI). The diameter measured by DLS,  $D_m$ , is about 200 nm in DI, which is slightly larger than the TEM data and may reflect some aggregation.

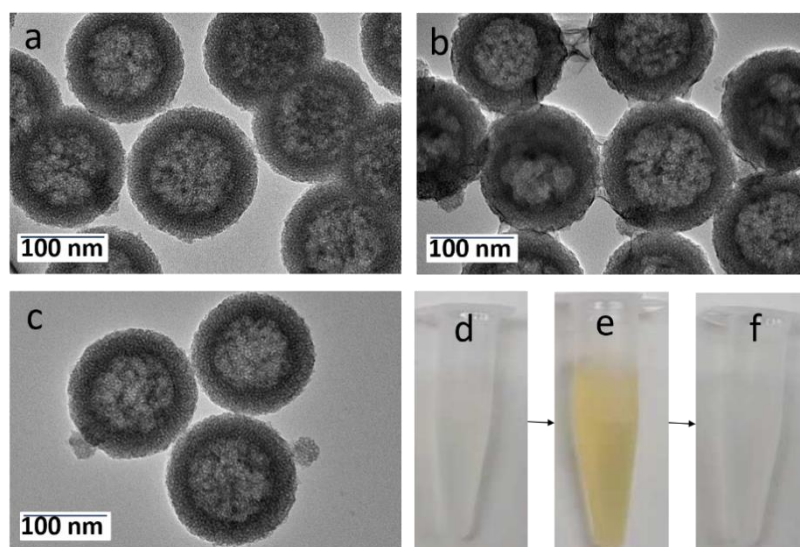


**Figure 3-2** TEM images of (a) HMSNs, (b) HMSN@ $\text{MnO}_2/\text{apt}$ , (c) HMSN@ $\text{MnO}_2/\text{apt}$  after GSH treatment and the corresponding digital images from left to right (d, e, f)

The contrast between shell and core of the silica nanospheres confirms their hollow structure. The shell of the HMSN with a thickness of  $\sim 25$  nm displays an obvious mesoporous silica

structure generated by the removal of pore templates. In DI water, the obtained HMSNs exhibited a negative zeta potential  $\zeta$  of -18.4 mV, as expected for silica surfaces (**Table 3-1**).

**Table 3-1** Mean diameter  $D_m$  from DLS with corresponding polydispersity index (PDI) and Zeta potential  $\zeta$  in deionized water

Sample	$D_m$ DLS (nm)	PDI	$\zeta$ (mV)
HMSNs	$200 \pm 18$	0.254	$-18.4 \pm 0.5$
HMSNs-NH <sub>2</sub>	$256 \pm 27$	0.317	$+10.4 \pm 0.3$
HMSNs@MnO <sub>2</sub>	$319 \pm 41$	0.579	$-15.4 \pm 0.2$
HMSNs@MnO <sub>2</sub> (DOX)	$316 \pm 26$	0.500	$-7.3 \pm 0.8$
HMSNs@MnO <sub>2</sub> (DOX)/apt	$248 \pm 15$	0.279	$-16.1 \pm 0.3$

The N<sub>2</sub> adsorption-desorption isotherm of the HMSN showed a type IV curve quite typical of surfactant-assisted mesoporous silica with a double, strong, and sharp adsorption step at intermediate relative partial pressure values around 0.4 (**Figure 3-3a**). This feature is associated with the nitrogen condensation inside the mesopores by capillarity. The application of the Brunauer-Emmett-Teller (BET) model resulted in a high value for the specific surface of 840 m<sup>2</sup> g<sup>-1</sup>. In parallel, the Barrett-Joyner-Halenda (BJH) model applied on the adsorption branch of the isotherms led to an average pore diameter of 3.89 nm (**Figure 3-3b**).

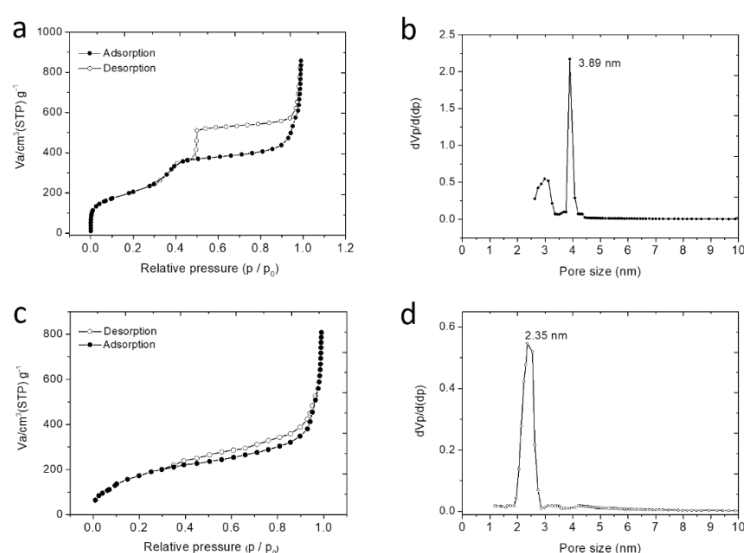


**Figure 3-3** (a, c) N<sub>2</sub> adsorption-desorption isotherm at 77 K and (b,d) the corresponding pore diameter distribution obtained by the BJH method on the adsorption branch for (a,b) HMSNs and (c,d) HMSNs@MnO<sub>2</sub>

The successful surface functionalization of silica nanoparticles using APTES could be checked by the increase of the zeta potential that reached a positive value (+10.4 mV) (**Table 3-1**). Upon contact with MES and  $\text{KMnO}_4$ , a visual color change from white to brown was observed (**Figure 3-2e**). After extensive washing, UV-vis spectra clearly evidenced a strong absorption at 400 nm, that can be attributed to the  $\text{MnO}_2$  nanosheets, whose intensity increase with the initial  $\text{KMnO}_4$  concentration (**Figure 3-4a**). The formation of composite nanoparticles ( $\text{HMSN@MnO}_2$ ) with a rough capping layer was confirmed by TEM images (**Figure 3-2b**). Moreover, the average diameter of  $\text{HMSN@MnO}_2$  was changed from 200 nm to *ca.* 320 nm, accompanied by a PDI change from 0.254 to 0.579, which suggests that the  $\text{MnO}_2$  coating induces a slight tendency for the particles to aggregate. The zeta potential of nanoparticles was also modified, from +10.4 mV down to -15.4 mV after functionalization, in agreement with values in the literature<sup>46</sup>. Sorption isotherms also confirmed the coating of the nanoparticles.  $\text{HMSN@MnO}_2$  presented flat sorption curves when compared to those of HMSN (at  $P/P_0 = 0.4$ ) (**Figure 3-3a**), thus indicating a significant pore blocking. Nonetheless,  $\text{HMSN@MnO}_2$  showed an additional inflection at  $P/P_0 > 0.8$ , that can correspond to secondary macropores resulting from the  $\text{MnO}_2$  capping layer with rough surface. A weak peak at pore diameter of 2.35 nm was also obtained, confirming the partial pore blocking effect of the  $\text{MnO}_2$  layer. Finally, when  $\text{HMSN@MnO}_2$  were put in contact with GSH (10 mM), the color of the suspension changed back from brown to white, indicative of the disappearance of the  $\text{MnO}_2$  layer (**Figure 3-2f**). TEM images clearly confirmed the regeneration of the smooth surface and clear mesoporous structure of HMSN (**Figure 3-2c**).

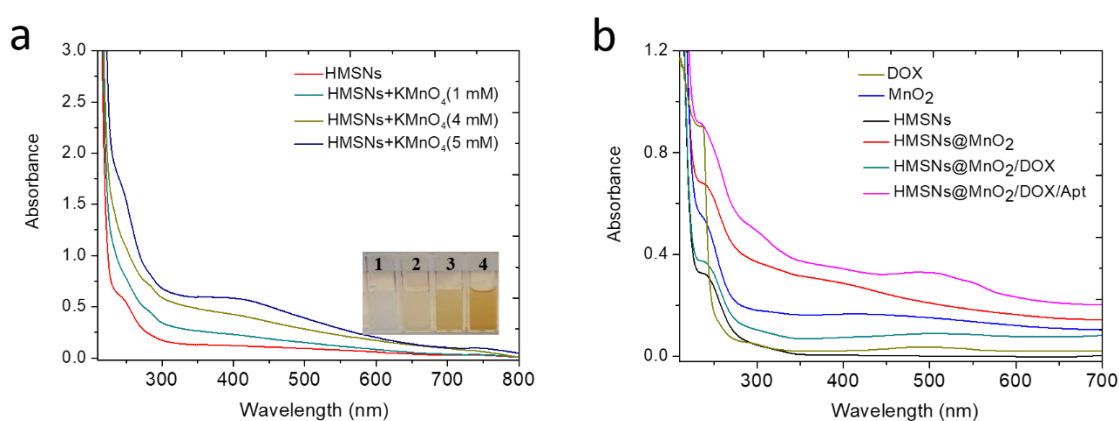


**Figure 3-4** Absorbance spectra of the HMSNs after addition of  $\text{KMnO}_4$  with different concentrations and the corresponding insert images with color change. (b) Absorbance spectra of the DOX,  $\text{MnO}_2$ , and a series of nanoparticles

Doxorubicin (DOX) was then selected as a guest molecule to confer anticancer properties to the nanoparticles. The loading was performed by a simple impregnation route in a mixed aqueous/organic medium. The resulting DOX-loaded HMSN@MnO<sub>2</sub> particles had a size distribution similar to unloaded particles but the zeta potential changed from -15.4 mV to -7.3 mV, suggesting that at least part of the drug is adsorbed on the MnO<sub>2</sub> coating. The UV-vis spectra of the loaded particles showed an additional absorption band at ca. 480 nm similar to the one of DOX (**Figure 3-4b**). The DOX loading of HMSN@MnO<sub>2</sub>, as estimated by fluorescent emission measurements of the supernatant after impregnation, reached ca. 80 µg.mg<sup>-1</sup>. As a final step, the anti-nucleolin AS1411 was adsorbed on the HMSNs@MnO<sub>2</sub>(DOX) particles which resulted in a significant decrease in the average particle diameter and of the PDI (**Table 3-1**). This can be correlated with the more negative value of the zeta potential (from -7.6 mV without aptamer to -16.1 mV after AS1411 adsorption), that results in an enhanced particle colloidal stability thanks to additional electrostatic repulsion.

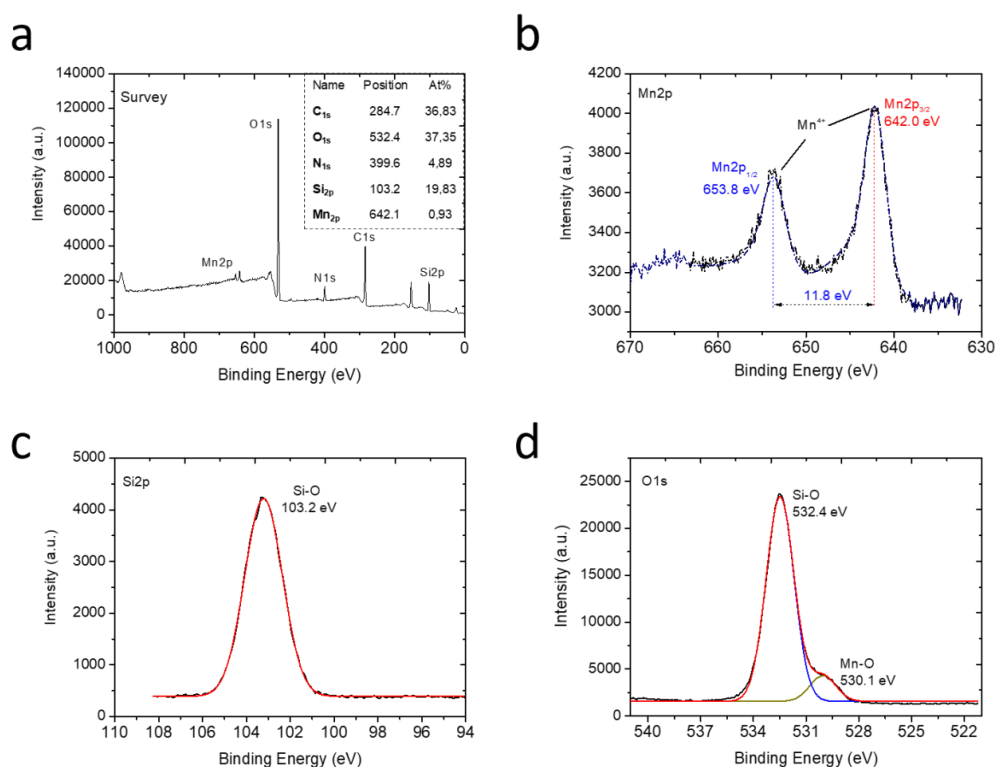


**Figure 3-5** XPS analysis of the HMSNs@MnO<sub>2</sub>(DOX)/apt nanoparticles: (a) full XPS spectrum with atomic analysis and deconvoluted signals with proposed attributions at the (b) Mn2p, (c) Si2p and (d) O1s levels

To characterize the chemical compositions of the final HMSNs@MnO<sub>2</sub>(DOX)/apt nanoparticles, their element composition was determined by XPS (**Figure 3-5a**). Mn, Si, C, O



and N peaks were observed. Indeed, considering that the analysis depth of XPS analysis is 10 nm at maximum, it only probes the outer surface of the particles. It is therefore not surprising that the content of Si is rather low (19.8 %), corresponding to ca. 40 wt% of SiO<sub>2</sub>. In contrast, the contribution of Mn (0.9 wt %) and of organic molecules (DOX and AS1411) (> 35 % C) is enhanced compared to the whole particle volume.

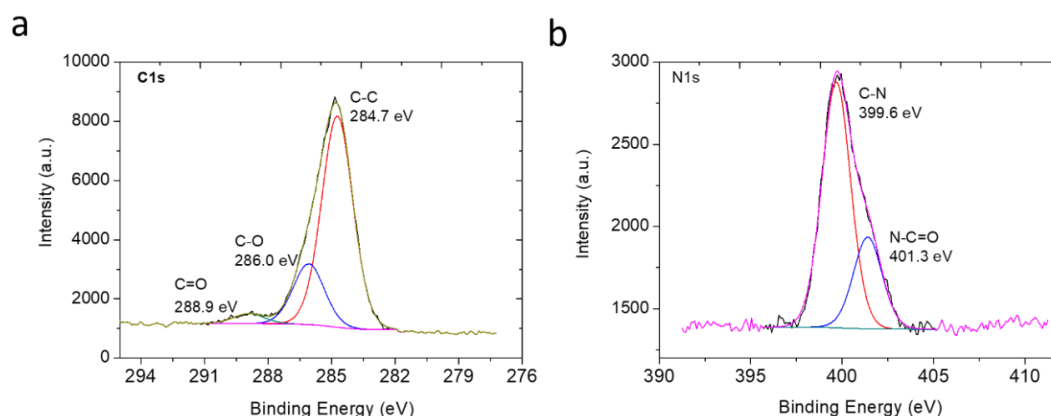


**Figure 3-6** Deconvoluted XPS spectra of (a) C1s, (b) N1s for HMSNs@MnO<sub>2</sub>(DOX)/apt

At the Mn2p level (**Figure 3-5b**), the two peaks at 642 eV and 653.8 eV unambiguously sign for the presence of MnO<sub>2</sub>, as also confirmed by the peak at 530.1 eV on the O1s spectrum<sup>47</sup> (**Figure 3-5d**). The peaks at 103.2 eV on the Si2p spectrum (**Figure 3-5c**) and 532.4 eV on the O1s spectrum are characteristic of hydrated silica<sup>48</sup>. Additionally, deconvoluted spectra at the C1s and N1s levels evidenced the presence of C-C, C-O, C=O, C-N and N-C=O groups (**Figure 3-6**). The latter indicates the presence of the aptamer on the particle surface<sup>49</sup>, while the others can belong to both AS1411 and DOX.

### 3.3.2 Drug release and MRI imaging properties of the nanoplatforms.

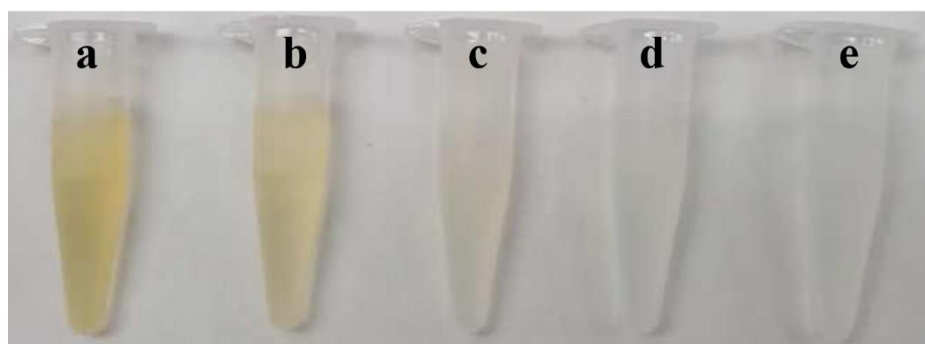


**Figure 3-7** Images of HMSNs@MnO<sub>2</sub>/apt suspensions in different conditions, (a) pH 7.4; (b) pH 5.5; (c) pH 7.4, 5mM GSH; (d) pH 7.4, 10mM GSH; (e) pH 5.5, 5mM GSH

The feasibility of  $\text{MnO}_2$  degradation when treated with GSH and pH was first investigated. As shown in the **Figure 3-7**, the  $\text{HMSNs@MnO}_2/\text{apt}$  nanoplateforms were stable at neutral pH, but after interaction with GSH, the color of the system quickly changed from brown to colorless, with a more pronounced effect when GSH concentration was increased from 5 mM to 10 mM. Acidic pH slightly destabilized the nanoplateform, due to the intrinsic instability of  $\text{MnO}_2$  in these conditions, as well as enhanced the effect of GSH. These observations were quantitatively assessed by monitoring DOX release in different conditions (**Figure 3-8**). In the absence of GSH, the DOX release was less than 10 % over 50 h at pH 7.4. When the  $\text{MnO}_2$  coating was destabilized, either in acidic conditions or by addition of GSH at neutral pH, ca. 20 % of the DOX content was released within 10 h and then a slower release, up to ca. 35-40 %, occurred in the next 40 h. When GSH was added in acidic conditions, the shape of the release curve was quite similar (i.e. fast release during 10 h followed by slower release) but the amount of released DOX at the end of the first phase was much higher (ca. 50 %) than in the two previous conditions and the total release after 50 h was larger than 60 %.

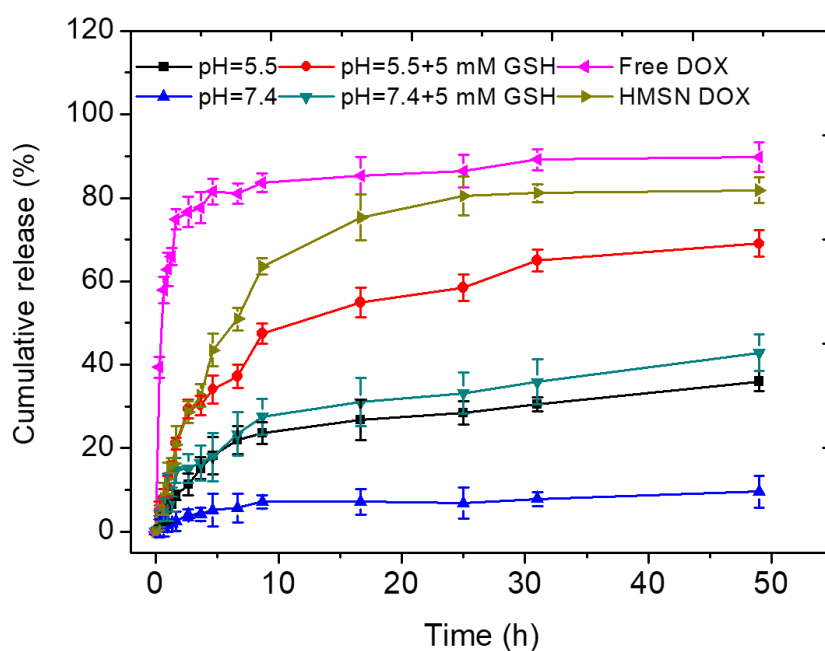


**Figure 3-8** Cumulative release of the  $\text{HMSNs@MnO}_2(\text{DOX})/\text{apt}$  in different conditions: (blue) pH 7.4, (black) pH 5.5, (green) pH 7.4+ 5 mM GSH, (red) pH 5.5 + 5 mM GSH. Control samples: (pink) free DOX and (pale green) uncoated HSMNs(DOX) in PBS solution (pH =7.4)

As pointed out earlier, DOX molecules may be located on the  $\text{MnO}_2$  surface, inside the porous silica shell and within the particle empty core. Assuming that the GSH-free neutral pH conditions induce no significant dissolution of the  $\text{MnO}_2$  nanosheets, then the measured low

release (less than 10 % of the initial dose) should correspond to surface-adsorbed DOX molecules. Upon GSH addition or acidification, much more DOX molecules are released following a two-step process.

It is worth emphasizing that silica nanoparticles are less soluble in acidic than in neutral pH conditions and not sensitive to GSH unless specifically modified<sup>50</sup>. Thus it can be suggested that the first step corresponds to the release of DOX molecules both adsorbed on the surface and trapped in the porous shell due to the MnO<sub>2</sub> coating dissolution, while the second one would sign for the slow diffusion of the drug located within the particles. However, when both acidic conditions and GSH addition are combined, the overall release profile, and especially the duration of the fast-release period, is not significantly modified but more DOX is initially released. This may be interpreted considering that, in these conditions, the MnO<sub>2</sub> degradation is efficient enough to unclog all pores before diffusion of DOX molecules from the inside of the particle starts. In contrast, in GSH-only or acidic pH-only conditions, the MnO<sub>2</sub> degradation process is less efficient and only part of the pores is unclogged before diffusion from the inside compartment becomes effective.

Because the reduction of MnO<sub>2</sub> by intracellular GSH could produce a large amount of Mn<sup>2+</sup>, which are efficient T<sub>1</sub> contrast agents, the nanoplatform could also afford GSH/pH-activated detection by MRI. To verify this hypothesis, T<sub>1</sub>-weighted MR images of HMSN@MnO<sub>2</sub>/apt aqueous suspensions under different conditions were first performed. As shown in Figure 3-9a, the MRI signal of the HMSN@MnO<sub>2</sub>/apt sample in PBS at pH 7.4 didn't exhibit an obvious T<sub>1</sub>-MRI signal difference compared to that of deionized water. A significant T<sub>1</sub>-MRI signal enhancement could be observed at pH 5.5. Adding 5 mM GSH in neutral and then acidic conditions further improved the T<sub>1</sub>-MRI signal intensity. The r<sub>1</sub> relaxivity of the nanoplatform suspensions was also measured (**Figure 3-9b**) for HMSN@MnO<sub>2</sub>/apt at pH 5.5 in the presence of GSH, reaching a value of 9.25 mM<sup>-1</sup> s<sup>-1</sup> which is remarkably higher than that of the GSH-free solution at pH 7.4 (r<sub>1</sub> = 1.68 mM<sup>-1</sup> s<sup>-1</sup>). Importantly such r<sub>1</sub> values are higher than those reported for other Mn-based nanocontrast agents (Mn<sub>3</sub>O<sub>4</sub> nanoparticles, 8.26 mM<sup>-1</sup> s<sup>-1</sup>; Mn-MSNs, 2.28 mM<sup>-1</sup> s<sup>-1</sup> and MnO nanoplates, 5.5 mM<sup>-1</sup> s<sup>-1</sup>)<sup>51-53</sup>. The above results suggest that the MnO<sub>2</sub> nanosheets can efficiently be converted into Mn<sup>2+</sup> in a mildly acidic/GSH environment, explaining the rapid enhancement of the longitudinal relaxation rate with concentration. In conclusion, HMSNs@MnO<sub>2</sub>/apt present a clear pH/GSH-responsive T<sub>1</sub>-MRI performance.

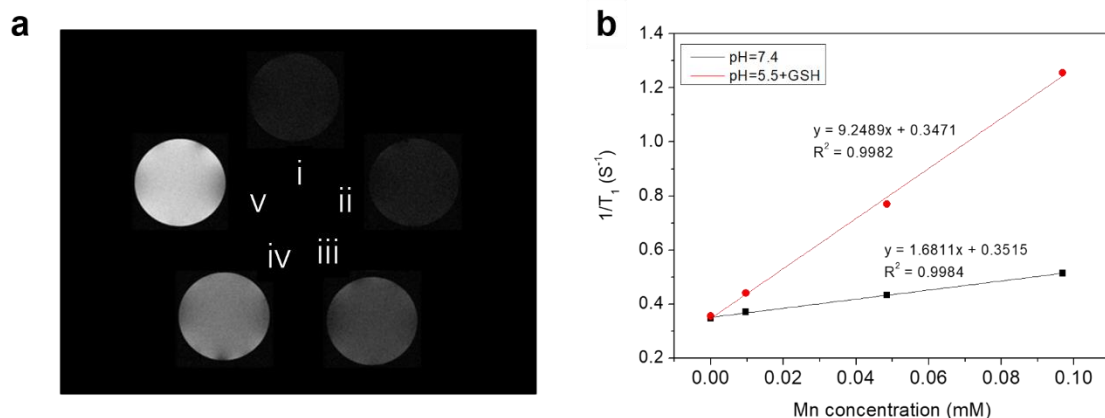


**Figure 3-9** T1-weighted MR images of HMSN@MnO<sub>2</sub>/apt under different conditions. (i: H<sub>2</sub>O; 2: pH 7.4; 3: pH 5.5; iv: pH 7.4 + GSH 5 mM and v: pH5.5 + GSH 5 mM). (b)  $1/T_1$  versus Mn concentrations for HMSN@MnO<sub>2</sub>/apt at (black) pH 7.4 and (red) pH 5.5 + 5 mM GSH

In a second step, it was necessary to check that the designed nanoplateforms could efficiently kill cancer cells while being safe for normal cells. Firstly, the impact of HMSNs@MnO<sub>2</sub>(DOX) and HMSNs@MnO<sub>2</sub>(DOX)/apt particles on HeLa cells viability after 24 h of contact was studied using the Alamar blue test and compared to free DOX.

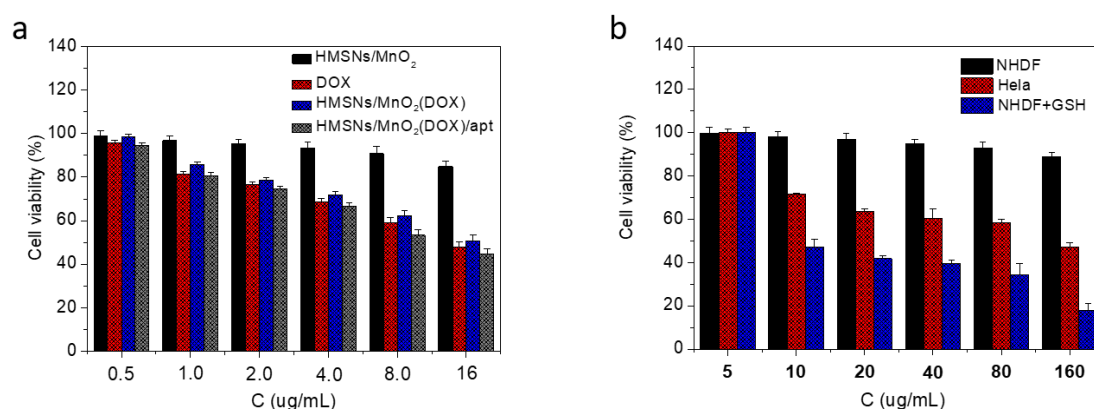


**Figure 3-10** (a) HeLa cell viability after incubation with DOX, HMSNs@MnO<sub>2</sub>, HMSNs@MnO<sub>2</sub>(DOX) and HMSNs@MnO<sub>2</sub>(DOX)/apt for 24 h as a function of DOX dose. (b) Cell cytotoxicity of HMSNs@MnO<sub>2</sub>(DOX)/apt after 24 h of incubation with NHDF, HeLa and NHDF cells treated with GSH as a function of particle concentration

The concentrations indicated on **Figure 3-10a** correspond to DOX, either free or within the particles. No difference in performance between free and encapsulated drug could be observed, with a continuous decrease of HeLa cells activity with increasing DOX dose down to ca. 50 % for the highest investigated dose (16 μg/mL). The presence of the aptamer had no influence either. Control experiments performed with DOX-free HMSNs@MnO<sub>2</sub> in the same particle

amount as for HMSNs@MnO<sub>2</sub>(DOX) showed negligible cytotoxicity. In a second step, the effect of HMSNs@MnO<sub>2</sub>(DOX)/apt particles on HeLa and NHDF cells was monitored. In this case, the dose is presented in particle concentration (**Figure 3-10b**). In the 5-160  $\mu\text{g mL}^{-1}$  range, HMSNs@MnO<sub>2</sub>(DOX)/apt particles have no obvious impact on NHDF while they are toxic for HeLa cells (i.e. viability below 80 %) for particle concentrations of 10  $\mu\text{g mL}^{-1}$  or more. Importantly, if GSH (5 mM) was present in the NHDF culture medium, then high cytotoxicity was also measured, confirming its ability to trigger DOX release.

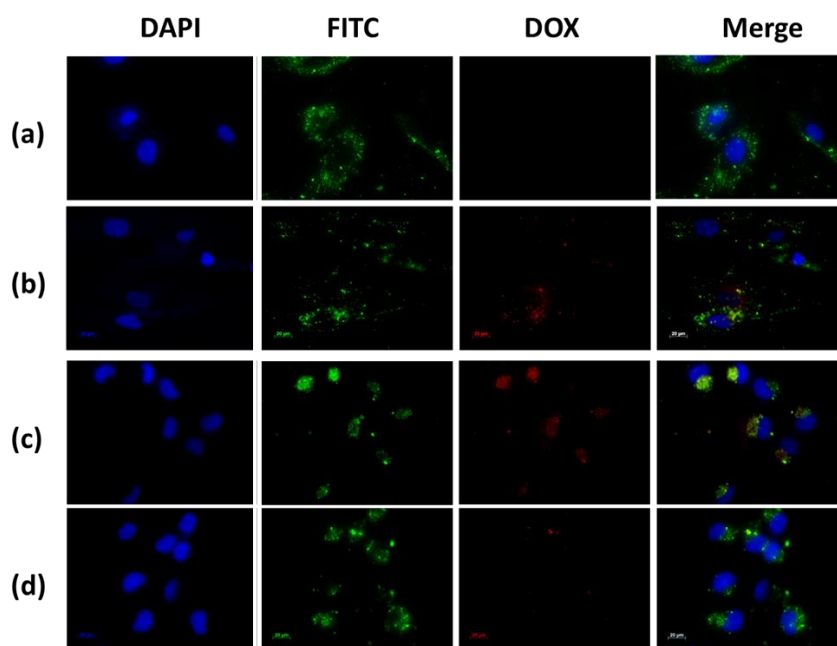


**Figure 3-11** Fluorescent images of (a) NHDF cells incubated with HMSNs@MnO<sub>2</sub>(DOX)/apt nanoparticles, (b) NHDF cells incubated with HMSNs@MnO<sub>2</sub>(DOX)/apt nanoparticles and 5 mM GSH, (c) HeLa cells incubated with HMSNs@MnO<sub>2</sub>(DOX)/apt nanoparticles, (d) HeLa cells incubate

To confirm this hypothesis, the internalization of the HMSNs@MnO<sub>2</sub>(DOX)/apt was studied. As shown in **Figure 3-11a-d**, accumulation of the nanoplateforms, visualized by the green fluorescence of encapsulated FITC, in contact or within the cells could be observed for NHDF, without or with GSH, and HeLa cells. In the latter case, bright green aggregates are located near the nuclei, which appear blue after DAPI staining, strongly supporting their intracellular localization. For this sample, colocalization of the nanoplateform (green signal) and the DOX molecules (red signal) is evidenced. Noticeably, when no aptamer was present on the surface, low particle accumulation was observed and no clear red signal could be imaged (**Figure 3-11d**). For NHDF cells without GSH, the red areas are hardly seen whereas they are more clearly visible/detectable when GSH was present. It is important to point out that MnO<sub>2</sub> nanosheets

have previously been shown to efficiently quench the fluorescence of dyes in the UV-visible range<sup>54</sup>. Thus the observation of red signals on the fluorescence images indicates that DOX is no longer interacting with the manganese oxide coating, probably because the MnO<sub>2</sub> nanosheets were reduced to Mn<sup>2+</sup> by GSH. Noticeably, in the case of HMSNs@MnO<sub>2</sub>(DOX)/apt interacting with HeLa, the strong co-localization of FITC and DOX inside the cells would suggest that the MnO<sub>2</sub> layer has been degraded but that part of the drug remains inside the particles (**Fig 3-11c**). In sharp contrast, for HMSNs@MnO<sub>2</sub>(DOX)/apt interacting with NHDF in the presence of GSH, many particles visualized by monitoring the green fluorescence do not exhibit a red fluorescence (**Fig 3-11b**). This can be attributed to the fact that the MnO<sub>2</sub> layer is degraded by GSH leading to DOX release before the internalization process.

Altogether, HMSNs@MnO<sub>2</sub>(DOX)/apt nanoplateforms have the ability to be internalized by HeLa cells with a clear benefit of the presence of the targeting aptamer on the efficiency of this process. After degradation of the MnO<sub>2</sub> coating, that may be due to both acidic pH of the lysosome and enhanced GSH expression, the particles can thereby release DOX molecules at the vicinity of the nucleus, resulting in an efficient cancer cell killing. At the same time, the formation of Mn<sup>2+</sup> ions should allow for the detection of the cancer tissue via T<sub>1</sub>-weighted MRI. Very importantly, our experiments also indicate that these nanoplateforms are safe for normal NHDF cells in the absence of GSH.

### 3.3.3 Functionality of nanoplateforms in 3D biomimetic collagen matrices

At this stage of similar studies, *in vivo* evaluations are usually undertaken using tumor-bearing animals. However, in this work, we chose instead to go deeper into the understanding of the impact of a 3D environment on the functionality of the nanoplateform, a point that was not previously assessed in the literature. For this we prepared type I collagen matrices in conditions compatible with cell immobilization and particle encapsulation or diffusion<sup>40, 41</sup>.

To check whether the nanoparticles preserved their efficiency and selectivity as cancer cell killing agents, the viability of NHDF and HeLa cells co-encapsulated with HMSNs@MnO<sub>2</sub>, HMSNs@MnO<sub>2</sub>(DOX), and HMSNs@MnO<sub>2</sub>(DOX)/apt at a dose of 100 µg/mL within the collagen matrices was studied (**Figure 3-12a**).

After 24 h, compared to the control group, the unloaded HMSNs@MnO<sub>2</sub>/apt showed very little toxicity for both types of cells. After DOX-loading, the HMSNs@MnO<sub>2</sub>(DOX)/apt nanoparticles neither showed much effect the viability of NHDF cells but exhibited a clear cytotoxic effect on HeLa cells, that was independent of the presence of the aptamer on the

surface. Importantly, the decrease of HeLa cell viability was more significant than in the 2D experiments (see Figure 3-10b above), suggesting that the confinement of the cells and particles within the matrices strongly favors their interaction. As a matter of fact, SEM imaging allowed for the observation of nanoparticle aggregates at the close vicinity of the HeLa cells (Figure 3-12b). In such conditions, our results suggest that it may be no longer necessary to specifically target the cells by using the AS1411 aptamer.

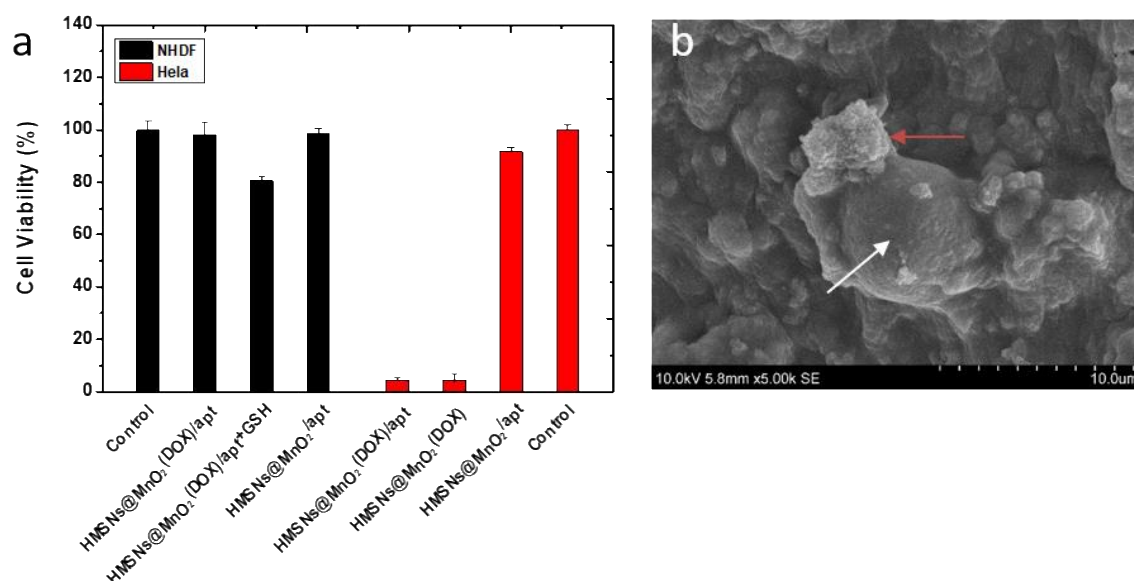


**Figure 3-12** (a) Viability of NHDF and HeLa cells within different types of 3D collagen/silica nanocomposites after 24 h of incubation. (b) SEM image of nanoparticles (red arrow) interacting with HeLa cells (white arrow) within collagen hydrogels

Fluorescence imaging of the encapsulated HeLa cells also evidenced the co-localization of DOX with the nuclei-staining DAPI, signing for their successful internalization (**Figure 3-13**). However red fluorescence signals could also be visualized outside the cells, suggesting that some MnO<sub>2</sub> degradation also occurred outside the cells.



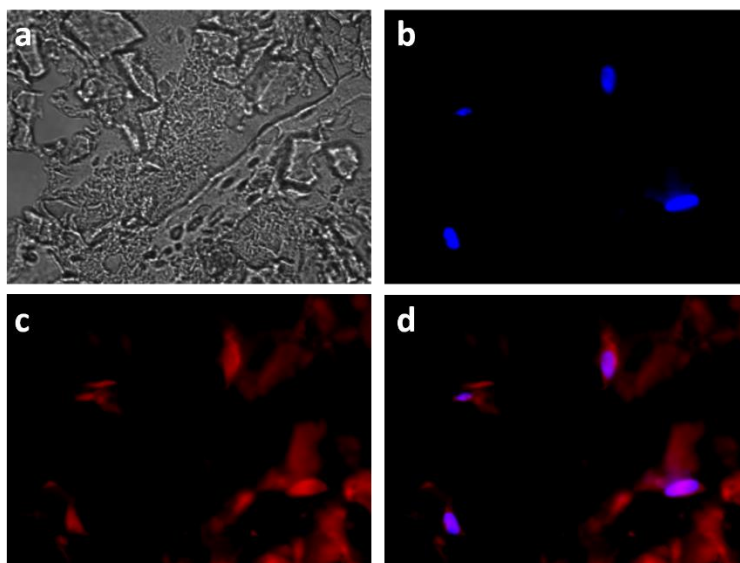


**Figure 3-13** Fluorescent images of HeLa cells incubated with HMSNs@MnO<sub>2</sub>(DOX)/apt within a collagen hydrogel for 24 h, (a) bright field; (b) blue channel (DAPI); (c) red channel (DOX) and (d) merge

Finally, to evaluate whether such an ultrasensitive GSH-responsive is suitable for *in vivo* tumor imaging by magnetic resonance, another configuration was used where selected nanoparticles were placed onto cellularized collagen hydrogels and left to diffuse for 3 h.

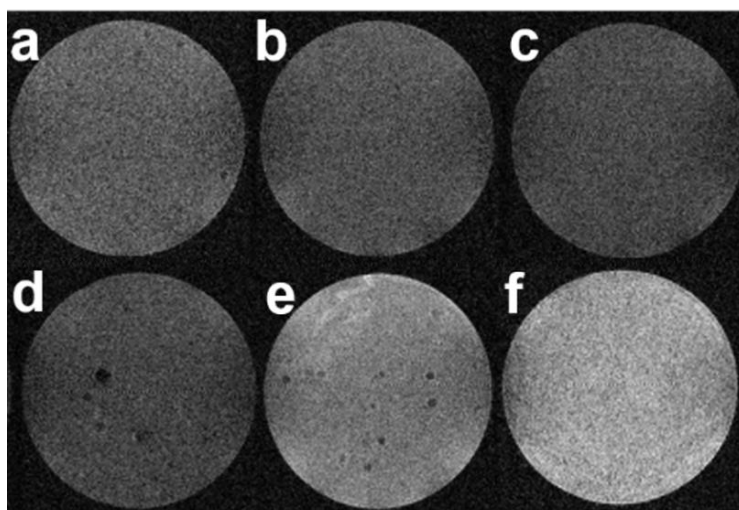


**Figure 3-14** T1-weighted MR images of collagen gels (a) without cells, (b,c) with NHDF cells and (d-f) with HeLa cells after 3h diffusion of (b,d) 0.2 mg/mL HMSNs@MnO<sub>2</sub>(DOX) (c,e) 0.2 mg/mL HMSNs@MnO<sub>2</sub>(DOX)/apt and (f) 0.4 mg/mL HMSNs@MnO<sub>2</sub>(DOX)/apt.

As shown in **Figure 3-14**, a weak MRI signal was obtained for all samples prepared in the absence of HeLa cells or in the presence of NHDF cells, in agreement with the fluorescence



image in Figure 3-13 that suggested partial destabilization of the nanoplateforms in contact with the collagen network. While comparable results were obtained when the aptamer-free particles were added to HeLa cells, HMSNs@MnO<sub>2</sub>(DOX)/apt particles led to a significant enhancement of the intensity of T<sub>1</sub>-weighted images, that was increased when the initial particle concentration was increased. These results clearly demonstrate that the functionality and specificity of the HMSNs@MnO<sub>2</sub>(DOX)/apt nanoplateforms is preserved within the 3D models.

Interestingly, in this configuration, particles are not initially confined at the proximity of the cells but must find their way through the collagen network and bind to HeLa cells. This explains why, in contrast to the previous system, the presence of the aptamer does have a significant beneficial effect on the MRI signal. In these 3D models, determination of the  $r_1$  value is difficult as it would require to determine the precise amount of particles that have diffused inside the matrices and interacted with the cells. However, when comparing Figure 3-9 and 3-13, it is quite clear that the T<sub>1</sub> relaxation time is lower in the matrix than in suspension and that the decreased stability of the nanoplateforms in the collagen gels ultimately impacts on its contrasting efficacy, i.e. its ability to differentiate safe and tumor tissues.

### 3.4 Conclusion

In this work, we were able to synthesize and fully characterize well-defined multi-functional nanoparticles combining several complementary properties that fit with the requirements of theranostic systems for cancer treatment<sup>12</sup>. Indeed many other similar or closely-related systems have been described in the literature, to which our particles must be compared<sup>1-3</sup>. The main advantages of our strategy is the use of MnO<sub>2</sub> as both a gating system and source of MRI-active species that makes our system simpler to prepare, especially compared to many other examples where complex modifications of the silica particles with stimuli-responsive organic molecules are described<sup>55</sup>. This coating also allows for the direct conjugation of the targeting aptamer without any additional surface modification. This is indeed of deep interest because an increase in the number of synthetic steps not only impact cost but it is also usually correlated with a decrease in the batch-to-batch reproducibility of the resulting particles in terms of size and composition, complexifying scale-up processes. However, compared to other hollow silica-based nanosystems, our doxorubicin loading is quite moderate (8 w/w % compared to up to ca. 30 % in Liu group's work<sup>56</sup>). This is due to the fact that the MnO<sub>2</sub> coating is deposited before the loading step to avoid DOX degradation by KMnO<sub>4</sub>. We must also point out that certain MnO<sub>2</sub> nanoparticles have been shown to exhibit toxicity in rat models, although this study

involved a repeated oral exposure over *ca.* 1 month<sup>57</sup>. Therefore, only *in vivo* evaluation of our particles would allow to fully assess their full clinical potential.

However, there is currently an increasing growing consensus to limit animal tests and, consequently, a rapid development of new *in vitro* methods with a better ability to predict the *in vivo* behavior of pharmaceuticals<sup>58, 59</sup>. This is in fact one of the main motivations for the development of artificial tissues and organs. Indeed the collagen hydrogels we used in this study do reflect the chemical and structural complexity of *in vivo* environments. However they allowed us to get some insights on the influence of cells confinement in a 3D environment on the ability of our nanoparticles to interact with them. Based on the encouraging observations of the preserved functionality and specificity of our nanoplateforms, it is now necessary to improve our model hydrogel, including increasing collagen concentration as well as adding other components of the extracellular matrices such as other proteins of glycosaminoglycans.

Coming back to the objective of this PhD project, we have shown here the possibility to transfer the functionality of suspensions of silica-based nanoparticles from 2D cell culture liquid medium to cellularized 3D environments. In the rest of this manuscript, we will describe our studies of the mirror configuration, when silica particles are placed within a hydrogel, i.e. in a 3D environment, and cells cultured on their surface, i.e. in 2D.

## References

1. Xie, J.; Lee, S.; Chen, X., Nanoparticle-based theranostic agents. *Advanced drug delivery reviews* **2010**, 62, (11), 1064-1079.
2. Kelkar, S. S.; Reineke, T. M., Theranostics: combining imaging and therapy. *Bioconjugate chemistry* **2011**, 22, (10), 1879-1903.
3. Muthu, M. S.; Leong, D. T.; Mei, L.; Feng, S.-S., Nanotheranostics- application and further development of nanomedicine strategies for advanced theranostics. *Theranostics* **2014**, 4, (6), 660.
4. Han, L.; Zhang, X.-Y.; Wang, Y.-L.; Li, X.; Yang, X.-H.; Huang, M., et al. Wei, Y., Redox-responsive theranostic nanoplateforms based on inorganic nanomaterials. *Journal of Controlled Release* **2017**, 259, 40-52.
5. Otsuka, H.; Nagasaki, Y.; Kataoka, K., PEGylated nanoparticles for biological and pharmaceutical applications. *Advanced drug delivery reviews* **2012**, 64, 246-255.
6. Xiang, D.; Shigdar, S.; Qiao, G.; Wang, T.; Kouzani, A. Z.; Zhou, S.-F., et al. Duan, W., Nucleic acid aptamer-guided cancer therapeutics and diagnostics: the next generation of cancer medicine. *Theranostics* **2015**, 5, (1), 23.

7. Jiang, T.; Zhang, Z.; Zhang, Y.; Lv, H.; Zhou, J.; Li, C., et al. Zhang, Q., Dual-functional liposomes based on pH-responsive cell-penetrating peptide and hyaluronic acid for tumor-targeted anticancer drug delivery. *Biomaterials* **2012**, 33, (36), 9246-9258.
8. Dixit, S.; Novak, T.; Miller, K.; Zhu, Y.; Kenney, M. E.; Broome, A.-M., Transferrin receptor-targeted theranostic gold nanoparticles for photosensitizer delivery in brain tumors. *Nanoscale* **2015**, 7, (5), 1782-1790.
9. Mura, S.; Nicolas, J.; Couvreur, P., Stimuli-responsive nanocarriers for drug delivery. *Nature materials* **2013**, 12, (11), 991.
10. Cheng, R.; Meng, F.; Deng, C.; Klok, H.-A.; Zhong, Z., Dual and multi-stimuli responsive polymeric nanoparticles for programmed site-specific drug delivery. *Biomaterials* **2013**, 34, (14), 3647-3657.
11. Tarn, D.; Ashley, C. E.; Xue, M.; Carnes, E. C.; Zink, J. I.; Brinker, C. J., Mesoporous silica nanoparticle nanocarriers: biofunctionality and biocompatibility. *Accounts of chemical research* **2013**, 46, (3), 792-801.
12. Fan, Z.; Fu, P. P.; Yu, H.; Ray, P. C., Theranostic nanomedicine for cancer detection and treatment. *Journal of food and drug analysis* **2014**, 22, (1), 3-17.
13. Hu, X.; Liu, G.; Li, Y.; Wang, X.; Liu, S., Cell-penetrating hyperbranched polyprodrug amphiphiles for synergistic reductive milieu-triggered drug release and enhanced magnetic resonance signals. *Journal of the American Chemical Society* **2014**, 137, (1), 362-368.
14. Tang, F.; Li, L.; Chen, D., Mesoporous silica nanoparticles: synthesis, biocompatibility and drug delivery. *Advanced materials* **2012**, 24, (12), 1504-1534.
15. Kim, J.; Kim, H. S.; Lee, N.; Kim, T.; Kim, H.; Yu, T., et al. Hyeon, T., Multifunctional uniform nanoparticles composed of a magnetite nanocrystal core and a mesoporous silica shell for magnetic resonance and fluorescence imaging and for drug delivery. *Angewandte Chemie* **2008**, 120, (44), 8566-8569.
16. Chen, Y.; Chen, H.; Zeng, D.; Tian, Y.; Chen, F.; Feng, J.; Shi, J., Core/shell structured hollow mesoporous nanocapsules: a potential platform for simultaneous cell imaging and anticancer drug delivery. *ACS nano* **2010**, 4, (10), 6001-6013.
17. Zhu, Y.; Shi, J.; Shen, W.; Dong, X.; Feng, J.; Ruan, M.; Li, Y., Stimuli-responsive controlled drug release from a hollow mesoporous silica sphere/polyelectrolyte multilayer core-shell structure. *Angewandte Chemie* **2005**, 117, (32), 5213-5217.

18. Zhao, W.; Chen, H.; Li, Y.; Li, L.; Lang, M.; Shi, J., Uniform rattle-type hollow magnetic mesoporous spheres as drug delivery carriers and their sustained-release property. *Advanced Functional Materials* **2008**, 18, (18), 2780-2788.
19. Cheng, Y.-J.; Luo, G.-F.; Zhu, J.-Y.; Xu, X.-D.; Zeng, X.; Cheng, D.-B., et al. Zhuo, R.-X., Enzyme-induced and tumor-targeted drug delivery system based on multifunctional mesoporous silica nanoparticles. *ACS applied materials & interfaces* **2015**, 7, (17), 9078-9087.
20. Zhang, B.; Luo, Z.; Liu, J.; Ding, X.; Li, J.; Cai, K., Cytochrome c end-capped mesoporous silica nanoparticles as redox-responsive drug delivery vehicles for liver tumor-targeted triplex therapy in vitro and in vivo. *Journal of Controlled Release* **2014**, 192, 192-201.
21. Tang, Y.; Hu, H.; Zhang, M. G.; Song, J.; Nie, L.; Wang, S., et al. Chen, X., An aptamer-targeting photoresponsive drug delivery system using “off-on” graphene oxide wrapped mesoporous silica nanoparticles. *Nanoscale* **2015**, 7, (14), 6304-6310.
22. Huang, M.; Li, F.; Dong, F.; Zhang, Y. X.; Zhang, L. L., MnO<sub>2</sub>-based nanostructures for high-performance supercapacitors. *Journal of Materials Chemistry A* **2015**, 3, (43), 21380-21423.
23. Chen, Y.; Chen, H.; Zhang, S.; Chen, F.; Sun, S.; He, Q., et al. Zhang, L., Structure-property relationships in manganese oxide-mesoporous silica nanoparticles used for T1-weighted MRI and simultaneous anti-cancer drug delivery. *Biomaterials* **2012**, 33, (7), 2388-2398.
24. Zhang, M.; Xing, L.; Ke, H.; He, Y.-J.; Cui, P.-F.; Zhu, Y., et al. Chen, H., MnO<sub>2</sub>-Based Nanoplatfrom Serves as Drug Vehicle and MRI Contrast Agent for Cancer Theranostics. *ACS applied materials & interfaces* **2017**, 9, (13), 11337-11344.
25. Jin, L.; Liu, J.; Tang, Y.; Cao, L.; Zhang, T.; Yuan, Q., et al. Zhang, H., MnO<sub>2</sub>-Functionalized Co-P Nanocomposite: A New Theranostic Agent for pH-Triggered T1/T2 Dual-Modality Magnetic Resonance Imaging-Guided Chemo-photothermal Synergistic Therapy. *ACS applied materials & interfaces* **2017**, 9, (48), 41648-41658.
26. Zhang, X.-L.; Zheng, C.; Guo, S.-S.; Li, J.; Yang, H.-H.; Chen, G., Turn-on fluorescence sensor for intracellular imaging of glutathione using g-C<sub>3</sub>N<sub>4</sub> nanosheet-MnO<sub>2</sub> sandwich nanocomposite. *Analytical chemistry* **2014**, 86, (7), 3426-3434.

27. Liu, J.; Meng, L.; Fei, Z.; Dyson, P. J.; Jing, X.; Liu, X., MnO<sub>2</sub> nanosheets as an artificial enzyme to mimic oxidase for rapid and sensitive detection of glutathione. *Biosensors and Bioelectronics* **2017**, 90, 69-74.
28. Zhao, Z.; Fan, H.; Zhou, G.; Bai, H.; Liang, H.; Wang, R., et al. Tan, W., Activatable fluorescence/MRI bimodal platform for tumor cell imaging via MnO<sub>2</sub> nanosheet–aptamer nanoprobe. *Journal of the American Chemical Society* **2014**, 136, (32), 11220-11223.
29. Wu, G.; Fang, Y.-Z.; Yang, S.; Lupton, J. R.; Turner, N. D., Glutathione metabolism and its implications for health. *The Journal of nutrition* **2004**, 134, (3), 489-492.
30. Meng, F.; Cheng, R.; Deng, C.; Zhong, Z., Intracellular drug release nanosystems. *Materials today* **2012**, 15, (10), 436-442.
31. Gerweck, L. E.; Seetharaman, K., Cellular pH gradient in tumor versus normal tissue: potential exploitation for the treatment of cancer. *Cancer research* **1996**, 56, (6), 1194-1198.
32. Yang, X.; He, D.; He, X.; Wang, K.; Zou, Z.; Li, X., et al. Yang, X., Glutathione-Mediated Degradation of Surface-Capped MnO<sub>2</sub> for Drug Release from Mesoporous Silica Nanoparticles to Cancer Cells. *Particle & Particle Systems Characterization* **2015**, 32, (2), 205-212.
33. Li, X.; Zhao, W.; Liu, X.; Chen, K.; Zhu, S.; Shi, P., et al. Shi, J., Mesoporous manganese silicate coated silica nanoparticles as multi-stimuli-responsive T<sub>1</sub>-MRI contrast agents and drug delivery carriers. *Acta biomaterialia* **2016**, 30, 378-387.
34. Bertrand, N.; Wu, J.; Xu, X.; Kamaly, N.; Farokhzad, O. C., Cancer nanotechnology: the impact of passive and active targeting in the era of modern cancer biology. *Advanced drug delivery reviews* **2014**, 66, 2-25.
35. Edmondson, R.; Broglie, J. J.; Adcock, A. F.; Yang, L., Three-dimensional cell culture systems and their applications in drug discovery and cell-based biosensors. *Assay and drug development technologies* **2014**, 12, (4), 207-218.
36. Huang, H.; Zhang, P.; Chen, H.; Ji, L.; Chao, H., Comparison between polypyridyl and cyclometalated ruthenium (II) complexes: anticancer activities against 2D and 3D cancer models. *Chemistry–A European Journal* **2015**, 21, (2), 715-725.
37. Helary, C.; Ovtracht, L.; Coulomb, B.; Godeau, G.; Giraud-Guille, M. M., Dense fibrillar collagen matrices: a model to study myofibroblast behaviour during wound healing. *Biomaterials* **2006**, 27, (25), 4443-4452.

38. Guille, M. M. G.; Mosser, G.; Helary, C.; Eglin, D., Bone matrix like assemblies of collagen: from liquid crystals to gels and biomimetic materials. *Micron* **2005**, 36, (7-8), 602-608.
39. Tidu, A.; Ghoubay-Benallaoua, D.; Lynch, B.; Haye, B.; Illoul, C.; Allain, J.-M., et al. Mosser, G., Development of human corneal epithelium on organized fibrillated transparent collagen matrices synthesized at high concentration. *Acta biomaterialia* **2015**, 22, 50-58.
40. Quignard, S.; Hélar, C.; Boissière, M.; Fullana, J.-M.; Lagrée, P.-Y.; Coradin, T., Behaviour of silica nanoparticles in dermis-like cellularized collagen hydrogels. *Biomaterials Science* **2014**, 2, (4), 484-492.
41. Wang, X.; Hélar, C.; Coradin, T., Local and sustained gene delivery in silica-collagen nanocomposites. *ACS applied materials & interfaces* **2015**, 7, (4), 2503-2511.
42. Bates, P. J.; Laber, D. A.; Miller, D. M.; Thomas, S. D.; Trent, J. O., Discovery and development of the G-rich oligonucleotide AS1411 as a novel treatment for cancer. *Experimental and molecular pathology* **2009**, 86, (3), 151-164.
43. Reyes-Reyes, E. M.; Teng, Y.; Bates, P. J., A new paradigm for aptamer therapeutic AS1411 action: uptake by macropinocytosis and its stimulation by a nucleolin-dependent mechanism. *Cancer research* **2010**, canres. 0920.2010.
44. Fang, X.; Zhao, X.; Fang, W.; Chen, C.; Zheng, N., Self-templating synthesis of hollow mesoporous silica and their applications in catalysis and drug delivery. *Nanoscale* **2013**, 5, (6), 2205-2218.
45. Chen, F.; Hong, H.; Shi, S.; Goel, S.; Valdovinos, H. F.; Hernandez, R., et al. Cai, W., Engineering of hollow mesoporous silica nanoparticles for remarkably enhanced tumor active targeting efficacy. *Scientific reports* **2014**, 4, 5080.
46. He, X.; Yang, X.; Hai, L.; He, D.; He, X.; Wang, K.; Yang, X., Single-layer MnO<sub>2</sub> nanosheet quenched fluorescence ruthenium complexes for sensitive detection of ferrous iron. *RSC Advances* **2016**, 6, (82), 79204-79208.
47. Militello, M. C.; Gaarenstroom, S. W., Manganese Dioxide (MnO<sub>2</sub>) by XPS. *Surface Science Spectra* **2001**, 8, (3), 200-206.
48. Soulé, S.; Bulteau, A.-L.; Faucher, S.; Haye, B.; Aimé, C.; Allouche, J., et al. Martinez, H., Design and Cellular Fate of Bioinspired Au–Ag Nanoshells@ Hybrid Silica Nanoparticles. *Langmuir* **2016**, 32, (39), 10073-10082.

49. Petrovykh, D. Y.; Kimura-Suda, H.; Whitman, L. J.; Tarlov, M. J., Quantitative analysis and characterization of DNA immobilized on gold. *Journal of the American Chemical Society* **2003**, 125, (17), 5219-5226.
50. Quignard, S.; Masse, S.; Laurent, G.; Coradin, T., Introduction of disulfide bridges within silica nanoparticles to control their intra-cellular degradation. *Chemical Communications* **2013**, 49, (33), 3410-3412.
51. Huang, C.-C.; Khu, N.-H.; Yeh, C.-S., The characteristics of sub 10 nm manganese oxide T1 contrast agents of different nanostructured morphologies. *Biomaterials* **2010**, 31, (14), 4073-4078.
52. Peng, Y.-K.; Tsang, S. C. E.; Chou, P.-T., Chemical design of nanoprobe for T1-weighted magnetic resonance imaging. *Materials Today* **2016**, 19, (6), 336-348.
53. Lee, S. H.; Kim, B. H.; Na, H. B.; Hyeon, T., Paramagnetic inorganic nanoparticles as T1 MRI contrast agents. *Wiley Interdisciplinary Reviews: Nanomedicine and Nanobiotechnology* **2014**, 6, (2), 196-209.
54. He, D.; He, X.; Wang, K.; Yang, X.; Yang, X.; Zou, Z.; Li, X., Redox-responsive degradable honeycomb manganese oxide nanostructures as effective nanocarriers for intracellular glutathione-triggered drug release. *Chemical Communications* **2015**, 51, (4), 776-779.
55. Meng, H.; Xue, M.; Xia, T.; Zhao, Y.-L.; Tamanoi, F.; Stoddart, J. F., et al. Nel, A. E., Autonomous in vitro anticancer drug release from mesoporous silica nanoparticles by pH-sensitive nanovalves. *Journal of the American Chemical Society* **2010**, 132, (36), 12690-12697.
56. Liu, Y.; Chen, Q.; Xu, M.; Guan, G.; Hu, W.; Liang, Y., et al. Liu, H., Single peptide ligand-functionalized uniform hollow mesoporous silica nanoparticles achieving dual-targeting drug delivery to tumor cells and angiogenic blood vessel cells. *International journal of nanomedicine* **2015**, 10, 1855.
57. Singh, S. P.; Kumari, M.; Kumari, S. I.; Rahman, M. F.; Mahboob, M.; Grover, P., Toxicity assessment of manganese oxide micro and nanoparticles in Wistar rats after 28 days of repeated oral exposure. *Journal of Applied Toxicology* **2013**, 33, (10), 1165-1179.
58. ECHA, The Use of Alternatives to Testing on Animals for the REACH Regulation. In European Chemicals Agency Helsinki, Finland: **2011**.
59. Chapman, K. L.; Holzgreve, H.; Black, L. E.; Brown, M.; Chellman, G.; Copeman, C., et al. Hoberman, A., Pharmaceutical toxicology: designing studies to reduce animal

use, while maximizing human translation. *Regulatory Toxicology and Pharmacology* **2013**, 66, (1), 88-103.





# Chapter 4 Silica nanorods-collagen composite hydrogels: preparation, properties and magnetic engineering

“爱人者，人恒爱之”

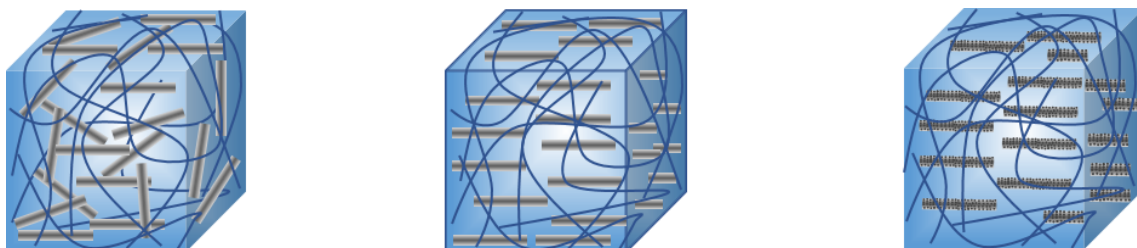
《孟子》

## Abstract

Nanocomposite hydrogels associating biological polymers with nanomaterials have been widely used as tissue engineering scaffolds and wound dressings. Especially collagen-silica bionanocomposites have shown great promises due to their versatility and good biocompatibility. In this chapter, we aimed at constructing new 3D collagen-based nanocomposites using silica nanorods instead of spherical nanoparticles previously reported. We have studied the relationships between the composite composition, structure and mechanical properties, emphasizing the key role of collagen-silica interactions. The influence of these parameters on the adhesion and proliferation of fibroblast cells was also investigated. In addition, we prepared and used magnetic silica nanorods to control particle orientation within the collagen network thanks to an external magnetic field. Our results bring new insights on the preparation and properties of bionanocomposites and open the route to multifunctional hydrogels.

<b>4.1 Introduction .....</b>	<b>133</b>
<b>4.2 Experimental section.....</b>	<b>134</b>
4.2.1 Chemicals .....	134
4.2.2 Synthesis of SiNRs/collagen hydrogel composite .....	135
4.2.3 Characterizations .....	136
4.2.4 Cell experiments.....	138
4.2.5 Statistical Analysis .....	139
<b>4.3 Results and discussion.....</b>	<b>139</b>
4.3.1 Synthesis and characterization of Fe <sub>3</sub> O <sub>4</sub> -coated silica nanorods .....	139
4.3.2 SiNRs-collagen hydrogel composites .....	144
4.3.3 Magnetic SiNR-collagen hydrogels .....	154
<b>4.4 Conclusion.....</b>	<b>158</b>

# Hydrogels composites à base de collagène et de nano-bâtonnets de silice : synthèse, propriétés et contrôle magnétique



## Résumé

Plusieurs études ont déjà démontré l'intérêt d'associer le collagène et des nanoparticules de silice pour la mise au point de biomatériaux tri-dimensionnels. Dans ce contexte, cette étude vise à étudier la possibilité d'utiliser des nanoparticules anisotropes, en forme de bâtonnets, plutôt que sphériques, pour atteindre un meilleur contrôle des propriétés mécaniques des nanocomposites et moduler leur influence sur des cellules animales. Pour cela, des hydrogels présentant des concentrations en collagène et en silice variables ont été préparés, caractérisés structuralement et nous avons étudié leurs propriétés rhéologiques. Le rôle clé joué par les interactions silice-collagène a alors pu être mis en évidence. La culture de fibroblastes humains sur ces nanocomposites a aussi été réalisée, montrant qu'un excès de nano-bâtonnets est défavorable à leur survie puisque celle-ci est liée à leur capacité à coloniser le réseau de collagène. Dans un deuxième temps, des nanobâtonnets magnétiques ont été synthétisés par croissance *in situ* de nanoparticules de magnétite à la surface de la silice. Nos premiers résultats indiquent qu'il est possible d'utiliser un champ magnétique externe pour contrôler l'orientation de ces particules au sein des nanocomposites. Ceci ouvre la voie à des hydrogels nanocomposites multifonctionnels.

## 4.1 Introduction

Hydrogels are three-dimensional networks that crosslink through a hydrophilic polymer chain within an aqueous microenvironment<sup>1</sup>. The water-rich nature of hydrogels makes them widely used in many fields, including tissue engineering, drug delivery, soft electronics, and actuators<sup>2-4</sup>. However, hydrogels generally have limited mechanical properties and are prone to permanent cracking<sup>5</sup>. Often, the lack of required dynamic cues and structural complexity within the hydrogel further limits their function, especially in a biological context. Therefore, extended applications of hydrogels require advanced parametric design, such as mechanical and spatiotemporal properties of the active or biologically active portion. The incorporation of nanostructured fillers into hydrogels has recently been developed as an innovative approach to create new materials with multiple functions and meet new challenges. The innovative combination of these two completely different types of materials is believed to produce not only structural diversity, but also a variety of performance enhancements. These enhancements are a major focus of hydrogel-nanoparticle composite research, which leads to improvements in mechanical strength and stimuli response (eg, optical, thermal, magnetic, and electrical). By using alternating layers of polyacrylamide hydrogel with and without polystyrene(PS) nanoparticle fillers, Thevenot et al. have developed composite materials having different elastic moduli<sup>6</sup>. The physical deformation of the double layer gel creates an electrical potential that can be used to develop soft tactile sensing devices. Polypyrrole is a semiconductor conjugated polymer for organic based optoelectronic devices. Luo et al. developed an agarose/alginate double-network hydrogel containing polypyrrole nanoparticles for use as an infrared response release system, much like those using reduced graphene oxide NP<sup>7</sup>. In another example, gold nanoparticles were immobilized poly N-isopropylamide hydrogel, inducing significant changes in mechanical properties and thermal response<sup>8</sup>. Thus, the combination of nanoparticles and hydrogels results in advanced materials with unique properties that currently catalyzes intense research activities of nanoparticle hydrogel composite interfaces and is expected to be used in many applications.

As already pointed out in the Chapter I, type I collagen is a protein of choice to prepare biomaterials<sup>9</sup>. Collagen-based hydrogels are used as carriers for cell and drug delivery in bone and cartilage tissue engineering, wound dressings and substrates in cell culture<sup>10-12</sup>. The incorporation of nanoparticles into collagen matrices to develop functional hydrogel composites has become an important and active area. For instance, the incorporation of magnetic nanoparticles within collagen hydrogels has been reported. Thanikaivelan et al. have

described collagen-based magnetic nanocomposites for selective oil absorption and magnetic tracking, making them useful for degreasing applications<sup>13</sup>. Magnetic hybrid hydrogels have also been used in biomedical applications in magnetic guided nerve repair. Shefi and colleagues developed magnetic particle/collagen hydrogel composites under external magnetic fields<sup>14</sup>. These hydrogels can control gel orientation and neuronal cell growth, which shows a significant promise for therapeutic engineering scaffolds. In parallel, as presented before, silica nanoparticles were also widely used to design collagen-based nanocomposites. As early as 2010, Desimone et al. prepared a silica nanoparticle-doped composite nanohydrogel scaffold for cell fixation<sup>15</sup>. Yu et al. prepared a silica hybrid collagen hydrogel as a three-dimensional cell matrix. The results showed that the viscoelasticity and mechanical properties of the hybrid gel were significantly improved, and the observed cell behavior in the 3D gel matrix was completely different from that previously reported on the 2D substrate<sup>16</sup>. Recently, many spherical silica hybrid composite gels have been used for the delivery of antibacterial drugs and genes<sup>17, 18</sup>.

However, silica nanorods have not been used to prepare such hybrid hydrogels. One-dimensional nanorods have a large aspect ratio compared to spherical nanomaterials and have a large potential to enhance the mechanical strength of hydrogels. Thus we have here prepared such silica nanorods and used them to prepare collagen-based composite hydrogels. Their mechanical properties and biological behavior were studied. In a step further, we have prepared magnetic nanorods by inducing the *in situ* growth of iron oxide nanoparticles on the surface of the silica particles and used them to design a magnetic nanocomposite gel. Preliminary results are very encouraging in the capacity of this strategy to allow a better control of nanorods orientation and also open perspectives to use these magnetic properties in biomedical applications.

## **4.2 Experimental section**

### **4.2.1 Chemicals**

All chemical reagents were analytical grade and used without further purification. Tetraethylorthosilicate (TEOS), absolute ethanol, n-pentanol, concentrated hydrochloric acid, 3-Triethoxysilylpropylamine (APTES), polyvinylpyrrolidone (PVP, 40 kDa), sodium citrate dihydrate, ammonium aqueous solution (28%), Acetic acid (AR), tetraethylene glycol (TEG), Iron (III) acetylacetonate were obtained from Sigma. MilliQ water (18 M $\Omega$ , Millipore, France)

was used for the preparation of the solutions and for all rinses. 4,6-diamidino-2-phenylindole (DAPI), Fetal bovine serum, Dulbecco's Modified Eagle's Medium (DMEM), trypsin, glutamine, and penicillin-streptomycin solution were purchased from ThermoFisher.

#### **4.2.2 Synthesis of SiNRs/collagen hydrogel composite**

##### **Synthesis of silica nanorods (SiNRs)**

The rod-like silica particles having lengths of about 3  $\mu\text{m}$  and diameters of about 300 nm were synthesized according to the recipe recently reported by Kuijk et al.<sup>19</sup> Typically, 30 g of PVP was added to 300 mL of n-pentanol and sonication for 3 hours. When all PVP had been dissolved, then 30 mL absolute ethanol, 8.4 mL ultrapure water and 2 mL of 0.18 M sodium citrate dihydrate aqueous solution were added to the solution following a sequence. The flask was shaken by hand to mix the content. Then, 6.75 mL of ammonia was added, the flask was shaken again and then 3 mL of TEOS was added to the mixture. After shaking again, the bottle was put into a water bath in 30 °C and the reaction was allowed to proceed 24 h. Next, the reaction mixture was centrifuged at 8000 rpm for 20 min. The supernatant was removed and the particles in the sediment were redispersed in ethanol. This centrifugation procedure was repeated at 4000 rpm for 15 minutes, 2 times with ethanol, 2 times with water and finally again with ethanol. To remove small rods and improve size dispersity, the rods were centrifuged two times at 500 g for 15 minutes and redispersed in fresh ethanol.

##### **Synthesis of Fe<sub>3</sub>O<sub>4</sub>-silica nanorods.**

Fe<sub>3</sub>O<sub>4</sub>-silica nanorods were prepared by high temperature thermal decomposition of iron precursor on the surface of silica nanorods. First, 100 mg of silica nanorods was dispersed in 1 mL of water and sonication for 30 min. Then 10 g of TEG and 0.177 g (0.5 mmol) of Fe(acac)<sub>3</sub> were added. The mixture was first heated to 110 °C under vacuum for 1 h to remove water and then to 200 °C for 2 h under a flow of nitrogen. The system was finally refluxed at 300 °C for 1 h and then cooled to room temperature. The final products also include a small fraction of unbound Fe<sub>3</sub>O<sub>4</sub> nanocrystals. For the purification, acetone was added to the synthesis solution, and an external magnetic field was applied to precipitate the Fe<sub>3</sub>O<sub>4</sub>@SiO<sub>2</sub>. The supernatant that contained free Fe<sub>3</sub>O<sub>4</sub> nanocrystals was then decanted. This process was repeated five times, and the product was dried under vacuum<sup>20</sup>.

### **Preparation of collagen-based hydrogel composites**

Type I collagen was purified from rat tails and the final concentration was estimated by hydroxyproline titration, as described in previous chapter. Nanocomposites were prepared by mixing a 5, 10, 20, 30 mg.mL<sup>-1</sup> collagen suspension in 17 mM acetic acid solution with a 10 X phosphate buffer saline (PBS) solution containing the suitable amount of silica nanorods to reach a final pH of 7.0 and a final concentration of silica nanorods ranging from 30 to 120 mg.mL<sup>-1</sup>. Resulting sols were quickly dispatched into different shaped mold and incubated at 37°C to trigger gel formation. Finally, gels were rinsed three times with PBS. For Fe<sub>3</sub>O<sub>4</sub>@SiO<sub>2</sub> hybrid collagen hydrogels, similar process was preformed except by mixing 10 mg.mL<sup>-1</sup> collagen suspensions (17 mM acetic acid) with 30 mg Fe<sub>3</sub>O<sub>4</sub>@SiNRs in absence or in presence of external field.

### **4.2.3 Characterizations**

#### **Characterization of nanorods-based silica materials**

Zeta potential ( $\zeta$ ) were measured in DI water using a Zetasizer Nano (Malvern Instruments Ltd., Worcestershire, UK). Particles were also imaged using Transmission Electron Microscopy (TEM) on a FEI Tecnai G2 Spirit microscope operating at 120 kV (TEM) (FEI Company, Philips, Netherlands). Nitrogen (N<sub>2</sub>) sorption measurements were performed at 77K using an accelerated surface area and porosimetry analyzer with Brunauer-Emmett-Teller (BET) calculations for the surface area. FTIR was performed by Perkin Elmer Spectrum 65 FTIR Spectrometer. X-ray Photoelectron Spectroscopy (XPS) analyses were performed with a PHOIBOS 100 spectrometer from SPECS GmbH. X-ray diffractometer was obtained using a Philips X-ray diffractometer with Cu-K  $\alpha$  radiation (Philips PW 1830, Holland). Magnetic properties of Fe<sub>3</sub>O<sub>4</sub>@SiNRs was measured by a Quantum Design SQUID magnetometer MPMS XL-7.

#### **Quantification of iron concentration**

Inductively coupled plasma quadrupole mass spectrometry (ICP-QMS) was performed on an Agilent 7900 apparatus. For sample processing, a mass of nanoparticles was first weighed, then digested with nitric acid-perchloric acid (4:1) overnight, followed by evaporation of the solvent at high temperature, and the residues were dissolved in 0.5 N nitric acid with a series of concentrations of Fe ions and analyzed.

### **Behavior of Fe<sub>3</sub>O<sub>4</sub>@SiNRs in collagen solution in presence of magnetic field**

The Fe<sub>3</sub>O<sub>4</sub>@SiNRs powder was added into the collagen solution. The mixture was vortexed for 2 minutes to ensure uniform dispersion of the nanoparticles. Then, the mixed solution was suctioned with a dropper and uniformly coated on a glass slide with a cover glass, and then the behavior of the sample under external magnetic field was observed under a LEICA fluorescence microscope with bright field.

### **Scanning electron microscopy (SEM) analysis**

The collagen nanocomposites were fixed in dimethyl citrate/sucrose buffer (0.05 M/ 0.3 M, pH 7.4) at 4 ° C for 1 hour using 3.63% glutaraldehyde. After fixation, the samples were washed three times in the same buffer and dehydrated from 70% to 100% ethanol by a continuously increasing concentration of ethanol bath. Thereafter, the samples were freeze-dried and sputtered with gold (20 nm) for analysis. Samples were observed with a Hitachi S-3400N SEM operating at 8 kV or 10kV.

### **Transmission electron microscopy (TEM) analysis**

The collagen nanocomposite was fixed with 4% PFA. After fixation and washing, the samples were fixed using 2% osmium tetroxide in cacodylate/sucrose buffer (0.05 M / 0.3 M, pH 7.4) at 4 ° C for 1 hour. The sample was then washed three times in cacodylate/sucrose buffer, dehydrated with ethanol and embedded in araldite. Thin araldite transverse sections (100-200 nm) were made by Ultracut ultramicrotome (Reichert, France) and compared to phosphotungstic acid. It was then analyzed by a Cryomicroscope Tecnai spirit G2 electron microscope operating at 120 kV.

### **Rheological measurements**

Shear oscillation measurements were performed on collagen nanocomposite discs using a Bohlin Gemini rheometer (Malvern) equipped with a flat acrylic 40 mm diameter geometry. Both the base and the geometric surface are rough to avoid slippage of the sample during the measurement. All tests were performed at 37 °C. The mechanical spectra were recorded at the applied 1% strain, ie the G' and loss G'' modulus versus frequency measurements were recorded, which correspond to linear and non-destructive conditions. In order to test all collagen matrices under similar conditions, the gap between the base and the geometry was chosen before each



run so that a slight positive normal force was exerted on the gel during the measurement. Four samples of each nanocomposite hydrogel were tested.

### **Magnetic measurements**

Magnetic measurement. Variable temperature (2.0-200K) magnetic measurements were applied to the external field of 1T using a Quantum Design SQUID magnetometer MPMS XL-7. To prevent loss of uncoordinated solvent, fresh samples were introduced at 200 K is frozen under a helium flow and purged under vacuum. Measurements were first made at 200K to 2.0K and then from 2.0 K to higher. These experiments were performed by Dr Yanling Li (IPCM, SU).

## **4.2.4 Cell experiments**

### **Cell culture**

Normal Human Dermal Fibroblasts (NHDF) were cultured in complete cell culture medium (DMEM with GlutaMAX™, without phenol red supplement, with 10% fetal serum, 100 U.mL<sup>-1</sup> penicillin, 100 µg/mL streptomycin). Tissue culture flasks (75 cm<sup>2</sup>) were kept at 37 °C in a 95% air: 5% CO<sub>2</sub> atmosphere. Before confluence, the cells were removed from culture flasks by treatment with 0.1% trypsin and 0.02% EDTA. Cells were rinsed and resuspended in the above culture medium before use.

### **Viability tests**

For viability test, NHDFs were seeded onto the hydrogel discs at a density of 5,000 cells/cm<sup>2</sup>. Following 24 h of culture, cell activity was evaluated by the Alamar Blue assay. Control experiments were performed using the pure collagen hydrogel by incubating NHDFs. There are four parallel samples for each sample.

### **Cell adhesion and proliferation on hydrogels**

For adhesion and proliferation assessments, NHDFs were seeded onto the hydrogel discs at a density of 5,000 cells/cm<sup>2</sup>. Following 24 h, 48h and 72 h of culture, cells on hydrogel surfaces were washed with PBS twice and treated with a 4% PFA solution for 1h. Cells were then stained with DIPA. Fluorescence images of stained cells were used to quantify cell adhesion and fraction area coverage. Fluorescence images were transformed into 8-bit digital grayscale images using ImageJ software, followed by the selection of a threshold on gray levels in order to separate lighter appearing cells from the darker background.

#### 4.2.5 Statistical Analysis

Graphical results are presented as mean  $\pm$  SD (standard deviation). Statistical significance was assessed using one-way analysis of variance (ANOVA) followed by Tukey (compare all pairs of groups) or Dunnett (compare a control group with other groups) post-hoc test. The level of significance in all statistical analyses was set at a probability of  $P < 0.05$ .

### 4.3 Results and discussion

#### 4.3.1 Synthesis and characterization of Fe<sub>3</sub>O<sub>4</sub>-coated silica nanorods

The Fe<sub>3</sub>O<sub>4</sub> attached silica nanorods was prepared according to the method depicted in **Figure 4-1**. In the first step, silica nanorods (SiNRs) were prepared using a wet-chemical synthesis method in one pot. Then, the magnetic Fe<sub>3</sub>O<sub>4</sub> nanoparticle shell was deposited on the surface of the silica nanorods by *in situ* thermal decomposition of iron acetylacetonate.

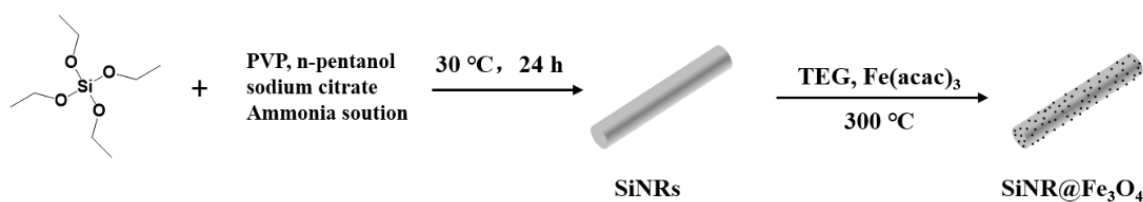


**Figure 4-1** Schematic illustration of the preparation of Fe<sub>3</sub>O<sub>4</sub> attached silica nanorods

Fairly uniform silica rods were obtained using the Kuijk's method, at a reaction temperature at of 30 °C. As shown from the TEM images in **Figure 4-2**, the synthesized silica nanorods exhibit good homogeneity, no spherical structure appears, and the nanorods have a diameter of about 300 nm and a length of 3  $\mu$ m (*i.e* the aspect ratio is 1 to 15). The shape of these nanomaterials is somewhat special, with one end being rather flat and the other end being like a tip, more like the shape of a nail.

Measurements by DLS were difficult because of the micron-size length of the rods. It was nevertheless possible to obtain a stable measurement of the zeta potential of prepared silica nanorods, -53.8 eV, similar to the surface charge of similar silica nanomaterials.

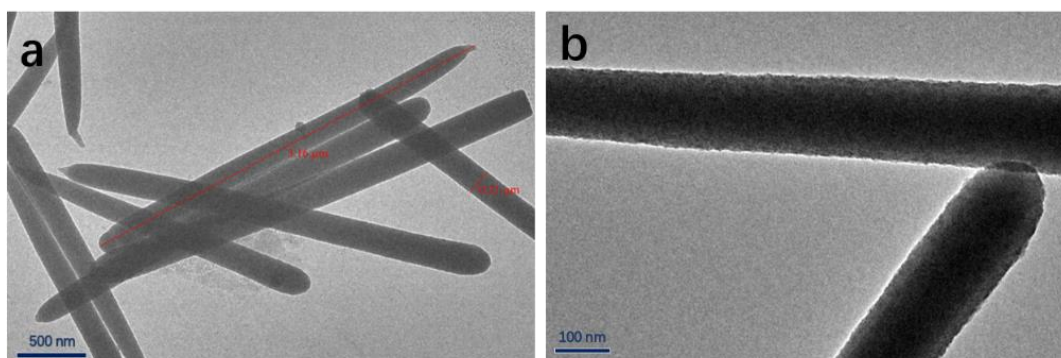


**Figure 4-2** TEM images of silica nanorods with different magnifications

Fourier transform infrared spectroscopy (FTIR) was used to further characterize the SiNRs. As shown in **Figure 4-3**, the typical peaks for hydrated silica can be observed at  $1044\text{ cm}^{-1}$ , that is caused by Si-O-Si stretching vibration, and at  $953\text{ cm}^{-1}$  and  $792\text{ cm}^{-1}$  which corresponds to Si-OH mode and inter-tetrahedral Si-O-Si bending vibration, respectively. The presence of adsorbed water was observed near  $3350\text{ cm}^{-1}$ . The band at  $1645\text{ cm}^{-1}$  may also sign for the presence of remaining PVP on or within the SiNRs particles.

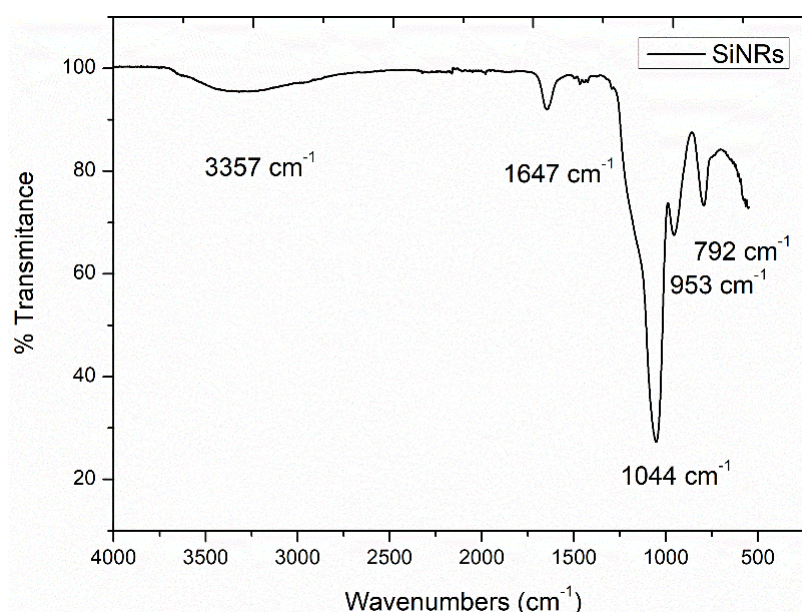


**Figure 4-3** The FTIR spectra of silica nanorods

Attachment of the iron oxide nanoparticles to the SiNRs was operated by direct high temperature thermal decomposition of iron precursors on the surface of silica nanorods. The iron content of the rods, as obtained by ICP-QMS, was 9.6 %. Successfully coating the  $\text{Fe}_3\text{O}_4$  nanoparticles on the surface of the silica can be clearly on the TEM images. It can be seen a

high density of nanoparticles having an average diameter of *ca.* 10 nm that form a thin layer which is almost uniformly distributed on the surface of the silica nanorods (**Figure 4-4**). This size range was in good agreement with that obtained for iron oxide nanoparticles prepared by the same method but in the absence of silica nanorods (**Figure 4-4**). No separate magnetite nanoparticles were observed near the silica or in any other sample area. To examine the stability of the magnetite on the silica surface, a small vial containing a dispersion of as-prepared SiNR@ Fe<sub>3</sub>O<sub>4</sub> was immersed in a 40 kHz ultrasonic bath for several different intervals. No observable change was found on the samples after continuous ultrasonic treatment, suggesting strong interaction of deposited nanoparticles with the silica surface.

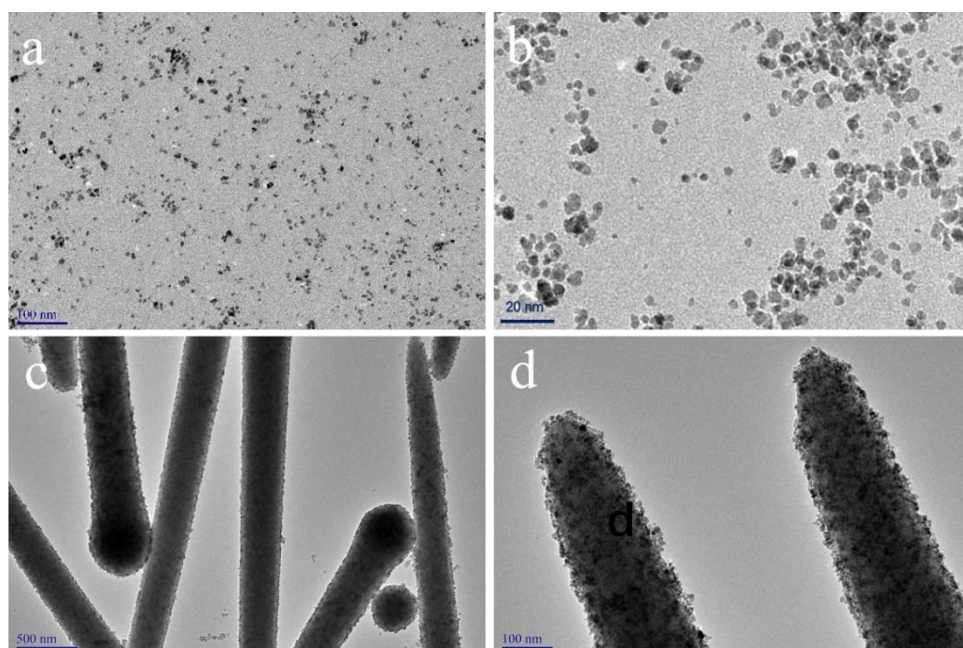


**Figure 4-4** TEM images of (a-b) Fe<sub>3</sub>O<sub>4</sub> nanoparticles, (c-d) SiNR@Fe<sub>3</sub>O<sub>4</sub> materials

XRD analysis confirmed that the nanocrystals on the silica surface were consisting of magnetite (Figure 4-5).

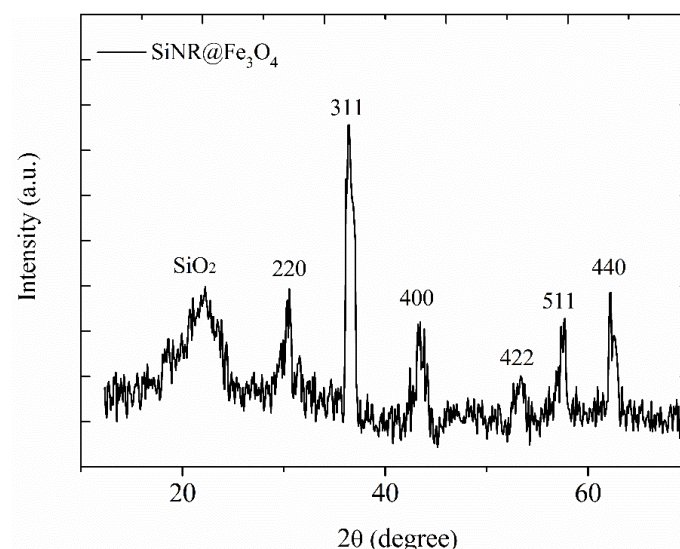


**Figure 4-5** The XRD patterns of SiNR@Fe<sub>3</sub>O<sub>4</sub> with standard reference magnetite (JCPDS No.19-0629)

To further confirm the nature of deposited nanoparticles, the as-prepared materials were studied by XPS (**Figure 4-6**). The two photoelectron peaks at 710.6 and 724.1 eV are very close to the previously reported binding energy value of core-level Fe 2p lines in magnetite, confirming the phase of the iron oxide nanoparticles on silica surface.

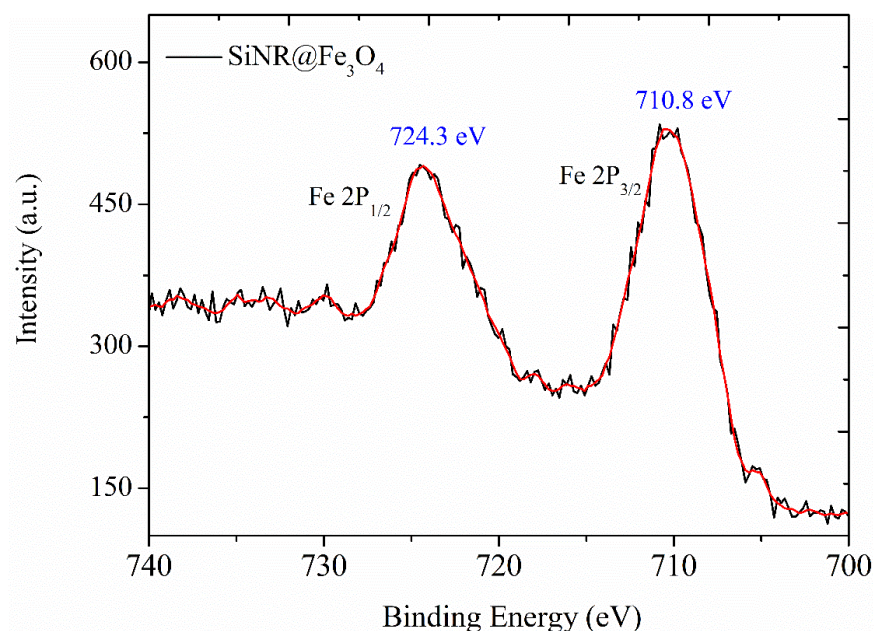


**Figure 4-6** XPS spectrum at the Fe2p level of SiNR@Fe<sub>3</sub>O<sub>4</sub> nanomaterials

The composition of SiNR@Fe<sub>3</sub>O<sub>4</sub> was examined in FTIR (**Figure 4-7**). The band at 588 cm<sup>-1</sup> supported the formation of the magnetite phase. The emerging peaks in the 2800-3000 cm<sup>-1</sup>



domain, that were absent in pure silica nanorods, should arise from the C-H bond stretching from methylene groups, suggesting the presence of TEG molecules.

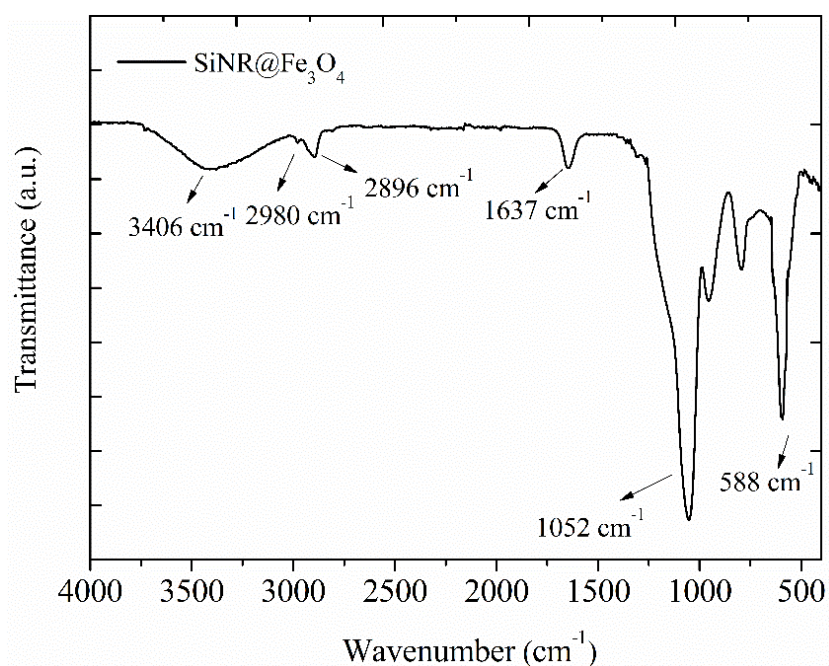


**Figure 4-7** The FTIR spectra of SiNR@Fe<sub>3</sub>O<sub>4</sub> nanomaterials

As a first insight into the magnetic properties of the modified nanorods, we observed that applying a magnet at the proximity of a SiNR@Fe<sub>3</sub>O<sub>4</sub> aqueous suspension allow for its fast and efficient attraction on the glassware wall (**Figure 4-8**).

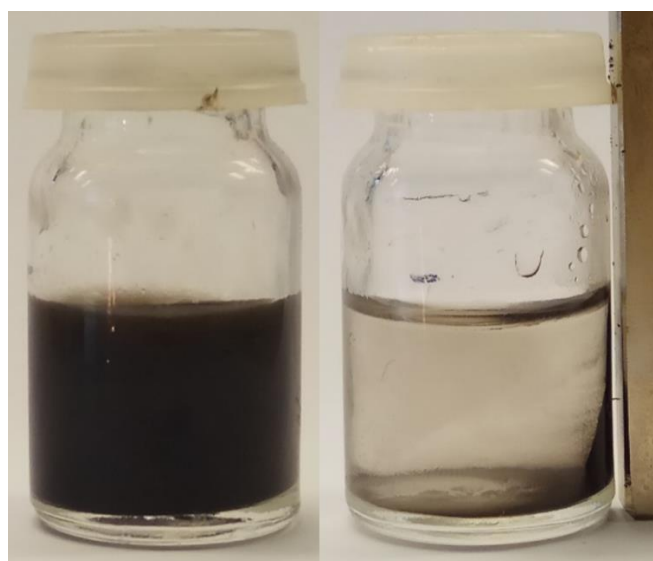


**Figure 4-8** SiNR@Fe<sub>3</sub>O<sub>4</sub> dispersed in distilled water are efficiently attracted by an external magnetic field

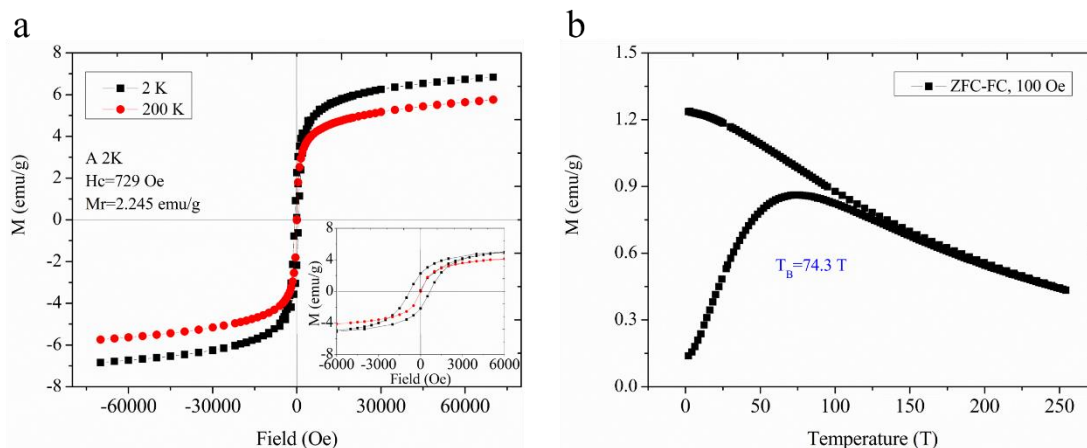


**Figure 4-9** (a) Hysteresis cycle recorded at temperature 2 K and 200 K for SiNR@  $\text{Fe}_3\text{O}_4$ . Inset are the hysteresis cycles at low fields (b) ZFC and FC magnetization curves of SiNR@  $\text{Fe}_3\text{O}_4$  at 100 Oe

The magnetic properties of as-synthesized SiNR@ $\text{Fe}_3\text{O}_4$  were then studied using SQUID magnetometer. **Figure 4-9a** shows the magnetization of SiNR@ $\text{Fe}_3\text{O}_4$  as a function of applied field,  $M(H)$ , recorded at 2 and 200 K. An open hysteresis loop is observed at 2 K with a coercive field  $H_c = 729$  Oe. The hysteresis curve is substantially saturated at the highest applied field ( $>0.6\text{T}$ ). However, when the temperature rises to 200K, the hysteresis loop becomes a straight line and the coercive force is almost zero. This is because the nanomaterial exhibits strong paramagnetism at room temperature of 200K. **Figure 4-9b** shows the zero-field-cooled (ZFC) and field-cooled (FC) magnetization of a powder sample of SiNR@ $\text{Fe}_3\text{O}_4$ . The ZFC magnetization curve increases with temperature, reaching a maximum at temperatures  $T = 74.3$  K, which can be assumed, as a first approximation, to coincide with the blocking temperature  $T_B$ . The FC curve increases as the temperature decreases and never reaches saturation at low temperature, suggesting that interparticle interactions do not significantly affect the relaxation dynamics. The ZFC and FC curves start to diverge at a temperature far above the  $T_B$  estimated with the ZFC curve. This is due to relatively broad size and shape distributions of the samples. Indeed for this sample, according to the Néel model, the transition from the blocked to the superparamagnetic regime occurs at different temperatures for different particle sizes.

#### 4.3.2 SiNRs-collagen hydrogel composites

The prepared silica nanorods were mixed with the collagen solution in acidic conditions by physical action, followed by adjusting the pH value of the mixed system to yield the SiNRs-collagen hydrogel nanocomposites (**Figure 4-10**).



**Figure 4-10** Schematic illustration of the preparation of SiNRs-collagen hydrogels

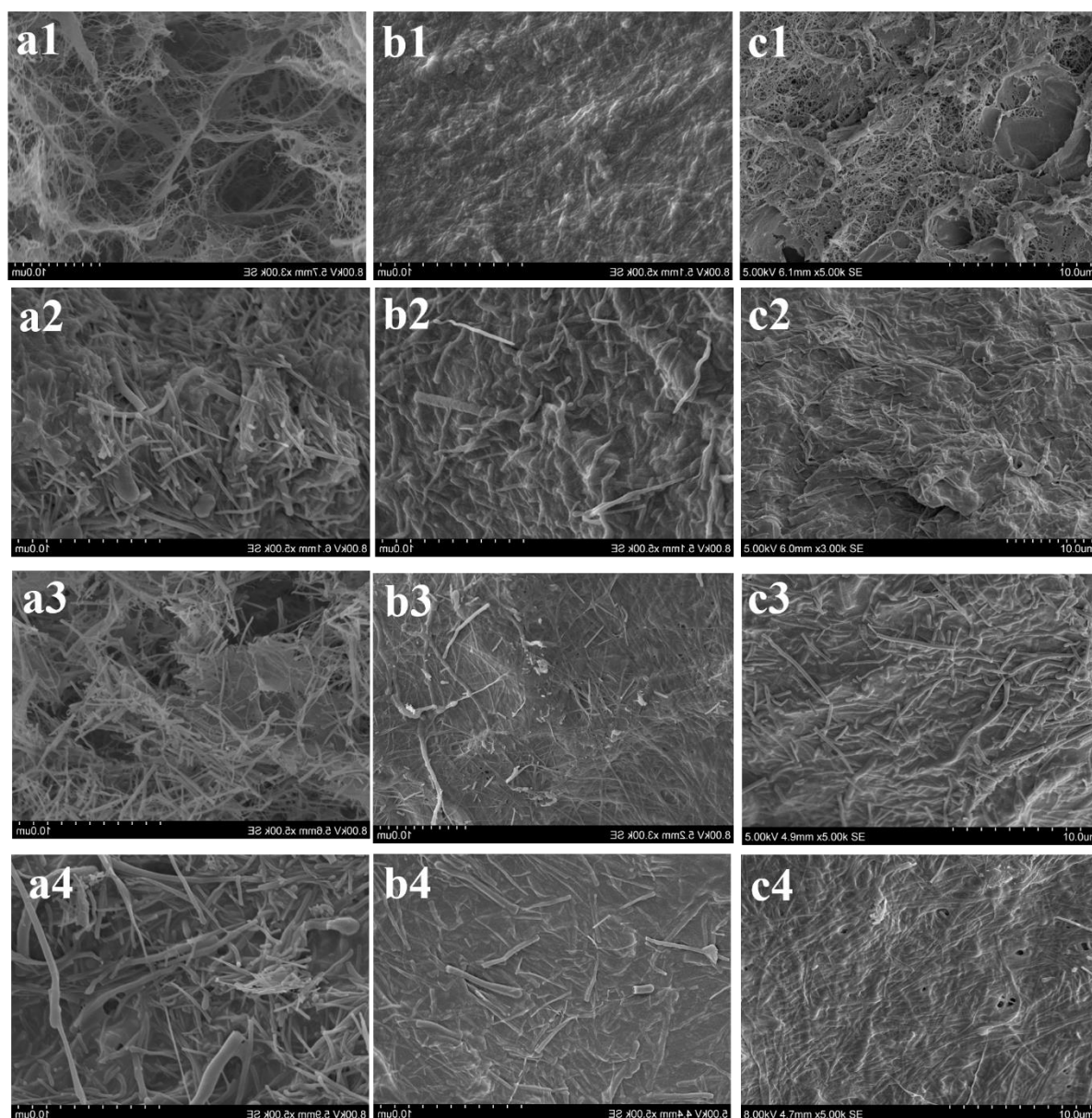


**Figure 4-11** SEM of SiNR-collagen composite hydrogels. (a) 10 mg/mL, (b) 20 mg/mL and (c) 30 mg/mL collagen with concentrations of SiNRs: 1-30 mg.mL<sup>-1</sup>, 2-60 mg.mL<sup>-1</sup>, 3-90 mg.mL<sup>-1</sup>, 4-120 mg.mL<sup>-1</sup>



Nanocomposite materials were prepared with collagen concentrations of 10 mg/mL, 20 mg/mL, 30 mg/mL, and silica rod concentrations from 30 mg.mL<sup>-1</sup> to 120 mg.mL<sup>-1</sup> (final concentration) and imaged by SEM (**Figure 4-11**). [Note: for sake of clarity, we have selected the mg/mL notation for collagen and mg.mL<sup>-1</sup> for silica]

At 10 mg/mL collagen (Figure 4-11a), nanorods are initially difficult to identify within the highly porous fibrillar network. They become more and more easily evidenced with higher SiNRs amounts. However, at 120 mg.mL<sup>-1</sup>, different particles resembling SiNRs coated with some organic material are sometimes observed. At 20 mg/mL, the material appears denser and nanorods are sparingly observed on the surface or can be guessed below it, without a clear tendency as a function of silica concentration. Almost the same trend is observed at 30 mg/mL, except for the lowest silica concentration. However it is important to point out that, because of their high water content, hydrogel morphology as observed by SEM can strongly vary with drying conditions and surface (“crust”) effects are often detrimental to their accurate study by this technique.

The mechanical properties of the nanocomposites were investigated by rheological measurements and compared to pure collagen hydrogels (**Figure 4-12, Appendix 4**). For all materials, the storage modulus  $G'$  was much higher than the loss modulus  $G''$ , as expected for hydrogels with significant elastic properties. The measured moduli for the nanocomposites vary from *ca.* 750 to 3500 Pa. As a general trend, at a given silica concentration,  $G'$  increased with collagen concentration. At a fixed collagen concentration, the evolution of  $G'$  with SiNR content could significantly depend on the collagen content.

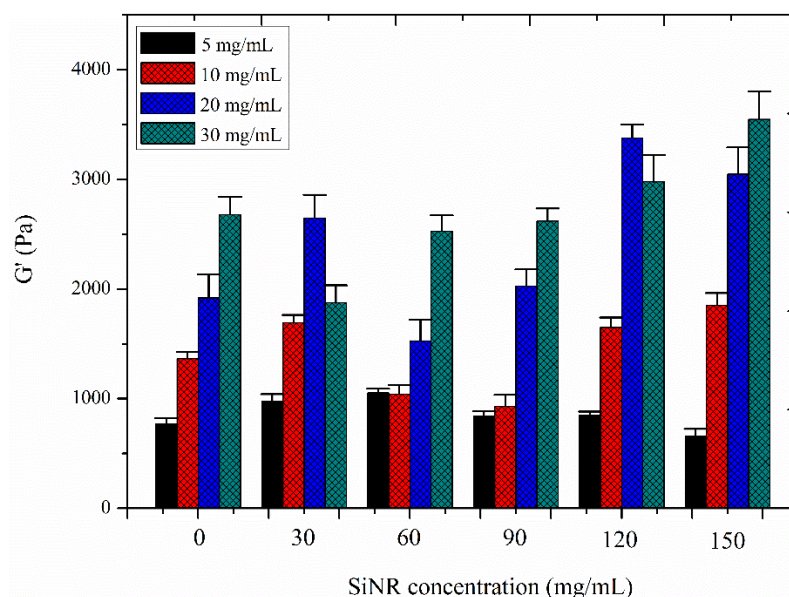


**Figure 4-12** Storage ( $G'$ ) of SiNR-collagen composite hydrogels with various composition

In more details, when the concentration of collagen is low (5mg/mL),  $G'$  value increases for low silica content (30 and 60 mg.mL<sup>-1</sup>) and then slightly decreases. At 10 mg/mL collagen, there is a first maximum for 30 mg.mL<sup>-1</sup> then  $G'$  decreases with 60 and 90 mL<sup>-1</sup> SiNR and rises again for larger silica amount. A very similar trend is also observed at 20 mg/mL collagen. At 30 mg/mL collagen, a decrease of  $G'$  is observed after addition of 30 mg.mL<sup>-1</sup> silica but increasing further the SiNR content allows to obtain the highest modulus.

It is important to consider that the  $G'$  value reflects the response of the collagen or composite network to a shearing force. In pure collagen, the network cohesion is insured by inter-fibrillar interactions and its strength therefore increases with fibril density. When nanorods are added, several effects can occur: (i) the nanorods can perturb the fibrillar organization of collagen and therefore weaken its cohesion, (ii) the nanorods can bridge the fibrils and therefore increase the cohesion and (iii) interactions between nanorods can contribute to the response of the composite network to the shearing stress. In the conditions of formation of these materials, *i.e.* near neutral pH, no favorable chemical interactions are expected between the silica nanoparticles. In fact, being negatively-charged, it can even be expected a repulsive electrostatic interaction between them. However, it is possible to assume that collagen fibrils can bridge SiNRs together.

Overall, introduction of silica nanorods in low amounts in the collagen network may destabilize the inter-fibril interactions but this can be at least partially compensated by favorable silica-collagen interactions. If silica amount increases, SiNR-SiNR unfavorable interactions become prevalent and weaken the composite network. However, at higher silica concentration, the network mainly consists of close-packed silica nanorods that can be favorably bridged by collagen. Thus, at low collagen concentration (5 mg/mL), it can be suggested that SiNRs at low concentration can compensate the perturbation of the collagen network by introducing new collagen-silica interactions but the protein density is not enough to stabilize the close packed SiNRs network formed at high silica concentration. On the contrary, such a stabilization is observed at silica concentration from 120 mg.mL<sup>-1</sup> at 10 mg/mL collagen, 90 mg.mL<sup>-1</sup> at 20 mg/mL collagen and 60 mg.mL<sup>-1</sup> at 30 mg/mL collagen.

To clarify this point, we selected hydrogels with similar rheological behaviour but different collagen/SiNR concentrations (**Table 4-1**).

**Table 4-1** Selected composite hydrogels with similar mechanical properties

Sample	a	b	c	d
Collagen	20 mg/mL	10 mg/mL	20 mg/mL	30 mg/mL
Silica rods	0	120 mg.mL <sup>-1</sup>	60 mg.mL <sup>-1</sup>	30 mg.mL <sup>-1</sup>

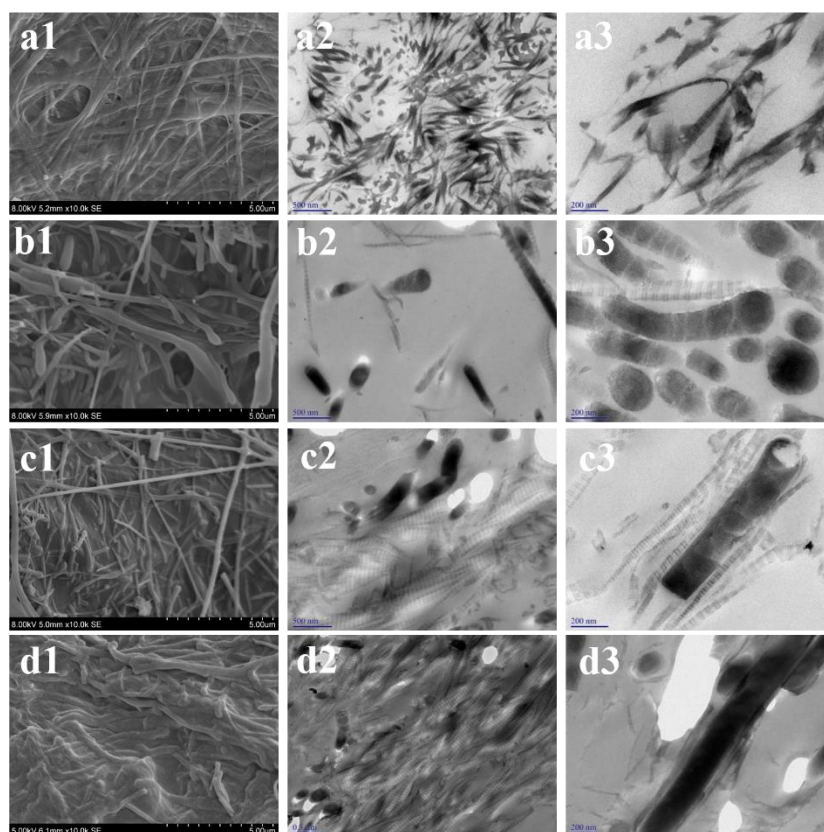


**Figure 4-13** SEM and TEM of (a) 20 mg/mL collagen. (b) 10 mg/mL collagen, 120 mg.mL<sup>-1</sup> SiNRs. (c) 20 mg/mL collagen, 60 mg.mL<sup>-1</sup> SiNRs. (d) 30 mg/mL collagen, 30 mg.mL<sup>-1</sup> SiNRs

The pure collagen hydrogel with a concentration of 20 mg/mL showed an obvious fibrous collagen network on SEM and TEM evidenced densely-packed fibrils exhibiting a periodic band pattern of 67 nm, which is a typical feature of the physiological structure of type I collagen (**Figure 4-13a**). At 10 mg/mL collagen and 120 mg.mL<sup>-1</sup> silica (**Figure 4-13b**), elongated objects with a rather undefined morphology are observed by SEM, that was, in a first instance, attributed to nanorods coated with collagen. By TEM, it was possible to visualize both striated collagen fibrils and other objects that we attributed to sections of nanorods cut at different orientations. This attribution was supported at higher magnification where various sections of the rods were clearly observed. Interestingly, when transversal sections are visualized, the core-shell structure of the rods is revealed. In the case of longitudinal sections, it is possible to observed that, during the sample preparation, the ultramicrotome knife has fragmented the rods in slices, that could reflect the layer-by-layer growth mechanism of these particles. The nanorods appear highly densely packed, in agreement with the high silica concentration, and at least one large striated collagen fiber can be found in between the elongated mineral particles.

When increasing collagen concentration and decreasing SiNR concentration (**Figure 4-13c**), the nanorods are more easily distinguished on the SEM image. On TEM, many collagen fibrils are seen and less nanorod sections, in agreement with the higher collagen:silica ratio used here compared to the previous sample. At higher magnification, a very interesting phenomenon is evidenced: several striated fibers are observed that are aligned along the direction of the rods. Such an alignment not only concerns those fibers that are in close proximity with the silica surface but at least two other layers of collagen fibers also follow this direction.

Finally, increasing further the collagen:silica ratio to 1:1 (**Figure 4-13d**), it becomes difficult to accurately decipher protein fibers from nanorods on the SEM images. Accordingly, on TEM, a very dense network of collagen is observed in which some nanorods appear to be buried. At high magnification, the silica nanorod appear surrounded by a continuous sheath of dense and well-aligned.

The first important and surprising information resulting from these images is the high ability to the nanorods to orient the collagen fibers. To our knowledge, such an orientation was never reported before for collagen self-assembly in the presence of anisotropic particles. This observation clearly confirms the possible existence of strong interactions between the protein and the nanorods.

The second point to raise is that, despite well-distinct structures, the four materials studied here have very similar  $G'$  values. Taking the pure 20 mg/mL collagen hydrogel (a) as a reference, the introduction of 60 mg.mL<sup>-1</sup> SiNR (c) does not significantly modify its rheological behavior. Introducing more particles with lower collagen concentration (b) or less particles with more collagen (d) has a similar effect on  $G'$ . This confirms that densely packed silica nanorods can be efficiently “glued” by collagen fibers. At lower content, SiNRs have both positive and negative effect on collagen. On the one hand, surface interaction should enhance the strength of the mineral-protein bond. On the other hand, it will deplete the solution in collagen molecules available to form a network. The relative contribution of these two diverging effects is expected to depend on both collagen and SiNRs concentration. From a composite perspective, it means that the weakening of the matrix is compensated by the strengthening of the charge/matrix interactions.

It is now well-admitted that the behavior of cells on a considered substrate is highly dependent on its mechanical properties. However, it is often difficult to modify these properties without changing other parameters of the substrate such as its composition or structure. Here we had the possibility to prepare materials with similar rheological properties but different compositions and structures, offering a fruitful opportunity to establish possible correlations

between cell activity and substrate properties. For this we used NHDF cells that were seeded and grown for 72 hours. Their metabolic activity was evaluated by the Almar blue test.

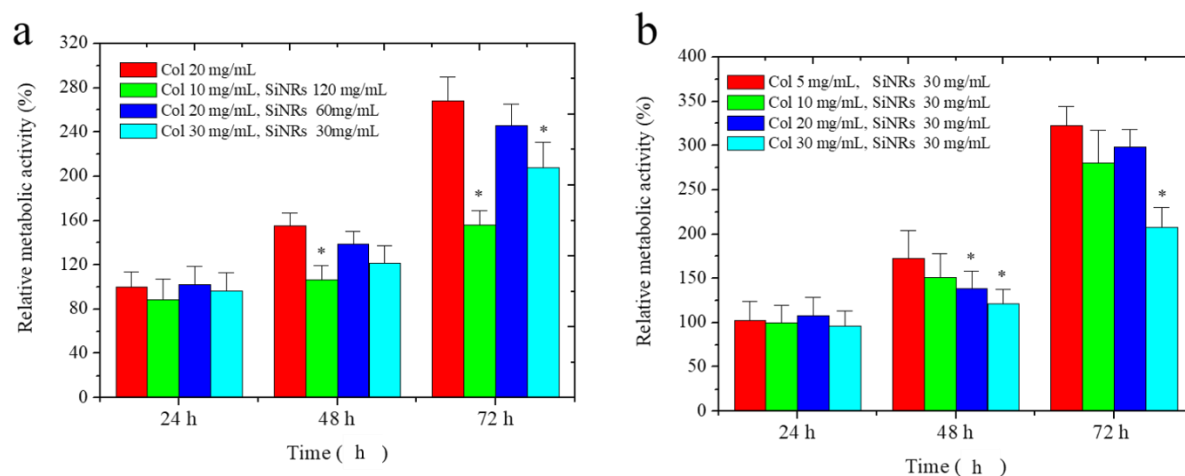


**Figure 4-14** Metabolic activity of surface-cultured fibroblasts (Alamar blue assay) (a) at constant G' (ca. 2 kPa) value and (b) at constant SiNRs content. Control collagen hydrogels (20 mg/mL) at day 1 were normalized to 100%.

The pure collagen at 20 mg/mL after 24 h was taken as the 100 % reference. First, when comparing the four materials exhibiting similar G' values (ca. 2 kPa), no significant difference was observed after 24 h, indicating that cell adhesion was similar in all cases (**Figure 4-14a**). After 48 h, cell proliferation has occurred for all samples to a similar extent, except for sample (b) (10 mg/mL, 120 mg.mL<sup>-1</sup>). This difference was even more marked after 72 h and sample (d) (30 mg/mL, 30 mg.mL<sup>-1</sup>) also showed lower cell activity. The low activity measured for (b) is not completely unexpected as it contains the highest SiNRs concentration that are very likely to dissolve during the incubation and may therefore have some cytotoxic effect. The decrease in activity for sample (d) is more surprising. Since sample (c) with higher SiNR content does not show detrimental effect, direct cytotoxic effect from silica cannot account for the effect of (d).

Aiming at understanding better these results, we compared a series of composite prepared at constant SiNR concentration (30 mg.mL<sup>-1</sup>) but various collagen content. As shown on **Figure 4-14b**, the initial cell adhesion is similar for all hydrogels. After 48 h cell proliferation has occurred but to an extent that decreases with increasing collagen concentration. After 72 h, the cellular activity is the same for all samples except for the 30 mg/mL collagen, 30 mg.mL<sup>-1</sup> SiNR composite (i.e. sample (d)). Again, if this detrimental effect was directly related to silica, then we could have expected that it would be more effective for the highest silica:collagen ratio. In fact, we observe the opposite trend.

We then used fluorescence microscopy and SEM to image the different samples. **Figure 4-15** gathers selected images for the first series of samples (similar G' but different compositions).

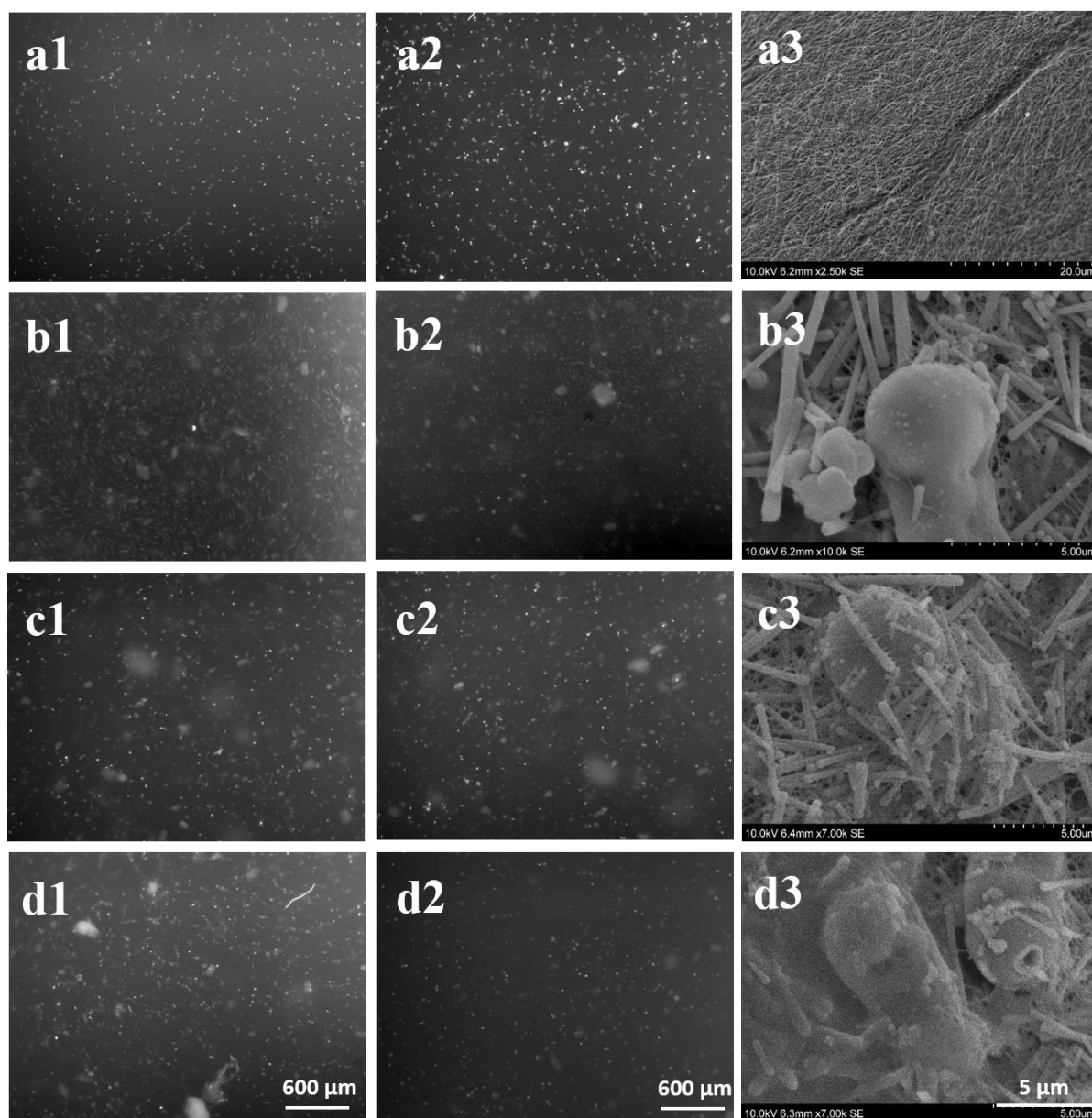


**Figure 4-15** Fluorescence (1-24 h, 2-72h) and SEM (3-72 h) images of NHDF incubated with (a) 20 mg/mL collagen. (b) 10 mg/mL collagen, 120 mg.mL<sup>-1</sup> SiNRs. (c) 20 mg/mL collagen, 60 mg.mL<sup>-1</sup> SiNRs. (d) 30 mg/mL collagen, 30 mg.mL<sup>-1</sup> SiNRs

For the pure collagen, the extent of proliferation between 24 h (a1) and 72 h (a2) is validated by fluorescence microscopy. It was also quite clear that all cells are not in the same focus plan, especially after 72 h, indicating that colonization of the matrix has started. In the case of the composites, the presence of the silica nanorods made the imaging more difficult. However, it is possible to confirm that very few cells are present on the (b) sample and less are observed on (d) compared to (c) after 72 h. SEM imaging after 72 h (right hand column of Figure 4-15)

provided complementary information. The first striking observation is that silica nanorods are found in very large amount at the surface of the composite, in contrast to the initial cell-free SEM images shown in **Figure 4-11**. A second interesting point is seen for sample c (c3), where cells appear coated by a mixture of collagen fibrils and nanorods. However, it must be pointed out that observed NHDFs in b3 and c3 have a round shape which indicate poor adhesion. In the case of d3, it is even difficult to clearly identify the cells.

Taken together, it appears that cells have strongly interacted and remodeled the composite hydrogel surface. It is fact well-known that upon adhesion on collagen, fibroblasts can rearrange their environment by pulling on the protein fibers and contract the collagen network. This remodeling is all the more efficient as the collagen network is weak. Noticeably, here, all composites have similar  $G'$  value but the collagen matrix itself, to which NHDFs are more likely to adhere rather than on the silica nanorods, varies from one sample to the other.

The key role played by the collagen matrix itself is clearly evidenced in the second series of composite hydrogels (constant SiNR concentration of  $30 \text{ mg.mL}^{-1}$ ) (**Figure 4-16**). Fluorescent imaging allows to point out the decrease in cell density with increasing collagen concentration, especially after 72 h (column 2). Thanks to the low SiNR content, it is also possible to better observe cells that have penetrated inside the matrix. In SEM, highly-adhering well-spread NHDF are observed after 72 h for all composites except for  $30 \text{ mg/mL}$  collagen,  $30 \text{ mg.mL}^{-1}$  SiNRs, in agreement with cellular activity measurements.

The most straightforward explanation for these observations is related to the influence of collagen concentration on hydrogel colonization. It has been previously demonstrated in our group that the rate of penetration of NHDFs within collagen hydrogels, that involves the degradation of the protein network by metalloprotease enzymes, decreases with increasing concentration. We should remind that the previous set of experiments has suggested that cell adhesion and proliferation is not favored on silica nanorods that were found in large amounts on the composite surface. Therefore, in low collagen composites, NHDFs cells may be able to penetrate the protein network and find a favorable environment for proliferation. On the contrary, for high collagen content, fibroblasts are stuck on the surface and their proliferation is hindered by the high density of silica nanorods.



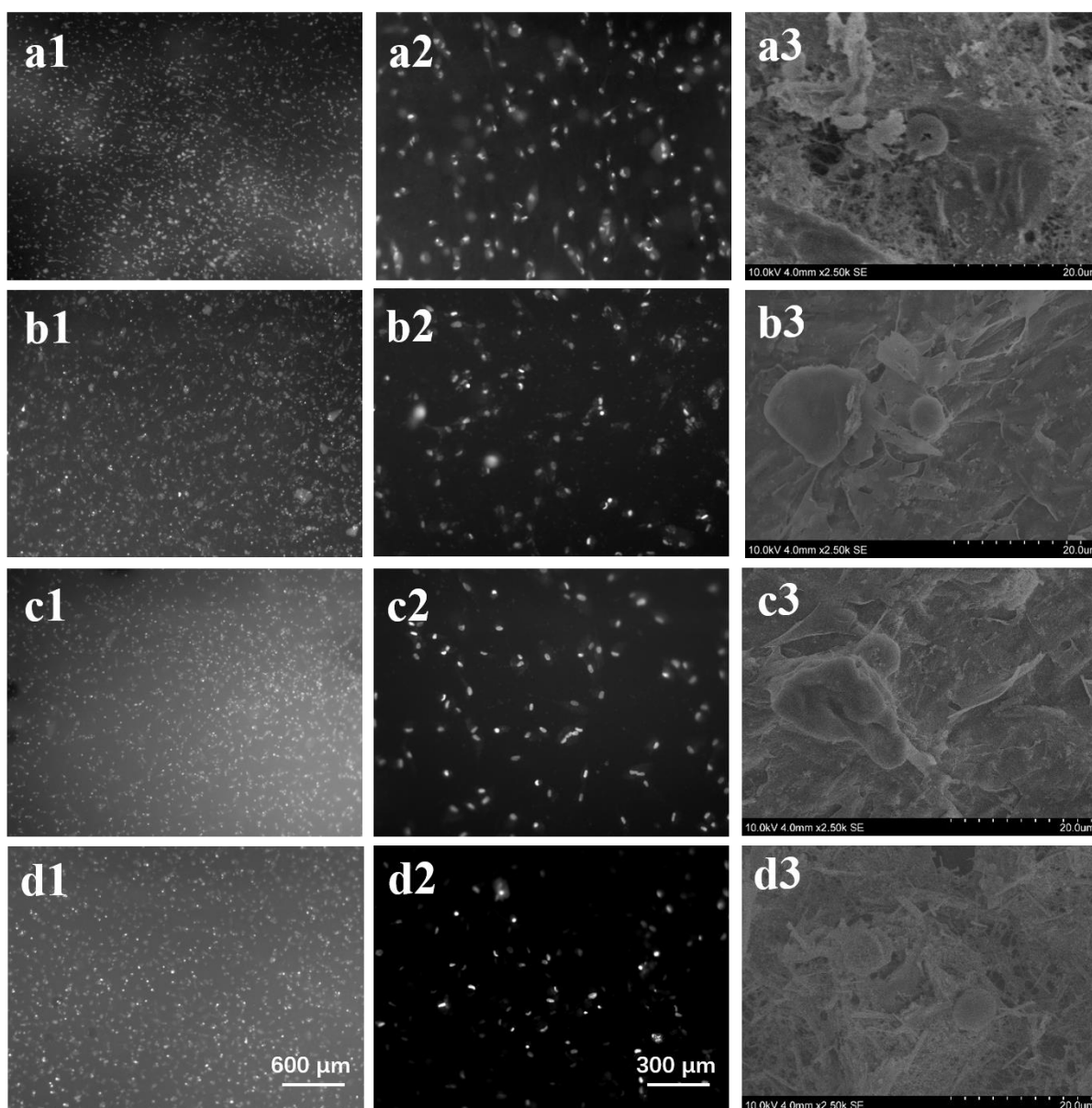


**Figure 4-16** Fluorescence (1, 2-72h) and SEM (3-72 h) images of NHDF incubated with (a) 5 mg/mL collagen. (b) 10 mg/mL collagen (c) 20 mg/mL collagen (d) 30 mg/mL collagen, all supplemented with 30 mg.mL<sup>-1</sup> SiNRs

In summary, we were able to new nanocomposites materials with a wide range of collagen and silica nanorods content. It allowed us to obtain variable structures, from dense collagen networks entrapping dispersed nanoparticles to closely-packed assemblies of nanorods within which collagen fibrils can be formed. Interestingly, the rheological behavior of these composites did not vary in proportion to the content in one or the other component neither on their respective ratio. As evidenced by TEM, one reason for this is that strong interactions exist between silica and collagen, resulting in the striking observation of protein fiber alignment along the nanorod main axis. These results clearly enlighten that these materials can be truly



considered as composite structures at the macroscopic scale. However, our study of the behavior of NHDF seeded on their surface suggest that the cells do discriminate between the protein and the mineral phases, all the more as collagen represents a favorable environment for their proliferation whereas silica nanoparticles have a detrimental effect on their adhesion, and may even be cytotoxic in large amounts. Since such an inhibition of cell proliferation was not reported previously for collagen-silica nanocomposites prepared with smaller (up to *ca.* 400 nm) spherical silica nanoparticles, it can be assumed that it is related to the fact that the length of the rods (*ca.* 3  $\mu\text{m}$ ) is in the same order of magnitude as fibroblasts dimensions (10-15  $\mu\text{m}$ ). It can also be noticed that, whatever the conditions, the improvement of the  $G'$  value was quite moderate (max. 50 %). This can be due, at least for some part, to the lack of control of nanorods organization within the collagen hydrogels. As an answer to this problem, we attempted to take advantage of the magnetic properties  $\text{SiNR}@Fe_3O_4$  to tune their orientation within the composite structure.

#### 4.3.3 Magnetic SiNR-collagen hydrogels

The magnetic composite hydrogels were first prepared following the same procedure as for SiNR nanorods, i.e. in the absence of external magnetic field. From SEM, the morphology of the magnetic composite hydrogel (10 mg/mL collagen, 30  $\text{mg}\cdot\text{mL}^{-1}$   $\text{SiNR}@Fe_3O_4$ ) is very similar to the one obtained with non-magnetic nanorods (**Figure 4-17**).

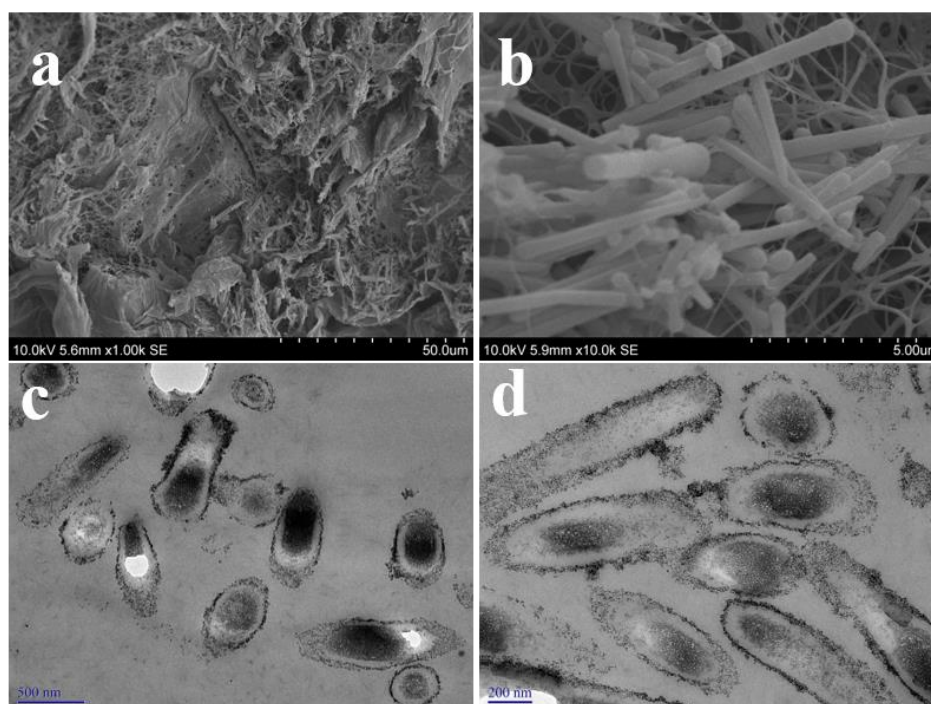


**Figure 4-17** SEM (a, b) and TEM (c, d) images of  $\text{SiNR}@Fe_3O_4$ -collagen composite hydrogels

TEM also allows to evidence sections of the nanorods with various orientations. The thin layer of magnetic nanoparticles coating the rods is also easily visualized. The background collagen network is difficult to observe, probably due to the high contrast of the iron oxide nanoparticles. Indeed, once the collagen matrix is formed, the nanorods can no longer orient if an external magnetic field is applied. Such an orientation must therefore be achieved in the acidic collagen-nanoparticle mixture before inducing gelation. We hypothesized that this process will highly depend on collagen concentration. More convincing results were obtained using a 10 mg/mL collagen concentration (**Figure 4-18**).

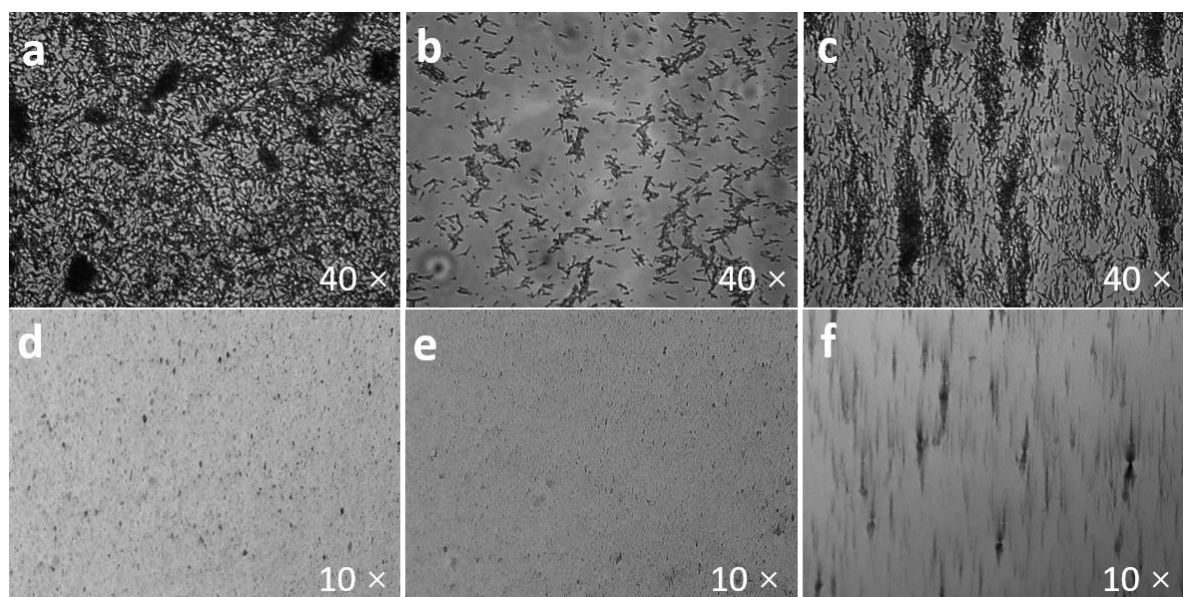


**Figure 4-18** Magnetically controlled nanomaterial behavior in 10 mg/mL collagen solution. (a) No magnetic field. (b) Magnetic fields in the opposite direction (N-N, or S-S). (c) Magnetic fields in the same direction (N-S, S-N). (d-f) Magnetic response time is 0, 2, 5 min, respectively. In these experiments, a drop of the collagen solution was deposited on a glass slide and left as such (a) or placed between two plate magnets. The two plates were oriented with either same poles (*i.e.* fields in opposite directions) (b) or opposite poles (*i.e.* fields in same direction) (c) facing each other. As seen by bright-field optical microscopy, the initially randomly aggregated nanorods tend to form more local assemblies in (b) and are very well-aligned in configuration (c). We also conducted a study of the kinetics of the process under the microscope with magnets placed around the glass slide. As shown on Figure 4-18(d-f), it took only 5 minutes for the nanorods to be aligned.

These conditions were then repeated for bulk hydrogels and the resulting composites were imaged by SEM and TEM. As seen on **Figure 4-19**, it is quite difficult to ascertain orientation of the nanorods on the sole basis of SEM characterization. TEM images are more informative. On the one hand, it seems that two nanorod orientations are favored, one parallel to the plane of the image, one perpendicular to it. On the other hand, and maybe more significantly, two rods well aligned along their main axis are observed. Indeed we would have needed to analyze much more images to ascertain these facts but they were quite encouraging.

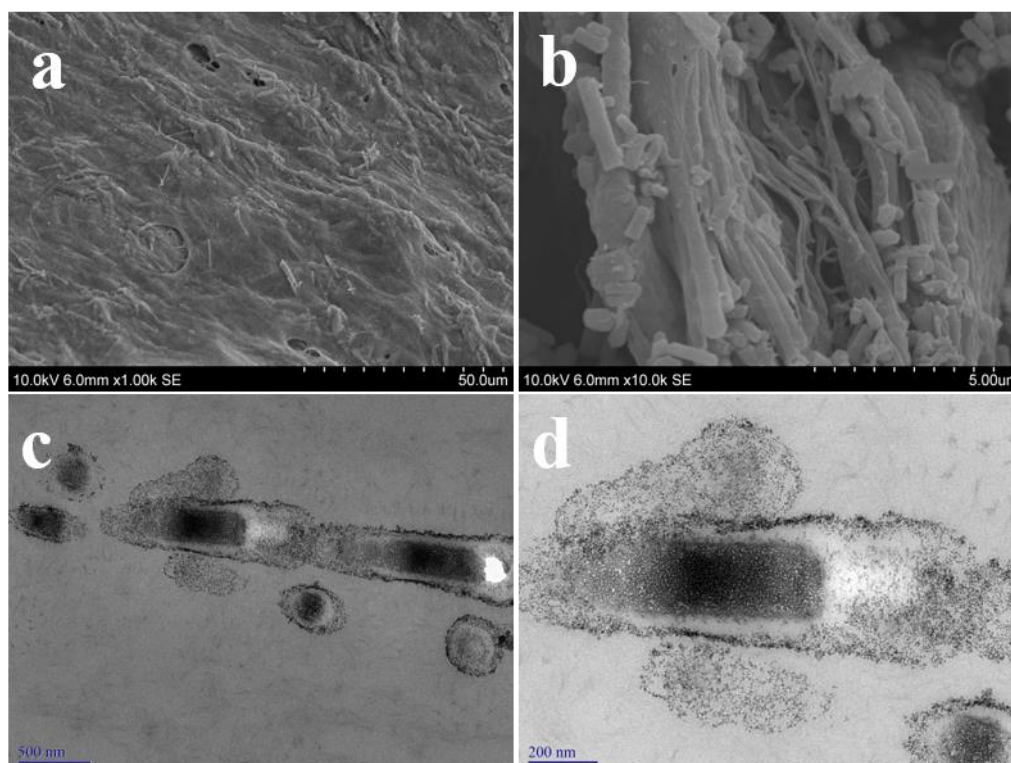


**Figure 4-19** SEM and TEM images of SiNR@Fe<sub>3</sub>O<sub>4</sub>-collagen composite hydrogels under external magnetic field

Subsequently, we prepared three samples of magnetic hydrogel composites. **Figure 4-20** shows the three configurations that we have explored.

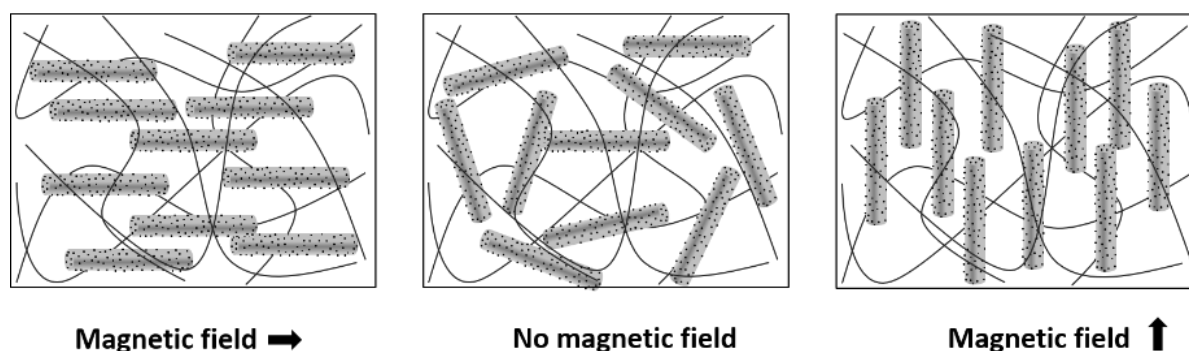


**Figure 4-20** Three different magnetic composite hydrogel models. (ii) horizontal magnetic field, (i) without magnetic field, (iii) vertical magnetic field

These hydrogels were formed directly in the polymer capsule used for SQUID measurements, allowing to preserve their initial orientation when placed in the machine

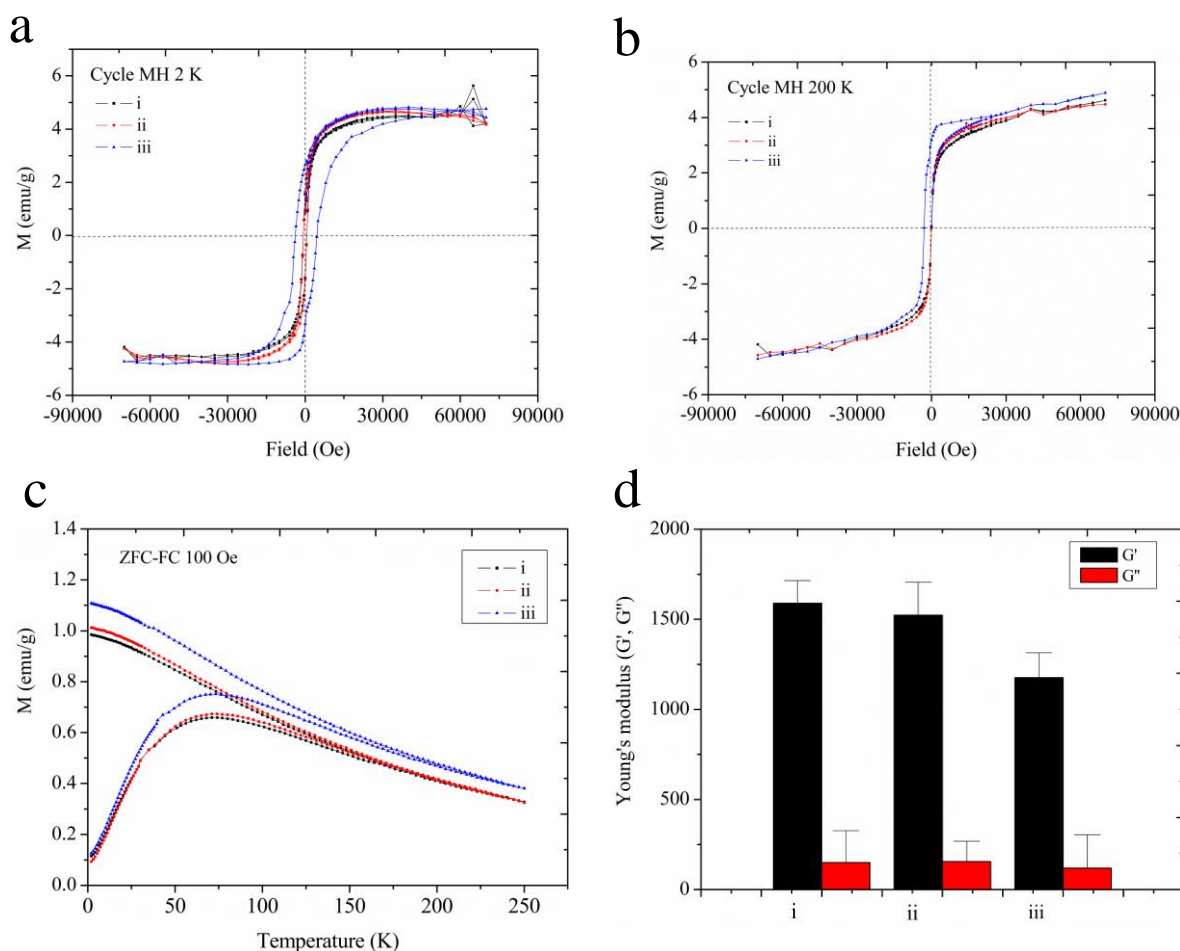


**Figure 4-21** Hysteresis cycle recorded at (a) 2 K and (b) 200 K, (c) FC/ZFC curves and (d) rheological properties for magnetic composite hydrogels (i) without magnetic field. (ii) with horizontal magnetic field and (iii) with vertical magnetic field

While composite hydrogels obtained without applied magnetic field or field applied parallel to the upper gel surface have almost identical magnetic behaviors, sample (iii) is clearly different: it presents a wider hysteresis at 2K and higher magnetizations in FC/ZFC curves (**Figure 4-21**). Although we don't have a clear explanation for this difference, it should be related to the relative direction of the magnetic field within the SQUID equipment compared to the favored orientation of the nanorods within the samples.

Accordingly, when the rheological properties under a shear stress parallel to the upper gel surface were measured, a lower  $G'$  value was found for sample (iii). It is in agreement with the

fact that nanorods oriented perpendicular to the shear direction should have less impact on the deformation of the network compared to nanorods oriented in the same direction.

Thus both methods are able to distinguish between vertically-oriented samples and horizontally or random composites. Although the effects are small, they at least indicate that the applied magnetic field had a measurable impact on the organization of the nanorods. This is a first validation of our strategy but we unfortunately lacked of sufficient time to progress further in the study of these original magnetic nanocomposites

## 4.4 Conclusion

Nanocomposite hydrogels combining biomacromolecules and nanomaterials offer versatile platforms whose mechanical properties can be adjusted and that can also exhibit multiple functions. Whereas the benefits of associating collagen hydrogels and silica nanomaterials have already been described, we have explored here a new approach using silica nanorods. The first expected benefit of the rod shape of the particles was to achieve a higher improvement of the mechanical properties of the collagen network at a lower silica concentration compared to spherical nanoparticles. What we found out is that this change of morphology also has an important impact on silica-collagen interactions as well as on the response of fibroblast cells to the composite materials.

With the aim of minimizing the required amount of silica nanoparticles to be introduced in the collagen network, we have designed and use magnetically-responsive nanorods. Our first results show that this strategy allows, at least to some extent, to control the orientation of the mineral particles within the collagen network. There is indeed plenty of room for improvement, including the preparation of smaller nanorods, while preserving their high aspect ratio, that may orient more easily along the external magnetic field in the initial collagen solution. Besides, another interesting option to explore in the future is to study the effect of such an external field once the nanocomposite is formed, which may open broad application prospects in biomedical applications whether in imaging, drug release, or medical treatment.

## References

1. Peppas, N.; Huang, Y.; Torres-Lugo, M.; Ward, J.; Zhang, J., Physicochemical foundations and structural design of hydrogels in medicine and biology. *Annual review of biomedical engineering* **2000**, 2, (1), 9-29.

2. Bertassoni, L. E.; Cecconi, M.; Manoharan, V.; Nikkhah, M.; Hjortnaes, J.; Cristino, A. L., et al. Yang, Y., Hydrogel bioprinted microchannel networks for vascularization of tissue engineering constructs. *Lab on a Chip* **2014**, 14, (13), 2202-2211.
3. Xu, J.; Strandman, S.; Zhu, J. X.; Barralet, J.; Cerruti, M., Genipin-crosslinked catechol-chitosan mucoadhesive hydrogels for buccal drug delivery. *Biomaterials* **2015**, 37, 395-404.
4. Lin, S.; Yuk, H.; Zhang, T.; Parada, G. A.; Koo, H.; Yu, C.; Zhao, X., Stretchable hydrogel electronics and devices. *Advanced Materials* **2016**, 28, (22), 4497-4505.
5. Xing, Q.; Yates, K.; Vogt, C.; Qian, Z.; Frost, M. C.; Zhao, F., Increasing mechanical strength of gelatin hydrogels by divalent metal ion removal. *Scientific reports* **2014**, 4, 4706.
6. Thévenot, C.; Khoukh, A.; Reynaud, S.; Desbrières, J.; Grassl, B., Kinetic aspects, rheological properties and mechanoelectrical effects of hydrogels composed of polyacrylamide and polystyrene nanoparticles. *Soft Matter* **2007**, 3, (4), 437-447.
7. Luo, R.-C.; Lim, Z. H.; Li, W.; Shi, P.; Chen, C.-H., Near-infrared light triggerable deformation-free polysaccharide double network hydrogels. *Chemical Communications* **2014**, 50, (53), 7052-7055.
8. Park, M.-Y.; Lim, S.; Lee, S.-W.; Park, S.-E., Relative parameter contributions for encapsulating silica-gold nanoshells by poly (N-isopropylacrylamide-co-acrylic acid) hydrogels. *Macromolecular research* **2009**, 17, (5), 307-312.
9. Fratzl, P., Collagen: structure and mechanics, an introduction. In *Collagen*, Springer: **2008**; pp 1-13.
10. Sheu, M.-T.; Huang, J.-C.; Yeh, G.-C.; Ho, H.-O., Characterization of collagen gel solutions and collagen matrices for cell culture. *Biomaterials* **2001**, 22, (13), 1713-1719.
11. An, B.; Lin, Y.-S.; Brodsky, B., Collagen interactions: Drug design and delivery. *Advanced drug delivery reviews* **2016**, 97, 69-84.
12. Helary, C.; Abed, A.; Mosser, G.; Louedec, L.; Letourneur, D.; Coradin, T., et al. Meddahi-Pellé, A., Evaluation of dense collagen matrices as medicated wound dressing for the treatment of cutaneous chronic wounds. *Biomaterials science* **2015**, 3, (2), 373-382.
13. Thanikaivelan, P.; Narayanan, T.; Gupta, B.; Reddy, A.; Ajayan, P., Nanobiocomposite from Collagen Waste Using Iron Oxide Nanoparticles and Its Conversion Into Magnetic Nanocarbon. *Journal of nanoscience and nanotechnology* **2015**, 15, (6), 4504-4509.

14. Antman-Passig, M.; Shefi, O., Remote magnetic orientation of 3D collagen hydrogels for directed neuronal regeneration. *Nano letters* **2016**, 16, (4), 2567-2573.
15. Desimone, M. F.; H  lary, C.; Rietveld, I. B.; Bataille, I.; Mosser, G.; Giraud-Guille, M.-M., et al. Coradin, T., Silica–collagen bionanocomposites as three-dimensional scaffolds for fibroblast immobilization. *Acta Biomaterialia* **2010**, 6, (10), 3998-4004.
16. Yu, H.-S.; Lee, E.-J.; Seo, S.-J.; Knowles, J. C.; Kim, H.-W., Feasibility of silica-hybridized collagen hydrogels as three-dimensional cell matrices for hard tissue engineering. *Journal of biomaterials applications* **2015**, 30, (3), 338-350.
17. Wang, X.; H  lary, C.; Coradin, T., Local and sustained gene delivery in silica-collagen nanocomposites. *ACS applied materials & interfaces* **2015**, 7, (4), 2503-2511.
18. Alvarez, G. S.; H  lary, C.; Mebert, A. M.; Wang, X.; Coradin, T.; Desimone, M. F., Antibiotic-loaded silica nanoparticle–collagen composite hydrogels with prolonged antimicrobial activity for wound infection prevention. *Journal of Materials Chemistry B* **2014**, 2, (29), 4660-4670.
19. Kuijk, A.; van Blaaderen, A.; Imhof, A., Synthesis of monodisperse, rodlike silica colloids with tunable aspect ratio. *Journal of the American Chemical Society* **2011**, 133, (8), 2346-2349.
20. Qu, H.; Tong, S.; Song, K.; Ma, H.; Bao, G.; Pincus, S., et al. O'Connor, C., Controllable in situ synthesis of magnetite coated silica-core water-dispersible hybrid nanomaterials. *Langmuir* **2013**, 29, (33), 10573-10578.



## Conclusions and perspectives

### *Summary*

A variety of structures based on silica nanomaterials are highly attractive in the field of biology, not only because of their variable and tunable physical and chemical properties and surface characteristics, but also because of their generally good biocompatibility. Although silica has been successfully explored for many applications in the biomedical field, such as bioimaging, drugs and gene delivery, there is still a long way to go for the design of materials with clinical application prospects. Therefore, studying the physical and chemical properties of silica nanomaterials and their behavior in a biological environment remains of high importance. In particular, in many *in vivo* situations, nanoparticles are very likely to interact cells incorporated in a 3D extracellular matrix. Such considerations have been so far poorly addressed in the literature and were the focused on this PhD project.

With this aim, we conducted a large diversity of investigations involving silica nanomaterials, including physicochemical properties and biodegradation studies of nanostructured silica nanoparticles, control drug release and imaging performance of multifunctional silica nanoplatfroms from 2D to 3D models, as well as preparation, structural properties and biological effects of multifunctional composite collagen hydrogels using rod-shaped silica nanomaterials.

First of all, we prepared and characterized PEGylated fluorescent silica nanoparticles with various internal structures (core-shell bio-composite, multilayered and hollow mesoporous) whose morphology and surface properties were extensively characterized. Their degradation behavior in a buffer, a culture medium and in contact with human dermal fibroblasts were studied. Results showed that the degradation pathways are very similar in all conditions although their structure, composition and their precise environment can impact on the kinetics of the degradation. A major outcome of this work is that, under these conditions, the silica nanoparticles must be mainly considered as degraded by hydrolysis and not biodegraded. This suggests that the intracellular fate of silica-based nanomaterials can be controlled and predicted on the basis on physico-chemical considerations. However, when these nanomaterials are used in actual



biological applications, different situations will be encountered. In this case, complex biological systems make prediction of nanoparticle behavior more difficult. Therefore, from a practical point of view, the setting of biomimetic environmental conditions may contribute to a more reliable *in vitro* assessment of functional nanomaterials.

With this in mind, for the second step, we synthesized nanoparticles for theranostic applications and evaluated the influence of a three-dimensional environment on their functionality. Specifically, we use the hollow silica nanoparticles prepared above as a carrier to form an ultra-thin manganese dioxide sheet *in situ* on the surface by reduction reaction and further physically attached a targeting AS1411 aptamer. The main advantage of our strategy is the use of  $\text{MnO}_2$  as both a gating system and source of MRI-active species, making our system rather simple to prepare. A number of characterizations were conducted that indicate the existence of the  $\text{MnO}_2$  nanosheets on the surface of the hollow silica nanoparticles. The hollow nanomaterials have a high specific surface area and a small microporous structure which results in a high loading of doxorubicin hydrochloride. Both drug release profiles and MR imaging under physiological conditions indicate that the modified nanomaterials have pH and redox responsiveness characteristics. Cell experiments in 2D cultures showed that the nanoplatform has low cytotoxicity and confirmed that the degradation of manganese dioxide sheets allows for controlled release and enhanced imaging performances. Subsequently, we used a collagen hydrogel as a 3D model to evaluate the functional properties of the nanoplatforms. We found that the particles could find their way through the collagen network to the cells, with the help of the targeting aptamer. However the T1 relaxation time is lower in these 3D compared to the suspension, which can be attributed to the reduced stability of the nanoplatform within the collagen gel. This again enlightens the interest of designing and using 3D biomimetic models to evaluate nanomaterials prior to *in vivo* studies.

Another possible application of silica nanoparticles in the biomedical field is their incorporation in 3D scaffolds for tissue repair or engineering. Previous silica-biopolymer 3D nanocomposite hydrogels have shown good biocompatibility and high application prospects in wound dressings. However many questions remain about the benefit/risk balance of such composites compared to polymer-only hydrogels. Here, for the first time to our knowledge, highly anisotropic silica nanoparticles (ca. 300 nm in diameter and 3  $\mu\text{m}$  in length) were used to form a composite hydrogel with type I

collagen. A thorough investigation of the structure of these composites was performed, evidencing strong interactions between silica particles and collagen that result in a striking alignment of collagen fibrils along the main axis of the silica nanorods. Our results show that silica nanorods can improve the mechanical stability of the materials but that too high silica contents can be cytotoxic to human fibroblasts. Moreover, too high collagen concentrations were also unsuitable as they slow down the colonization of the protein network by the cells, exposing them to unfavorable interactions with the nanorods. One step further, it was possible to prepare magnetic silica nanorods by the *in situ* thermal decomposition of  $\text{Fe}(\text{acac})_3$  yielding to a homogenous coating of magnetite nanoparticles. By using an external magnetic field, it was possible to align these magnetic silica rods in a collagen solution prior to gelation. Magnetic hydrogels were thus prepared whose directional alignment not only causes a change in the magnetic properties of the composite hydrogel, but also affects its mechanical properties. Such magnetically operable hydrogel composites have great application prospects as multifunctional biomaterials where the magnetic properties may be used for controlled drug release and imaging.

## Outlook

Altogether, in this work, we could fully take advantage of the versatility of silica nanochemistry to design a wide range of nanomaterials with various shapes and internal nanostructures and associate them with other inorganic nanoparticles ( $\text{MnO}_2$ ,  $\text{Fe}_3\text{O}_4$ ), molecules (doxorubicin, aptamer) and biomacromolecules (type I collagen). Some proofs of concept of their potentiality as drug release and/or imaging systems have been provided and there is plenty of room for future improvement in terms of composition, morphology and structure.

However, understanding and controlling their behavior in a biological context- from *in vitro* degradation to *in vivo* metabolism-, although being a necessary stage before clinical application, remains highly challenging. Indeed not only silica “bio-chemistry” is still poorly known but, as multi-functional nanoparticles and composites are receiving more and more attention for the development of diagnostic and therapeutic integrated materials, the complexity of the underlying mechanisms is also increasing. Here our approach has been mainly focused on chemical and physico-chemical aspects. It is very clear that a more biological approach is now necessary, especially to identify

in a more detailed manner (*i.e.* besides viability tests) the cellular response to the different materials we prepared. Identification of the biological pathways driving the intracellular trafficking of silica nanoparticles would be of particular interest.

We had hypothesized that going from a 2D to a more biomimetic 3D context would have a significant impact on silica-based nanomaterials reactivity and fate in a biological context, and therefore on their biofunctionality. Our results emphasize that two cases must be distinguished, whether the particles are present at the time of the formation of the 3D matrix and are therefore embedded within it or if they are added afterwards. Accordingly, the fact that the cells are encapsulated within the hydrogels or seeded on their surface also has strong consequences on their interactions with particles and/or their dissolution products. Facing this complexity, it seems more reasonable in to select the configuration that more closely mimic the targeted *in vivo* situation. Meanwhile future efforts must be devoted to elaborate more complex biomimetic matrices, for instance by introducing additional important components of the extracellular matrix, such as hyaluronic acid or glycosaminoglycans, in the collagen hydrogels

## List of Abbreviations

<b>US:</b>	Ultrasound
<b>CT:</b>	Computed tomography
<b>MR:</b>	Magnetic resonance
<b>SPECT:</b>	Single-photon emission computed tomography
<b>PET:</b>	Positron emission tomography
<b>PEG:</b>	Polyethylene glycol
<b>PEI:</b>	Polyethylenimine
<b>PLGA:</b>	Poly(lactic-co-glycolic acid
<b>PVP:</b>	Polyvinyl pyrrolidone
<b>PLLA:</b>	Poly (L-lactic acid)
<b>PAA:</b>	Polyacrylic acid
<b>PHPMA:</b>	Poly(N-(2-hydroxypropyl)methacrylamide
<b>PVA :</b>	Poly(vinyl acetate
<b>FITC:</b>	Fluorescein isothiocyanate
<b>FRET</b>	Fluorescence resonance energy transfer
<b>TEOS</b>	Tetraethyl orthosilicate
<b>APTES</b>	(3-Aminopropyl)triethoxysilane
<b>NPs</b>	Nanoparticles
<b>SiNPs</b>	Silica nanoparticles



## List of Figures

<b>Figure 1-1</b> Nanotechnology is a highly interdisciplinary field of science .....	15
<b>Figure 1-2</b> Various of nanomaterials in biomedical applications <sup>9</sup> .....	16
<b>Figure 1-3</b> Applications of nanomedicine in clinical theranostics.....	17
<b>Figure 1-4</b> Five types of common routes of drug administration .....	18
<b>Figure 1-5</b> Different types of nanocarriers. (a) lipid; (b) polymer; (c) inorganic nanoparticles .....	20
<b>Figure 1-6</b> The structure of liposome nanocarriers .....	21
<b>Figure 1-7</b> Architecture of dendrimer involves different construction units .....	23
<b>Figure 1-8</b> Polymeric micelles as supramolecular nanomedicines .....	24
<b>Figure 1-9</b> Schematic illustration of QD-aptamer (DOX) Bi-FRET system .....	25
<b>Figure 1-10</b> A schematic diagram of preparing DOX-MWCNTs-PEG-TAT for drug delivery .....	25
<b>Figure 1-11</b> A dual-stimuli triggered anti-cancer drug delivery system based on GNRs.....	27
<b>Figure 1-12</b> The hydrolysis (1) and condensation (2a, 2b) reaction of silicon alkoxide precursors.....	28
<b>Figure 1-13</b> The process of sol-gel in silica formation with different conditions.....	29
<b>Figure 1-14</b> Two mainly methods to synthesis of silica nanoparticles. (a) Stöber method; (b) Reverse phase microemulsion.....	30
<b>Figure 1-15</b> Silica nanoparticles with various shape: cone, sphere, matchstick, hollow rod .....	32
<b>Figure 1-16</b> Soft template synthesis of mesoporous silica nanoparticles .....	33
<b>Figure 1-17</b> Synthesis routes of periodic mesoporous organosilicas.....	34
<b>Figure 1-18</b> The structures of the hollow and rattle-type mesoporous silica nanoparticles .....	35
<b>Figure 1-19</b> The three approaches for silica/polymer nanocomposites synthesis. (a) Surface modification. (b) Internal encapsulation. (c) Uniform compounding.....	37
<b>Figure 1-20</b> Schematic (a-e) pictures of different structure of core-shell nanoparticles .....	38
<b>Figure 1-21</b> Mechanisms and regulating factors of the degradation of silica nanoparticles in aqueous media <sup>122</sup> . .....	41

<b>Figure 1-22</b> Structure of mesoporous silica nanoparticles applied for delivery of siRNA .....	43
<b>Figure 1-23</b> Passive or active mechanisms of silica nanoparticles applied for drug delivery .....	45
<b>Figure 1-24</b> Schematic illustration for the fabrication of pH-responsive carrier systems based on polyelectrolyte multilayer-MSN .....	46
<b>Figure 1-25</b> Schematic illustration of the behavior of dual-responsive release system in aqueous medium .....	47
<b>Figure 1-26</b> Cross-linked nanocellulose hydrogel and their applications in wound dressing .....	49
<b>Figure 1-27</b> Schematic illustration of typical nanocomposite hydrogels from hydrogels and drug-loaded nanoparticles .....	50
<b>Figure 1-28</b> The hierarchical structure of collagen fibers .....	52
<b>Figure 1-29</b> (A) Collagen hydrogel. (B) Collagen sponge. (C) Collagen hydrogel scaffold. (D) Hematoxylin and eosin staining of collagen hydrogel scaffold .....	52
<b>Figure 1-30</b> Various configurations for gene delivery in silica-collagen nanocomposites: (1) particles out/cells in; (2) particles and cells in; (3) particles in/cells out .....	53
 <b>Figure 2-1</b> The structure of PEGylated silica nanoparticles (BSNPs, PSNPs, HSNPs) .....	76
<b>Figure 2-2</b> Process for preparing PEGylated BSA@silica nanoparticles .....	77
<b>Figure 2-3</b> Process for preparing PEGylated double-layered PEI-silica nanoparticles .....	77
<b>Figure 2-4</b> Process for preparing PEGylated hollow mesoporous silica nanoparticles .....	78
<b>Figure 2-5</b> Process for measurement of nanoparticles by DLS .....	79
<b>Figure 2-6</b> The principle of zeta point measurement .....	80
<b>Figure 2-7</b> Schematic view of imaging and diffraction modes in TEM .....	81
<b>Figure 2-8</b> TEM images of the as-prepared PEGylated fluorescent silica nanoparticles: (a, d) BSNPs; (b, e) PSNPs and (e, f) HSNPs .....	84
<b>Figure 2-9</b> Particle size distribution of a) BSNPs; b) PSNPs; c) HSNPs d) BSNPs just after sonication measured by DLS in deionized water .....	85

<b>Figure 2-10</b> N <sub>2</sub> -sorption isotherms at 77 K and pore size distribution of HSNPs particles .....	87
<b>Figure 2-11</b> Evolution of the zeta potential of BSNP, PSNP and HSNP nanoparticles with pH.....	87
<b>Figure 2-12</b> FTIC fluorescence spectra in solution and within silica nanoparticles: a) FITC, 1.0 µg/mL and b) BSNPs; c) PSNPs; d) HSNPs 50 µg/mL, respectively.....	88
<b>Figure 2-13</b> TEM imaging of the structural evolution of silica nanoparticles in PBS after (a-c) one and (d-f) two weeks .....	89
<b>Figure 2-14</b> TEM imaging of the structural evolution of silica nanoparticles in DMEM culture medium after (a-c) on week and (d-f) two weeks. (scale bar = 100 nm) .....	89
<b>Figure 2-15</b> Evolution of the content of the culture medium over 2 weeks in the presence of silica nanoparticles as monitored by the fluorescence intensity of FITC-labelled soluble forms of silica .....	90
<b>Figure 2-16</b> (a) NHDF cells after incubation with silica nanoparticles at various concentrations (25-400 µg/mL) for 2 days. (b) NHDF cells after incubation with 400 µg/mL of silica nanoparticles at various time intervals .....	91
<b>Figure 2-17</b> Fluorescence optical imaging of human dermal fibroblast cells after (a-c) 7 days and (d-f) 14 days of contact with 400 µg/mL silica nanoparticles .....	92
<b>Figure 2-18</b> TEM images of NHDF cells after (a-c) 1 week and (d-f) 2 weeks of contact with 400 µg/mL silica nanoparticles .....	92
<b>Figure 2-19</b> Evolution of the content of the NHDF cells culture medium as monitored by the fluorescence intensity of FITC-labelled condensed and soluble forms of silica (filled symbols) and soluble forms only (open symbols) (a) over 1 week in the presence of silica nanoparticles and (b) over 1 additional week in a fresh medium ...	93
<b>Figure 2-20</b> Fluorescence optical imaging of human dermal fibroblast cells after 7 days of contact with 400 µg/mL BSNPs nanoparticles using FITC-labelled BSA. (Scale bar = 40 µm).....	95
<b>Figure 2-21</b> Schematic representation of the degradation pathways of BSNPs, HSNPs and PSNPs in DMEM culture medium.....	96
 <b>Figure 3-1</b> Schematic illustration of the preparation of HMSN@MnO <sub>2</sub> (DOX)/apt and the drug release mechanism .....	110



<b>Figure 3-2</b> TEM images of (a) HMSNs, (b) HMSN@MnO <sub>2</sub> /apt, (c) HMSN@MnO <sub>2</sub> /apt after GSH treatment and the corresponding digital images from left to right (d, e, f).....	110
<b>Figure 3-3</b> (a, c) N <sub>2</sub> adsorption-desorption isotherm at 77 K and (b,d) the corresponding pore diameter distribution obtained by the BJH method on the adsorption branch for (a,b) HMSNs and (c,d) HMSNs@MnO <sub>2</sub> .....	111
<b>Figure 3-4</b> Absorbance spectra of the HMSNs after addition of KMnO <sub>4</sub> with different concentrations and the corresponding insert images with color change. (b) Absorbance spectra of the DOX, MnO <sub>2</sub> , and a series of nanoparticles .....	112
<b>Figure 3-5</b> XPS analysis of the HMSNs@MnO <sub>2</sub> (DOX)/apt nanoparticles: (a) full XPS spectrum with atomic analysis and deconvoluted signals with proposed attributions at the (b) Mn2p, (c) Si2p and (d) O1s levels .....	113
<b>Figure 3-6</b> Deconvoluted XPS spectra of (a) C1s, (b) N1s for HMSNs@MnO <sub>2</sub> (DOX)/apt.....	114
<b>Figure 3-7</b> Images of HMSNs@MnO <sub>2</sub> /apt suspensions in different conditions, (a) pH 7.4; (b) pH 5.5; (c) pH 7.4, 5mM GSH; (d) pH 7.4, 10mM GSH; (e) pH 5.5, 5mM GSH .....	114
<b>Figure 3-8</b> Cumulative release of the HMSNs@MnO <sub>2</sub> (DOX)/apt in different conditions: (blue) pH 7.4, (black) pH 5.5, (green) pH 7.4+ 5 mM GSH, (red) pH 5.5 + 5 mM GSH. Control samples: (pink) free DOX and (pale green) uncoated HSMNs(DOX) in PBS solution (pH =7.4) .....	115
<b>Figure 3-9</b> T1-weighted MR images of HMSN@MnO <sub>2</sub> /apt under different conditions. (i: H <sub>2</sub> O; 2: pH 7.4; 3: pH 5.5; iv: pH 7.4 + GSH 5 mM and v: pH5.5 + GSH 5 mM). (b) 1/T1 versus Mn concentrations for HMSN@MnO <sub>2</sub> /apt at (black) pH 7.4 and (red) pH 5.5 + 5 mM GSH.....	117
<b>Figure 3-10</b> (a) HeLa cell viability after incubation with DOX, HMSNs@MnO <sub>2</sub> , HMSNs@MnO <sub>2</sub> (DOX) and HMSNs@MnO <sub>2</sub> (DOX)/apt for 24 h as a function of DOX dose. (b) Cell cytotoxicity of HMSNs@MnO <sub>2</sub> (DOX)/apt after 24 h of incubation with NHDF, HeLa and NHDF cells treated with GSH as a function of particle concentration .....	117
<b>Figure 3-11</b> Fluorescent images of (a) NHDF cells incubated with HMSNs@MnO <sub>2</sub> (DOX)/apt nanoparticles, (b) NHDF cells incubated with HMSNs@MnO <sub>2</sub> (DOX)/apt nanoparticles and 5 mM GSH, (c) HeLa cells incubated with HMSNs@MnO <sub>2</sub> (DOX)/apt nanoparticles, (d) HeLa cells incubate.....	118

<b>Figure 3-12</b> (a) Viability of NHDF and HeLa cells within different types of 3D collagen/silica nanocomposites after 24 h of incubation. (b) SEM image of nanoparticles (red arrow) interacting with HeLa cells (white arrow) within collagen hydrogels.....	120
<b>Figure 3-13</b> Fluorescent images of HeLa cells incubated with HMSNs@MnO <sub>2</sub> (DOX)/apt within a collagen hydrogel for 24 h, (a) bright field; (b) blue channel (DAPI); (c) red channel (DOX) and (d) merge .....	121
<b>Figure 3-14</b> T1-weighted MR images of collagen gels (a) without cells, (b,c) with NHDF cells and (d-f) with HeLa cells after 3h diffusion of (b,d) 0.2 mg/mL HMSNs@MnO <sub>2</sub> (DOX) (c,e) 0.2 mg/mL HMSNs@MnO <sub>2</sub> (DOX)/apt and (f) 0.4 mg/mL HMSNs@MnO <sub>2</sub> (DOX)/apt.....	121
 <b>Figure 4-1</b> Schematic illustration of the preparation of Fe <sub>3</sub> O <sub>4</sub> attached silica nanorods.....	139
<b>Figure 4-2</b> TEM images of silica nanorods with different magnifications .....	140
<b>Figure 4-3</b> The FTIR spectra of silica nanorods .....	140
<b>Figure 4-4</b> TEM images of (a-b) Fe <sub>3</sub> O <sub>4</sub> nanoparticles, (c-d) SiNR@Fe <sub>3</sub> O <sub>4</sub> materials.....	141
<b>Figure 4-5</b> The XRD patterns of SiNR@Fe <sub>3</sub> O <sub>4</sub> with standard reference magnetite (JCPDS No.19-0629).....	142
<b>Figure 4-6</b> XPS spectrum at the Fe2p level of SiNR@Fe <sub>3</sub> O <sub>4</sub> nanomaterials .....	142
<b>Figure 4-7</b> The FTIR spectra of SiNR@Fe <sub>3</sub> O <sub>4</sub> nanomaterials.....	143
<b>Figure 4-8</b> SiNR@Fe <sub>3</sub> O <sub>4</sub> dispersed in distilled water are efficiently attracted by an external magnetic field.....	143
<b>Figure 4-9</b> (a) Hysteresis cycle recorded at temperature 2 K and 200 K for SiNR@Fe <sub>3</sub> O <sub>4</sub> . Inset are the hysteresis cycles at low fields (b) ZFC and FC magnetization curves of SiNR@Fe <sub>3</sub> O <sub>4</sub> at 100 Oe .....	144
<b>Figure 4-10</b> Schematic illustration of the preparation of SiNRs-collagen hydrogels.....	145
<b>Figure 4-11</b> SEM of SiNR-collagen composite hydrogels. (a) 10 mg/mL, (b) 20 mg/mL and (c) 30 mg/mL collagen with concentrations of SiNRs : 1-30 mg.mL <sup>-1</sup> , 2-60 mg.mL <sup>-1</sup> , 3-90 mg.mL <sup>-1</sup> , 4-120 mg.mL <sup>-1</sup> .....	145
<b>Figure 4-12</b> Storage (G') of SiNR-collagen composite hydrogels with various composition.....	146

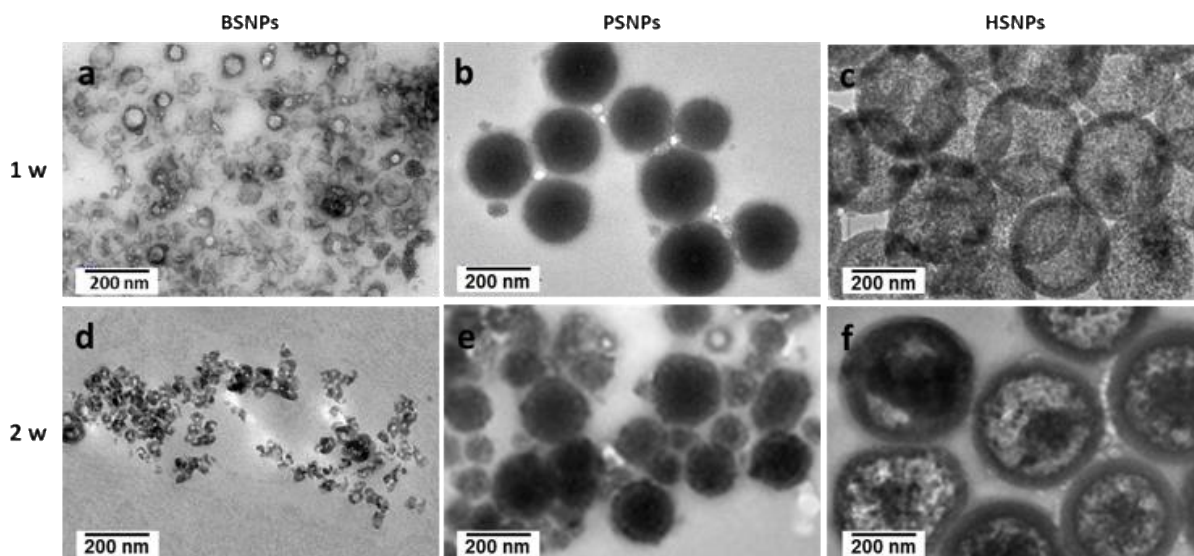
<b>Figure 4-13</b> SEM and TEM of (a) 20 mg/mL collagen. (b) 10 mg/mL collagen, 120 mg.mL <sup>-1</sup> SiNRs. (c) 20 mg/mL collagen, 60 mg.mL <sup>-1</sup> SiNRs. (d) 30 mg/mL collagen, 30 mg.mL <sup>-1</sup> SiNRs .....	148
<b>Figure 4-14</b> Metabolic activity of surface-cultured fibroblasts (Alamar blue assay) (a) at constant G' (ca. 2 kPa) value and (b) at constant SiNRs content. Control collagen hydrogels (20 mg/mL) at day 1 were normalized to 100%. Results are expressed as mean SD from triplicates experiments. * indicates statistical significance ( p < 0.05) from Student test.....	150
<b>Figure 4-15</b> Fluorescence (1-24 h, 2-72h) and SEM (3-72 h) images of NHDF incubated with (a) 20 mg/mL collagen. (b) 10 mg/mL collagen, 120 mg.mL <sup>-1</sup> SiNRs. (c) 20 mg/mL collagen, 60 mg.mL <sup>-1</sup> SiNRs. (d) 30 mg/mL collagen, 30 mg.mL <sup>-1</sup> SiNRs.....	151
<b>Figure 4-16</b> Fluorescence (1-24 h, 2-72h) and SEM (3-72 h) images of NHDF incubated with (a) 5 mg/mL collagen. (b) 10 mg/mL collagen (c) 20 mg/mL collagen (d) 30 mg/mL collagen, all supplemented with 30 mg.mL <sup>-1</sup> SiNRs.....	153
<b>Figure 4-17</b> SEM and TEM images of SiNR@Fe <sub>3</sub> O <sub>4</sub> -collagen composite hydrogels.....	154
<b>Figure 4-18</b> Magnetically controlled nanomaterial behavior in 10 mg/mL collagen solution. (a) No magnetic field. (b) Magnetic fields in the opposite direction (N-N, or S-S). (c) Magnetic fields in the same direction (N-S, S-N). (d-f) Magnetic response time is 0, 2, 5 min, respectively .....	155
<b>Figure 4-19</b> SEM and TEM images of SiNR@Fe <sub>3</sub> O <sub>4</sub> -collagen composite hydrogels under external magnetic field.....	156
<b>Figure 4-20</b> Three different magnetic composite hydrogel models. (ii) horizontal magnetic field, (i) without magnetic field, (iii) vertical magnetic field.....	157
<b>Figure 4-21</b> Hysteresis cycle recorded at (a) 2 K and (b) 200 K, (c) FC/ZFC curves and (d) rheological properties for magnetic composite hydrogels (i) without magnetic field. (ii) with horizontal magnetic field and (iii) with vertical magnetic field .....	157

## List of Tables

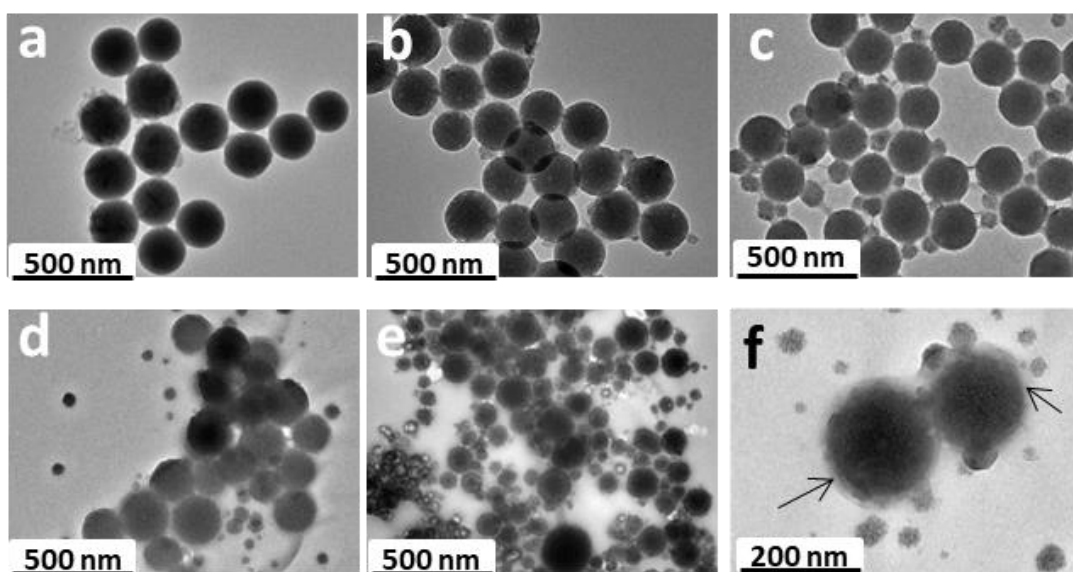
<b>Table 2-1</b> Mean diameter Dm from DLS and TEM, Zeta potential $\zeta$ in deionized water and culture medium.....	85
<b>Table 2-2</b> Average diameter (by DLS) and zeta-potentials of nanoparticles at various stages of their synthesis .....	86
<b>Table 3-1</b> Mean diameter Dm from DLS with corresponding polydispersity index (PDI) and Zeta potential $\zeta$ in deionized water .....	110
<b>Table 4-1</b> Selected composite hydrogels with similar mechanical properties .....	147



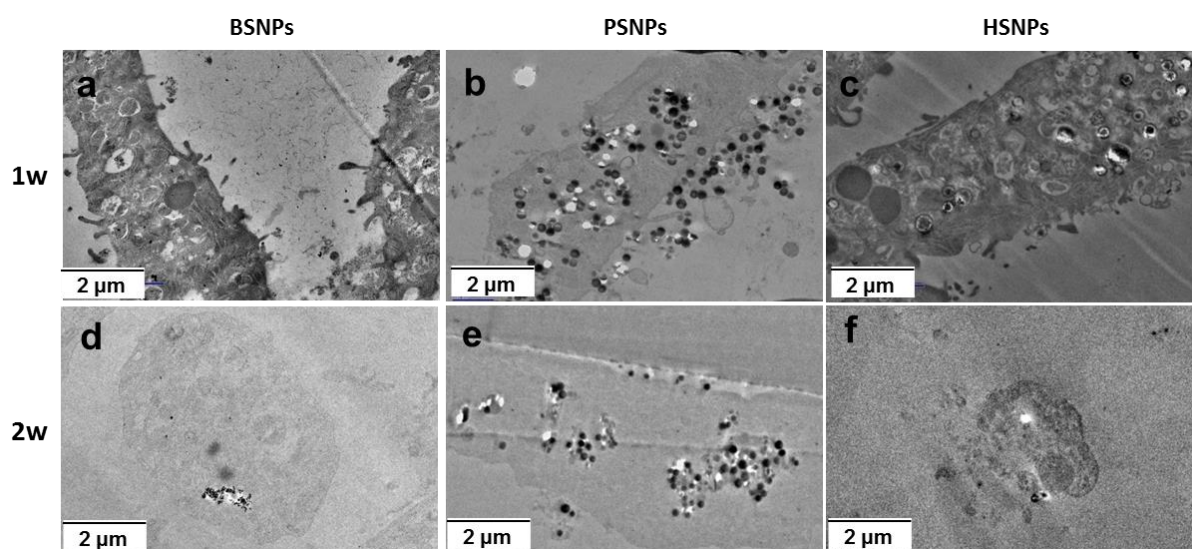
## Appendix



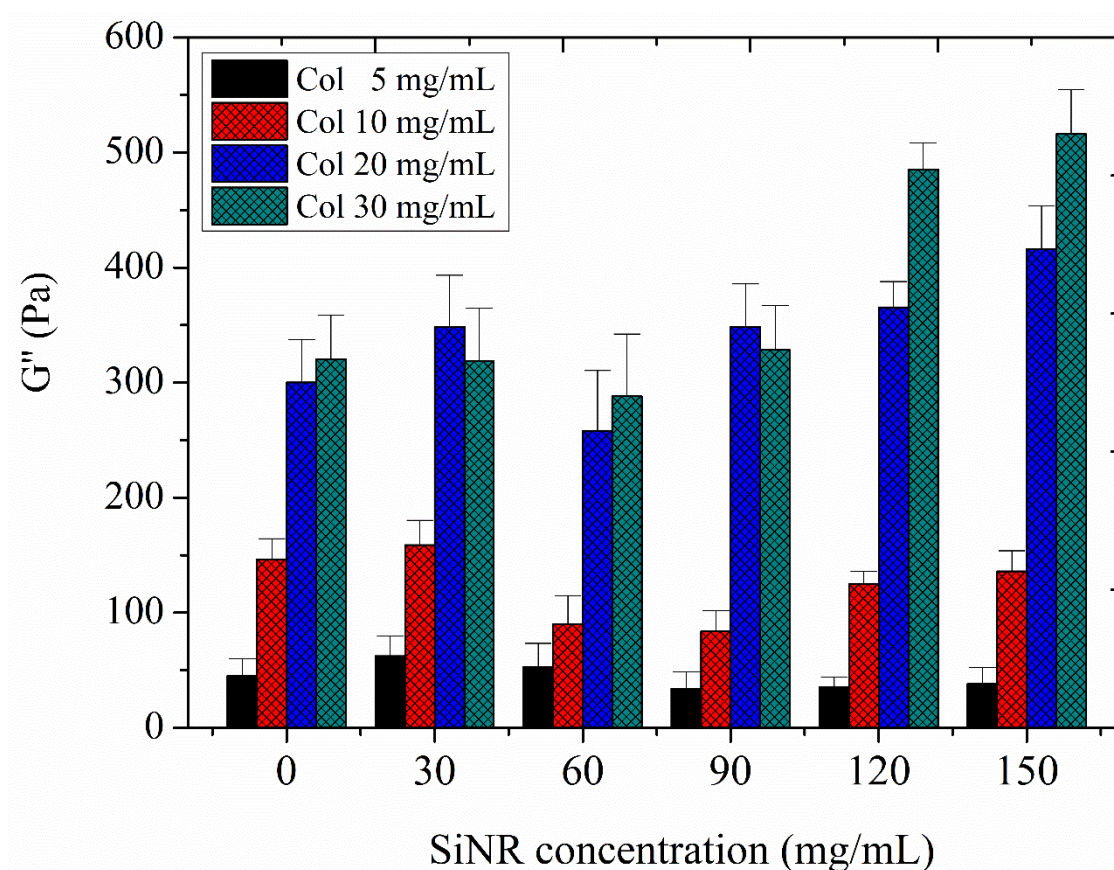
**Appendix 1** TEM imaging of the structural evolution of silica nanoparticles in DMEM culture medium after (a-c) on week and (d-f) two weeks. (scale bar = 200 nm)



**Appendix 2** Additional TEM imaging of the structural evolution of PSNPs nanoparticles in DMEM culture medium after (a-e) 0, 1, 3, 7, 14 days, and f) the magnification image of the PSNPs in the medium in 7 days.



**Appendix 3** TEM images of NHDF cells after (a-c) 1 week and (d-f) 2 weeks of contact with 400 µg/mL silica nanoparticles



**Appendix 4** Loss modulus ( $G''$ ) of SiNR-collagen composite hydrogels with various composition